



Enhanced Burning of Oil Slicks

Contract No. E15PC00004

**Final Report
September 29, 2017**

WPI Personnel:

Dr. Kemal S. Arsava, Dr. Hayri Sezer,
Panyawat (Oat) Tukaew, Trevor J. Borth, David J. Petrow,
Dr. Shijin P. Kozhumal, Glenn Mahnken, Prof. Robert G. Zalosh,
Prof. Jose L. Torero,
Prof. Ali S. Rangwala (PI)

USCG Personnel:

Kurt A. Hansen, Scott Fields, Lt. Chuck Clark

BSEE Personnel:

Karen Stone, Caroline Laikin-Credno

Contact Information

Dr. Ali S. Rangwala
Worcester Polytechnic Institute
Department of Fire Protection
Engineering
Phone: (508) 831-6409
rangwala@wpi.edu

Table of Contents

List of Figures	iv
Acknowledgements.....	ix
Summary	x
1. Outline.....	1
2. Approach.....	2
3. Phase I – Small and Intermediate Scale	5
3.1 Phase I-a, Small Scale	5
3.1.1 Experimental setup of Phase I-a	5
3.1.2 Effect of controlling parameters on burning behavior.....	7
3.2 Phase I-b, Intermediate Scale	16
3.2.1 Experimental setup of Phase I-b.....	16
3.2.2 Instrumentation of Phase I-b.....	16
3.2.3 Effect of cooling system	17
3.2.4 In-depth temperature profiles with the blanket.....	18
3.2.5 Optimization of coil height.....	19
3.2.6 Blanket-Coil tests	21
3.3 Outcomes of Phase I.....	32
4. Phase II - Large Scale	34
4.1 Optimization of blanket and coil for Phase II	34
4.1.1 Blanket thickness	34
4.1.2 Coil height	35
4.1.3 Number of coils	36
4.1.4 Conclusions of Phase II optimization.....	37
4.2 Experimental setup of Phase II.....	38
4.2.1 Fuel level control system	39
4.2.2 Instrumentation of Phase II.....	40
4.3 Test results and discussion	41
4.3.1 Mass loss rate.....	41
4.3.2 Temperature profiles.....	42

4.3.3 Gas emissions	43
4.4 Outcomes of Phase II	45
5. Phase III – Field Trials.....	46
5.1 Optimization of blanket and coil for Phase III.....	46
5.1.1 Blanket thickness	46
5.1.2 Coil height	47
5.1.3 Number of coils	48
5.1.4 Conclusions of Phase III optimization.....	48
5.2 Experimental setup of Phase III	49
5.2.1 Burning tank	49
5.2.2 Burner ring.....	50
5.2.3 Blanket-Mesh-Coil system	51
5.2.4 Fuel monitoring system	52
5.2.5 Instrumentation of Phase III	52
5.2.6 Outdoor gas emission sampling system.....	53
5.3 Test results and discussion	56
5.3.1 Mass loss rate.....	57
5.3.2 Temperature profiles.....	58
5.3.3 Heat flux near fuel surface.....	63
5.3.4 Gas emissions	64
5.3.5 Residue removal	65
5.4 Outcomes of Phase III.....	67
5.5 Scale-up of Phase II and III test results to ISB applications	70
5.5.1 Baseline regression rates	70
5.5.2 Blanket performance.....	71
5.5.3 Blanket + Coil performance	72
5.5.4 Blanket + Coil performance	73
6. Computational Model	74
6.1 Heat transfer in metal wool - fuel.....	76
6.2 The convective heat transfer coefficient	77
6.3 Initial and boundary conditions.....	78

6.4 Mass loss rate (burning rate)	79
6.5 Application to Phase I	82
6.5.1 Model Validation	84
6.5.2 Influence of metal wool thickness	86
6.6 Application to Phase II	90
6.7 Application to Phase III.....	91
6.8 Extinction for the blanket and the coil system	92
6.9 Conclusions of computational model.....	95
7. Conclusion and Future Study	97
References	98
Appendix A – TC measurement correction	100
Appendix B – Phase II – Fuel level control system.....	101
Appendix C – Details of Fire dynamics simulator (FDS).....	102
Appendix D – Details of Phase III burner ring	104
Appendix E – Outdoor gas emission sampling system (OGES).....	105
Appendix F – Detailed gas-fuel-water temperatures	107
Appendix G – Checklist of Phase III assembly and instrumentation	108
Appendix H – Checklist of Phase III experiments.....	111
Appendix I –Derivation of Heat Flux Values in Sec 5.5.	116

List of Figures

Figure 1: Flame Refluxer TM for ISB. The part in the flame zone is termed “collector” and the part in the liquid fuel is termed “heater”. The primary heat transfer mechanisms are indicated. Subscripts <i>fl</i> = flame, <i>f</i> = fuel, <i>w</i> = water, <i>c</i> = collector, <i>h</i> = heater, <i>rad</i> = radiation, <i>conv</i> = convection, <i>cond</i> = conduction.	2
Figure 2: Experiments at small, intermediate, and large-scale.	4
Figure 3: Experimental layout of Phase I	5
Figure 4: Schematic of small-scale (10 cm dia.) experimental setup	6
Figure 5: Photograph of the small-scale experimental setup (Phase I-a). HFG = heat flux guage, TC = thermocouple.	6
Figure 6: Phase I-a Instrumentation.....	7
Figure 7: TCs and HFGs location. $H_1 - H_4$ represents 4 horizontal TC’s, $V_1 - V_6$, represent 6 vertical TC’s and $F_1 - F_6$ show the 6 TC’s measuring temperature in the flame zone.....	7
Figure 8: Effect of blanket thickness on Mass Loss Rate.....	8
Figure 9: Temperature measurements (V_6) vs time with various aluminum blanket thicknesses ..	9
Figure 10: a) Material b) Porosity – Effect on Steady State Mass Loss Rate.....	9
Figure 11: Blankets with different porosities a) Fine (91%) b) Medium (95%) c) Coarse (98%) . Thickness of one wire is indicated on the photograph.....	10
Figure 12: Horizontal temperature distribution vs. time for baseline (a) and 0.25 cm copper blanket (b).....	11
Figure 13: Radiative heat flux at 25 cm away from the pool centerline.....	12
Figure 14: a) Initial coil geometry to be optimized by experimental study b) Placement of integrated blanket-coil into 10 cm test setup	12
Figure 15: Comparison of flame heights (not to scale) (a) baseline (b) enhanced by blanket-coil	13
Figure 16: Effect of coil wire diameter on Mass Loss Rate	13
Figure 17: Effect of coil height on Mass Loss Rate ($W_d = 0.2$ cm, $p = 0$, $D = 1$ cm)	14
Figure 18: Effect of coil pitch on Mass Loss Rate ($W_d = 0.2$ cm, $h_c = 10$ cm, $D = 1$ cm)	14
Figure 19: Effect of coil diameter on Mass Loss Rate.....	15
Figure 20: Experimental setup at Phase I-b.....	16
Figure 21: TC and HFG locations. 15, 20, 12, and 8 TCs measuring temperatures in the hot plume zone, hot gas zone, oil, and water, respectively.....	17
Figure 22: Effect of cooling system, oil and water temperatures at the center (average of 120 second after reaching steady state)	17
Figure 23: Temperature vs time at the center for “with blanket” tests a) water circulation off, b) water circulation on.....	18
Figure 24: Temperature vs time at the center for a) Baseline, b) with a 0.25 cm thick copper blanket.....	19
Figure 25: Plume temperature vs time at center	20
Figure 26: Hot gas temperature vs time at corner (4 cm away from the rim).....	20

Figure 27: Placement of integrated blanket-coil into 28 cm test setup..... 21

Figure 28: Bent coils due to excessive heat 22

Figure 29: A schematic representation of the heat transfer mechanism 22

Figure 30: (a) Time history of the average coil temperature, (b) the predicted increase in the mass loss rate per coil 24

Figure 31: a) Conical coils, b) Integrated blanket-coil system 25

Figure 32: Optimization of # of coils on circumference - Mass Loss Rate 26

Figure 33: Optimization of # of coils at center - Mass Loss Rate 27

Figure 34: Blanket-8 coils-mesh system a) Top view, b) Side view 28

Figure 35: Optimization of # of coils with Cu blanket and mesh- based on Mass Loss Rate 28

Figure 36: Vertical temperature profile at the center for baseline, blanket, and blanket-8 coils-mesh 29

Figure 37: Vertical temperature profile at the corner for baseline, blanket, and blanket-8 coils-mesh 30

Figure 38: HFG – (a) Baseline (b) Blanket-8 coils-mesh 31

Figure 39: Oil accumulation of blanket 32

Figure 40: The time trace of the regression rate during the gradual burning of the 0.7 m diameter dodecane pool fire for the blanket thickness of 0.15-0.75 cm 35

Figure 41: Heat release and smoke visualizations at two instances in a dodecane pool fire of 0.7 m diameter. Simulation is carried out using FDS 35

Figure 42: Sketch of the *CR* variables 36

Figure 43: Intermediate-scale experiments (a) Baseline – without blanket (b) Blanket-mesh before testing (c) Blanket-mesh immersed in oil (d) Blanket-mesh + 36 coils immersed in oil 38

Figure 44: Experimental setup at Phase II 38

Figure 45: Photograph of the intermediate-scale experimental setup (Phase II). TC = Thermocouple. 39

Figure 46: (a) Centrifugal pump for oil supply (b) Level control mechanism 40

Figure 47: Phase II gas emission measurement hood 41

Figure 48: Optimization of # of coils on circumference - Mass Loss Rate 42

Figure 49: Vertical fuel temperature profile at the center for baseline, blanket, and blanket-24 coils-mesh 42

Figure 50: Vertical fuel temperature profile at the corner for baseline, blanket, and blanket-24 coils-mesh 43

Figure 51: (a) oxygen concentration (b) carbon dioxide concentration (c) carbon monoxide concentration 44

Figure 52: Carbon monoxide per carbon dioxide production ratio 45

Figure 53: Regression rate 1.4 m diameter dodecane pool fire for the blanket thickness of 0.15-0.75 cm 46

Figure 54: Visualization of instantaneous heat release and smoke for a dodecane pool fire of 1.4 m diameter. Distances are in meters and time is in seconds. 47

Figure 55: Blanket-mesh-coil configurations tested in Phase III, a) Baseline, b) Blanket, c) Blanket with 32 coils, d) Blanket with 48 coils (Same coil height) e) Blanket with 48 coils (Various coil heights).....	49
Figure 56: United States Coastal Guard, Joint Maritime Test Facility.....	50
Figure 57: Phase III burner ring a) Sketch b) Picture from Phase III tests.....	50
Figure 58: Blanket-mesh-coil system at Phase III a) Cross-sectional sketch b) Blanket + 48 coils (Same height) c) Coils engulfed in the flame.....	51
Figure 59: a) Instrumentation at Phase III, b) Detailed TC array for gas-phase, fuel and water, c) Locations of instrumentation.	52
Figure 60: The Outdoor Gas Emission Sampling System (OGES) at Phase III.....	53
Figure 61: Shipping crate: Exterior on Little Sand Island (left) and Open during loading (right).	54
Figure 62: FR blanket prior to (left) and during assembly (right).	54
Figure 63: Burner assembly with legs only (left) and with full instrumentation including heat flux gauges, fuel layer thermocouples, and thermocouple towers, ~290 data points in all (right).	55
Figure 64: Thermocouple tower transportation housing showing tower-end sockets (left) and transport-ready configuration (left). During transport, the thermocouples would be facing down to prevent vibrational damage.....	55
Figure 65: OGES tower assembly and raising: A base was welded to support the 7 meter tower (left) then raised via forklift (center) and instrumented (left).....	56
Figure 66: MLR of Phase III at steady state, VH: Various heights, SH: Same height.	57
Figure 67: The ratio of burning enhancement to the total mass of Cu, VH: Various heights, SH: Same height.....	58
Figure 68: Baseline fuel-gas interface determination by using the temperature gradient at steady state a) Phase I-b, b) Phase II and c) Phase III.....	59
Figure 69: Flame geometry and plume temperature contours at steady state a) flame tilt angle on downwind direction b) baseline, c) blanket, d) blanket with 48 coils (SH), Contour units are in °C, AWS = Average wind speed, AFH = Average flame height.....	60
Figure 70: Temperature contours at steady state for baseline, blanket and blanket with 48 coils	61
Figure 71: Heat flux contours 5 cm above fuel surface at steady state a) baseline – total heat flux, b) blanket with 48 coils (VH) – total heat flux, c) baseline – radiative heat flux, d) blanket with 48 coils (VH) – radiative heat flux, Contour units are in kW/m ²	63
Figure 72: Carbon monoxide per carbon dioxide production ratio for the baseline, blanket and blanket with 48 coils (VH) cases.	64
Figure 73: Picture of the smoke plume a) Baseline, b) Blanket with 48 Coils (VH).	65
Figure 74: Post burn residue left on water a) Baseline, b) Blanket with 48 coils.....	66
Figure 75: ISB example showing post burn residue removal a) Baseline, b) Blanket and coils (The efficiency of blanket + 48 coils were used to calculate bbl).	67
Figure 76: Additional heat flux and regression rate at steady state, SH: Same height, VH: Various heights	68

Figure 77: Post burn residue and carbon monoxide per carbon dioxide production ratio, SH: Same height, VH: Various heights.....	69
Figure 78: The mass and heat transfer mechanisms for a pool fire with the presence of an immersed metal wool in fuel layer.....	74
Figure 79: Simplified geometry of the problem	75
Figure 80: Schematic representation of the saturated porous media	76
Figure 81: Assumed flame and gas phase temperature profile.	78
Figure 82: Mass loss rate mechanisms for the liquid pool fire with the immersed thermally conductive metal wool	80
Figure 83: Convective heat transfer coefficient for dodecane. Boiling curves of water and light hydrocarbons [15] is also shown for comparison.	83
Figure 84. Experimental and predicted MLR during burning of the dodecane pool fire for metal wool thickness of 0.5 and 0.25.....	84
Figure 85. The temperature variation of a monitor point at 0.5 cm beneath the fuel surface during gradual burning of the fuel, and corresponding experimental results.	85
Figure 86: Influence of thickness of metal wool on the burning rate.	86
Figure 87: Contours of the temperature colored by the temperature magnitude at different time of a) 220 s, b) 670 s Contour line of the convection heat transfer coefficient inside the blanket at different time of c) 220 s, d) 670 s. Contour line of temperature difference (< excess temperature of critical heat flux, i.e. nucleate boiling regions) e) 220 s, f) 670 s for aluminum wool thickness of 0.15 cm.	87
Figure 88: Contours of the temperature colored by the temperature magnitude at different time of a) 220 s, b) 670 s for aluminum blanket thickness of 0.25 cm. Contour line of the convection heat transfer coefficient inside the blanket at different time of c) 220 s, d) 670 s for aluminum blanket thickness of 0.25 cm. Contour line of temperature difference (< excess temperature of critical heat flux, i.e. nucleate boiling regions) e) 220 s, f) 670 s for aluminum blanket thickness of 0.25 cm.	88
Figure 89: Contours of the temperature colored by the temperature magnitude at different time of a) 220 s, b) 670 s for aluminum blanket thickness of 0.5 cm. Contour line of the convection heat transfer coefficient inside the blanket at different time of c) 220 s, d) 670 s for aluminum blanket thickness of 0.5 cm. Contour line of temperature difference (< excess temperature of critical heat flux, i.e. nucleate boiling regions) e) 220 s, f) 670 s for aluminum blanket thickness of 0.5 cm.	89
Figure 90: The ratio of nucleation induced MLR to total MLR for different thickness of metal wool.....	90
Figure 91: The time trace of the regression rate during the burning of the 0.7 m diameter dodecane pool fire for blanket thicknesses of 0.15-0.75 cm.....	91
Figure 92: The temperature contours inside the blanket region at steady state for blanket case..	91
Figure 93: The temperature contours inside the blanket region at steady state for blanket + coils.	92

Figure 94: Schematic representation of the energy storage calculation process. Thermocouple locations are mapped into a finer grid to obtain a better accuracy for the energy storage calculation. 92

Figure 95: Indepth temperature profile at steady state during the field trial (blanket only case). 94

Acknowledgements

This study is funded by the Bureau of Safety and Environmental Enforcement, US Department of the Interior, Washington, D.C., under Contract Number E15PC00004. The authors would like to thank John Farley, Hung V. Pham, Vance Murphy, Jeff Christopher, MK1 Lauren M. Goodell, Michael J. Hering, James E. Fletcher and Gulf Strike Team for support during large-scale outdoor tests performed at the US Coast Guard Joint Maritime Test facility in Little Sand Island in Mobile Bay.

Many thanks to WPI personnel, who made contributions during this study, including:

Tahar El-Korchi (Interim Department Head of FPE), Raymond T. Ranellone (WPI Fire Laboratory Manager), Michael W. Dorsey (Director of Research Communications), Colleen B. Wamback (Public Relations Specialist), Nadia Mofidi (graduate student), Mahesh S. Kottalgi (graduate student), Aravind Krishnan (graduate student), Honggang Wang (graduate student).

Summary

The objective of the proposed study is to develop a simple and robust system to directly burn off oil slicks in booms at higher burn rates and with lower particulate emissions as compared to current in situ burning practices. The operating principle of the technology, named *Flame RefluxerTM* (FR), is to transfer the collected radiative and convective heat generated by the combustion back to the fuel to create a feedback loop that sustains a significantly increased burning rate. The Flame Refluxer can be any object capable of creating a low thermal resistance pathway between the flame and the fuel. In the case of thin oil slicks, one possible configuration is a porous metal blanket (metal-wool) that is immersed in the oil slick with protruding conical coils attached to the blanket, thus enabling heat capture from the flame and transfer to the slick.

To systematically explore the effect of immersed objects on burning efficiency (i.e, burning rate enhancement and emission reduction), experiments were performed in circular oil slicks of varying diameters (0.1 m to 1.4 m). The experiments were divided into 3 phases based on diameter: small/intermediate scale (0.1m and 0.28 m), large-scale (0.7 m) and field trial (1.4 m).

The experimental results showed that the heat generated by the combustion and directed back to the fuel significantly enhanced regression rate while reducing smoke emission. In Phase I (small/intermediate scale), the regression rate of the fuel (ANS crude oil) was enhanced by 360% with blanket and multiple coils, respectively. In Phase II (large-scale), Flame RefluxersTM (blanket and coils) enhanced the burning efficiency by 185% and reduced the CO/CO₂ by 50% for a 1 cm oil slick on water layer.

Phase III tests were performed in the field and resulted in three major outcomes.

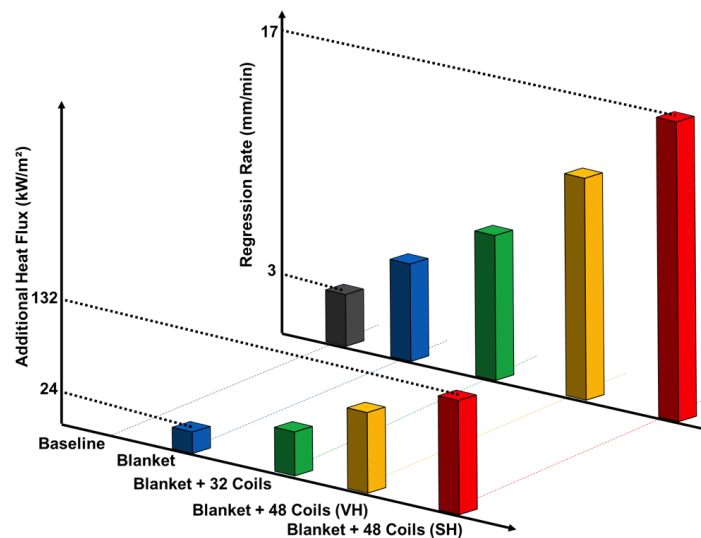


Figure i: Additional heat flux and regression rate at steady state, SH: Same height, VH: Various heights

The first outcome of Phase III tests was the significant increase in steady state regression rate achieved with the blanket-mesh-coil system as shown in Fig. i. The regression rate reached a value of 17 mm/min at 48 coils (with same height) placed on circumference. This is ~ 6 times of the baseline case (3 mm/min) which equates to an additional heat flux of 132 kW/m² transferred from the flame to the liquid fuel

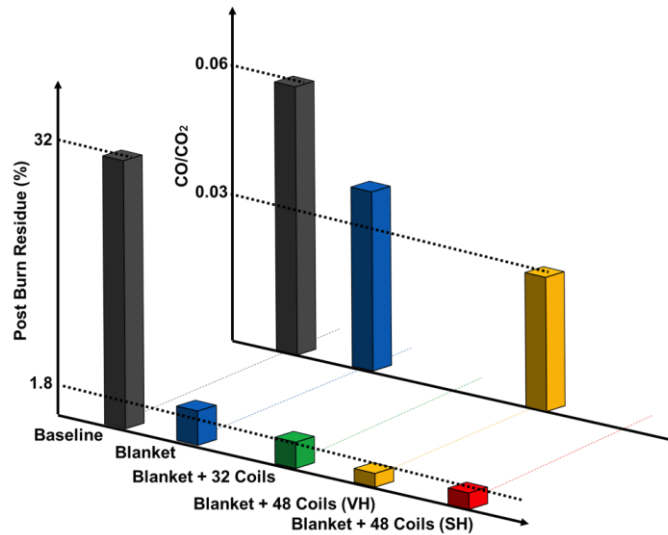


Figure ii: Post burn residue and carbon monoxide per carbon dioxide production ratio, SH: Same height, VH: Various heights

The second outcome, the reduction of post burn residue using the FR burner, is shown in Fig. ii. Only 1.8% of the oil was left on water when the blanket+48 coils (with same height) was used.

The third outcome, is the reduction in CO/CO₂ ratio in the steady state burning regime also shown in Fig. ii. The cleaner combustion was also observed visually. Figure iii compares the smoke plume in the steady state burning regime for the baseline and blanket+48 coils SH (with same height) cases.



Figure iii: Picture of the smoke plume a) Baseline, b) Blanket+48 Coils (SH)

Figure iii clearly shows that the color of the smoke plume is much lighter for the blanket+48 coils case. The lighter color of the smoke indicates a reduction in concentration of carbon particles due to more complete combustion.

In this exploratory study, the effect of the thickness, material and porosity of blanket and height and number of coils on burning efficiency was investigated. Additional parameters controlling heat collection and transfer by the Flame Refluxer™, such as geometry and shape of coils, need to be further examined.

The following publications resulted from this study:

Peer Reviewed Journal:

1. H. Sezer, K.S. Arsava, S.P. Kozhumal, and A.S. Rangwala, “The effect of embedded objects on pool fire burning behavior”, *International Journal of Heat and Mass Transfer*, Volume 108, Part A, 537-548, 2017.
2. H. Sezer, K.S. Arsava, and A.S. Rangwala, “Oil spill clean-up using immersed metal wool”, *Journal of Environmental Chemical Engineering*, In Press.
3. K.S. Arsava, G. Mahnken, A.S. Rangwala, “Enhanced oil spill cleanup in in-situ burning via immersed objects”, *Cold Region Science and Technology*, Under Review.

Peer Reviewed Conference:

1. K.S. Arsava, A.S. Rangwala and K. Hansen, “An Offshore In-situ Burn Enhanced by Floating Immersed Objects” The 40th AMOP Technical Seminar on Environmental Contamination and Response, October 3- 5, Canada, 2017.

Non-peer reviewed Conference:

1. K.S. Arsava, H. Sezer, and A.S. Rangwala, “A novel oil-water emulsion burner concept for offshore oil spill clean-up”, 2016 Mary Kay O’Connor Process Safety Center International Symposium, October 24-27, Texas A&M, 2016.
2. S. Arava, A. J. Walawalkar, K.S. Arsava, H. Sezer, and A.S. Rangwala, “A Novel In-situ Combustion Concept for Hazardous Waste Clean Up”, 10th U. S. National Combustion Meeting Organized by the Eastern States Section of the Combustion Institute, April 23-26, College Park, Maryland, 2017.
3. H. Sezer, K.S. Arsava, and A.S. Rangwala, “Burning Behavior of a Pool Fire on a Water Layer with a Thin Metal Wool”, 10th U. S. National Combustion Meeting Organized by the Eastern States Section of the Combustion Institute, April 23-26, College Park, Maryland, 2017.

Poster Presentation:

1. K.S. Arsava, S.P. Kozhumal, T.J. Borth and A.S. Rangwala, “Flame Refluxing: An Environment-friendly Alternative to Waste Incineration by Open Pit Burning”, Defense Innovation, October 3-5, 2017.

Conference Presentation:

1. K.S. Arsava, P. Tukaew, T.J. Borth, D.J. Petrow, H. Sezer, A.S. Rangwala, S. Fields, K. Hansen, “An offshore in-situ burn enhanced by floating immersed objects”, Clean Gulf 2017, December 5-7, 2017.

MS Thesis:

1. Tukaew (Oat) Panyawat. “Outdoor Gas Emission Sampling System: A Novel Method for Quantification of Fires in Outdoor Conditions”, MS Thesis, Worcester Polytechnic Institute, etd-050217-121733

1. Outline

This report is organized as:

- Section 2 present the scientific approach using small, intermediate, and large-scale experiments to explore the action of immersed objects during the burning of an oil slick on water.
- Section 3, 4, and 5 present experimental results for the small, intermediate, and large-scale experiments.
- Section 6 presents the mathematical model.
- Section 7 presents the conclusions and future work.
- Appendices A to J further discusses the below topics;
 - Appendix A: Procedure to correct the thermocouple (TC) measurements in hot gas zone.
 - Appendix B: Fuel level control system used in Phase II (0.7 m diameter burn)
 - Appendix C: Details of Fire dynamics simulator (FDS) in Phase II and Phase III (1.4 m diameter field test) that is used predict the optimum coil height.
 - Appendix D: CAD drawings and details of the 1.4 m diameter burner ring used in Phase III.
 - Appendix E: Details of outdoor gas emission sampling system (OGES) used in Phase III.
 - Appendix F: Detailed gas-fuel-water temperatures measured in Phase III.
 - Appendix G: Checklist of Phase III assembly and instrumentation
 - Appendix H: Checklist of Phase III experiments
 - Appendix I: Derivation of heat flux calculations for scaling-up of Phase II and III test results to ISB applications.

2. Approach

The current study aims to use the Flame Refluxer concept (BSEE Contract No. E14PC00043) to in situ burning (ISB) where the oil layer is thin (~ 1 cm) and in contact with a water sublayer. Figure 1 shows the Flame Refluxer™ (FR) and the controlling heat transfer mechanisms.

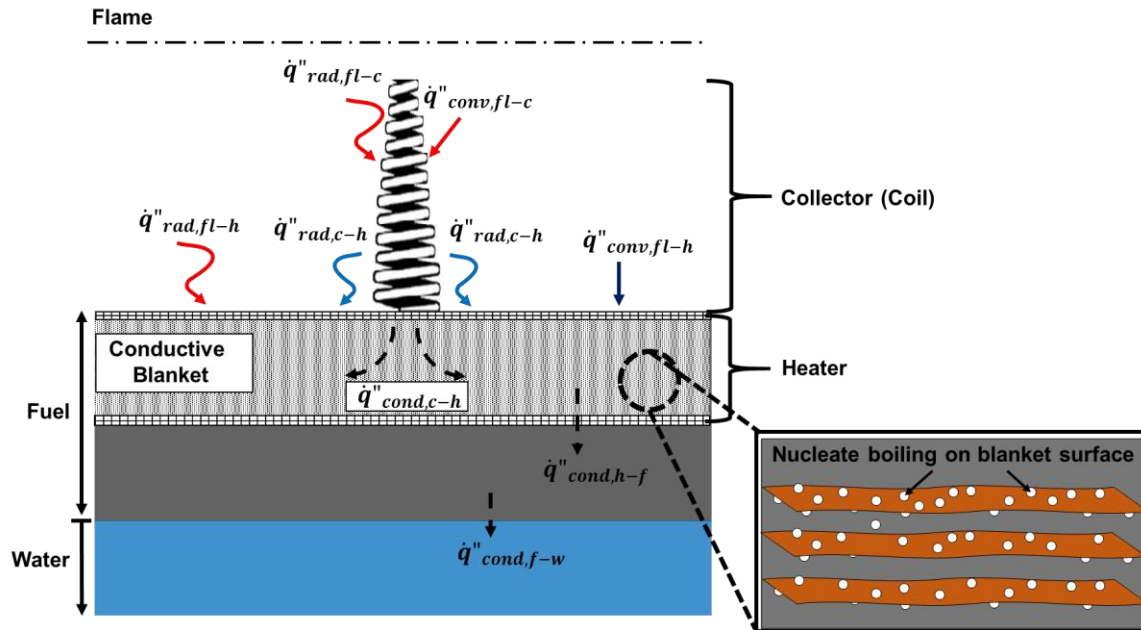


Figure 1: Flame Refluxer™ for ISB. The part in the flame zone is termed “collector” and the part in the liquid fuel is termed “heater”. The primary heat transfer mechanisms are indicated. Subscripts *fl* = flame, *f* = fuel, *w* = water, *c* = collector, *h* = heater, *rad* = radiation, *conv* = convection, *cond* = conduction.

As shown in Fig. 1, the FR comprises of two sections. The “collector” (coil in Fig. 1), and “heater” (blanket in Fig. 1). The coil collects the heat from the flaming region of the fire and transfers it to the blanket (heater), which is submerged inside the fuel layer (Fig. 1). Consequent conduction of heat to the liquid through the blanket (heater) significantly increases vaporization and therefore the crude oil burning rate. The enhancement of burning rate is mainly due to nucleate boiling occurring on the surface of the thin wires comprising the heater as shown in Fig. 1.

The efficiency of the FR is determined by different controlling parameters, which change with the type of cleanup application. For example, in BSEE Contract No. E14PC00043, a high efficiency burner was developed for fast and efficient cleanup of oil-water emulsions (Table 1). For the burner application, where skimmed oil-water emulsions were burned in a 1 m diameter pool, there were three controlling parameters: 1. number of FRs, 2. collector geometry and 3. heater geometry. With the change of application from a burner to ISB (current study) eight controlling parameters (listed in Table 1) were investigated.

Table 1. Comparison of the BSEE Contracts No. E14PC00043 and current study.

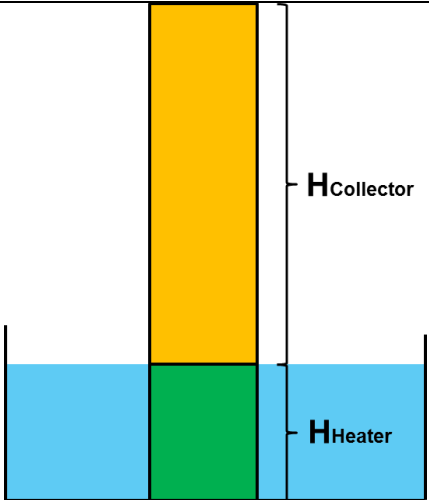
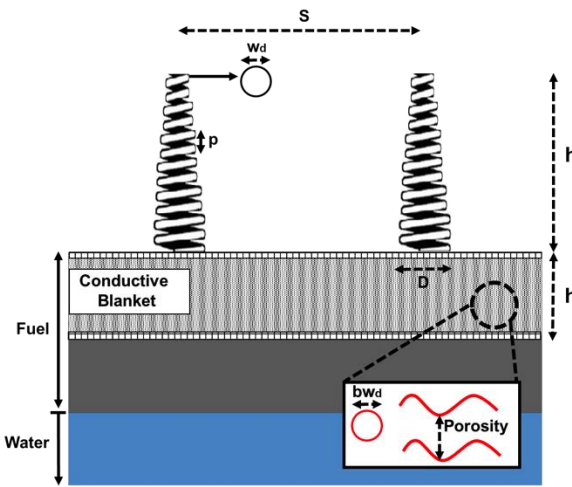
	
E14PC00043	E15PC00004
To design and construct a high efficiency burner for clean-up of oil water emulsions using combustion.	To design and construct an in-situ burn technology to clean up oil slicks.
Three controlling parameters, number of FRs, collector and heater height.	Eight controlling parameters, such as wire diameter (bw_d), porosity and thickness (h_b) of blanket and height (h_c), spacing (s), wire diameter (w_d), pitch (p) and base diameter (D) of coils.
D~1 m for practical application.	D>1 m for practical application.
Fuel thickness > 5 cm	Fuel thickness ~ 1 cm
No wicking	Wicking is possible because of blanket.

Figure 2 shows the progression of three phases of experimental testing adopted in this study:

Small and Intermediate Scale, Phase I comprising of 0.1 m (Phase I-a) and 0.28 m (Phase I-b) diameter tests to explore the parameters: blanket thickness, material, porosity and coil geometry controlling heat and mass transfer. The experiments and modeling during Phase I led to the design of indoor large-scale tests (Phase II)

Large Scale, Phase II comprising of seven tests performed in the WPI large-scale laboratory to determine the influence of number and configuration of coils on the burning efficiency and smoke emission. The experiments and computational model used as a guideline to design the field trials (Phase III).

Field Trial, Phase III comprising of proof of concept in an outdoor large-scale field test. Five experiments at the US Coast Guard outdoor test facility in Little Sand Island in Mobile Bay, Alabama (30 m x 12 m tank) showed that the FRs enhanced the burning efficiency by 500%, while reducing the gas emission by 50% over the baseline case.

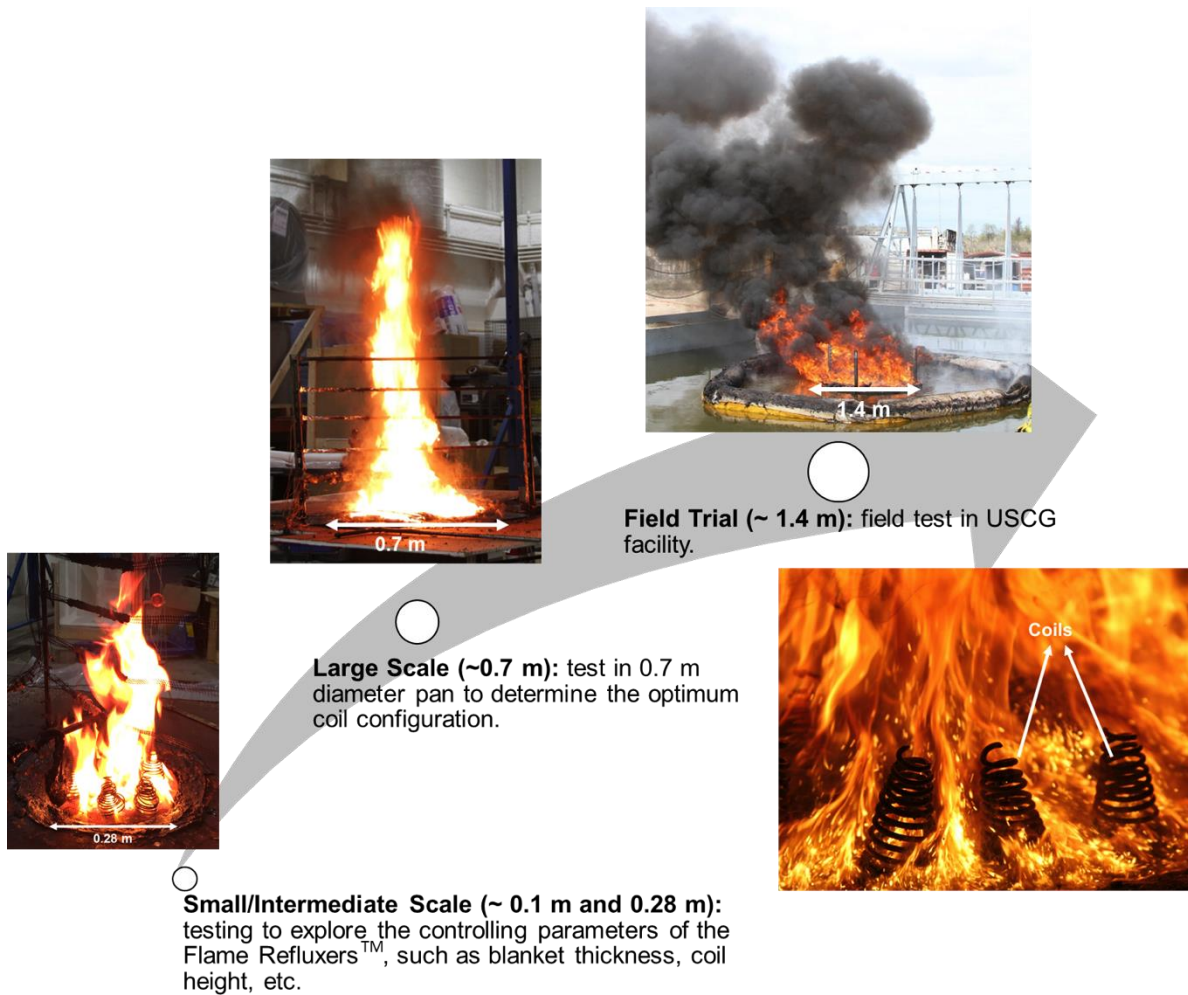


Figure 2: Experiments at small, intermediate, and large-scale.

The advantage of the proposed approach is that a large number of tests can be performed at the bench scale and intermediate scale. This enables systematic investigation of the controlling parameters related to the heat and mass transfer enhancement. The findings from the small and intermediate scale tests (Phase I) were validated with a limited number of large-scale (Phase II) and field trials (Phase III). This allowed a cost effective and fundamental understanding of the problem.

3. Phase I – Small and Intermediate Scale

The objective of Phase I is to explore the parameters controlling heat collection and transfer back to the fuel by the conductive blanket (heater) and coils (collector). The organization of Phase I is shown in Fig. 3. As shown in Fig. 3, in Phase I-a, various blankets (with different thickness, material, and porosity), and coils (with different wire diameter, length, pitch, and diameter) were tested in a 10 cm diameter dodecane pool fire configuration. The influence of changing the height and number of coils in a ~28 cm diameter pool fire was analyzed in Phase I-b. Alaska North Slope (ANS) crude oil was used in all Phase I-b tests.

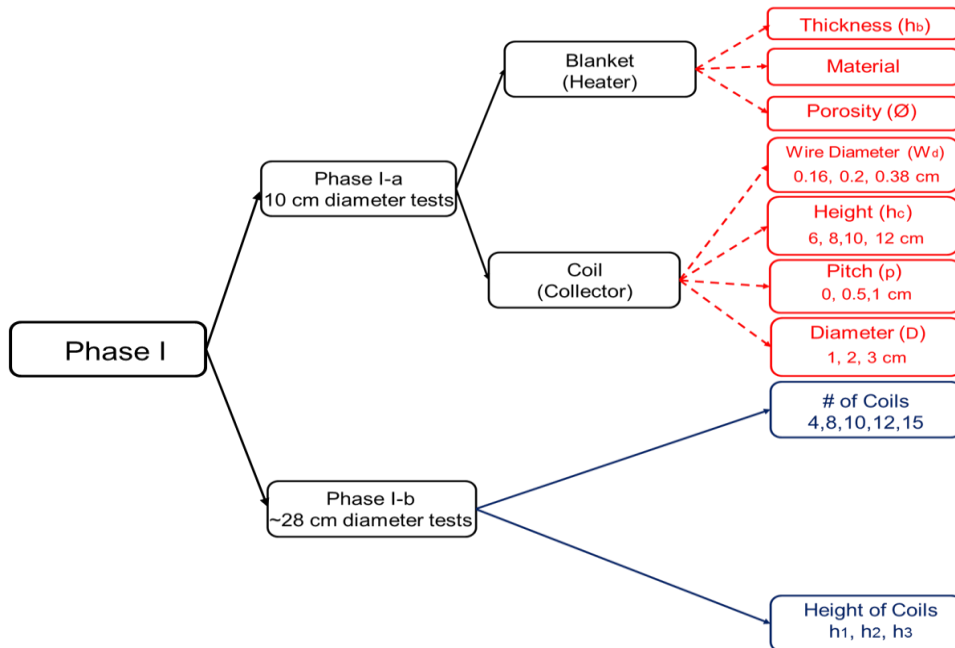


Figure 3: Experimental layout of Phase I

3.1 Phase I-a, Small Scale

A total of 30 experimental tests (10 sets with 3 repeats) were performed with various blanket thicknesses, materials and porosities.

3.1.1 Experimental setup of Phase I-a

Figure 4 shows the small-scale (10 cm diameter) test setup used during Phase I-a. Aluminum and copper blankets with various thicknesses and porosities were submerged in a 1 cm thick fuel - layer (dodecane) and the burning efficiencies were investigated. A 4 cm deep saline water (32 ppt) layer was maintained under the fuel layer.

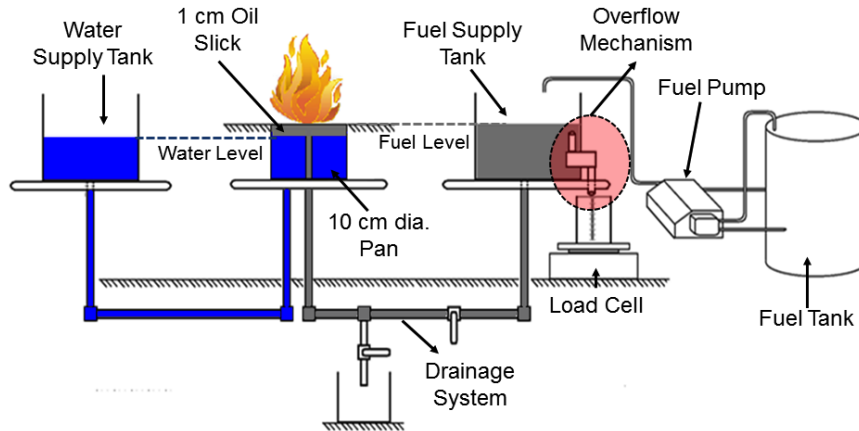


Figure 4: Schematic of small-scale (10 cm dia.) experimental setup

The fuel level was maintained using a gravity feedback system as shown in Fig. 4. An OMEGA FPU5MT peristaltic pump with a constant flow rate overfed the fuel supply tank. The overflow rate was measured by Sartorius ED6202S-CW load cell (Capacity of 6.2 kg with a sensitivity of 0.01 g and a factory uncertainty of ± 0.03 g). The mass loss rate was calculated by subtracting the overflow rate from the pumping rate. Figure 5 shows photograph of the experimental setup.

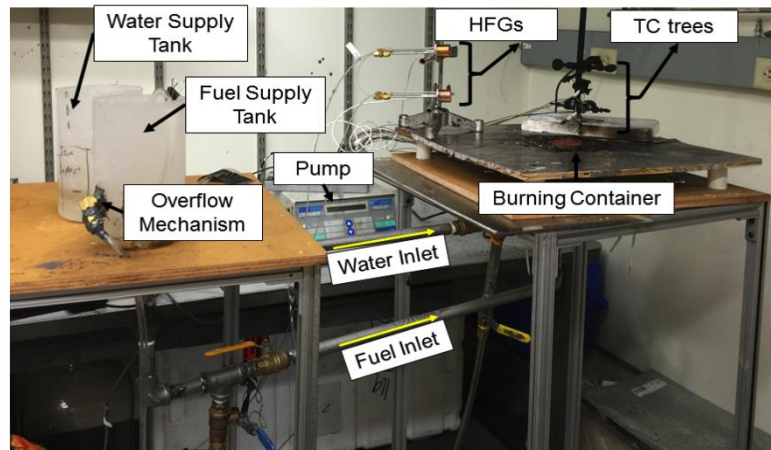


Figure 5: Photograph of the small-scale experimental setup (Phase I-a). HFG = heat flux gauge, TC = thermocouple.

Each test was performed for 15 min. Three repeat tests were performed for all cases to ensure that the experimental data is reproducible. A total of 17 K-type thermocouples (TC's) with a 0.025 cm (0.01") diameter were used to measure blanket, pan, fuel and water temperature at different locations shown in Fig. 6. The TC's were welded using K-type thermocouple wire and using an Omega Thermocouple and Fine Wire Welder "TL-WELD". Convective heat transfer from blanket (heater) to the fuel was measured by six TCs. Four TCs were horizontally placed 0.5 cm (0.2") below the fuel surface with 1 cm (0.4") spacing, while two TCs were used to measure the fuel surface and bottom temperatures. Additional four TCs were used to measure the vertical temperature distribution in water. Plume temperatures were measured by six TCs. All

thermocouples record temperatures at a sampling rate of 1 data point per second using a National Instrument "NI cDAQ-9178" which comprises 16 thermocouple channels per module (8 modules).

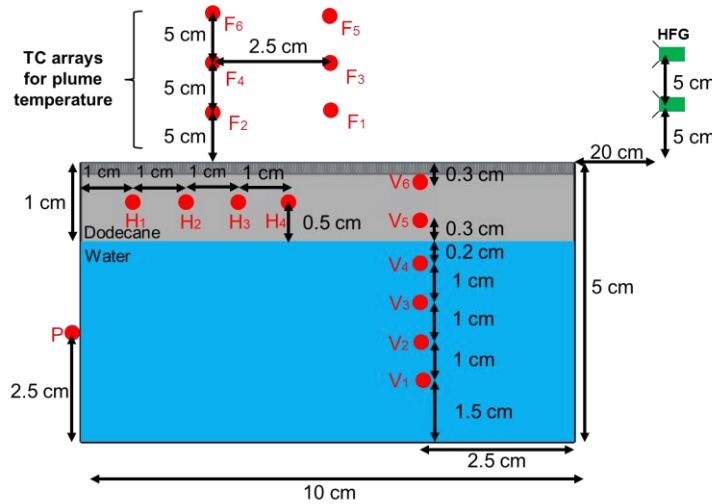


Figure 6: Phase I-a Instrumentation

Two Medtherm 64P-2-24 type Heat Flux Gauges (HFGs) were used to measure heat flux from the flame to the ambient (Fig. 7). HFGs were placed 20 cm (8") away from the burner with its measuring surface facing the flame.

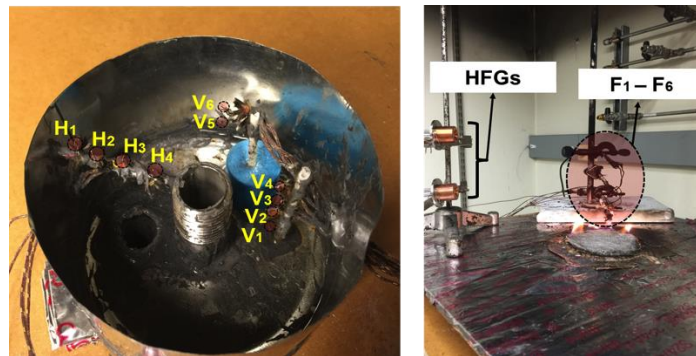


Figure 7: TCs and HFGs location. H₁ – H₄ represents 4 horizontal TC's, V₁ – V₆, represent 6 vertical TC's and F₁ – F₆ show the 6 TC's measuring temperature in the flame zone.

3.1.2 Effect of controlling parameters on burning behavior

3.1.2.1 Blanket thickness

To investigate the influence of the blanket thickness, aluminum (Al) blankets with thicknesses of 0.25, 0.5, and 1 cm (0.1", 0.2" and 0.4") were placed into the 1 cm deep fuel layer and the steady state mass loss rate and temperature profiles were analyzed. Figure 8 shows the comparison of the mass loss rates (average of 120 s after reaching steady state) for different Al blanket thicknesses. h_b represents blanket thickness.

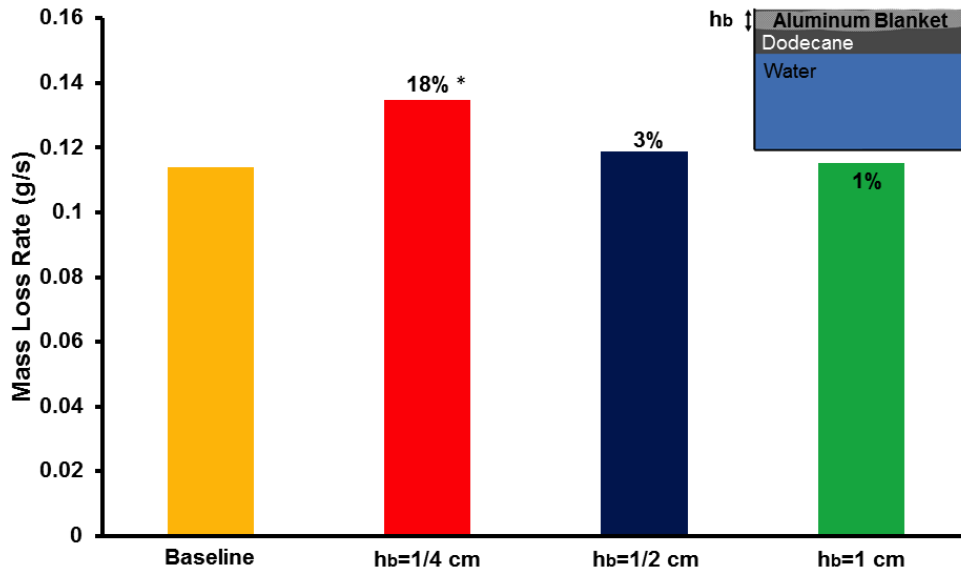


Figure 8: Effect of blanket thickness on Mass Loss Rate

* Enhancement over the baseline case.

When an Al blanket with 0.25 cm (0.1") is placed in the fuel, it is observed that the mass loss rate increases until a steady state of ~ 0.135 g/s is reached. This is ~ 18% increase over the baseline case (0.114 g/s). The experiments also show the importance of a “collector” in the Flame Refluxer. With blanket-only cases, the collection of heat from the flame is inefficient which is the main reason for the low increase. However, with just a blanket, there is still an increase because the blanket heats up by flame radiation and is efficient at laterally distributing the heat from the flame. The heated blanket also facilitates nucleate boiling which further enhances heat and mass transfer. However, as blanket thickness increases, the increase in the mass loss rate decreases as shown in Fig. 8 (compare $h_b = 1/4$ vs. $h_b = 1$). This is because at a critical thickness, the blanket losses more heat to the water sub-layer thereby behaving as a heat sink. The influence of the blanket thickness and heat loss by the water sublayer is further discussed in the mathematical model (Section 6).

The transient heating process is captured in Fig. 9 where the temperature of the fuel surface (V_6 in Fig 6.) for various Al blanket thicknesses is plotted as a function of time. It is observed that the presence of the conductive blanket increases the duration required to reach the steady state. Initially the flame heats up the blanket and the blanket mostly acts as a heat sink. Once this initial transient period passes, a steady state regime, where the blanket heats up the fuel and increases the mass loss rate is obtained. The results show that the contact between the blanket and water should be avoided. As shown in Fig 9., when the blanket is in contact with water ($h_b = 1$ cm) the steady state is reached after 8 min Also, the surface temperature in this case is lower than the baseline case.

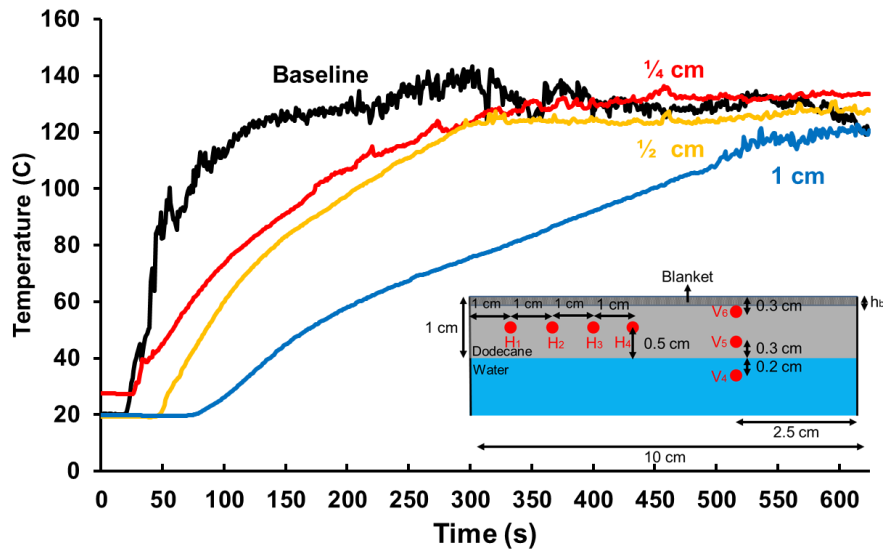


Figure 9: Temperature measurements (V_6) vs time with various aluminum blanket thicknesses

3.1.2.2 Blanket material and porosity

Two materials (Aluminum and Copper) and three different porosities were tested. Figure 10 shows the steady state mass loss rates for various materials and porosities.

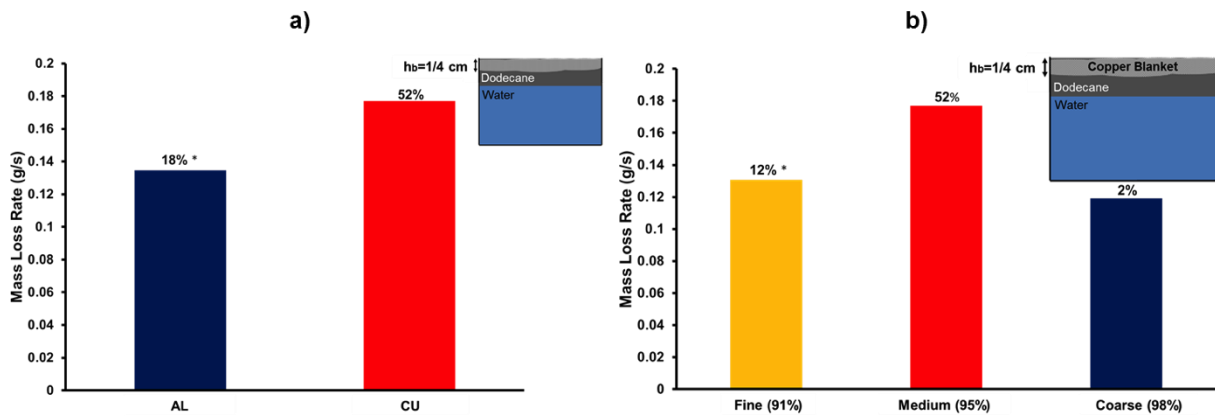


Figure 10: a) Material b) Porosity – Effect on Steady State Mass Loss Rate

* Enhancement over the baseline case.

The porosity of the blanket was calculated by the following equations;

$$V_s = m_b / \rho_b \tag{1}$$

where V_s , m_b , and ρ_b are the volume of the solid, mass of the blanket and density of the material. The volume of blanket, V_b , was calculated from Eq. 2, where t_b is blanket thickness.

$$V_b = \pi \times \left(\frac{D}{2}\right)^2 \times t_b \tag{2}$$

$$V_p = V_b - V_s \tag{3}$$

$$\text{Porosity} = V_p/V_b \tag{4}$$

Table 2 shows the porosity values of the blankets used in all three phases.

Table 2. Blanket porosities of Phase Ia-b, Phase II and Phase III

Case	Pool diameter (m)	Pool area (m ²)	Blanket thickness (m)	Weight of Cu wool (kg)	V _s × 10 ⁻⁶ (m ³)	V _b × 10 ⁻⁵ (m ³)	V _p × 10 ⁻⁵ (m ³)	Porosity (%)
Phase Ia - Fine	0.1	0.0078	0.0025	0.015	1.6778	1.9635	1.7957	91.4547
Phase Ia - Medium	0.1	0.0078	0.0025	0.008	0.8948	1.9635	1.8740	95.4425
Phase Ia - Coarse	0.1	0.0078	0.0025	0.004	0.4474	1.9635	1.9187	97.7212
Phase Ib	0.28	0.0615	0.0025	0.08	8.9485	15.3942	14.4989	94.1869
Phase II	0.7	0.3848	0.0035	0.8	89.4855	134.6962	125.7472	93.3564
Phase III	1.4	1.5393	0.0050	4.5	503.3561	769.6967	719.3546	93.4602

As shown in Fig. 10a, with the copper blanket, the burning enhancement ratio over the baseline (no blanket) increases from 18% to 52%. This increase is because of the higher thermal conductivity of copper (copper/aluminum≈~2). Figure 10b compares the mass loss rate for different porosities with Cu blanket. Fine porous blanket (91%) is made of 0.0051 cm (0.002") diameter wires, while medium (95%) and coarse porous (98%) blankets are made with 0.0127 cm (0.005") and 0.02 cm (0.008") diameter wires, respectively (Fig. 11). Experimental results showed that the fine porous blanket limits the fuel diffusion through the blanket and decreases the convective heat transfer from blanket to fuel. On the other hand, coarse porous blanket is not effective to transfer the heat to the fuel because of the larger void space. The maximum regression rate is obtained, reaching a value of 52%, with 0.25 cm thick medium porous (95%) copper blanket.

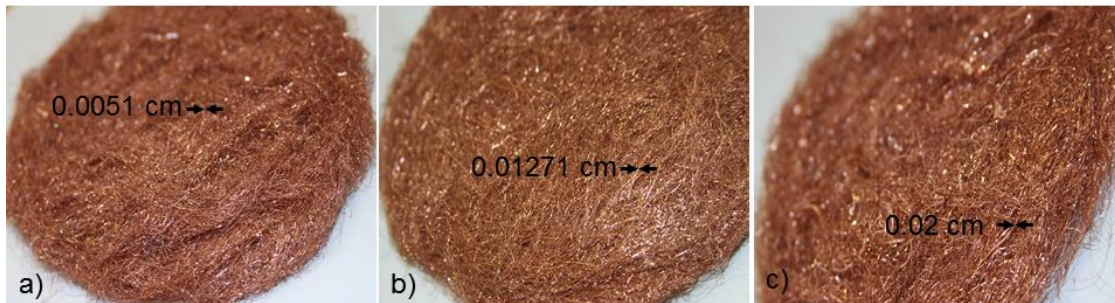


Figure 11: Blankets with different porosities a) Fine (91%) b) Medium (95%) c) Coarse (98%) . Thickness of one wire is indicated on the photograph.

Figure 12 shows the horizontal temperature distribution through the fuel (H_1 to H_4 in Fig. 6) for the baseline and copper blanket configuration with the maximum burning enhancement. Comparing Figures 12a and b show the capability of the blanket to distribute the heat laterally. For example, in the baseline case ΔT between H_1 to H_4 is ~ 30 °C as shown in Fig. 12a. However, ΔT between H_1 to H_4 ~ 0 °C when the blanket is added. The blanket also increases the volumetric heat capacity thereby heating the fuel layer up to 130 °C, while the maximum temperature reached for the baseline case was 100 °C. The results show improved storage of heat and transmission of heat both horizontally and vertically in the fuel layer with the presence of a suitably designed blanket.

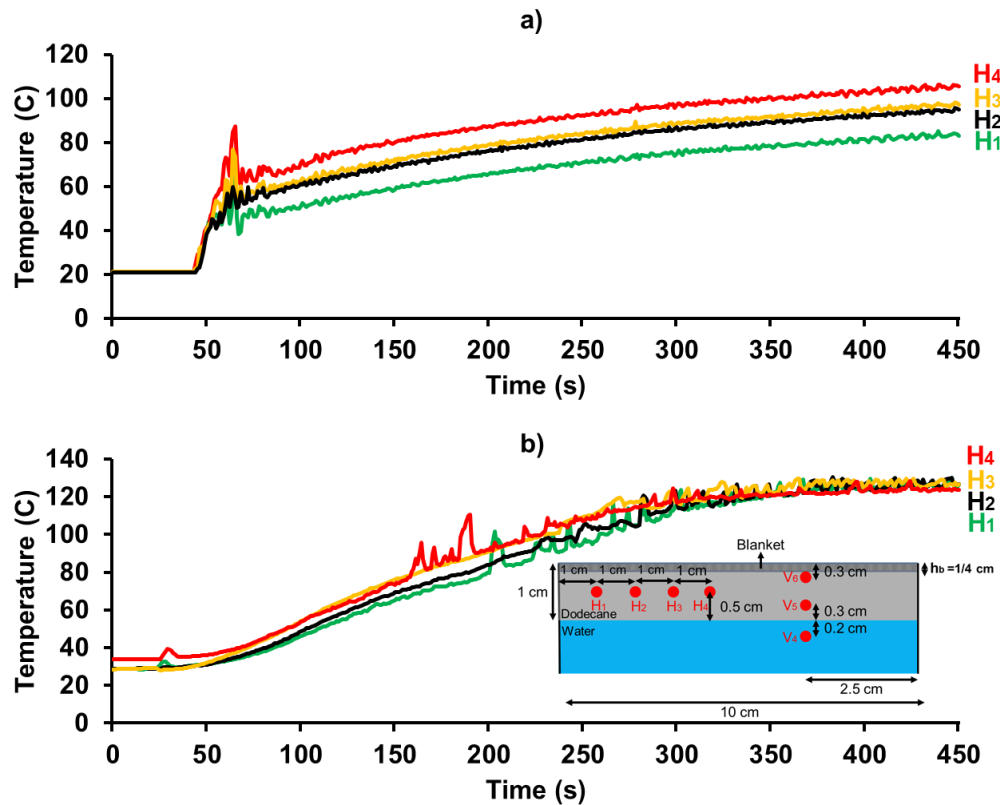


Figure 12: Horizontal temperature distribution vs. time for baseline (a) and 0.25 cm copper blanket (b)

Figure 13 depicts the HFG measurements for the baseline and 0.25 cm thick medium porous copper blanket.

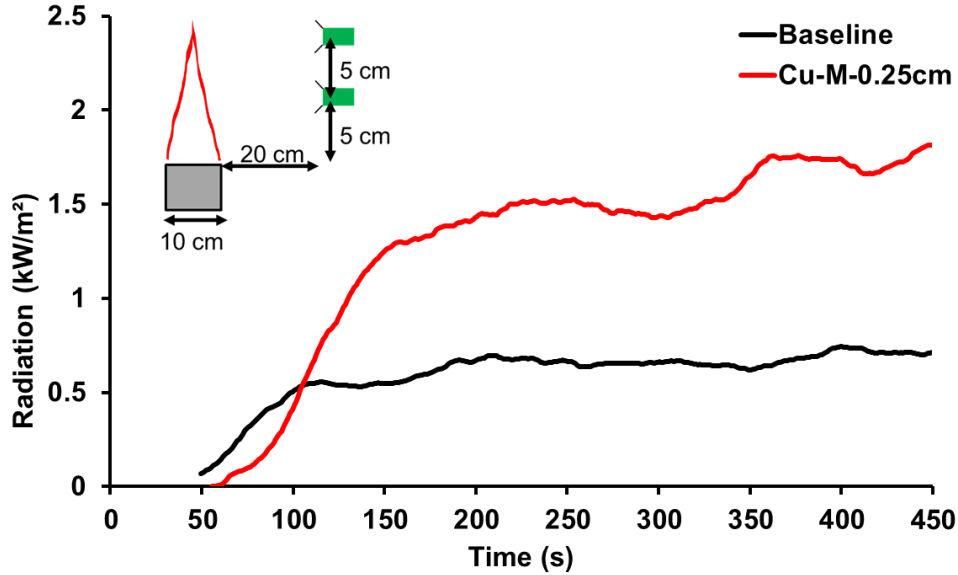


Figure 13: Radiative heat flux at 25 cm away from the pool centerline

As shown in Fig. 13, presence of the blanket resulted in enhanced combustion and higher radiative heat emission from the flame. This is mainly because of an increase in mass burning rate. The objective of the coils, which will be investigated in the second part of Phase I-a, is to collect the heat from the flame lost to the ambient and further enhance the combustion process.

3.1.2.3 Coil Wire Diameter

Initially, a 1 cm diameter continuous coil with 8 cm “Collector” and 5 cm diameter “Heater” was manufactured by a copper (Cu) wire (Figure 14a). Coil is submerged 0.5 cm below the fuel surface and 0.25 cm Cu blanket is placed on it (Figure 14b).

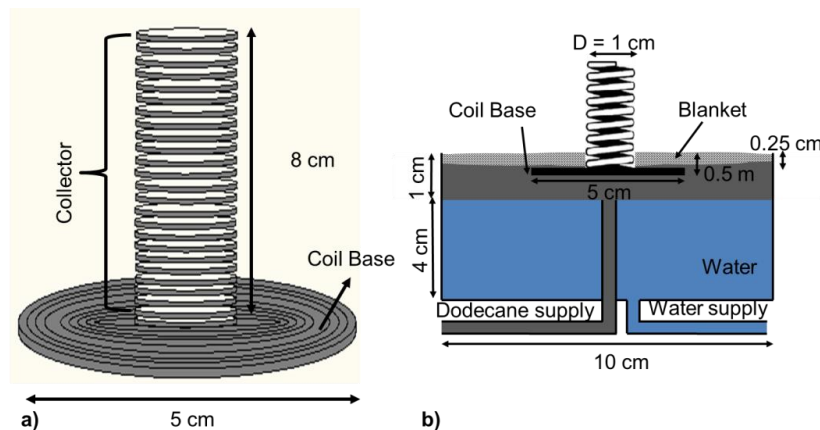


Figure 14: a) Initial coil geometry to be optimized by experimental study b) Placement of integrated blanket-coil into 10 cm test setup

Integrated blanket-coil system is optimized by varying the coil wire diameter, height, pitch, and diameter.

To investigate the influence of the coil wire diameter, Cu coils with wire diameter of 0.16, 0.2, and 0.38 cm (0.064", 0.08" and 0.125") were attached to the 0.25 cm thick Cu blanket. Figure 15 shows the flame behavior of the baseline and blanket-coil cases.

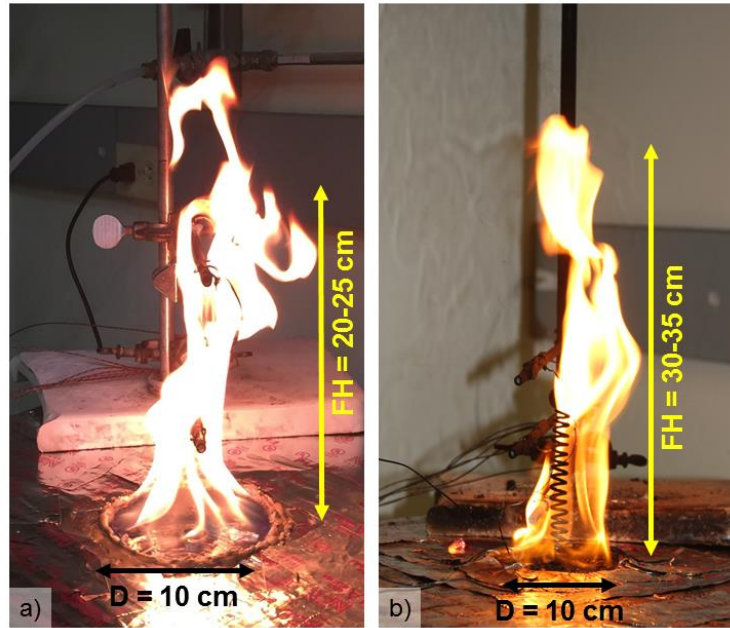


Figure 15: Comparison of flame heights (not to scale) (a) baseline (b) enhanced by blanket-coil

As shown in Fig. 15 the enhanced flame height is about 1.5 times of the baseline case. Figure 16 shows the MLR vs. time for different wire diameters. The MLR presented in this report is the polynomial fitting of the experimental data. W_d represents the wire diameter

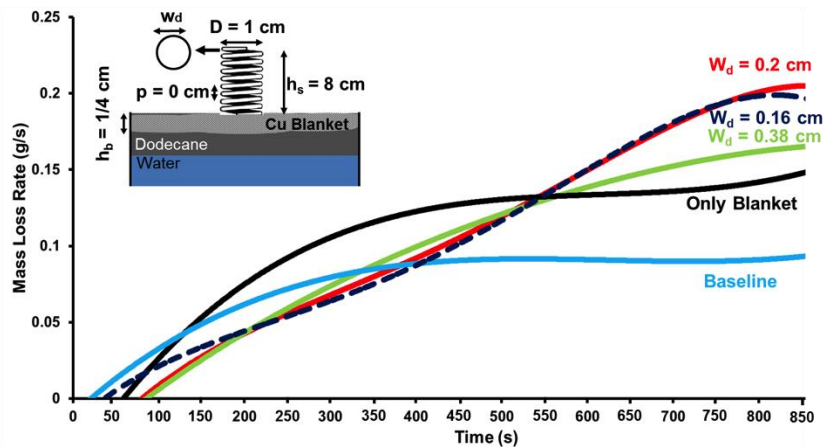


Figure 16: Effect of coil wire diameter on Mass Loss Rate

When the integrated blanket-coil system is placed in the fuel, it is observed that the MLR increases significantly. For 0.2 cm coil diameter (red line), it is observed that the mass loss rate

increases until a steady state of ~ 0.2 g/s is reached. This is $\sim 100\%$ increase over the baseline case (Light blue curve, 0.1 g/s).

3.1.2.4 Coil Height and Pitch

Four coil heights (6, 8, 10, 12 cm) and three different pitches (0, 0.5, 1 cm) were tested. Figure 17 shows the MLR vs. time for various coil heights (h_c).

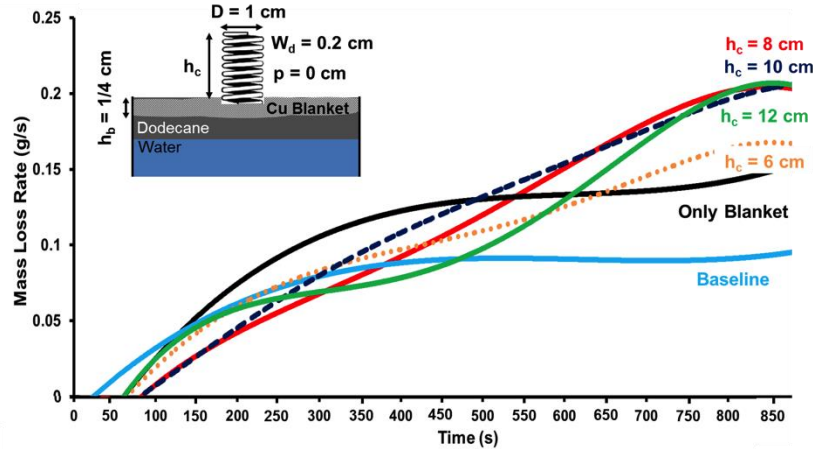


Figure 17: Effect of coil height on Mass Loss Rate ($W_d = 0.2$ cm, $p = 0$, $D = 1$ cm)

As shown in Fig. 17, that the MLR reaches an optimum value of 0.2 g/s at h_c is 8, 10 and 12 cm. To pick the optimum h_c , areas under the curves (before reaching steady state) were compared. Calculated area represents the efficiency until reaching the steady state. It is observed that the maximum burning efficiency was achieved by $h_c = 10$ cm case (Largest unsteady state area and high MLR). As h_c is further increased to 12 cm, the unsteady state area decreases and reaches the average level similar to $h_c = 6$ cm case. As a next step, various coil pitches were investigated by keeping $h_c = 10$ cm. The MLR vs. time graph for various coil pitches (p) is depicted in Figure 18.

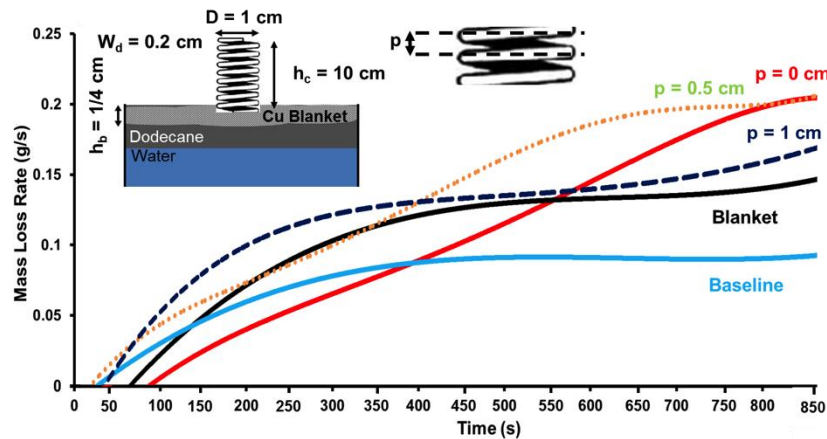


Figure 18: Effect of coil pitch on Mass Loss Rate ($W_d = 0.2$ cm, $h_c = 10$ cm, $D = 1$ cm)

As shown in Fig. 18, the coil with 10 cm high and 0.5 cm pitch resulted with the maximum burning efficiency. Increase in the flame – coil surface contact area (pitches allow flame to reach inner surface of the coil) and allowance of air diffusion through the pitches lead to quicker steady state and high MLR. As p is further increased to 1 cm, burning rate decreases and reaches the average level similar to only blanket case (compare the black and dark blue dashed curves).

3.1.2.5 Coil Diameter

As a last step, the effect of coil diameter on MLR was tested. 1, 2, and 3 cm Cu coils with 10 cm high and 0.5 cm pitch were manufactured. Figure 19 shows the MLR vs. time for various coil diameters (D).

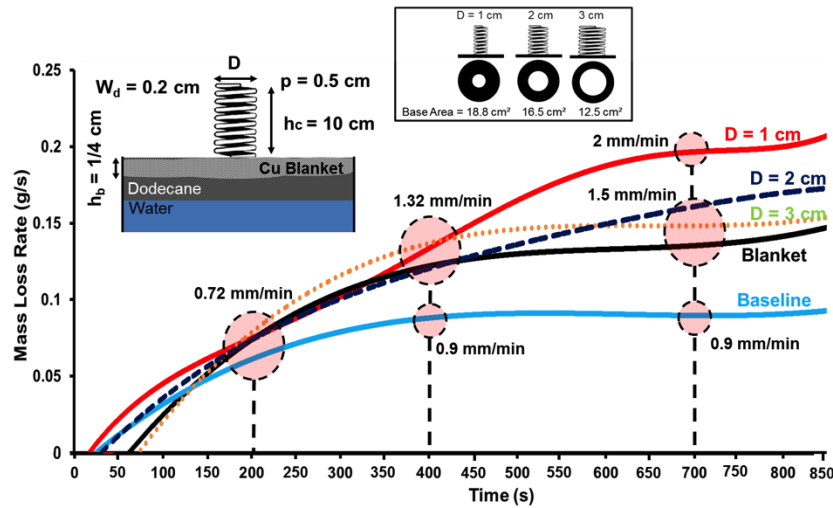


Figure 19: Effect of coil diameter on Mass Loss Rate

As shown in Fig. 19, with the optimized blanket-coil configuration, the time required to reach steady state decreased from 800 s to 600 s, while keeping the burning enhancement same (100% increase over the baseline case).

3.2 Phase I-b, Intermediate Scale

The influence of changing the height and number of coils in a ~0.28 m diameter pool fire was analyzed in Phase I-b. Alaska North Slope (ANS) crude oil was used in all Phase I-b tests.

3.2.1 Experimental setup of Phase I-b

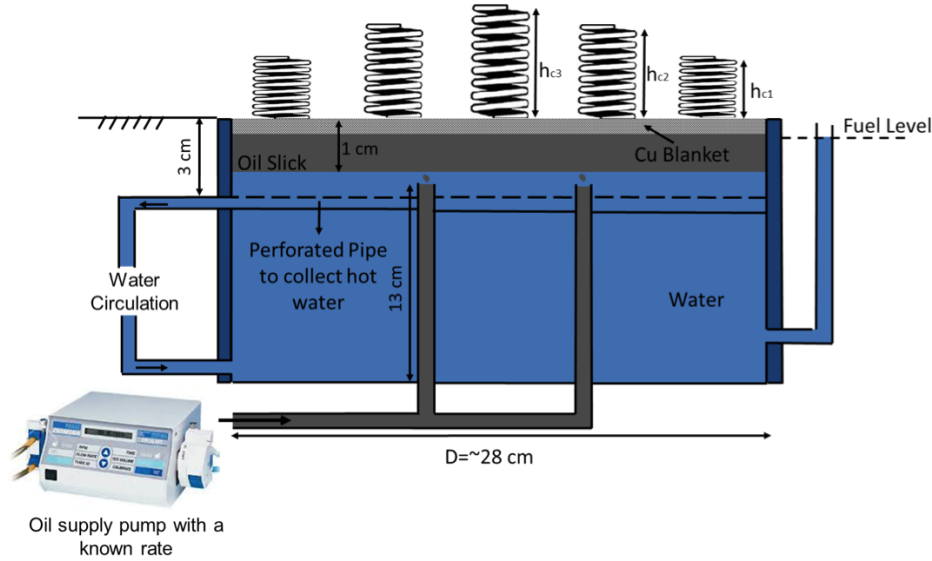


Figure 20: Experimental setup at Phase I-b

Figure 20 shows the experimental setup (Phase I-b) for burning ANS crude oil with multiple coils. The fuel layer was maintained at 1 cm above a 14 cm deep saltwater (35 ppt) layer using an OMEGA FPU5MT peristaltic pump that continuously feeds oil into the burner as shown in Fig. 5. A transparent polycarbonate pipe (shown on the right hand side of Fig. 20) was used to monitor the fuel level and a load cell measured the rate of fuel supplied (g/min). An additional feature that was added in the experimental setup was the ability to recirculate water from underneath the oil slick to replicate a field condition of ocean currents that continuously cool the bottom of the oil slick during ISB. As shown in Fig. 20 a perforated pipe was used to recirculate the water. The water-pumping rate was kept constant (300 ml/min) in all tests.

3.2.2 Instrumentation of Phase I-b

The temperature profiles of the plume, fuel layer and water sublayer were measured by thermocouple (TC) arrays as shown in Fig. 21. The horizontal and vertical gas phase temperature profiles were obtained by 15 TCs. Two TC arrays, which had 10 TCs (with 0.5 cm spacing) each, were used to measure the hot gas temperature from 1 cm to 6 cm above the fuel layer at the center and perimeter of the pool. Detailed liquid fuel and water temperature profiles were measured by 20 TCs. The external radiative heat flux was measured using four heat flux gauges placed 0.5 m away from the burner oriented towards the flame as shown in Fig. 21.

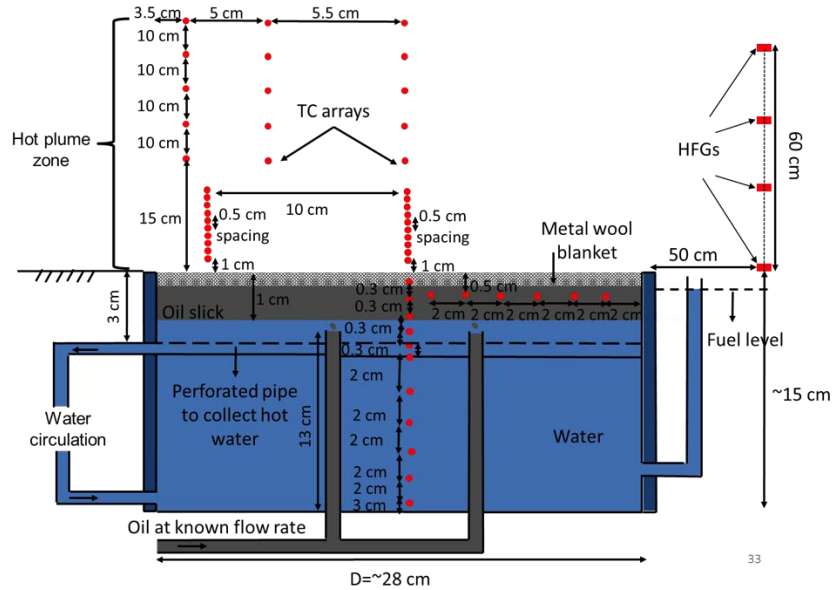


Figure 21: TC and HFG locations. 15, 20, 12, and 8 TCs measuring temperatures in the hot plume zone, hot gas zone, oil, and water, respectively.

3.2.3 Effect of cooling system

As shown in Fig. 20, a water recirculation system was added to simulate the water “current” passing below the oil layer while the slick is being dragged by the containment boom in the field. Figure 22 shows steady state in-depth temperature profiles from two baseline experimental trials (with and without water circulation).

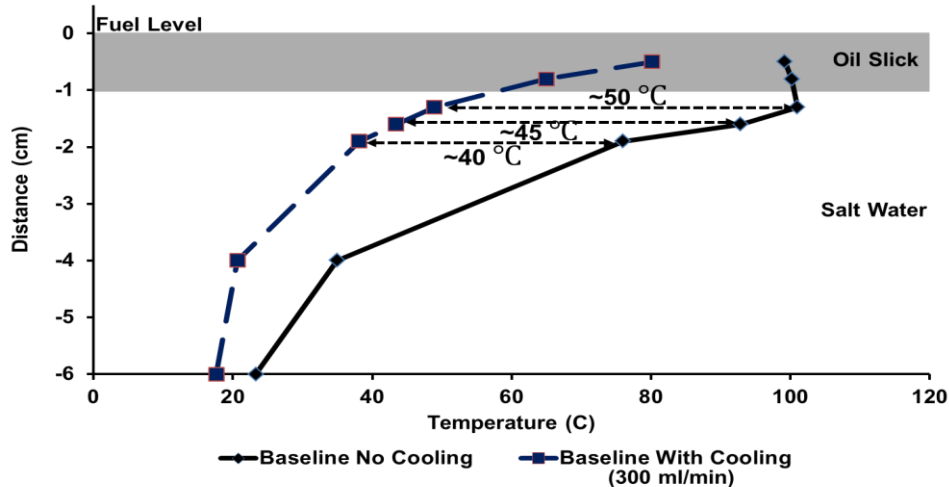


Figure 22: Effect of cooling system, oil and water temperatures at the center (average of 120 second after reaching steady state)

When the cooling system is on, it is observed that the temperature under the fuel layer is about 45 °C cooler than the “no cooling” case. The decrease in water temperature occurs because the pump continuously circulates the hot water under the fuel layer to the bottom as shown in Fig.

22. This cooling of the sublayer also cools the fuel layer, which results in lower burning rate. In the “no cooling” case, the MLR increases until a steady state of ~ 1.3 g/s is reached. This is $\sim 100\%$ increase over the “with cooling” case (0.7 g/s). Boilover was not observed for both baseline tests.

A second set of tests with and without cooling were performed with a copper wool blanket of thickness 0.25 cm. Figure 23 shows the water temperature vs. time profile at the center of the burner for the two cases. W1 to W3 show the vertical temperature distribution through the 1 cm water layer under the fuel.

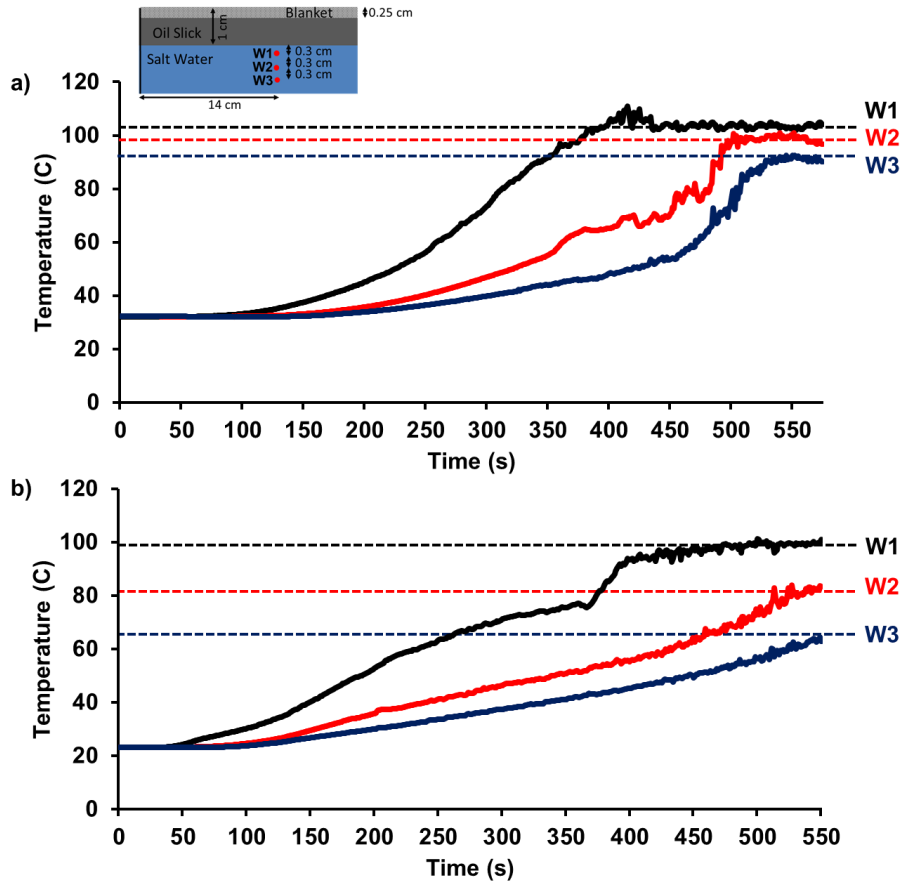


Figure 23: Temperature vs time at the center for “with blanket” tests a) water circulation off, b) water circulation on

For the test without cooling, boilover was observed after 8 minutes of ignition (Fig. 23a). This is because of the enhanced heat transfer from flame to the fuel by blanket. Rapid increase in the fuel and water temperature resulted with boilover. For the test “with cooling”, no boilover was observed. All experiments presented in this report henceforth are “with cooling.”

3.2.4 In-depth temperature profiles with the blanket

A Cu blanket with a thickness of 0.25 cm and porosity of 95% was placed into the 1 cm deep fuel layer. Porosity of the blanket in Phase I-b was calculated by using the Eqs. 1 to 4. Figure 24

shows the in-depth oil and water temperature profile at the center of the burner. F1 represents the fuel temperature 0.5 cm below the fuel surface. W1 – W5 show the vertical temperature distribution through the recirculated water sublayer.

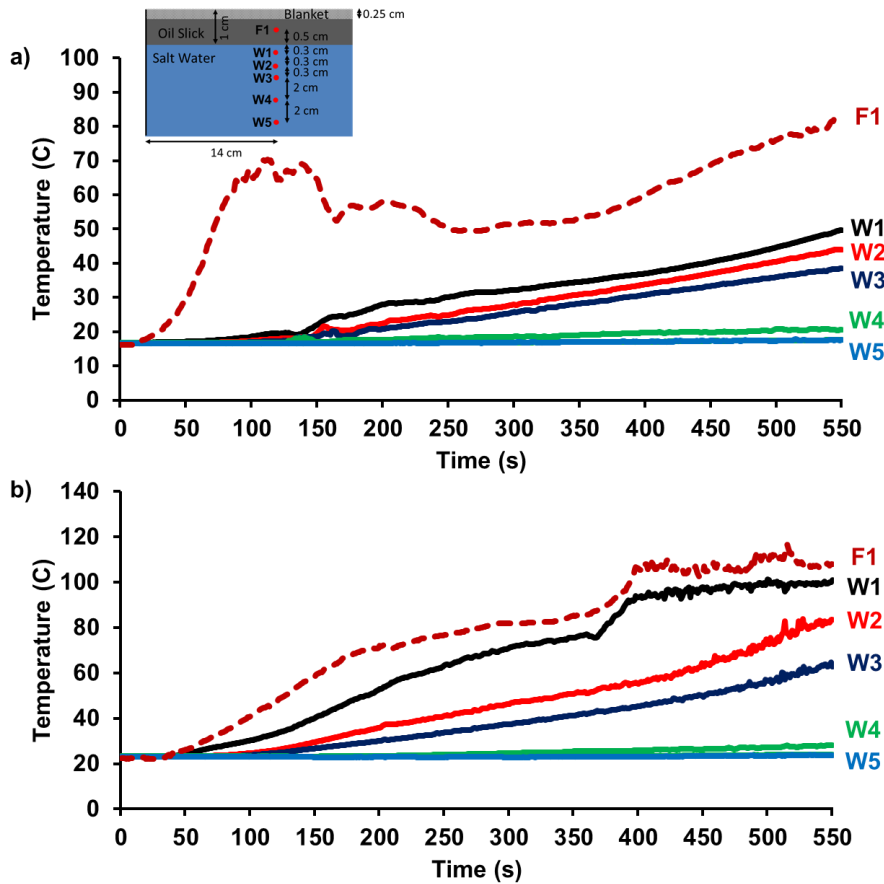


Figure 24: Temperature vs time at the center for a) Baseline, b) with a 0.25 cm thick copper blanket

When the blanket is placed in the fuel, it is observed that the fuel temperature (0.5 cm below the fuel level) increases by around 35 °C, while the MLR reaches a value of 1.7 g/s. This is ~ 150% increase over the baseline case (0.7 g/s).

3.2.5 Optimization of coil height

The effect of the height of an immersed cylindrical copper rod on burning efficiency of ANS crude oil was investigated in our previous study, BSEE Contract No. E14PC00043. The maximum burning efficiency was achieved when the immersed object was placed in the hot plume zone, whose location in the combusting plume varied with radial distance from the center of the pool fire. In this context, the detailed plume temperature data collected from 35 TCs located in the gas phase (see Fig. 21) were used to characterize the temperature field in the combusting plume region thereby optimizing the coil height. Figure 25 shows the plume temperature vs. time at the center. The plume temperatures are corrected for the losses due to radiation from the TC. The procedure is explained in Appendix A.

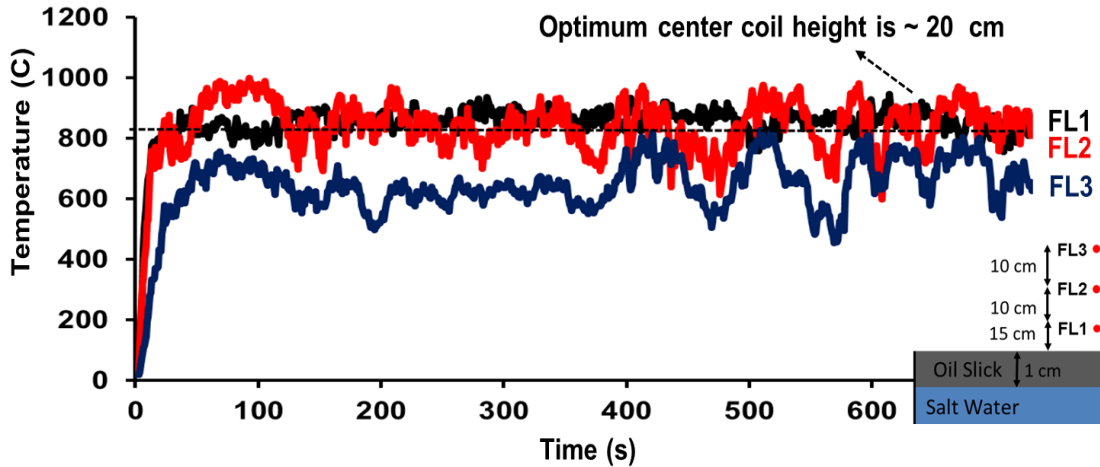


Figure 25: Plume temperature vs time at center

As shown in Fig. 25, that the plume temperature reaches a maximum value of 820 °C at ~25 cm above the fuel level. The plume temperature starts to decrease and reaches 700 °C at 35 cm above the fuel level (FL3); therefore 20 cm high coils at the center are used to stay in the hot plume zone.

The average flame height measured in the baseline test was 56 cm. By using this information, a relationship can be defined between the baseline flame height and optimum coil height. Half of the baseline flame height can be taken as the optimum coil height while scaling up the experimental setup. This result is in agreement with our previous study (BSEE Contract No. E14PC00043), which used half of the baseline flame height to calculate the optimum immersed object height.

Figure 26 shows the hot gas temperature vs. time at the corner (4 cm away from the rim).

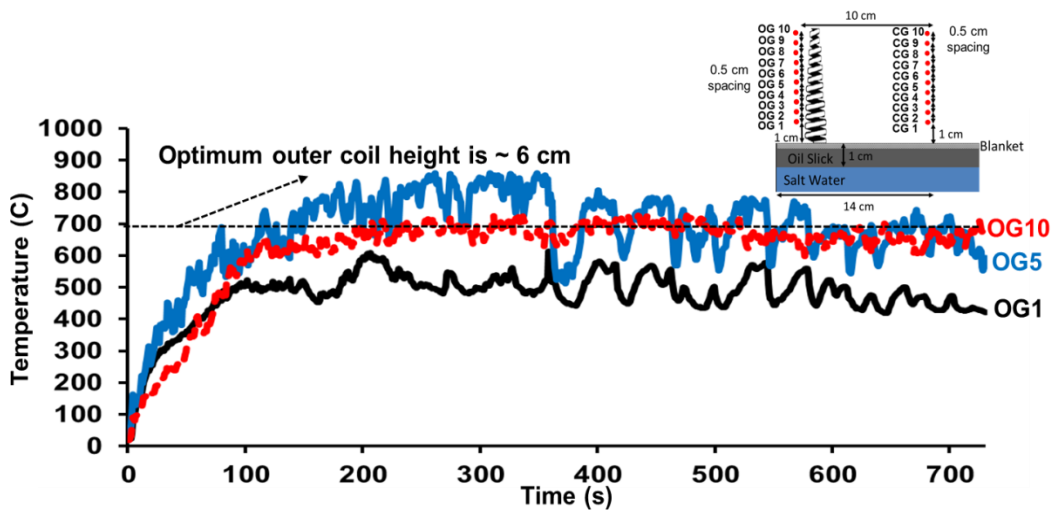


Figure 26: Hot gas temperature vs time at corner (4 cm away from the rim)

From Fig. 26 it can be observed that the coils along circumference should be ~6 cm high.

3.2.6 Blanket-Coil tests

3.2.6.1 Cylindrical coils

The results of the Phase I-a were used to design the Phase I-b collector. Coil pitch, diameter and wire diameter were 0.5 cm, 1 cm and 0.2 cm, respectively. Initially, four coils with 20 cm “Collector” and 4 cm diameter base “Heater” were manufactured by a 27 % Ni – Cu wire (Fig. 27). Coils were submerged 0.5 cm below the fuel surface and a 0.25 cm Cu blanket was placed in the fuel layer of thickness 1 cm.

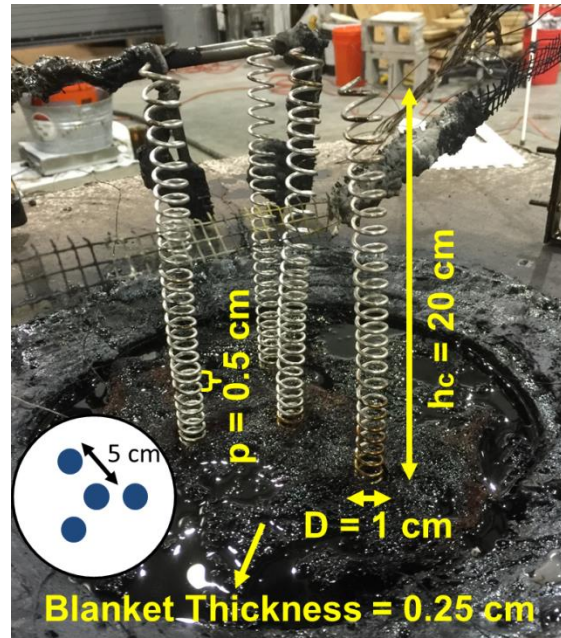


Figure 27: Placement of integrated blanket-coil into 28 cm test setup

At 5 minutes following ignition, it was observed that intense heat reduced rigidity and coils were not able to support their weight. The test was stopped due to failure of the coils. Figure 28 shows the bent coils.

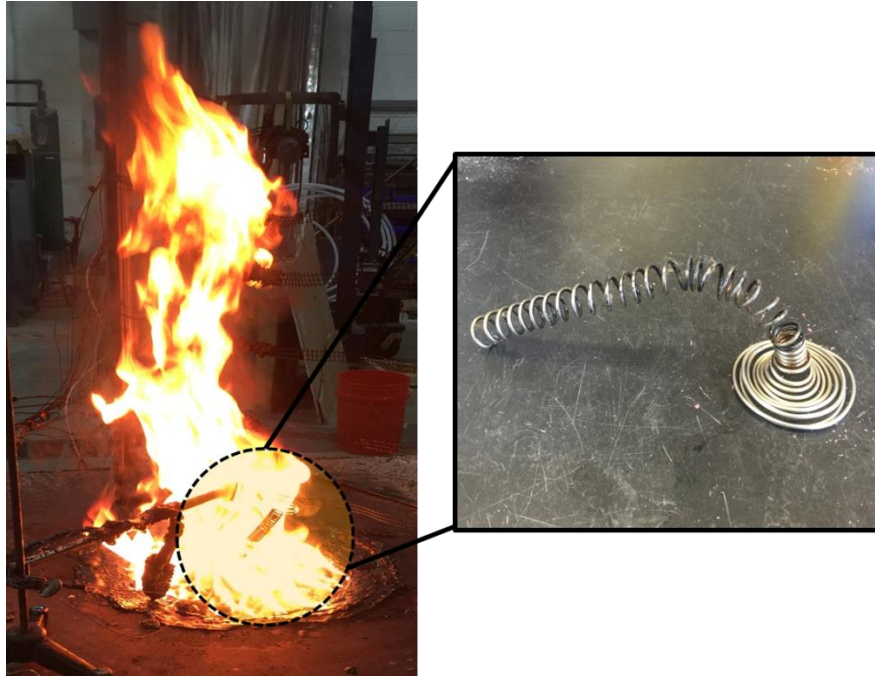


Figure 28: Bent coils due to excessive heat

The failure of the coils was analyzed numerically to have an approximate prediction of increase in the mean temperature of the coil with time. A control volume approach was used to solve the transient energy equation. The control volume includes the metallic coil and its base. A lumped thermal capacity was assumed. Figure 29 shows a schematic representation of the heat transfer mechanism. Heat is transferred to the coil from the flame through convection and radiation. The oil layer absorbs the heat from the base of the coil. The coil is made out of a 27 % Ni – Cu wire of 2 mm diameter.

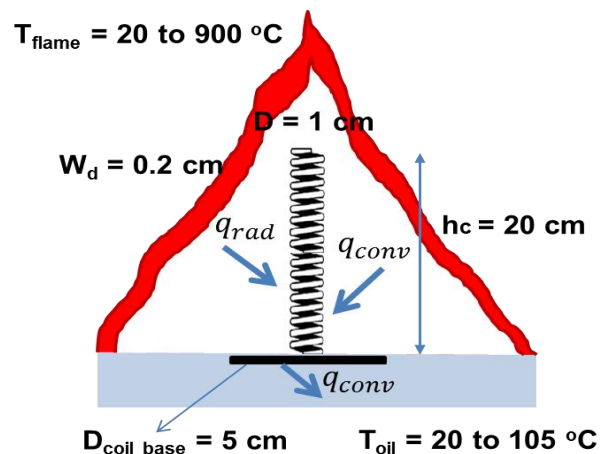


Figure 29: A schematic representation of the heat transfer mechanism

Equations 5-7 illustrate the mathematical formulation.

$$\rho V C_p \frac{dT}{dt} = (q''_{in} - q''_{out}) A = \varepsilon \sigma F (T_f^4 - T^4) A_s + h_f A_s (T_f - T) - h_o A_b (T - T_o) \quad (5)$$

$$dT = \frac{1}{\rho C_p} \left\{ \frac{A_s}{V} \sigma \varepsilon F (T_f^4 - T^4) + \frac{A_s}{V} h_f (T_f - T) - \frac{A_b}{V} h_o (T - T_o) \right\} dt \quad (6)$$

$$T(i+1) = T(i) + \frac{1}{\rho C_p} \left\{ \frac{A_s}{V} \sigma \varepsilon F (T_f(i)^4 - T(i)^4) + \frac{A_s}{V} h_f (T_f(i) - T(i)) - \frac{A_b}{V} h_o (T(i) - T_o(i)) \right\} dt \quad (7)$$

where,

ρC_p : Heat capacity of 27 % Ni – Cu = 8900 x 377 = 3.35 x 10⁶ J/K

V : Volume of the coil

A : Surface area

$q''_{in} - q''_{out}$: Net heat influx

dT : Change in coil temperature in time dt , (0.05 sec)

σ : Stefan-Boltzmann constant, 5.67x10⁻⁸ W/(m²K⁴)

ε : Emissivity

F : Radiation shape factor

h_f : Convective heat transfer coefficient between plume region and coil

h_o : Convective heat transfer coefficient between coil base and oil

$T_f(i)$, $T_o(i)$, $T(i)$: Temperature of the plume, oil and coil, respectively, at instant i

A_s : Surface areas of the coil exposed to flame, 0.00631 m²

A_b : Surface areas of the coil base exposed to oil, 0.003925 m²

$t(i)$: Time at instant i , $t(i) = 0 + i * dt$; $T_f(0) = T_o(0) = T(0) = 293$ K

A constant convective heat transfer coefficient, h_f , of 20 W/m²K was specified at the surface between the coil and the hot gaseous mixture. A constant convective heat transfer coefficient, h_o , of 80 W/m²K was specified at surface of the coil base lying inside the oil. The time dependent plume and oil temperatures, $T_f(i)$ and $T_o(i)$, were obtained from the experimental results with blanket (Figs. 25, 26). An effective emissivity of 0.2 from the flame surface to the coil is specified, following Agueda et al. [1]. A radiation shape factor of 0.75 was assumed from the flame to the coil.

A time step of 0.05 s was used for the transient calculation after initializing the temperatures of the plume, the oil and the coil as 293 K (20 °C). The time history of the predicted temperature of the coil and the predicted increase in the MLR per coil are shown in Fig. 30. The temperature of the coil increases because of increase in internal energy of the coil caused by a net heat inflow.

After around 500 s from ignition, a steady state is attained where the heat inflow from the plume to the control volume is balanced by the heat outflow from the control volume to the oil. The coil failure was observed in the experiments after 300 seconds from ignition. This suggests a significant decrease in the flexural rigidity at high temperatures around 500 °C.

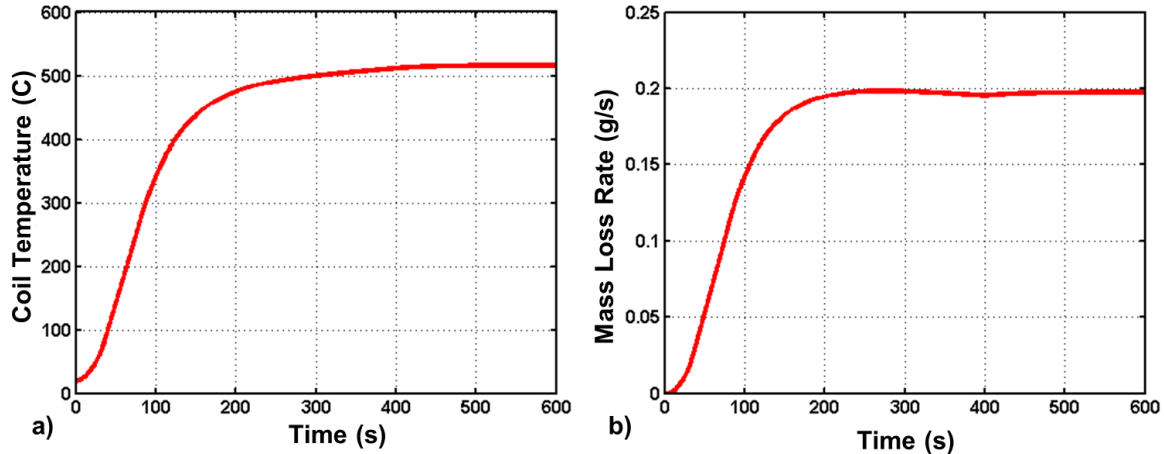


Figure 30: (a) Time history of the average coil temperature, (b) the predicted increase in the mass loss rate per coil

The predicted heat transfer rate to the oil from the coil at steady state is 129 W, which compares well with the experimental average heat transfer rate to the oil from the coil, over a period of 20 minutes, ~ 120 W. The increase in the mean heat transfer rate causes an increase of 0.184 g/s MLR (dividing it by the latent heat of vaporization of crude oil, 654 kJ/kg), neglecting possible increase in the heat losses and sensible heating due to introduction of the coils. From the experimental results, the increase in MLR per coil is around 0.175 g/s/coil for 4 and 8 coils cases. The predicted increase in the MLR is comparable to the experimental measurements up to the case with 8 coils. However, as a simplified lumped capacitance model is used, it cannot be relied upon to make quantitative comparisons. The increase in MLR is significantly low around 0.06 g/s/coil for the 10 coils case (Fig. 17). This suggests that there are many other factors influencing the heat transfer mechanism.

The high length to diameter ratio of the coil, $h_c/D = 20$, makes it difficult to mount the coils vertically. An inclined mounting can cause bending of the coil to the inclined side at high temperatures due to decrease in the flexural rigidity. One possible solution is to use a thicker coil wire. But, increasing the coil wire diameter will also increase its weight and decrease its surface area to volume ratio, resulting in an increase in its thermal response time. This might lead to a reduction in the heat transfer to the oil in the transient stage. A conical coil was therefore implemented to increase the structural stability. This simple geometry change also maintained the surface area to volume ratio and the thermal response time of the coil.

The optimum coil height on the circumference is shorter (6 cm) and has a lower risk of structural failure. Figure 31 shows the conical coil configuration used in Phase I-b.

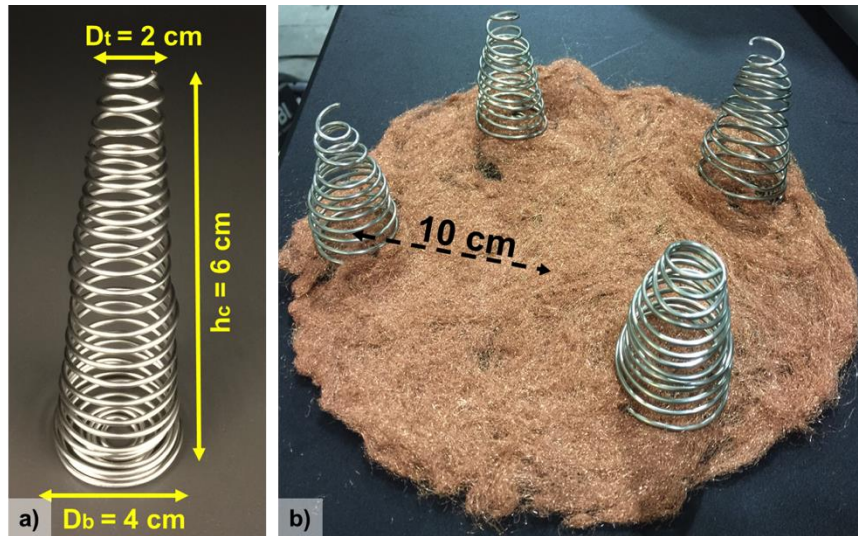







Figure 31: a) Conical coils, b) Integrated blanket-coil system

3.2.6.2 Conical Coils

Table 3 shows the experimental tests performed with various spacing, coil number, and coil height.

Table 3. Experimental layout of blanket-coil tests

Case	# of Coils	Coil Configuration	s (cm)	h ₁ (cm)	h ₂ (cm)	h ₃ (cm)
1	4 + Blanket		10	6	-	-
2	8 + Blanket		10	6	-	-
3	10 + Blanket		10	6	-	-
4	12 + Blanket		5	6	8	-
5	15 + Blanket		5	6	8	10

The initial focus was on the optimization of coil number on the circumference. Then, additional coils were placed at the center with different heights. Figure 32 shows the MLR at steady state for coils placed on circumference.

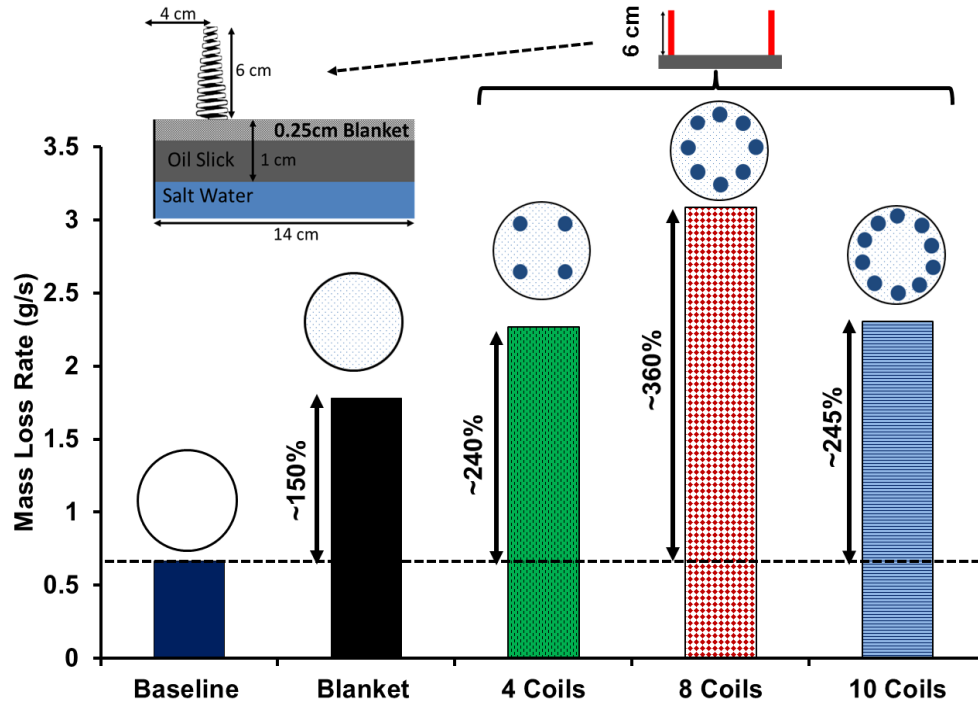


Figure 32: Optimization of # of coils on circumference - Mass Loss Rate

Figure 32 shows that the MLR reaches an optimum value of 3.1 g/s at 8 coils placed on circumference. This is ~ 360% increase over the baseline case (0.7 g/s). As number of coils is further increased to 10, the burning rate lowers and reaches the average level similar to “4 coils” case.

After optimizing the number of coils on circumference, the next step was adding more coils to center of the burner. The heights of the additional coils were optimized by using the center plume temperature obtained from “8 coils” case. The optimum coil height at the center was found as ~25 cm. A 12-coil configuration was prepared, which had four 15 cm high conical coils at center and eight 6 cm conical coils on circumference. Like in the cylindrical coil test, 15 cm high conical coils at the center bent after 10 minutes of testing. Thus, the maximum center coil height is limited to 10 cm to prevent coil failures with 0.2 cm wire thickness for the coil.

Figure 33 compares the MLR of the baseline, blanket, 8 coils, 12 coils, and 15 coils cases.

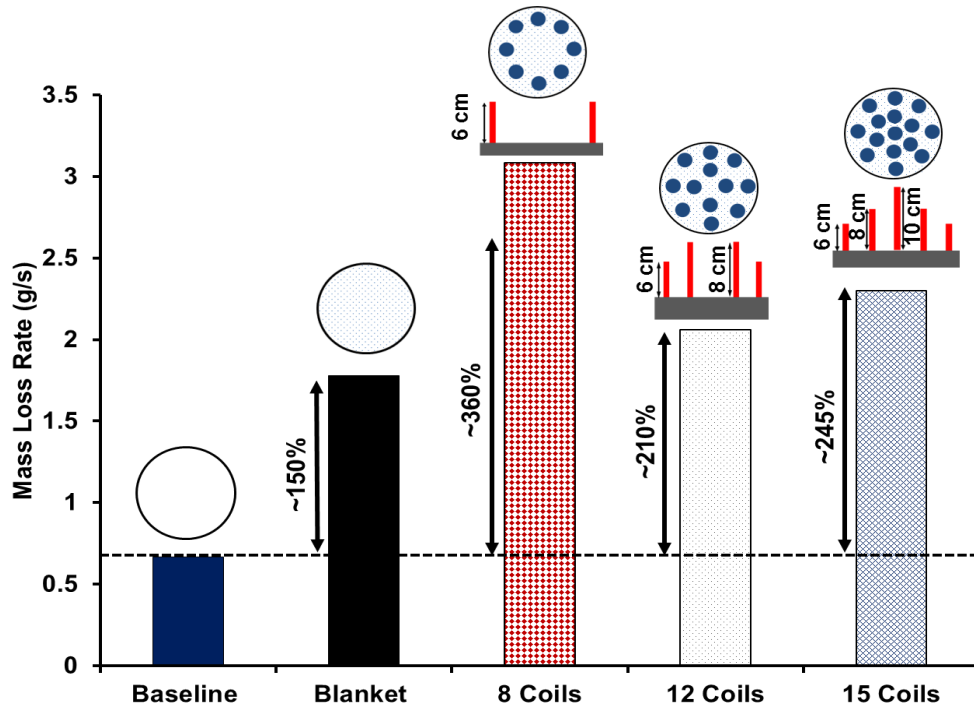


Figure 33: Optimization of # of coils at center - Mass Loss Rate

It is observed that adding coils at the center did not increase the burning efficiency compared to merely 8 coils on the circumference alone. This is because the center coils were not high enough to be fully exposed to hot plume zone. The high efficiency of coils on circumference is due to high contact area with the hot plume leading edge that increases the directed heat from the fire back to the liquid fuel. Based on temperature measurements of the hot zone in the combusting plume region, the height of the center coils should be ~25 cm to burn with higher efficiency. This length will increase even further with an increase in the diameter of the fire. Using longer coils is likely not practical in field applications due to potential for bending (due to heat, wind and waves) and decreased deploy-ability (higher chance to get tangled).

Another difficulty that was observed during the tests was placing the blanket-coil system into the burner. Due to high porosity (95%), the blanket absorbs a significant amount of oil. In order to improve handling ability, the blanket+8 coils system is placed between two Cu meshes (Fig. 34) which increases the structural integrity. The mesh material has a wire diameter of 0.05 cm (0.023") and has an opening of 0.15 cm between wires (Fig. 34b). The mesh also provided greater support to the coil (collector region of the flame refluser)

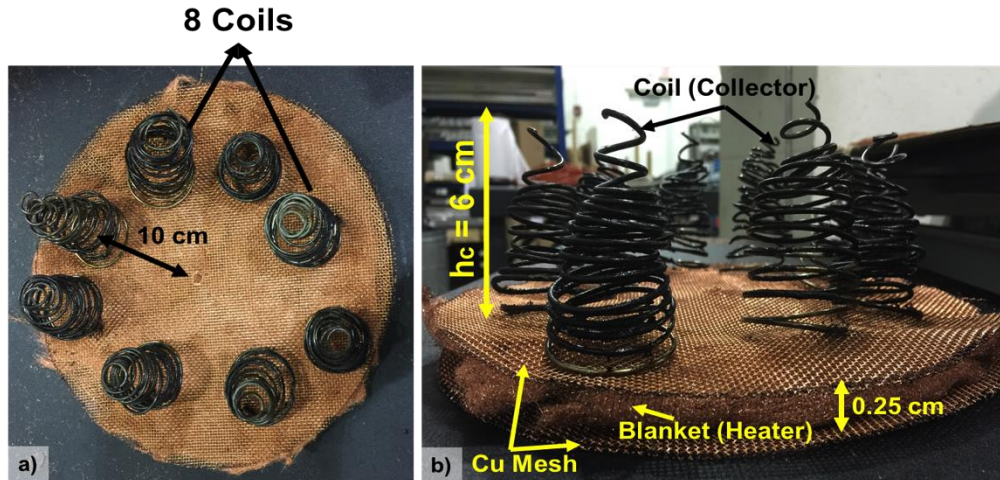


Figure 34: Blanket-8 coils-mesh system a) Top view, b) Side view

The MLR for “blanket-8 coils-mesh” case is depicted in Fig. 35.

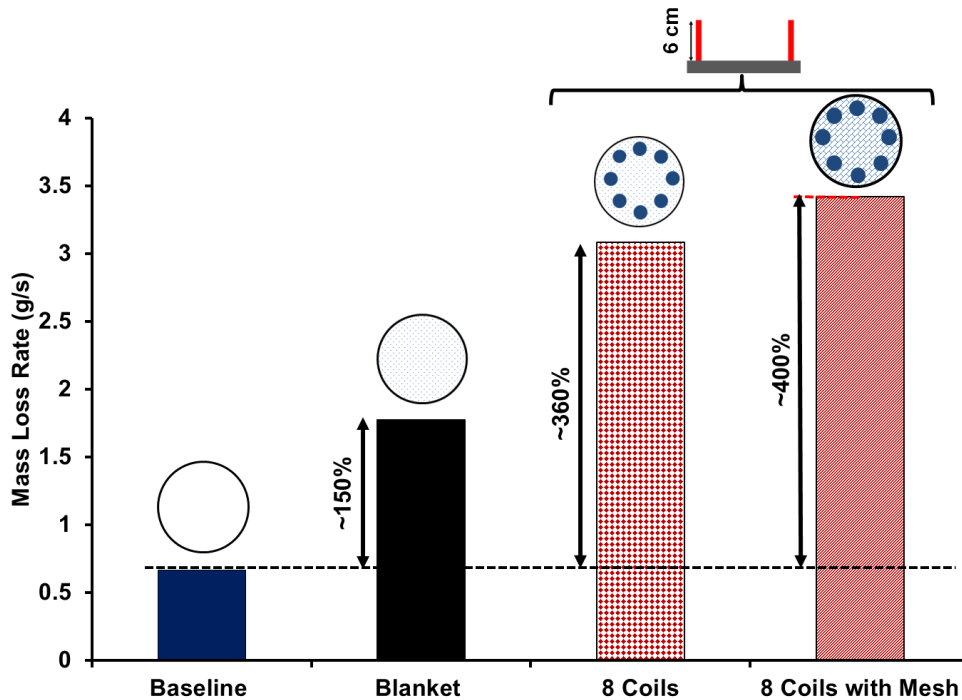


Figure 35: Optimization of # of coils with Cu blanket and mesh- based on Mass Loss Rate

As shown in Fig. 35, the 8 coils-mesh resulted in the maximum burning enhancement of 400% as compared to the baseline. The Cu mesh improved the contact between the coils and the blanket which increases the MLR as shown in Fig. 35.

Figure 36 shows the vertical temperature distribution at the center for the baseline, blanket and “blanket-8 coils-mesh” cases. The distribution is obtained using TC’s placed in the gas phase just

above the fuel, inside the fuel-layer, and the water sublayer. With an increase in the MLR, the curves move to the right as shown in the Fig. 36.

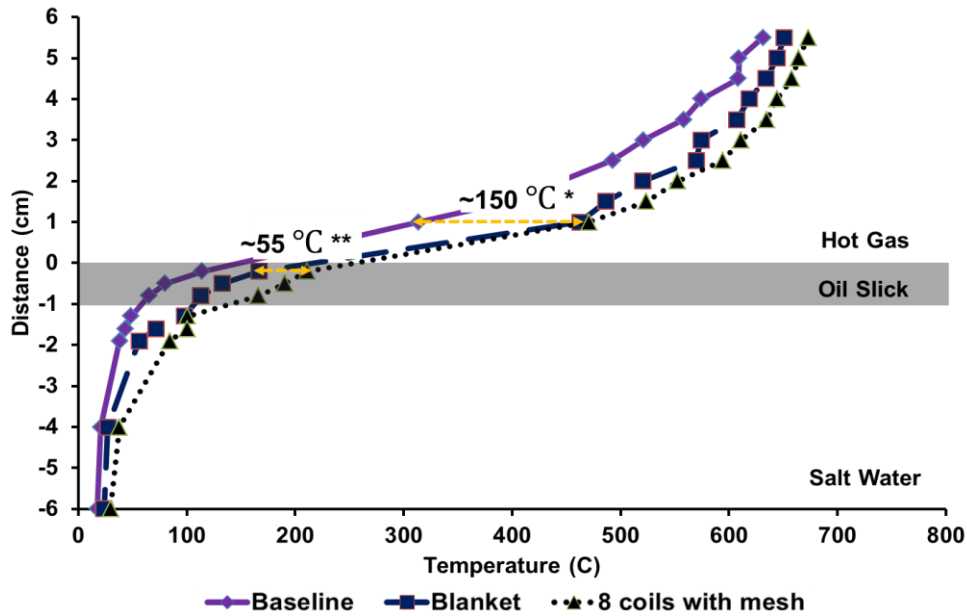


Figure 36: Vertical temperature profile at the center for baseline, blanket, and blanket-8 coils-mesh

When the “blanket-8 coils-mesh” is placed into the fuel, the temperature above 1 cm of the fuel layer reaches up to 470 °C, which is around 150 °C higher than the baseline case as shown in Fig. 36. The increased temperature causes an increase in MLR. Additionally, nucleate boiling is observed inside the blanket, which further enhances the MLR. When the blanket and “blanket-8 coils-mesh” cases are compared, it is observed that the hot gas temperature did not increase significantly, while the fuel temperatures increased about 55 °C**.

Figure 37 shows the vertical temperature distribution at the corner (4 cm away from the rim) for the baseline, blanket and “blanket-8 coils-mesh” cases.

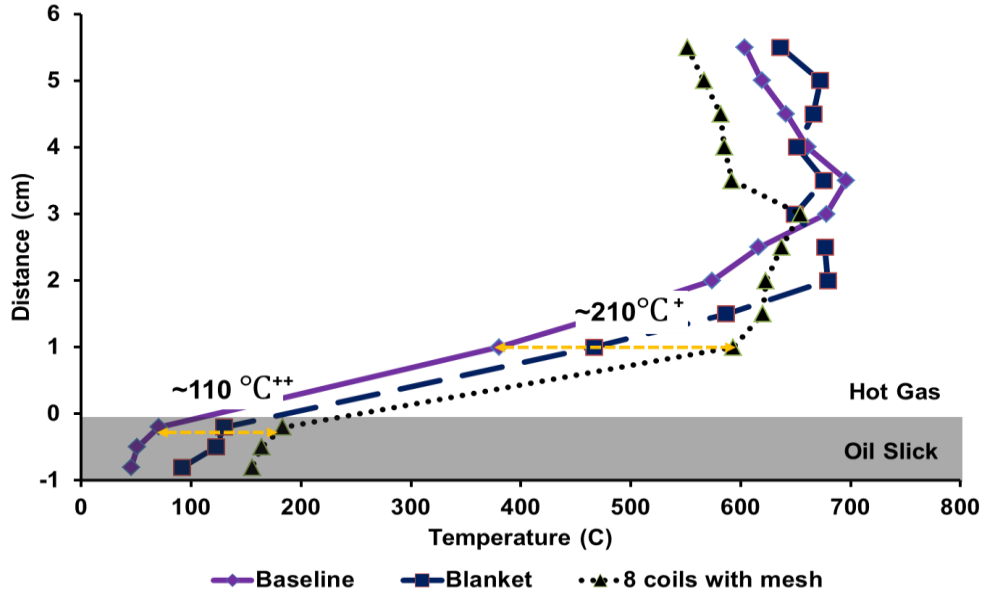


Figure 37: Vertical temperature profile at the corner for baseline, blanket, and blanket-8 coils-mesh

For “blanket-8 coils-mesh” case, the temperature above 1 cm of the fuel layer reaches up to 600 °C, while the maximum temperature reached for the baseline case was 390 °C ($\Delta T \approx 210$ °C⁺). It is observed that the hot gas temperature of the “blanket-8 coils-mesh” case starts to decrease and reaches to 550 °C at 6 cm above the fuel surface. The decrease in the gas temperature is due to presence of the coils. The coils act as a heat sink and direct the collected heat from plume to the fuel that lead to ~110 °C⁺⁺ temperature increase in fuel.

Figure 38 summarizes the HFG measurements for the baseline and “blanket-8 coils-mesh” cases, respectively.

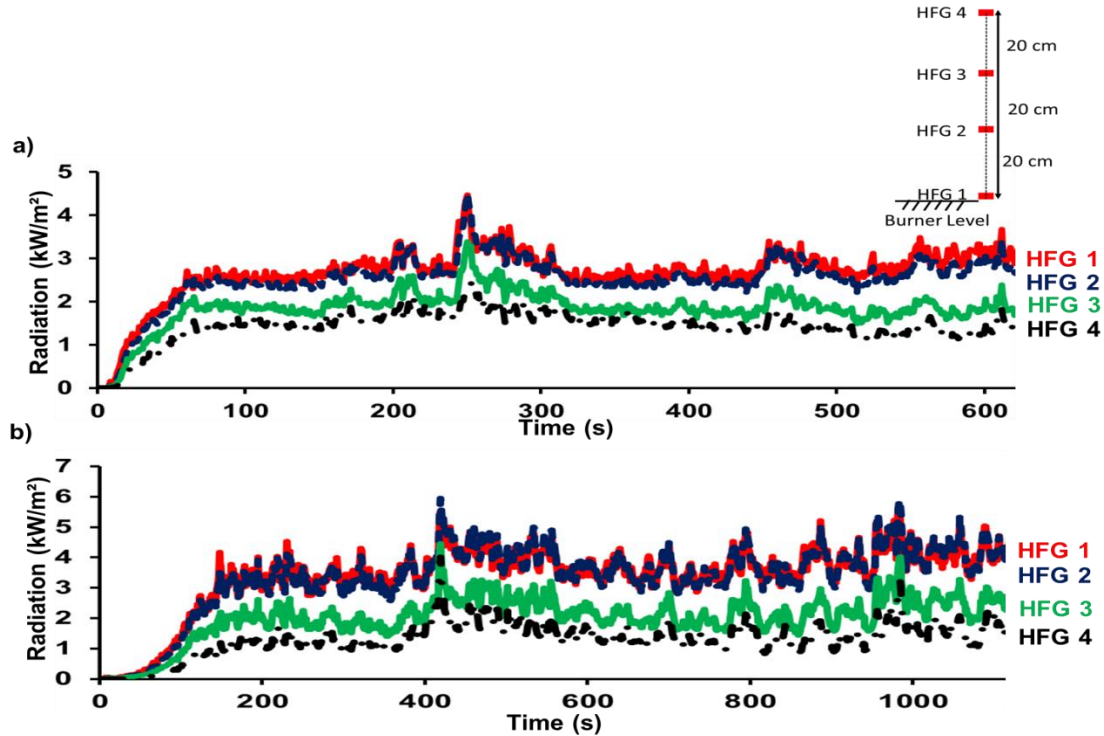


Figure 38: HFG – (a) Baseline (b) Blanket-8 coils-mesh

The radiation measurements of the “blanket-8 coils-mesh” case are close to the baseline case, mainly because of the black body behavior of the blanket, coils and mesh. They absorb most of the radiation thereby promoting less heat loss to the ambient and thereby aiding in complete combustion of the fuel. Because of this reason, HFGs measure relatively close values for the baseline and “blanket-8 coils-mesh” cases, although the MLR has enhanced about 400%.

3.2.7 Oil accumulation on blanket

The oil accumulation on the blanket was also studied in Phase I-b. The blankets were weighed before and after each experimental trial to calculate the oil accumulation. Figure 39 shows the oil accumulation for different tests.

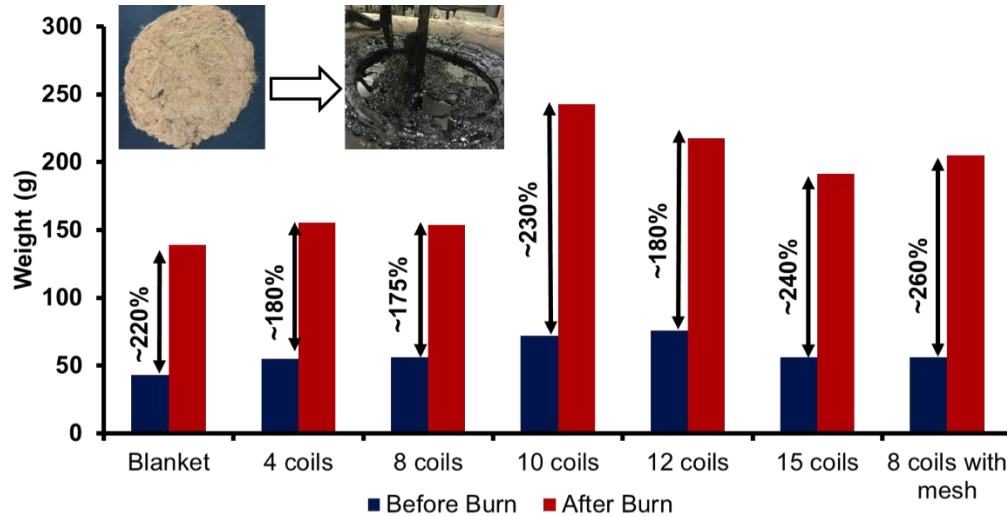


Figure 39: Oil accumulation of blanket

The oil accumulated on the blanket was ~215% of the blankets dry weight. The result showed that the blanket concept is also effective to collect the residues after burn. However, in the large scale tests, it was observed that the residue was even lesser because of additional radiative heat transfer with at the larger scale which caused burning-off the residue on the blanket. This is further discussed in section 5.3.5.

3.3 Outcomes of Phase I

Phase I aimed to explore the parameters controlling heat collection and transfer back to the fuel by the conductive blanket (heater) and coils (collector). In Phase I-a, various blankets (with different thickness, material, and porosity), and coils (with different wire diameter, length, pitch, and diameter) were tested in a 10 cm diameter dodecane pool fire configuration. Phase I-b explored the effect of the number and height of coils on burning enhancement in a 28 cm diameter ANS crude oil pan fire. The following key conclusions were drawn from Phase I:

1. Experiments demonstrated that the highest mass loss rate was obtained with 0.25 cm blanket thickness. The heat transfer model described in Section 6 shows quantitatively that, the region in which nucleate boiling occurs is largest when the blanket thickness is 0.25cm.
2. The intense heat resulted in reduced rigidity and cylindrical coils were not able to support their weight. A new conical geometry was developed and shown to be a viable solution.
3. Coils placed on the circumference significantly increased the burning rate. The high efficiency of coils on circumference was due to high contact area with the hot plume that increased the directed heat from the flame back to the liquid fuel.

4. In order to improve handling ability, the blanket-coil system was placed between two Cu meshes which increased the structural integrity.
5. The experimental study showed that the mass loss rate was enhanced by a maximum value of 400%, with Cu blanket (0.25 thick) + 8 Ni – Cu wire coils placed on circumference (6 cm high, 0.5 cm pitch, 2 cm top and 4 cm bottom diameter) + Cu mesh (wire diameter of 0.05 cm and has an opening of 0.15 cm between wires).

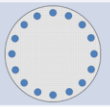

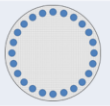


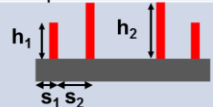
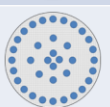
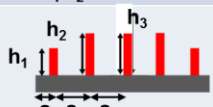
The results of Phase I (such as blanket thickness, coil shape and configuration) were used in the development of the intermediate-scale tests of 70 cm diameter in Phase II.

4. Phase II - Large Scale

The objectives of Phase II are to develop a mathematical model and demonstrate scale-ability using large-scale experiments, with the ultimate goal of guiding the field trial in the Joint Maritime Test Facility (JMTF) in Mobile Alabama. Technology Readiness Level (TRL) advancement [2], Phase II moved the project from the TRL 3 (Technology proof of concept was demonstrated in Phase I) through TRL 4 (Technology prototype demonstrated in a laboratory environment).

A total of 6 experimental tests were performed as shown in Table 4

Table 4. Experimental layout of blanket-coil tests

Case	# of Coils	Coil Configuration	s_1, s_2, s_3 (cm)	h_1, h_2, h_3 (cm)
1	0 (Baseline)	-	-	-
2	0 (Blanket)	-	-	-
3	16 + Blanket			5,-,- 10,-,-
4	24 + Blanket			5,-,- 10,-,-
5	32 + Blanket			5,10,- 10,15,-
6	36 + Blanket			5,10,10 10,15,15

4.1 Optimization of blanket and coil for Phase II

4.1.1 Blanket thickness

The mathematical model created in Phase I was used to determine the Phase II blanket thickness. The details of the mathematical model are discussed in Section 6. Figure 40 shows the regression rate of the fuel in a 0.7 m diameter burner for different Cu blanket thicknesses. Dodecane was used in the mathematical model because it is a single component medium flash point hydrocarbon that represents the median volatile-fraction of a typical crude oil.

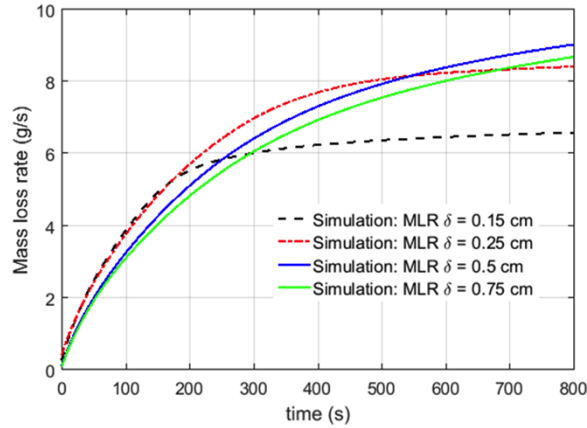


Figure 40: The time trace of the regression rate during the gradual burning of the 0.7 m diameter dodecane pool fire for the blanket thickness of 0.15-0.75 cm

The results demonstrated that the maximum regression rate can be obtained when the blanket thickness, δ , is between 0.25 cm and 0.5 cm. Based on the results, 0.35 cm thick blanket was used in Phase II experiments.

4.1.2 Coil height

The optimum coil height was obtained by using the Fire dynamics simulator (FDS) developed by the National Institute of Standards and Technology (NIST). The details of the FDS model are discussed in Appendix C. Figure 41 shows the flame height on the periphery determined by the FDS model. As done in the blanket thickness optimization, dodecane was used to represent the crude oil.

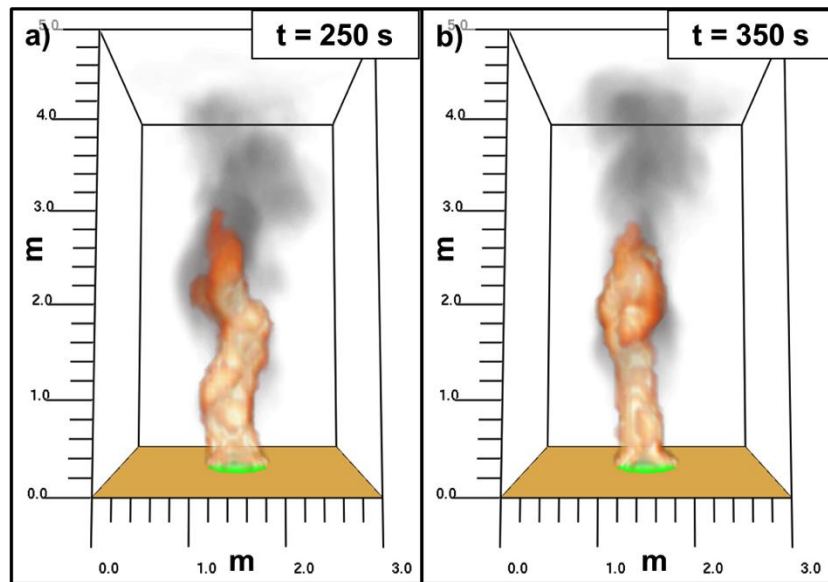


Figure 41: Heat release and smoke visualizations at two instances in a dodecane pool fire of 0.7 m diameter. Simulation is carried out using FDS

Figure 41 shows heat release visualization at two instances in a dodecane pool fire of 0.7 m diameter. Mean flame height was estimated based on a heat release cut-off of 200 W/m³. The mean flame height at the periphery (5 cm away from the burner rim) was found to be approximately 0.4 m. To maintain the structural integrity, 10 cm and 15 cm high coils with 0.3 cm wire thickness were used at the periphery and center respectively. The selected configurations ensure that the coils were engulfed in the hot gas zone.

4.1.3 Number of coils

The ratio of the volume of coils on the periphery to the oil slick volume, CR , was used to scale-up the number of coils (Eq. 8).

$$CR = \frac{\text{Coil volume}}{\text{Oil slick volume}}$$

$$CR = \frac{\# \text{ of coils} \times D_{CW} \times \left((L + \pi \times (R_{top})^2 + \pi \times (R_{base})^2) + (\pi \times (R_{base})^2) \right)}{\text{Fuel thickness} \times \pi \times (R_{pool})^2}, \quad (8)$$

$$L = \pi \times (R_{top} + R_{base}) \times s$$

$$s = \text{slant height} = \sqrt{(R_{base} - R_{top})^2 + h}$$

where R_{top} , R_{base} , and R_{pool} are the radius of coil top, coil base, and pool, respectively. L is the later surface of the “Collector” (Fig. 42). D_{CW} is the coil wire diameter.

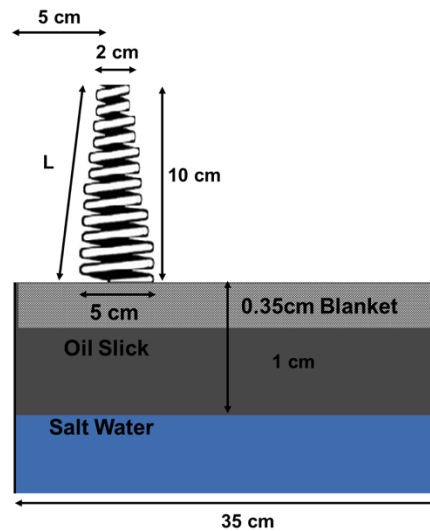


Figure 42: Sketch of the CR variables

Table 5 shows the parameters used in CR calculations.

Table 5. Parameters used in CR calculations – Phase II

	Phase Ib – Optimum case	Phase II predictions
Number of coils	8	24
Coil base diameter (cm)	5	5
Coil top diameter (cm)	2	2
Coil wire diameter (cm)	0.2	0.3
Coil height (cm)	6	10
Pool diameter (cm)	28	70
CR	0.46	0.42

Coil pitch, base and top diameters were kept constant as 0.5 cm, 5 cm and 2 cm, respectively. As shown in Table 5, *CR* value of the optimum case in Phase I-b was 0.46. To obtain a similar *CR*, 24 coils with 10 cm height needed to be used in Phase II.

4.1.4 Conclusions of Phase II optimization

The optimization results show that for a 1 cm oil layer thickness

- a) The blanket thickness of 0.35 cm – 0.5 cm provides the maximum efficiency (Fig. 41).
- b) 24 coils with 10 cm height, placed on the periphery, were needed to effectively collect the heat from the flame and transmit to the blanket.

In this context, various tests with different coil configurations, including 24 coils placed on the periphery, were performed as shown in Table 4. Cu coils are attached to a 0.35 cm thick Cu blanket placed between two Cu meshes (wire diameter of 0.05 cm (0.023") and has an opening of 0.15 cm between wires). The blanket (Heater) was immersed into 1 cm oil slick. Experiments showed that this configuration (24 coils on periphery with 0.35 cm thick blanket) provided the maximum enhancement in the burning rate. The results of the Phase II tests are discussed in the following section.

Figure 43 shows the blanket-mesh-coil system use in Phase II.

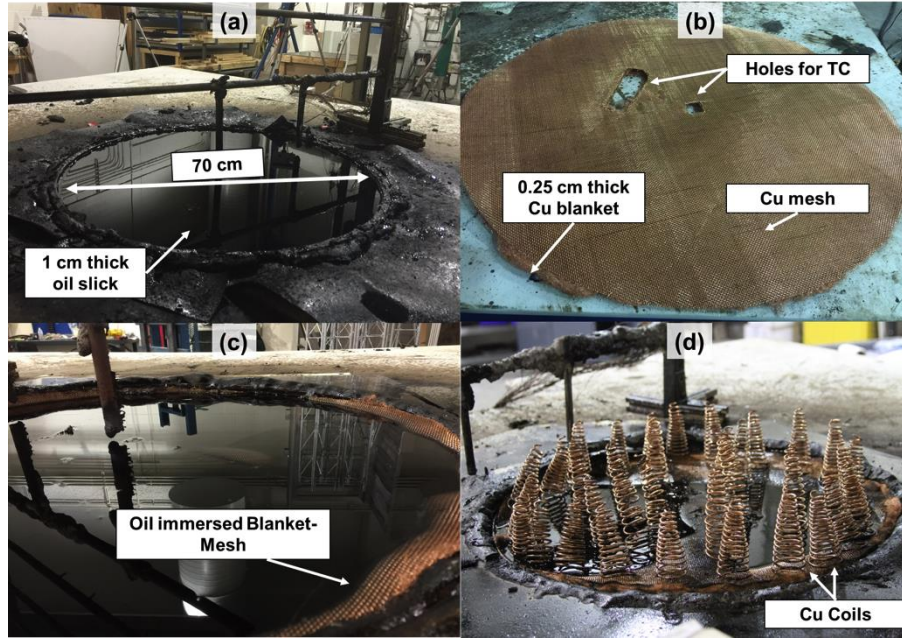


Figure 43: Intermediate-scale experiments (a) Baseline – without blanket (b) Blanket-mesh before testing (c) Blanket-mesh immersed in oil (d) Blanket-mesh + 36 coils immersed in oil

4.2 Experimental setup of Phase II

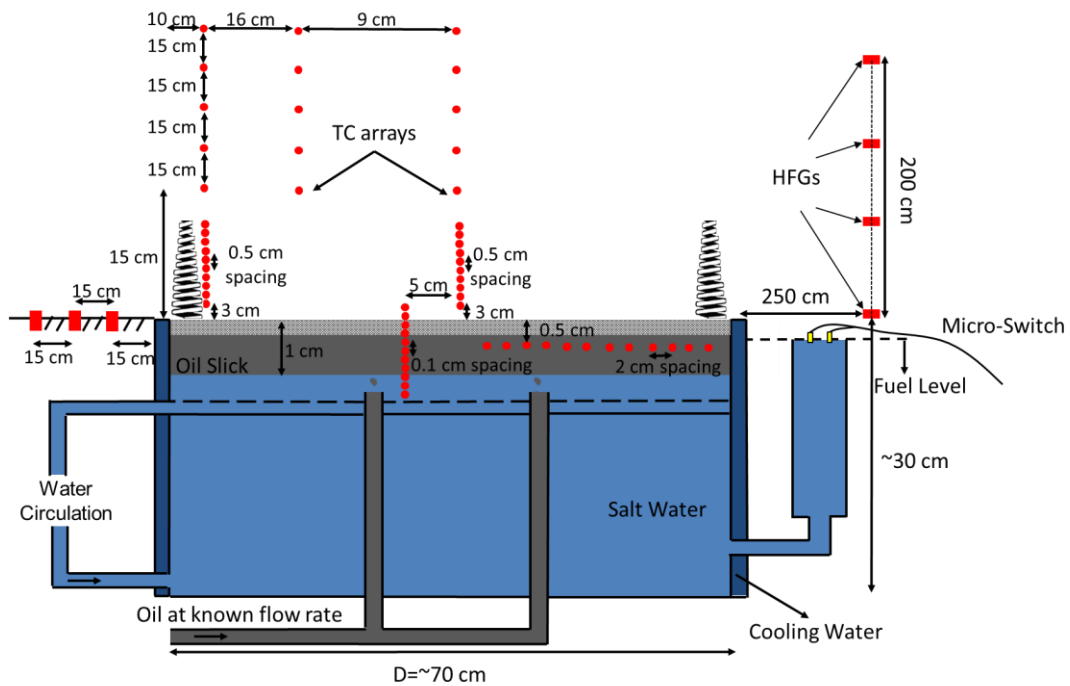


Figure 44: Experimental setup at Phase II

Figure 44 shows the experimental setup (Phase II) for burning ANS crude oil with multiple coils. The fuel layer was maintained at 1 cm depth while floating above a 29 cm deep saltwater (35

ppt) layer using a centrifugal pump that continuously feeds oil into the burner as shown in Fig. 44. A second container with a diameter of 15 cm (shown on the right hand side of Fig. 44) and a micro-switch actuated by a float were used to monitor the fuel level. A load cell was used to measure the rate of fuel supplied (g/min).

Figure 45 shows photograph of the phase II experimental set up. .

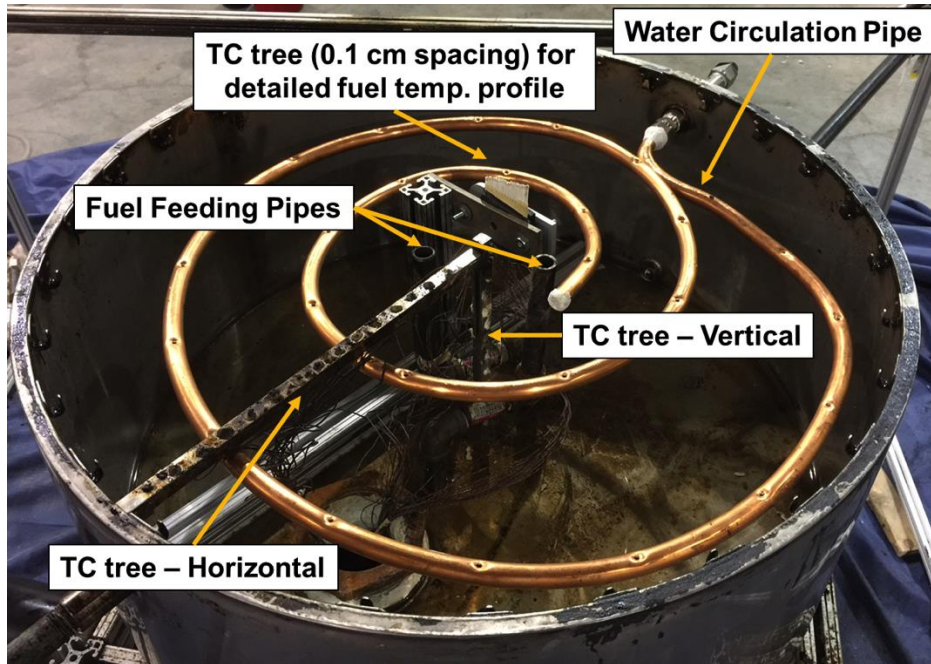


Figure 45: Photograph of the intermediate-scale experimental setup (Phase II). TC = Thermocouple.

A water recirculation system (perforated pipe) was placed underneath the oil slick to replicate a field condition of ocean currents cooling the bottom of the oil slick during ISB. Baseline tests with the recirculation system shown in Fig. 45 showed that a 1cm ANS crude oil layer did not boil over when the recirculation system was on.

4.2.1 Fuel level control system

The predictive model developed during Phase I (Explained in Section 6) was used to provide an approximate range of burning enhancement with the larger, 0.7 m diameter burner. The calculations showed that the capacity of the Omega peristaltic pumps used in the small-intermediate scale tests (Phase I) would be insufficient to supply the fuel and maintain a 1 cm fuel layer continuously during the larger scale (Phase II) experiment. Because of this reason, significant effort was devoted to develop a new pumping system to accommodate the increased burning rate. A centrifugal pump was used in conjunction with a pair of solenoid-operated valves controlled by a single-pull, double throw micro-switch actuated by a float system (Fig. 46a). Flow rate was controlled with a pin-type throttling valve, while the float serves as both a demand and a safety cutoff controller. When the oil level drops below the set point, the switch closes and an electrical signal opens the supply solenoid and closes the recirculation solenoid. When the oil

is at the set maximum, the switch opens, sending a signal to open the recirculation solenoid and close the supply solenoid (Fig. 46b). A pin-type throttle valve served to prevent cold oil flooding into the hot system and causing fluctuations to the temperature readings.

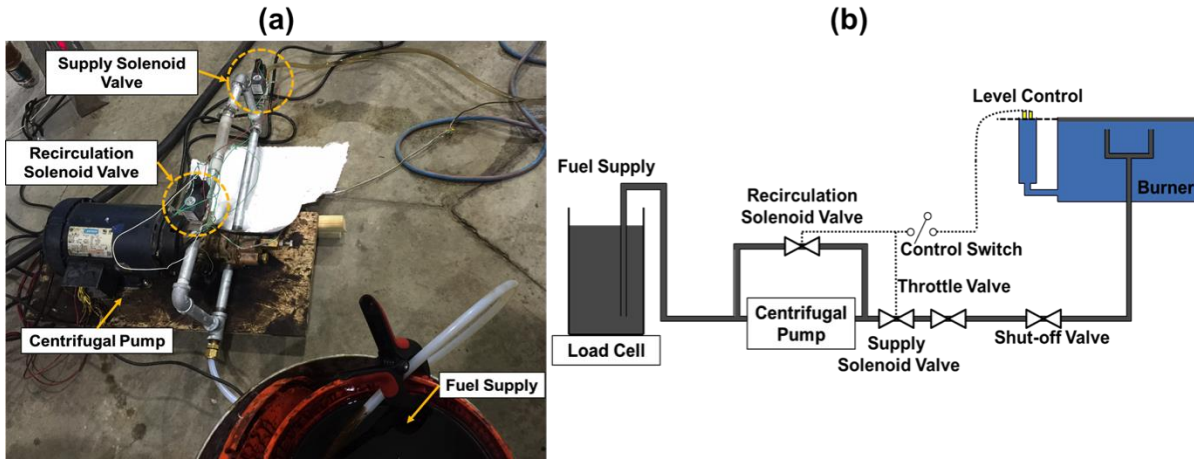


Figure 46: (a) Centrifugal pump for oil supply (b) Level control mechanism

Several experiments were performed to optimize the level control mechanism. The details of the different attempts can be found in Appendix B.

4.2.2 Instrumentation of Phase II

The temperature profiles of the plume, fuel layer and water sublayer were measured by thermocouple (TC) arrays as shown in Fig. 44. The horizontal and vertical gas phase temperature profiles were obtained by 15 TCs. Two TC arrays, which had 10 TCs (with 0.5 cm spacing) each, were used to measure the hot gas temperature from 3 cm to 8 cm above the fuel layer at the center and perimeter of the pool. Detailed liquid fuel and water temperature profiles were measured by 50 TCs. The external radiative heat flux was measured using four heat flux gauges placed 2.5 m away from the burner oriented towards the flame as shown in Fig. 44. Three additional heat flux gauges were used to measure the heat flux reaching the surface from the flame. These gauges pointed upwards as shown in Fig. 44.

A gas analyzing system was used to collect and measure the combustion products (O₂, CO, and CO₂). A sampling hood was placed directly above the burner pan (Fig. 47).

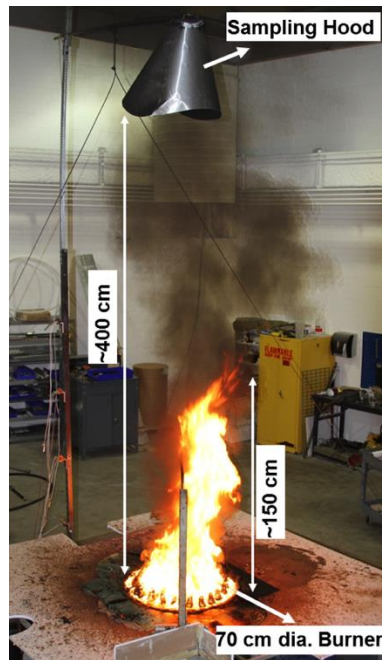


Figure 47: Phase II gas emission measurement hood

The sample gas was then passed through a cold-trap and particulate filtration system in order to cool the gas down before reaching the gas analyzer. The gas analyzer used was a Servomex 4200 Industrial Gas Analyzer.

4.3 Test results and discussion

4.3.1 Mass loss rate

Figure 48 shows the MLR at steady state for the large scale experiments performed in Phase II. ANS crude oil was used as the fuel with a slick thickness maintained at 1 cm by continuous feeding. The blanket thickness for all tests was 0.35 cm. The difference between each experiment is the number, placement, and height of the copper coils (collector region of the Flame Refluxer).

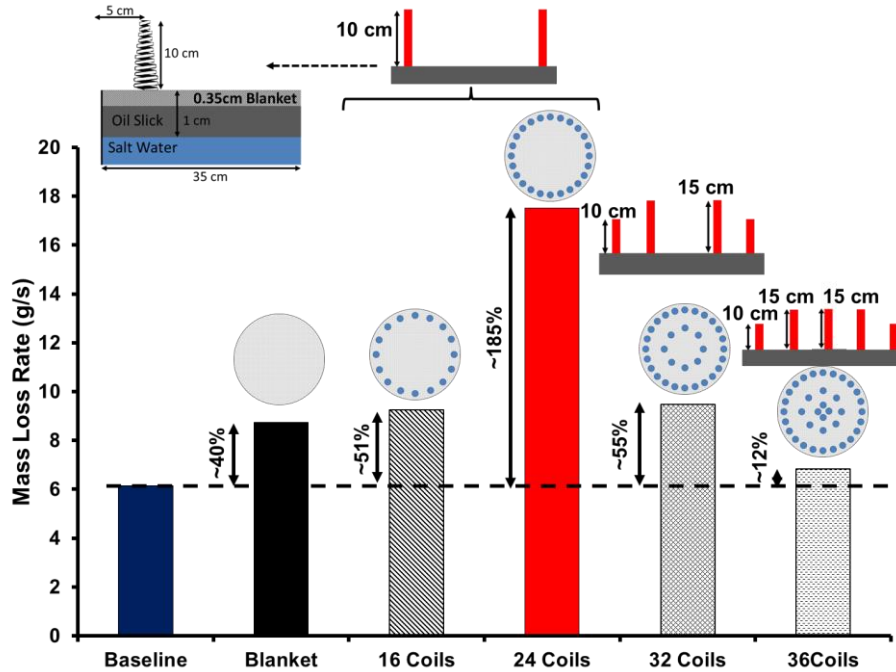


Figure 48: Optimization of # of coils on circumference - Mass Loss Rate

Figure 48 shows that the MLR reaches an optimum value of 17.5 g/s at 24 coils placed on circumference. This is ~3 times increase over the baseline case (6.1 g/s). As number of coils is further increased to 32, the burning rate decreases and similar to “16 coils” case. Adding coils at the center did not increase the burning efficiency. This is because the center coils were not high enough to be fully exposed to the hot plume zone.

4.3.2 Temperature profiles

Figure 49 shows the vertical fuel temperature distribution at the center for the baseline, blanket and “blanket-24 coils-mesh” cases. With an increase in the MLR, the curves move to the right as shown in the Fig. 49.

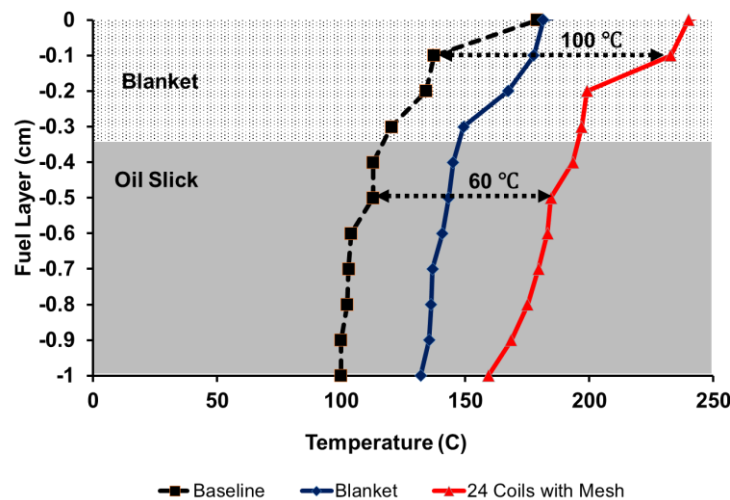


Figure 49: Vertical fuel temperature profile at the center for baseline, blanket, and blanket-24 coils-mesh

When the “blanket-24 coils-mesh” is placed into the fuel, the temperature below 0.1 cm of the fuel layer reaches 230 °C, which is around 100 °C higher than the baseline case as shown in Fig. 49. The increased temperature causes an increase in MLR. Additionally, nucleate boiling is observed inside the blanket, which further enhances the MLR. Figure 50 shows the vertical temperature distribution at the corner (5 cm away from the rim) for the baseline, blanket and “blanket-24 coils-mesh” cases.

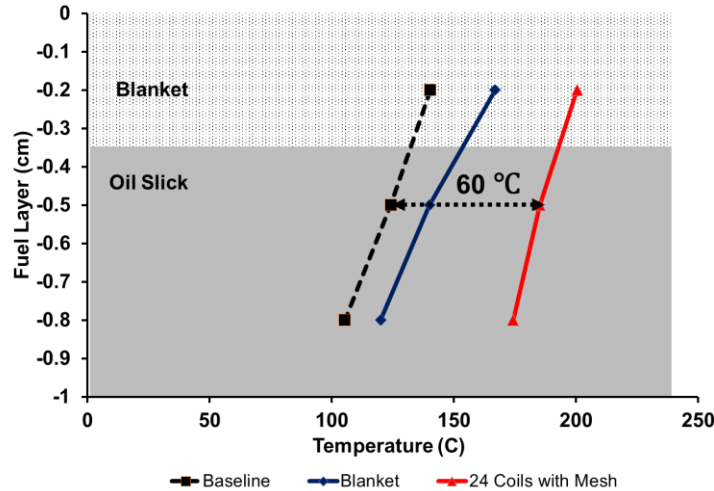


Figure 50: Vertical fuel temperature profile at the corner for baseline, blanket, and blanket-24 coils-mesh

For “blanket-24 coils-mesh” case, the temperature below 0.5 cm of the fuel layer reaches up to 185 °C, while the maximum temperature reached for the baseline case was 125 °C ($\Delta T \sim 60$ °C).

4.3.3 Gas emissions

As the fire increases intensity, more oxygen is consumed. This leads to a reduction in oxygen concentration and increased carbon dioxide concentration, which is a natural product of combustion reaction. Carbon monoxide production is the result of incomplete combustion. Oxygen (O₂), Carbon dioxide (CO₂) and Carbon monoxide (CO) were sampled in the non-combusting plume region using a conical shaped sampling hood as shown in Fig. 47. The experimental measurements are shown in Fig. 51.

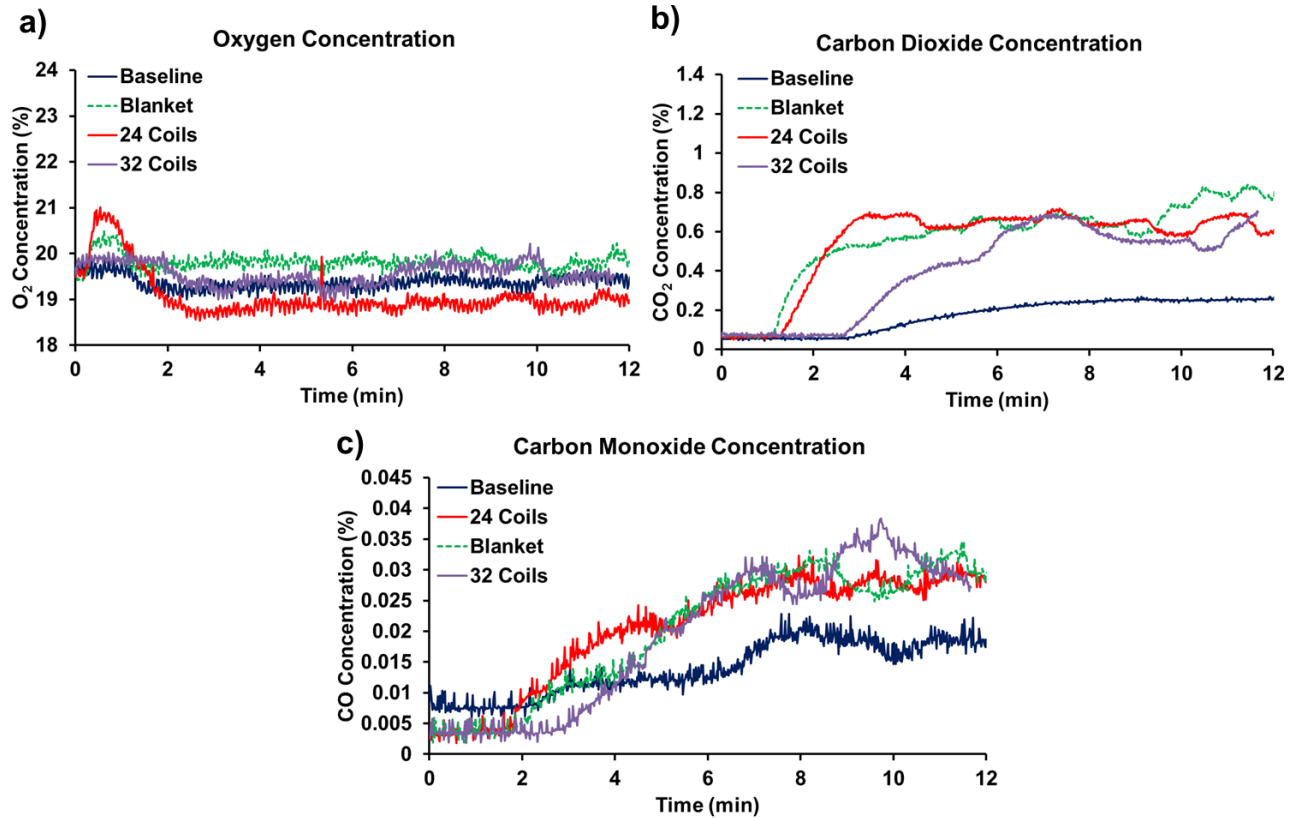


Figure 51: (a) oxygen concentration (b) carbon dioxide concentration (c) carbon monoxide concentration

Figure 51a-b show O₂ and CO₂ gas concentration from different blanket configurations. The blanket configuration with 24 coils burned 3 times faster which is clearly shown by the higher oxygen consumption and carbon dioxide production compared to the baseline case. Figure 52 shows the CO/CO₂ ratio for the four cases. It is clear that, during the steady state burning regime, the CO/CO₂ ratio is lowest for the blanket and 24 coils case. When a blanket with 24 coils was placed inside the pool, the ratio of carbon monoxide produced per carbon dioxide, was much lower than that of the baseline case (Fig. 52). Enhanced burning rates also promoted higher plume temperatures thereby aiding in complete combustion of the fuel and reducing quantity of unburned products of combustion.

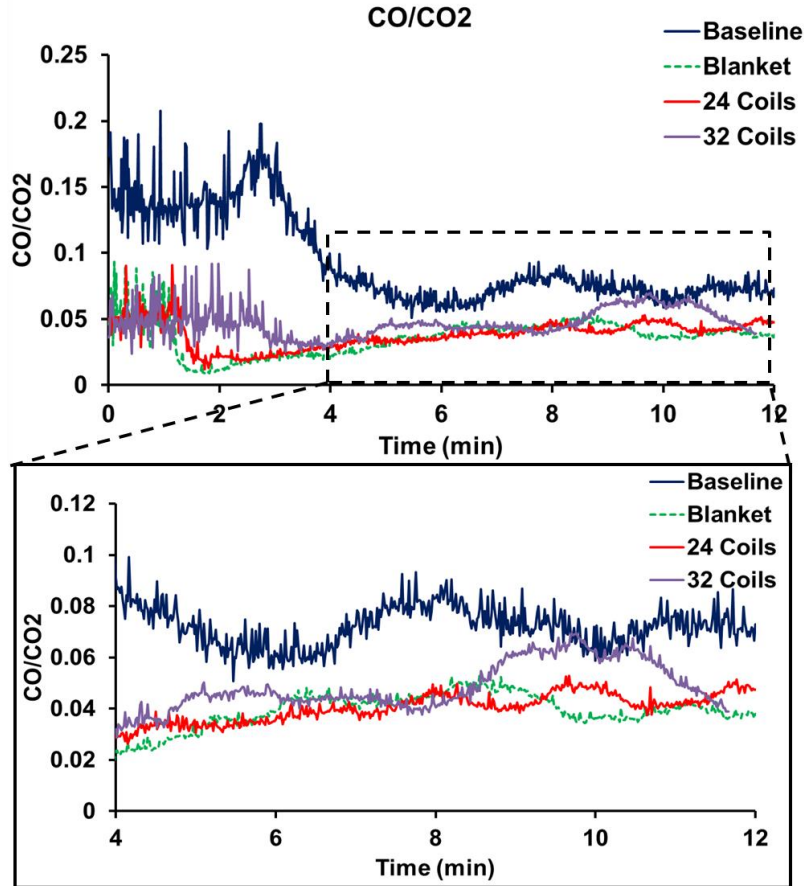


Figure 52: Carbon monoxide per carbon dioxide production ratio

4.4 Outcomes of Phase II

Phase II explored the effect of the number and height of coils on burning enhancement in a 70 cm diameter ANS crude oil pan fire. The following key conclusions were drawn from Phase II:

1. The experimental study showed that the mass loss rate was enhanced by a maximum value of 185%, with Cu blanket (0.35 thick) + 24 Cu coils placed on circumference (10 cm high, 0.5 cm pitch, 2 cm top and 5 cm bottom diameter) + Cu mesh (wire diameter of 0.05 cm and has an opening of 0.15 cm between wires).
2. The ratio of the volume of coils on the periphery to the oil slick volume was used to scale-up the number of coils. The optimum number of coils for Phase III tests was calculated as 48 (20 cm high, 0.5 cm pitch, 6 cm base and 2 cm top diameter). Details are explained in section 5.1.3.
3. The optimum coil height for Phase III was calculated as 20 cm by using the Fire dynamics simulator (FDS) developed by the National Institute of Standards and Technology (NIST). Details are in Appendix C.

5. Phase III – Field Trials

The objective of Phase III is to evaluate the designed prototype Flame Refluxer for field deployment by performing series of outdoor large-scale tests (1.4m diameter burner) in the Joint Maritime Test Facility (JMTF) in Mobile Alabama. In terms of Technology Readiness Level (TRL) advancement [2], Phase III moved the project from TRL 4 (Technology prototype demonstrated in laboratory environment – Phase II) through TRL 5 (Technology prototype tested in relevant environments).

5.1 Optimization of blanket and coil for Phase III

5.1.1 Blanket thickness

A mathematical model created in Section 6 was used to determine the Phase III blanket thickness. Figure 53 shows the predicted regression rate of the fuel in a 1.4 m diameter pool for different Cu blanket thicknesses (0.15, 0.25, 0.5 and 0.75 cm). Because of unavailability of boiling curves for a multicomponent crude oil in literature, a single component representative fuel, dodecane was used in the mathematical model.

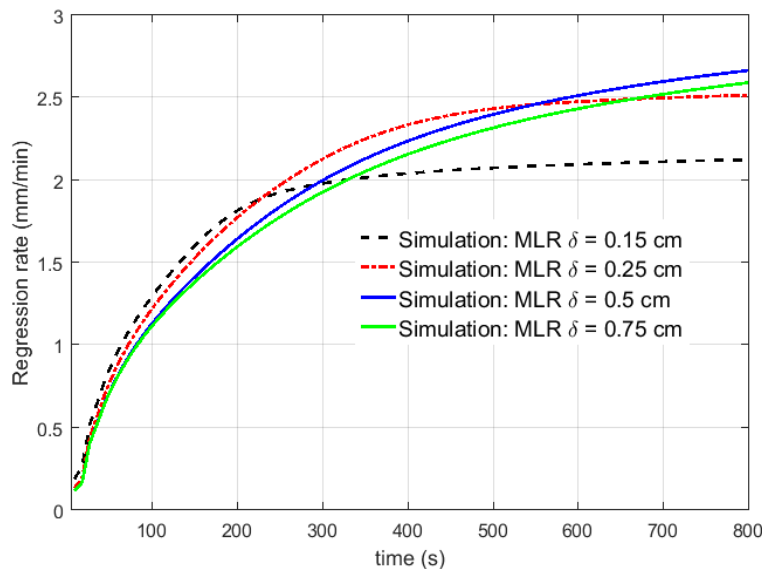


Figure 53: Regression rate 1.4 m diameter dodecane pool fire for the blanket thickness of 0.15-0.75 cm

The results demonstrated that the maximum regression rate can be obtained when the blanket thickness, δ , is 0.5 cm. Based on the results, 0.5 cm thick blanket was used in Phase III experiments.

Table 6 shows the regression rate of dodecane baseline pool fires as a function of pan diameter.

Table 6. Regression rate of dodecane baseline pool fires as a function of pan diameter

	Regression rate (mm/min)		
	Small scale (D = 0.1 m)	Intermediate scale (D = 0.7 m)	Large scale (D = 1.4 m)
Literature	0.75	2.00	3.51
Experiments	1.02	1.24	2.98
Model	0.81	1.13	2.00

5.1.2 Coil height

Figure 54 shows the predicted flame height by Fire Dynamic Simulator (FDS) [C.3]. Details of the FDS are in Appendix C.

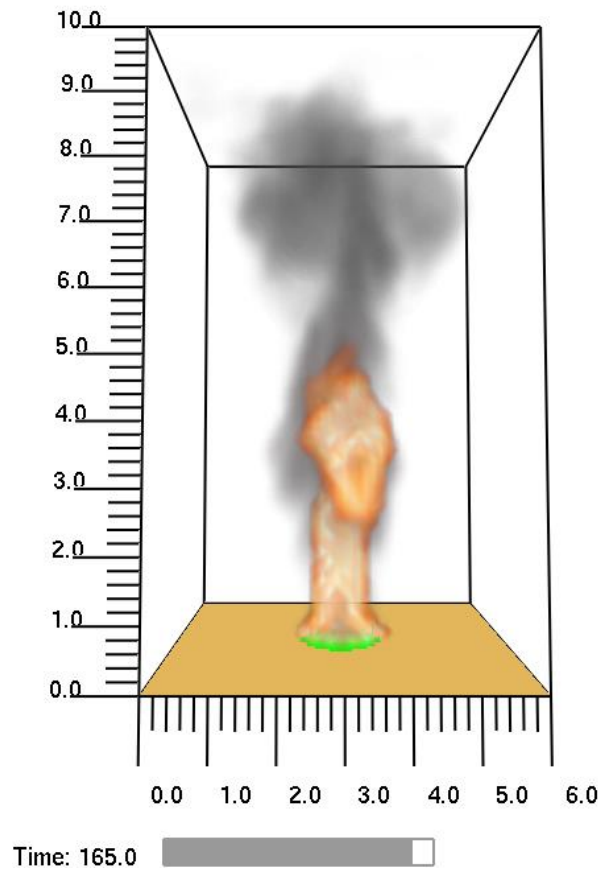


Figure 54: Visualization of instantaneous heat release and smoke for a dodecane pool fire of 1.4 m diameter. Distances are in meters and time is in seconds.

Figure 54 shows instantaneous heat release and smoke visualizations in a dodecane pool fire of 1.4 m diameter. Mean flame height is calculated based on a heat release cut off of 200 W/m³. The mean flame height close to the periphery (10 cm radially inside of the burner rim) is found to be approximately 69 cm in the absence of any wind. In the presence of a unidirectional wind of 10 Knot, the flame height at the same radial location reduces significantly to around 28 cm. From the small scale experimental results, it is seen that increase coil height leads to decrease in its structural stability. Based on the numerical predictions, and considering thermal and structural stability of the collector, coils of 20 cm (downwind direction) and 10 cm (upwind direction) height were selected.

5.1.3 Number of coils

The optimum number of coils was calculated by using Eq. 8. Table 7 shows the parameters used in the *CR* calculations

Table 7. Parameters used in *CR* calculations – Phase III

	Phase Ib	Phase II	Phase III predictions
Fuel thickness (cm)	1	1	1
Number of coils	8	24	48
Coil base diameter (cm)	5	5	6
Coil top diameter (cm)	2	2	2
Coil wire diameter (cm)	0.2	0.3	0.4
Coil height (cm)	6	10	20
Pool diameter (cm)	28	70	140
<i>CR</i>	0.46	0.42	0.5

To obtain a similar *CR* with Phase I and Phase II, 48 coils (20 cm high, 0.5 cm pitch, 0.4 cm wire diameter, 6 cm base and 2 cm top diameter), are used in Phase III.

5.1.4 Conclusions of Phase III optimization

The optimization results show that for a 1 cm oil layer thickness in a 1.4 m diameter oil slick;

- a) The blanket thickness of 0.5 cm provides the maximum efficiency.
- b) In low wind conditions, 48 coils with 20 cm height were chosen to collect the heat from the flame and transmit to the blanket. Calculations show that this will enhance the MLR ~4 - 5 times.
- c) In the presence of a unidirectional wind of 10 Knot, reducing the height of the coils on the upwind direction to 10 cm could reduce the heat loss and increase the burning efficiency.

In this context, two baselines and four blanket (with different coil configurations) tests were performed with HOOPs blend crude oil to quantify the enhancement in burning rate and reduction on gas emission due to blanket-mesh-coil system. Figure 55 shows the different blanket-mesh-coil configurations tested in Phase III.

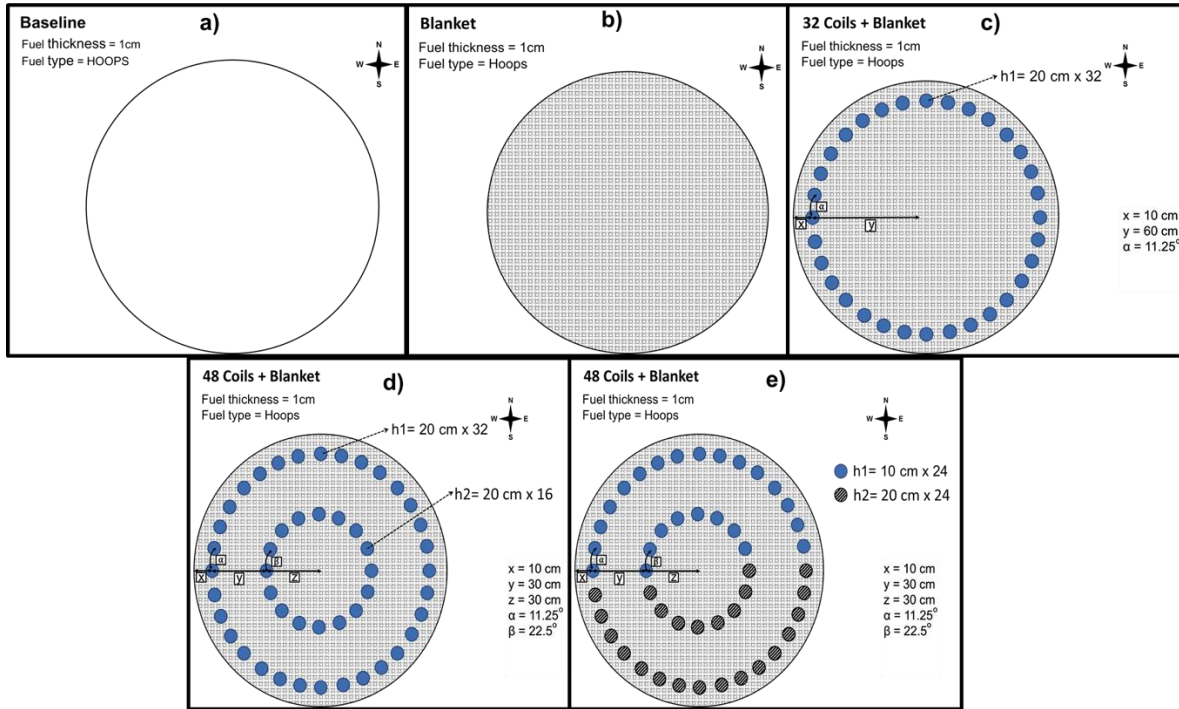


Figure 55: Blanket-mesh-coil configurations tested in Phase III, a) Baseline, b) Blanket, c) Blanket with 32 coils, d) Blanket with 48 coils (Same coil height) e) Blanket with 48 coils (Various coil heights)

Experiments showed that the configuration with 48 coils (same height) with 0.5 cm thick blanket provided the maximum enhancement in the burning rate for the performed set of tests. The setup and results of the Phase III tests are discussed in the following sections.

5.2 Experimental setup of Phase III

5.2.1 Burning tank

The designed prototype was tested in the 30.5 m (100 ft) long, 9.2 m (30 ft) wide and 1.5 m (5 ft) deep steel tank located at Joint Maritime Test facility in Little Sand Island (LSI) in Mobile Bay, Alabama (Fig. 56).

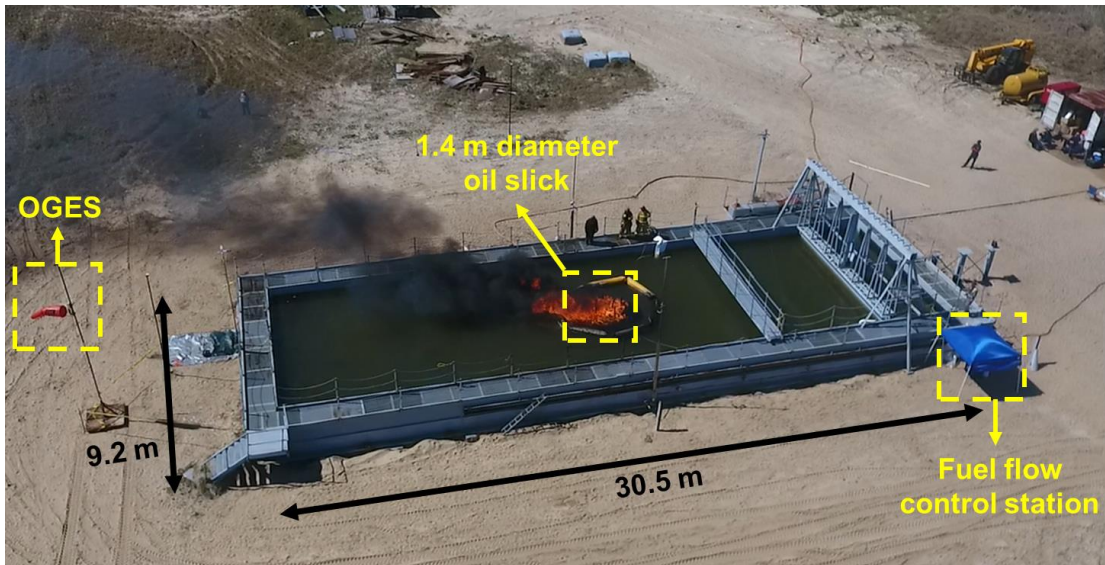


Figure 56: United States Coastal Guard, Joint Maritime Test Facility

During filling of the tank, a high volume submersible pump was placed on a small platform located between the Ex-USS *Shadwell* and LSI. The water used to fill the burn pan was drawn directly from Mobile Bay. During testing, the tank was only filled to the 1.2 m (about 4 foot) level.

5.2.2 Burner ring

The sketch and picture of the burner ring are shown in Fig. 57.

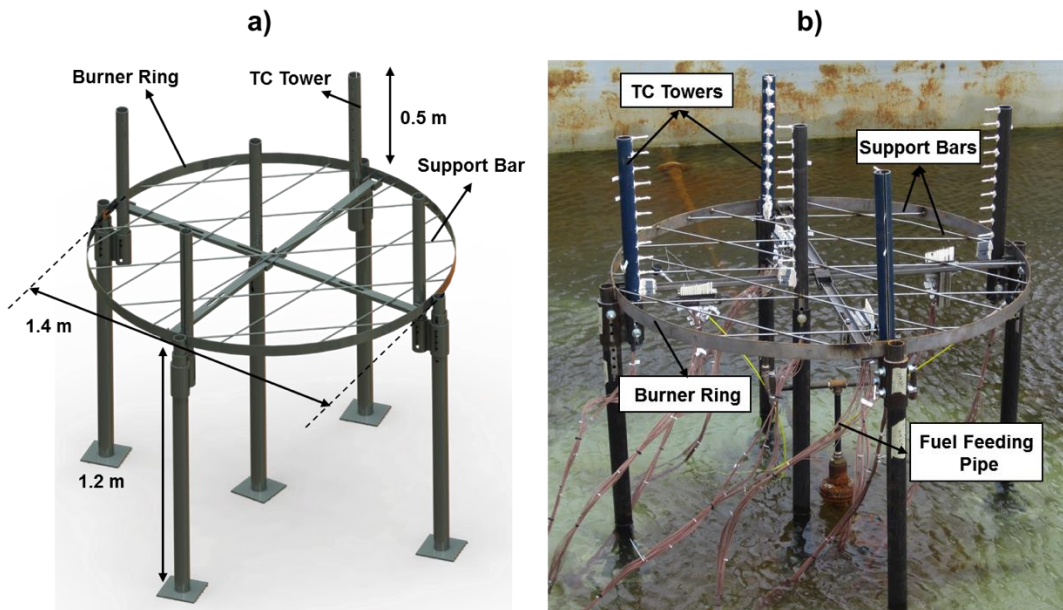


Figure 57: Phase III burner ring a) Sketch b) Picture from Phase III tests

A modular, 1.4 m diameter burner ring was designed to perform Phase III tests. The ring, placed at the center of the burning tank (Fig. 57b), features thin bars running across the center to provide support to the blanket and keep it level. Five 50 cm high thermocouple (TC) towers placed on four sides and center of the ring (Fig. 57) were used to measure gas phase temperature. These towers were designed with telescopic joints for individual adjustment. Detailed drawings of the burner ring are shown in Appendix D.

5.2.3 Blanket-Mesh-Coil system

Figure 58 shows the sketch and pictures of the blanket-mesh-coil system.

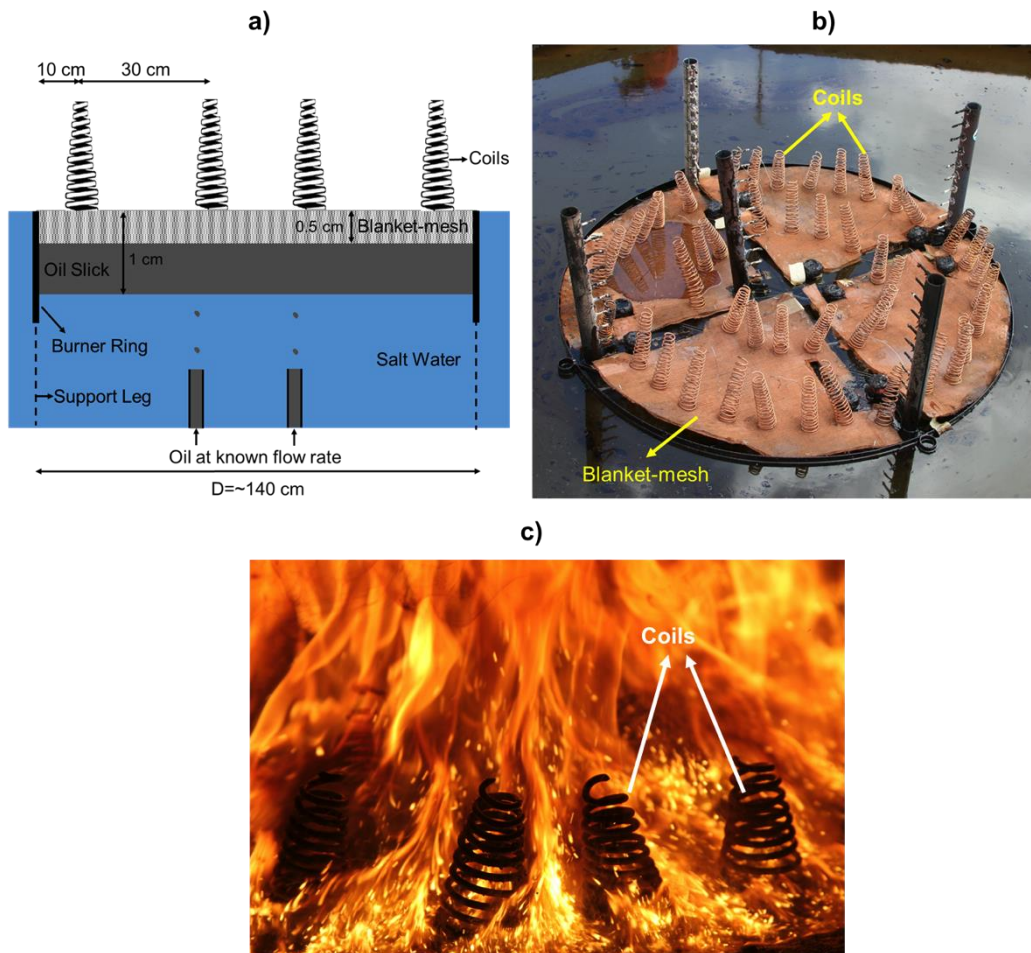


Figure 58: Blanket-mesh-coil system at Phase III a) Cross-sectional sketch b) Blanket + 48 coils (Same height) c) Coils engulfed in the flame

A 0.4 cm thick blanket with 0.0127 cm (0.005") diameter copper (Cu) fibers was placed between two Cu meshes (wire diameter of 0.05 cm (0.023") with an opening of 0.15 cm between wires). The blanket (Heater) was immersed into a 1 cm oil slick as shown in Fig. 58a. Figure 58b shows one of the tested coil configurations, which had 32 coils on the periphery and 16 coils close to the center. Figure 58c is the picture of the coils engulfed in the flames. The coils were 20 cm high.

5.2.4 Fuel monitoring system

A continuous fuel feeding system was used to keep the fuel level constant (1 cm) during the tests. To monitor the fuel thickness, two FORBEST FB-PIC3188D-130 portable cameras were placed under the North and South side of the burner ring (Fig. 59a). The wall of the ring was marked by 0.2 cm intervals. The 1 cm mark, where the bottom of the fuel layer stood, was continuously monitored visually by the cameras. The pumping rate was adjusted to keep the fuel level constant on the 1 cm mark. HOOPS blend crude oil was used in all tests.

An Omega Engineering FLR6115D Flow Meter, calibrated for crude oil, was used to monitor the fuel flow. The meter was connected to the main DAQ system to ensure time matching for all aspects of the testing.

5.2.5 Instrumentation of Phase III

Figure 59 shows the instrumentation used in Phase III.

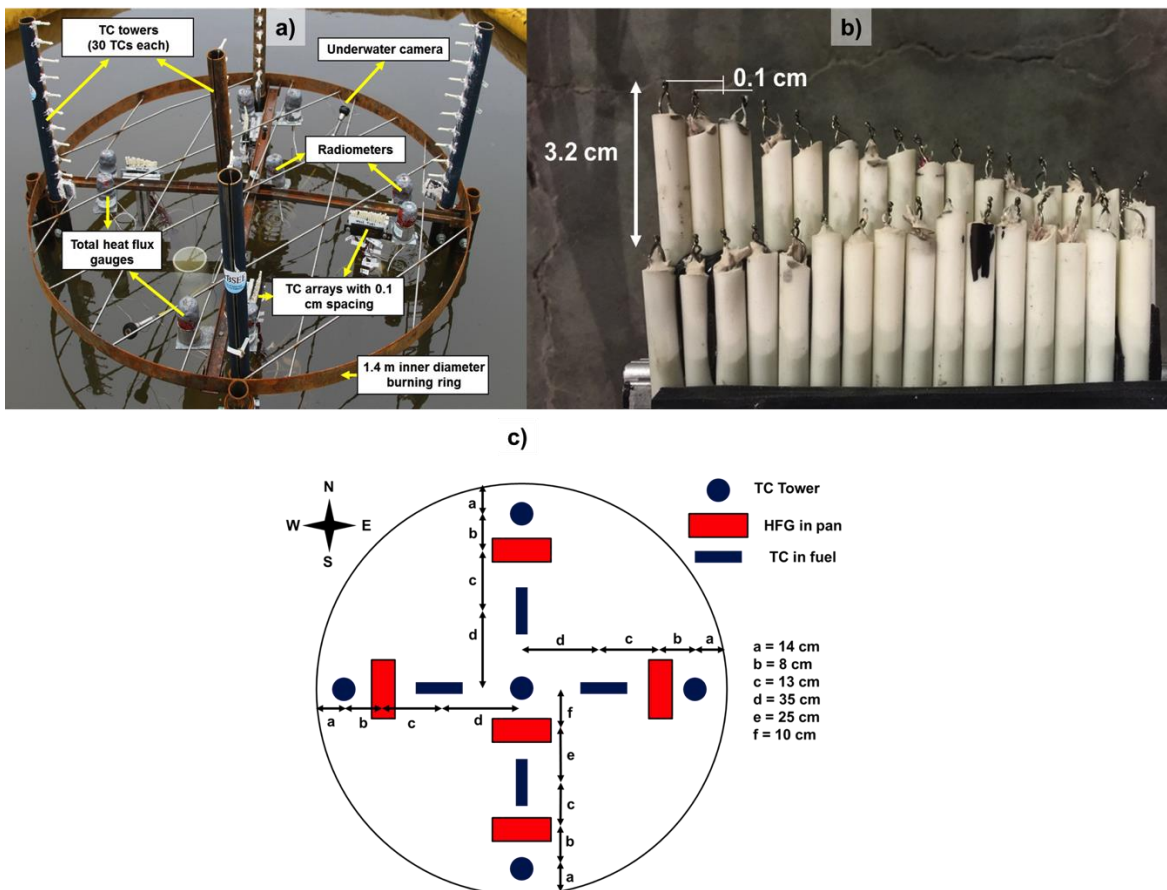


Figure 59: a) Instrumentation at Phase III, b) Detailed TC array for gas-phase, fuel and water, c) Locations of instrumentation.

The temperature profiles of the plume, fuel layer and water sublayer were measured by the TC arrays as shown in Fig. 59. The horizontal and vertical gas phase temperature profiles were obtained by five TC towers, which had 10 TCs (with 5 cm spacing) each. Detailed gas-phase, fuel, and water temperatures were measured by 228 TCs (Fig. 59b). 10 heat flux transducers (5 total and 5 radiative with 150 kW/m² capacity) were used to measure the heat flux reaching the surface from the flame. These gauges pointed upwards as shown in Fig. 59.

5.2.6 Outdoor gas emission sampling system

The Outdoor Gas Emission Sampling System (OGES) was used to sample and analyze the gas concentrations of O₂, CO₂, and CO (Fig. 60). The details of the OGES is given in Appendix E.



Figure 60: The Outdoor Gas Emission Sampling System (OGES) at Phase III

The Mobile expedition required a significant amount of forethought and logistics planning. The test apparatus, the data collection system, the fuel delivery system, and various assemblies of instrumentation were all required to be both robust and easily relocatable. Several design considerations are detailed below.

The first design consideration was the shipping crate. In order to economically transport the test equipment safely, a crate was constructed atop a 10-foot by 4-foot standard long pallet. The final crate dimensions were 11(l) x 4.5(w) x 5(h) feet, constructed in place for transport pickup. A single long pallet was determined to be more cost effective than multiple smaller pallets, and allowed for the transport of longer material.



Figure 61: Shipping crate: Exterior on Little Sand Island (left) and Open during loading (right).

The second design consideration was the ability to construct the test apparatus in such a manner that a single technician could unpack, assemble, and op-test the entire test apparatus and data collection system. Many systems, such as the OGES system required the final construction to occur on site, which necessitated the presence of all tooling on site. The test apparatus was designed to be modular in construction, with legs, burner ring, instrumentation towers, and HFG mounting to be accomplished on site. In total, the instrumentation and data collection encompassed more than 1.5 kilometers of thermocouple wire, 500 meters of stranded copper wire, 100 meters of cooling conduit, 100 meters of gas sampling hose, 100 meters of fiber optic cabling, a 7-meter gas sampling tower, and 5 separate cooling water pumps.

The blankets used in testing were sandwiched and cut at WPI, with all of the 112 copper coils being hand-wound of 6 gauge copper prior to shipping. The blankets were shipped sans coils, with the coils added on site as per the test designs.



Figure 62: FR blanket prior to (left) and during assembly (right).

The system contained several single-point-of-failure components that required extra effort and caution to transport. The transport of the NI-PXI data collection system was accomplished within a pelican case, along with the control computer and interface electronics. Desiccant was added as appropriate to prevent moisture buildup in the humid Alabama environment. The fiber optic cable was contained a second pelican case, along with the Servomex 4200 gas sampling system and associated sample conditioning components. The burner ring was considered robust and simple enough that any shipping damage could be repaired at the Coast Guard facility. Pelican cases were chosen for their history of shock-resistant and waterproof durability.



Figure 63: Burner assembly with legs only (left) and with full instrumentation including heat flux gauges, fuel layer thermocouples, and thermocouple towers, ~290 data points in all (right).

The thermocouple towers built for the Mobile expedition by WPI required special packaging, due to both their odd shape, and the delicate nature of the thermocouple arrays. To compensate for potential vibrational damage, the thermocouples were transported thermocouple-down, in a non-interference housing, bespoke for the expedition. Thermocouple wiring and PXI integration cards were transported within the same container, with the wiring isolated from the thermocouples via internal baffling. The non-interference housing was mounted within the container with rubber shock mounting. The thermocouple towers arrived intact to Mobile, with no repairs needed.



Figure 64: Thermocouple tower transportation housing showing tower-end sockets (left) and transport-ready configuration (left). During transport, the thermocouples would be facing down to prevent vibrational damage.

Every stage of data collection needed to be created and installed on site. The thermocouple and HFG wiring and led to a sheltered housing containing the NI-PX. This is the same container built to ship the thermocouple towers, an intended design choice. From this container, the fiber optic cable was routed through a hard PVC conduit to prevent inadvertent damage to the control shack that housed the VI computer. All DAQ components were powered via a 15-minute UPS with surge protection to prevent catastrophic failure due to weather events or power fluctuations.

The OGES system required completion on site, as the tower had never been fully assembled prior to deployment. The tower itself was constructed, then attached to a mobile base that was

constructed and welded on site. The gas collection sock was attached, but the pulley required modification to function, which was also accomplished on site. The tower was then raised, and counterweighted in order to prevent tip-over.



Figure 65: OGES tower assembly and raising: A base was welded to support the 7 meter tower (left) then raised via forklift (center) and instrumented (left).

Finally, the shipping crate contained all the material required for on-site cleanup of crude oil contaminated material. Comprehensive PPE for the handling of hazmat was shipped, including absorbent booms, absorbent sheets, Tyvek suits, boot covers, respirators with organic solvent filters, latex gloves in three sizes, and shoulder length industrial solvent gloves. Hazmat containment bags, designed for the holding and transport of wet hydrocarbon solids were used for site cleanup and shipment to an appropriate disposal site. There was zero oily waste left behind on the island after WPI departed.

5.3 Test results and discussion

Experimental results of Phase III are summarized in Table 8.

Table 8. Experimental matrix and results

Test	Test Duration (min)		Wind		Mass loss rate (mm/min)	CO/CO ₂	Residue removal
	wfs*	wofs**					
	Baseline	15	4	3.67			
Blanket	20	39	3.42	N-S	5.61	0.040	96.2
Blanket + 32coils	14	37***	1.76	NW-SE	8.36	-	97.1
Blanket + 48 coils (VH)	20	62	5.34	N-S	12.84	0.027	98.5
Blanket + 48 coils (SH)	12	59	4.08	NW-SE	17.36	-	98.2

*wfs: with fuel supply, **wofs: without fuel supply, ***extinguished by the fire team, VH: Various heights, SH: Same height.

Details of the experimental results are discussed in the following sections.

5.3.1 Mass loss rate

A continuous feeding system comprising an electric pump and a flowmeter was used to measure the mass loss rate (MLR) (Section 5.2.4). The pumping rate, which is equal to the MLR, was adjusted to keep the fuel level constant (1 cm) in the burner ring. Figure 66 shows the experimentally determined MLR at steady state with varying blanket and coil configurations. The steady state was determined from liquid phase temperature profile and was occurred with 6-10 minutes of the test.

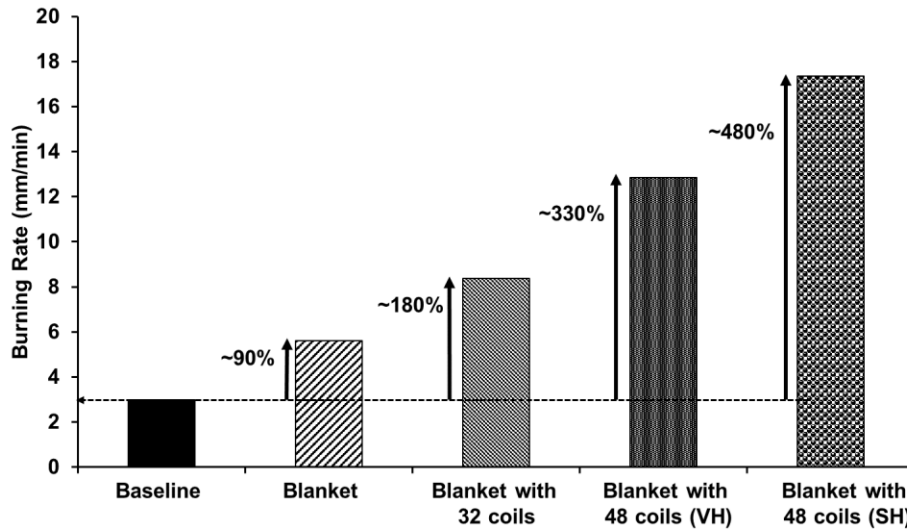


Figure 66: MLR of Phase III at steady state, VH: Various heights, SH: Same height.

As shown in Fig. 66, the additional heat provided by the blanket and coils significantly increased the steady state MLR. The MLR reached a maximum value of 17.3 mm/min at 48 coils (SH) placed on circumference and inner ring (Fig. 55d). This is ~ 480% increase over the baseline case (3 mm/min). The enhanced value is more than 3 times of the burning rate of highly volatile gasoline pool fires (1 m diameter gasoline pool fires have a steady state regression rate of ~ 5 mm/min) [3, 4].

The amount of Cu deployed into the pool is another important parameter. Achieving high burning rate by using minimum material will ease the deployment and cost. The weight of the blanket was kept constant (~6.5 kg) for all tests. For different coil configurations, the mass of the Cu deployed in to the pool changed accordingly. The burning enhancement per mass (BEPM) was calculated by the following equation;

$$BEPM = \frac{(MLR_{Test\ i} - MLR_{Baseline})}{MLR_{Baseline}} \times 100 / \text{Mass of Cu (Blanket + Coils)}, \tag{9}$$

$$i = 2,3,4,5$$

The ratio of burning enhancement to the total mass of Cu is presented in Fig. 67. It is observed that the coil configuration has a significant impact on BEPM. As an example, adding 32 coils on blanket (Fig. 55c) did not result an increase in BEPM (Fig. 67). This means that the number of coils was not sufficient to effectively collect heat from the flame and increase the thermal output. With the increase in number of coils from 32 to 48, the surface contact area with the hot plume increases and promotes more efficient heat collection and higher BEPM.

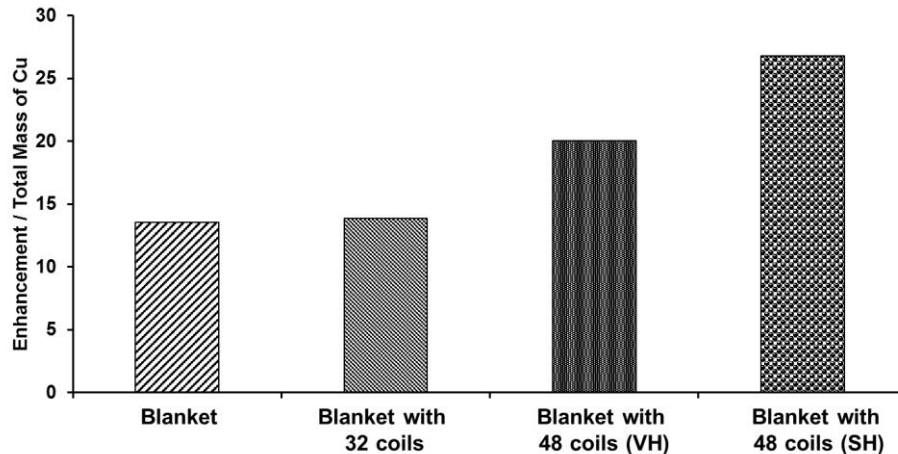


Figure 67: The ratio of burning enhancement to the total mass of Cu, VH: Various heights, SH: Same height.

5.3.2 Temperature profiles

A total of 288 TCs were used to measure detailed temperature profiles within the gas layer immediately above the fuel surface, oil layer, and water sublayer at nine radial locations of the pool, as shown in Fig. 59. Due to the substantial number of data points, a data analysis and visualization code was developed in MATLAB. The code extracts the data from the source (Excel spreadsheet) and smoothens it by using locally weighted linear regression and time averaging.

The code was used to determine the gas-fuel interface. To identify the gas-fuel interface, the previously measured data from Phase I-b and Phase II were used because of precise information of the location of the fuel surface during the experiments. In both phases, the temperature profiles were first plotted and the temperature behavior at the phase interface was analyzed (Fig. 68a, b). It was observed that the temperature gradient at the gas-fuel interface is much higher than the other regions. The temperature gradient at the interface was used to detect the fuel level in Phase III.

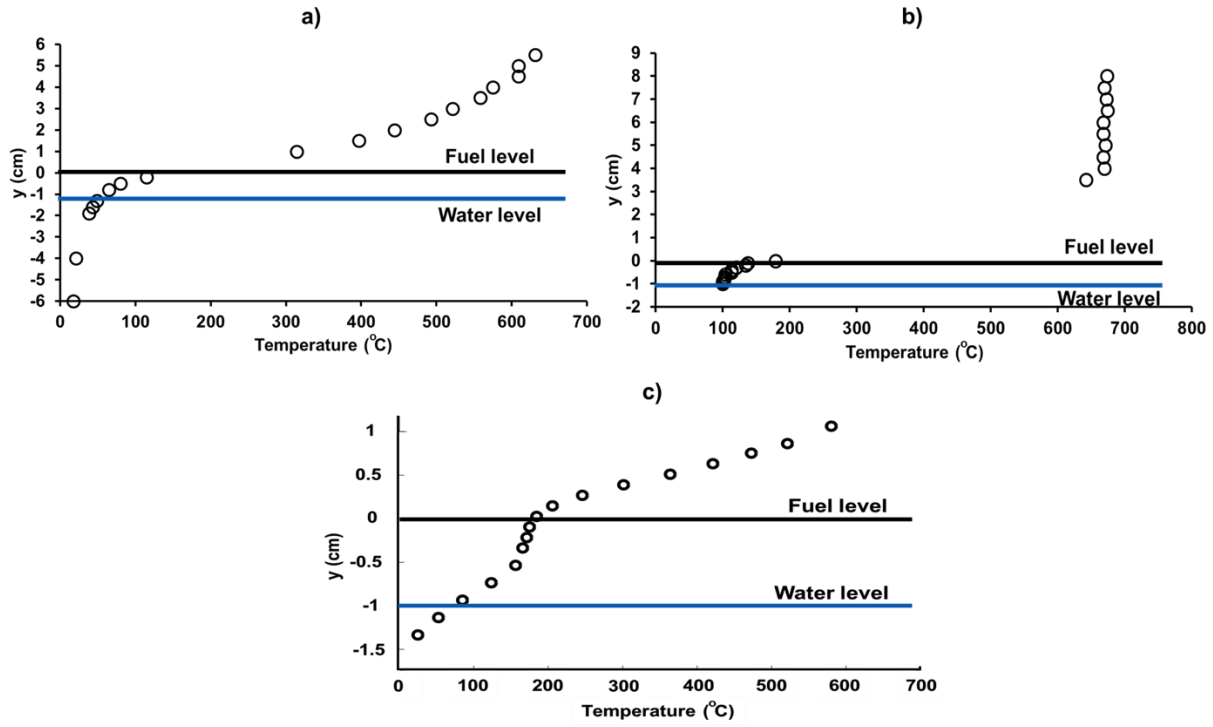


Figure 68: Baseline fuel-gas interface determination by using the temperature gradient at steady state a) Phase I-b, b) Phase II and c) Phase III

5.3.2.1 Gas phase temperature above the fuel surface

Figure 69 shows the flame geometry and gas temperature contours (average of 100 s at steady state) for the baseline, blanket and blanket with 48 coils (SH) cases.

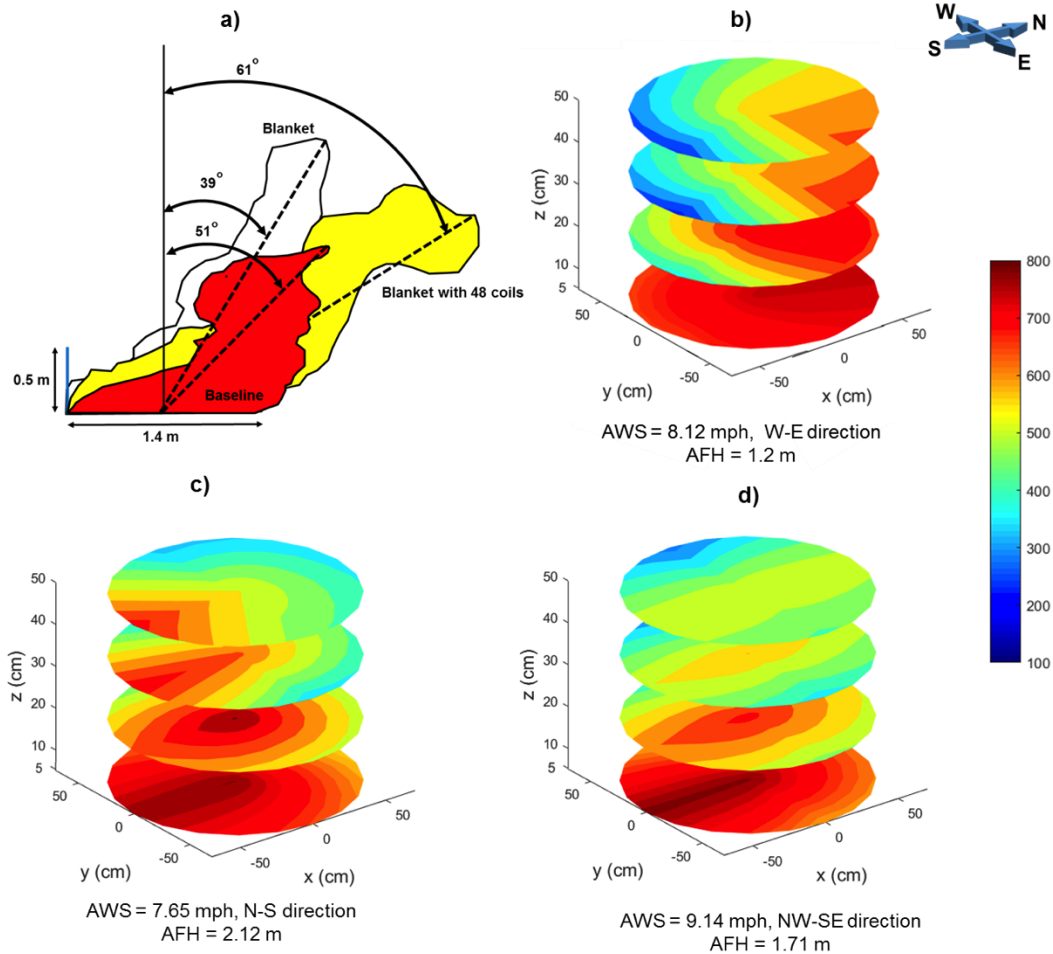


Figure 69: Flame geometry and plume temperature contours at steady state a) flame tilt angle on downwind direction b) baseline, c) blanket, d) blanket with 48 coils (SH), Contour units are in °C, AWS = Average wind speed, AFH = Average flame height.

The flame heights and tilt angles presented in Fig. 69 were calculated by averaging data from the videos taken by three cameras. For the baseline test, the average flame height was measured as 1.2 m with 51 degrees tilt on downwind direction (Fig. 69a, b). The high wind speed resulted with shifted temperature contour in the plume. The temperature profile from fuel surface to 50 cm high was measured by 5 TC arrays (10 TC each) (Fig. 59). The average temperature 5 cm above the fuel surface was measured as ~700 °C while, 50 cm above the fuel surface was ~400 °C (Fig. 69b). In the blanket test, the average flame height was 2.12 m and the tilt angle decreased to 39 degrees due to milder wind conditions (7.65 mph, N-S direction). The TC tower on the south side, downwind direction, measured the highest plume temperatures at 50 cm above the fuel level, while the others read lower values due to the flame tilt (Fig. 69c). It is observed that the flame anchored on the blanket, kept the blanket hot and promoted nucleate boiling therefore

higher burning rate (Fig. 69c). For the test with blanket and 48 coils (SH), the heat was maintained in the blanket longer and burned the residue collected in the blanket. This resulted in less post-burn residue discussed in section 5.3.5.

5.3.2.2 Gas-fuel-water temperatures

A total of 238 TCs were used to measure in-depth temperature profiles in gas-phase, oil layer and water sublayer at nine locations of the pool, as shown in Fig. 59. Figure 70 shows the temperature contours for the gas-fuel and water interfaces at steady state.

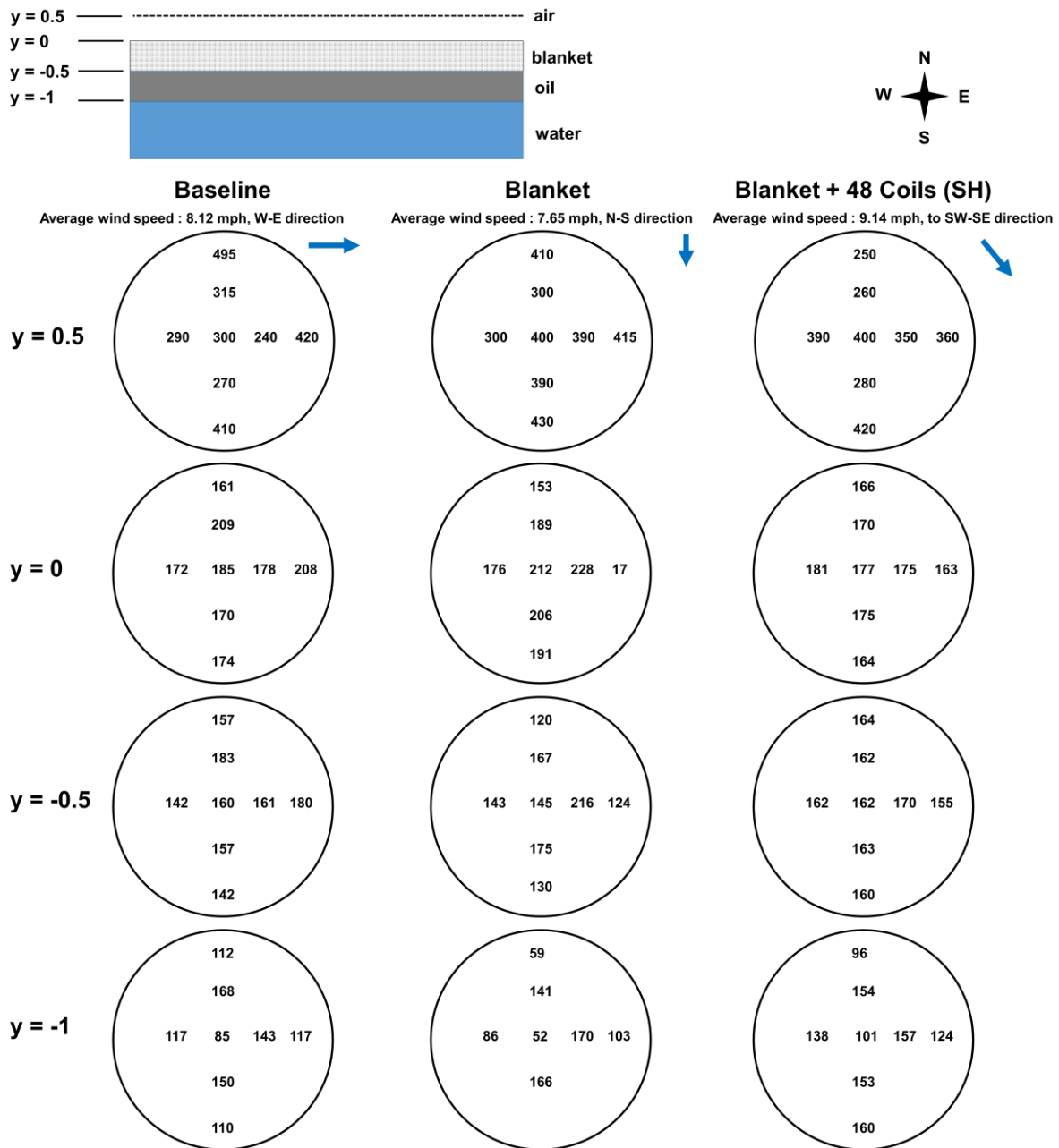


Figure 70: Temperature contours at steady state for baseline, blanket and blanket with 48 coils

Figure 70 shows the temperature contours of four locations: gas phase ($y = 0.5$ cm, gas-fuel interface ($y = 0$ cm), blanket-fuel interface ($y = -0.5$ cm), and fuel-water interface ($y = -1$ cm). The results show that the fuel temperatures did not change significantly with the presence of blanket and coils, contrary to the Phase II tests (an approximately 100 °C increase was observed in ANS – Fig. 49). The thermo-physical properties of the new fuel used in the field trials might be the reason for this difference. HOOPS crude is highly volatile and has a low specific heat and high thermal diffusivity. For the baseline test, the heat flux coming from the flame was sufficient to heat the 1 cm thick fuel slick to its boiling region. Thus, adding blanket and coils did not increase the fuel temperature. The blanket provided nucleate boiling zones, where enhanced mass transfer occurs. Adding coils provided more heat to the blanket and increased ΔT ($T_{\text{blanket}} - T_{\text{saturation}}$) value, therefore promoting higher heat transfer to the fuel (Fig. 83).

The detailed temperature profiles for the baseline, blanket and blanket with 48 coils are given in Appendix F. The temperature profiles were investigated for four burning phases: 1) transition/growth, 2) steady state burning with fuel supply, 3) burning without fuel supply, 4) extinction. Δt on the figures shows the time average. For example, after ignition, $\Delta t = 10$ (average of 10 data points) were used to observe the transition period. For steady state, Δt was increased to 60 data points (or seconds). For all figures, the blue line is the initial temperature. Temperature profiles show that the transition phase of the blanket with 48 coils (SH) is longer than the baseline and blanket cases. This indicates that the coils initially acted as a heat sink. The heat for vaporizing the fuel was used to preheat the coils. During this phase, the MLR was lower than the baseline due to presence of coils. Once the initial transient period passed, a steady state regime was reached, where the blanket and coils heat up the fuel and increase the mass loss rate.

At steady state, with the introduction of blanket and coils, the surface temperature of HOOPS crude oil remained almost same with the baseline case. As explained before, the high volatility of the HOOPS crude oil caused a uniform vertical temperature profile inside the fuel even for the baseline case.

For the baseline, the steady state burn was followed by the extinction phase. After stopping the fuel supply, the temperature rapidly decreased and the flame self-extinguished in ~ 5 minutes (Appendix F-Baseline). The presence of the blanket and coils extended the self-burning (no fuel supply) duration before extinction, ~ 13 minutes for blanket and ~ 20 minutes for blanket with 48 coils (SH). During extinction, the residue (heavy components of the crude oil) accumulated in the blanket burned effectively. The data collection was stopped at $t = 35$ minutes due to the storage limitations. Although it is not shown in Appendix F, in the blanket with 48 coils (SH), small pockets of fire were visible for 60 minutes after stopping the fuel supply. This shows that a heat feedback loop was created where the blanket heated the residue and the heat generated by combustion reheated the blanket.

5.3.3 Heat flux near fuel surface

Radiometers capable of measuring radiative heat flux alone and total heat flux gauges were used to distinguish the contributions from flame radiative and convective heat fluxes. In the first baseline tests and blanket with 48 coils (SH) test, heat flux measurements were not possible due to a hardware malfunction. The problem was solved on site and a second baseline test was performed to measure the heat flux near the pool surface. The second baseline test was performed in a low-wind condition (3.92 mph, NE-SW direction). The average flame height was measured as 2.82 m with 24 degrees tilt on downwind direction. The low wind speed resulted with a more stable flame. Figure 71 shows the total and radiative heat fluxes measured (average of 100 seconds at steady state) 5 cm above the oil surface for the baseline, and blanket with 48 coils (VH). It should be noticed that the wind speed in the blanket with 48 coils (VH) test was ~6 times higher ~ 11.96 mph.

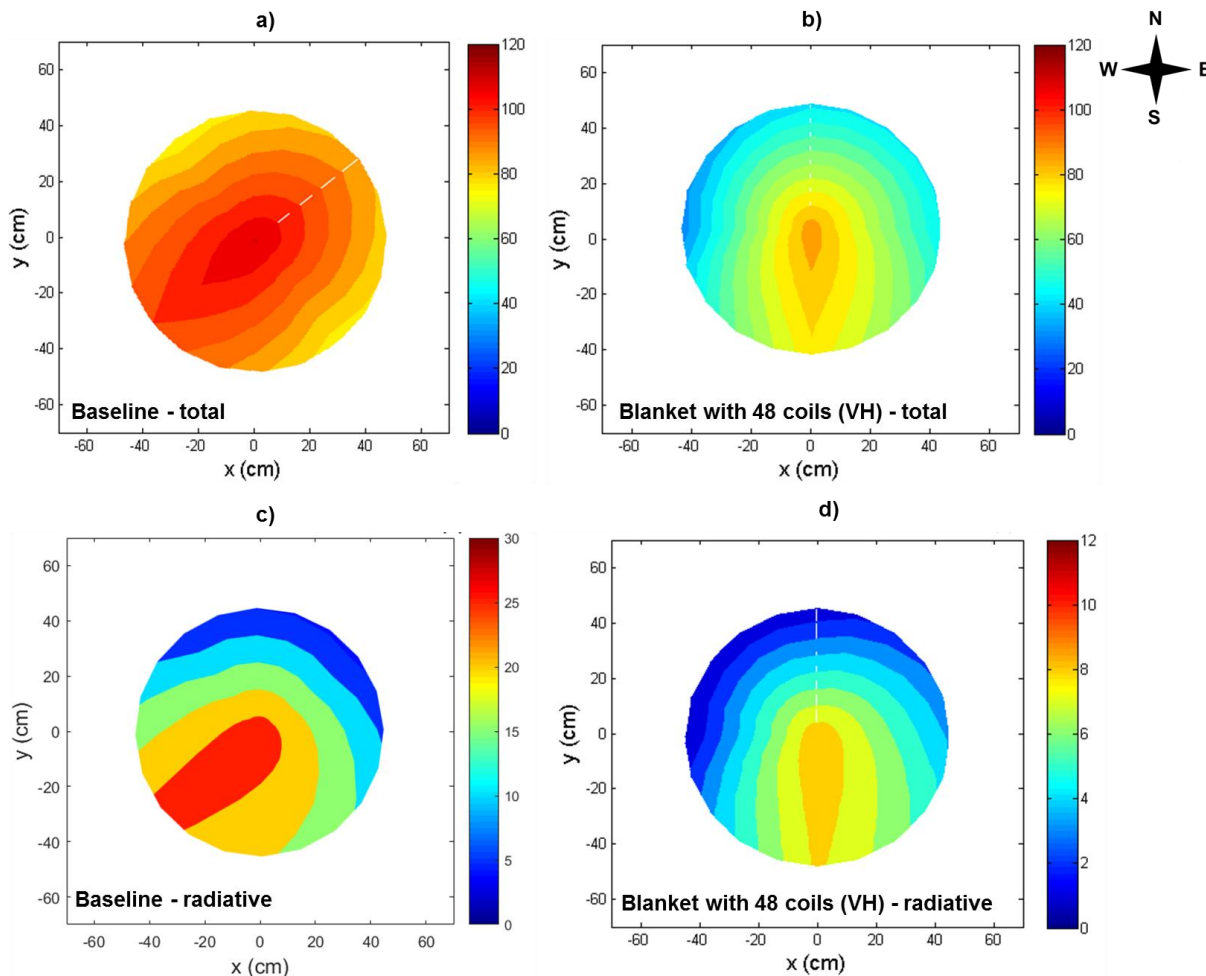


Figure 71: Heat flux contours 5 cm above fuel surface at steady state a) baseline – total heat flux, b) blanket with 48 coils (VH) – total heat flux, c) baseline – radiative heat flux, d) blanket with 48 coils (VH) – radiative heat flux, Contour units are in kW/m².

Figure 71a and b show that the ratio of radiative to total heat flux, χ (at the center), was about 0.6 during the steady state burning for the second (low-wind) baseline case. For pool fires with diameters larger than 1 m, it has been shown that χ is larger than 0.8 under calm conditions [5, 6, 7]. The low-wind during the test promoted a higher loss of radiative flux to the ambient, and therefore decreased the χ value. For the blanket with 48 coils (VH), with high wind speed (11.96 mph, NW-SE direction), a significant decrease in χ (~0.15 at the center) was observed. The 67 degrees tilted flame provided a very low amount of radiative heat feedback to pool surface (Fig. 71d). The cooling by the wind was clearly observed. It is interesting to note that the decrease in the radiative and net heat flux on the pool surface did not reduce the effectiveness of the blanket and coils. This shows that the nucleate boiling and conductive heat transfer from blanket to fuel are the significant processes in achieving increased burning rate.

5.3.4 Gas emissions

Figure 72 shows the CO/CO₂ ratio in the steady state burning regime for field trials: Baseline, blanket and blanket with 48 coils (VH). With the blanket and 48 coils (VH), the ratio of carbon monoxide produced per carbon dioxide, was half that of the baseline case (Fig. 72).

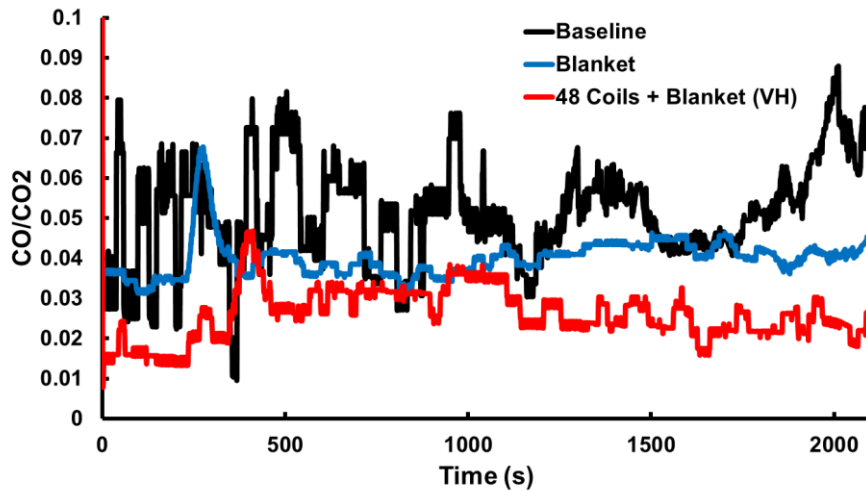


Figure 72: Carbon monoxide per carbon dioxide production ratio for the baseline, blanket and blanket with 48 coils (VH) cases.

Figure 73 shows the smoke plume in the steady state burning regime for the baseline and blanket with 48 coils (VH) cases.



Figure 73: Picture of the smoke plume a) Baseline, b) Blanket with 48 Coils (VH).

Figure 73 clearly shows that the color of the smoke plume is much lighter for the blanket with 48 coils case (VH). Quantitative smoke measurements were not possible. The light color smoke indicates reduction in small black particles of carbon and more complete combustion. It should also be noted that the blanket with 48 coils (VH) case was burning ~4 times faster.

5.3.5 Residue removal

Evaluation of the amount of post burn residue left on the water is important because it shows how efficiently the flame burns the tar (heavy components of oil) and reduces the post burn cleaning efforts/cost. Table 9 summarizes the residue removal for Phase III.

Table 9. Residue removal results

	Baseline	Blanket	Blanket + 32 coils	Blanket + 48 coils (VH)	Blanket + 48 coils (SH)
Fuel pumped into the burner ring (kg)	62.15	150.78	156.81	349.16	279.00
Residue left on water (kg)	20.03	2.87	1.83	2.30	1.04
Residue accumulated in blanket (kg)	-	2.95	2.82	3.06	4.00
Residue removal (%)	32.2	3.8	2.9	1.5	1.8

The residue removal was calculated as follows:

$$Residue\ removal = \frac{Residue\ left\ on\ water}{Total\ fuel\ pumped} \times 100 \tag{10}$$

Table 9 shows that only 68 percent (62 kg fresh oil pumped, 20 kg residue collected) of the oil pumped into the burning ring was burned in the baseline case. The residue removal increased with the introduction of blanket and coils into the pool. As an example, only 1.8% of the oil pumped into the system was left on water for the blanket with 48 coils (SH) case (Table 9).

Figure 74 shows the picture of the post burn residue remaining on the water after the baseline and blanket with 48 coils tests.

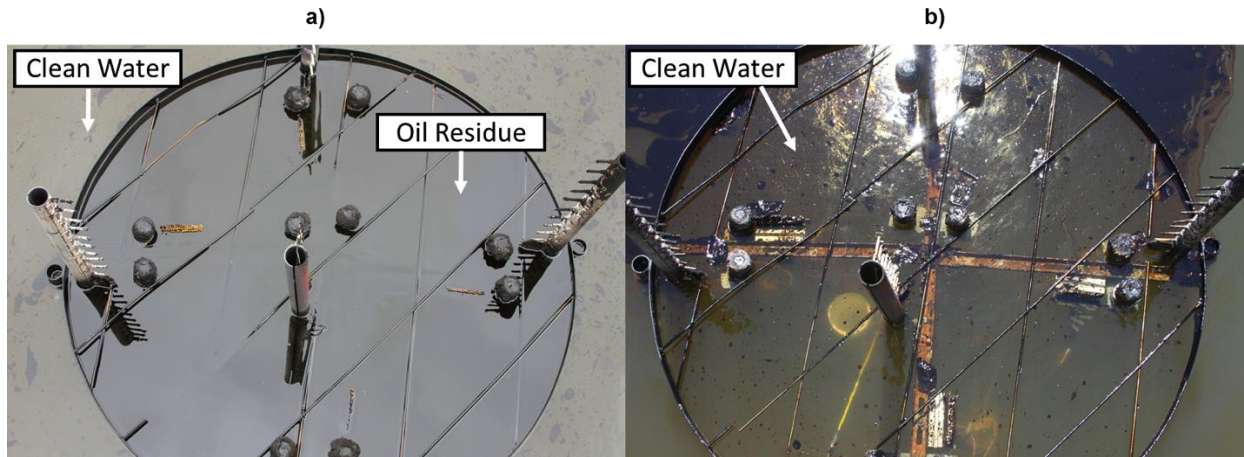


Figure 74: Post burn residue left on water a) Baseline, b) Blanket with 48 coils.

Figure 74a shows the unburned residue remained as a thick layer (~3 mm) of tar on water. Figure 74b shows the burner ring after removing the blanket with 48 coils. Except the small oil pockets, the water was clean.

The blanket increases the residue removal by extending the extinction time, adding nucleate boiling regions, and acting as a wick. During ISB, the natural extinction of the flame occurs because of the heat loss to the water sublayer. With addition of blanket, heat generated by the burn stored in the blanket and facilitates sustained combustion even in very thin oil slicks (2-3 mm). High thermal capacity of the blanket, which is explained in section 6, prevents the blanket to cool down even when it is in touch with water (heat sink).

Figure 75 shows an example of an ISB application where 2000 m³ of oil burned in an area about 10,000 m² [9]. The post burn residue removal with and without blanket-coil system are compared.

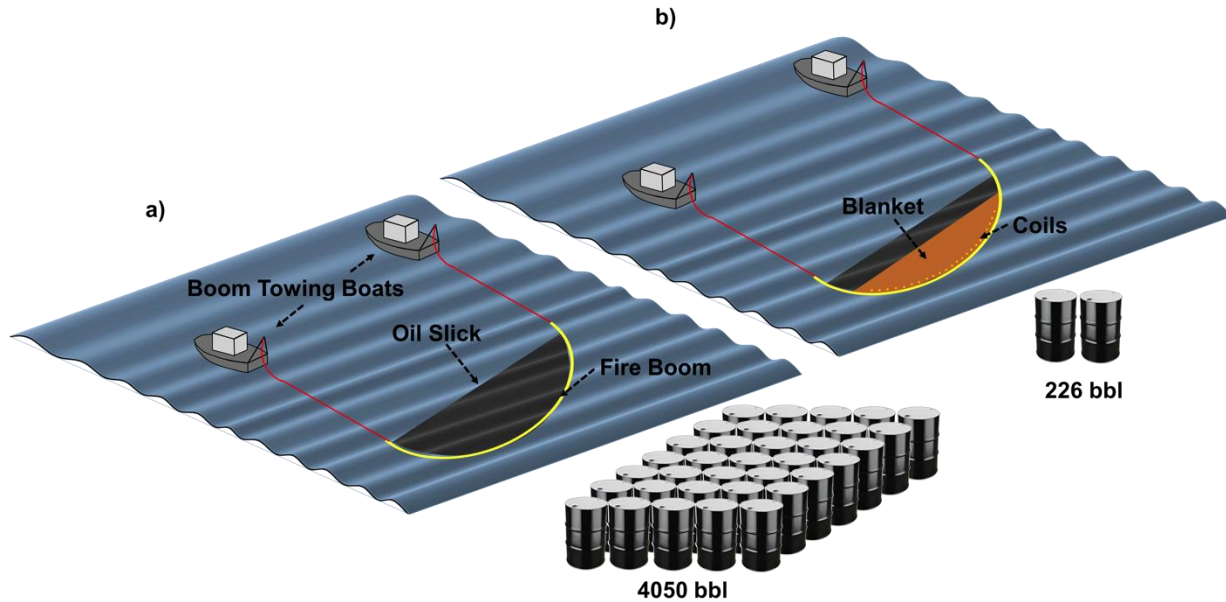


Figure 75: ISB example showing post burn residue removal a) Baseline, b) Blanket and coils (The efficiency of blanket + 48 coils were used to calculate bbl).

As shown in Fig. 75, by taking the baseline experiment as basis (32.2% removal), 4050 bbl (barrels) of post burn residue will be collected after a conventional ISB application. By using the blanket-coil system, the number of barrels with post burn residue can be reduced from 4050 to 226.

5.4 Outcomes of Phase III

Phase III tests resulted with three major outcomes. The steady state mass loss rate (MLR) and additional heat flux because of the blanket-coil system, increased by nearly 5 times as shown in Fig. 76.

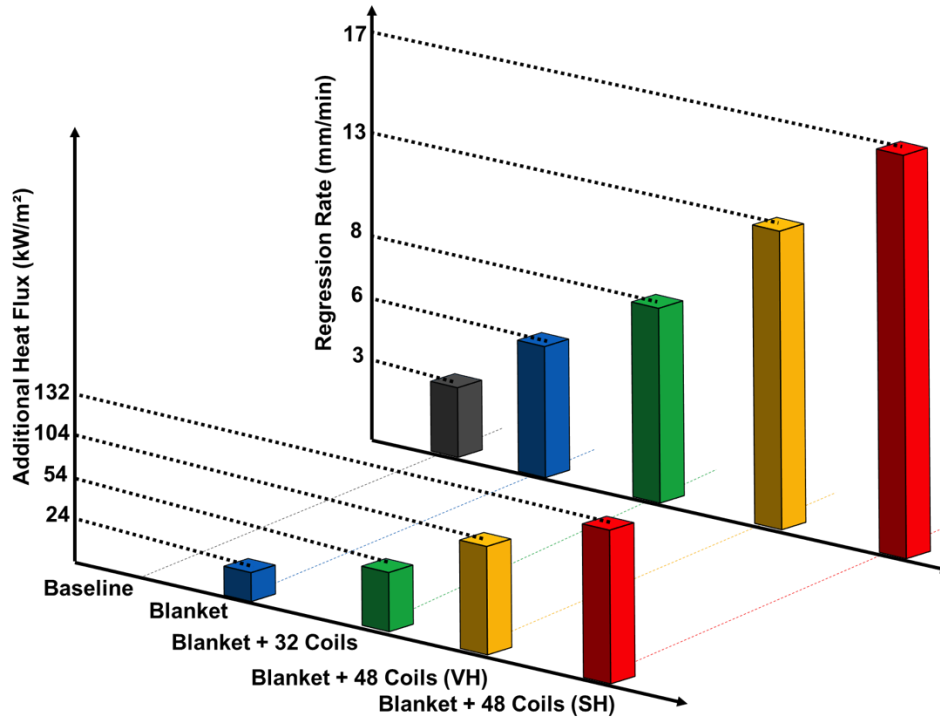


Figure 76: Additional heat flux and regression rate at steady state, SH: Same height, VH: Various heights

Figure 76 shows that the test with 48 coils (SH) yielded an additional heat flux of 132 kW/m² on the pool surface, including both direct (via the blanket and coils) and derivative (via the pool surface) pathways. Additional heat flux and the nucleate boiling on blanket promoted an increase in MLR.

Additional heat flux on the pool was calculated by the following equation;

$$\dot{q}''_{additional} = (\dot{m}''_{blk_configuration_i} - \dot{m}''_{baseline}) \times \Delta H_V, \text{ for } i = 1,4 \quad (11)$$

The first outcome of Phase III tests was the significant increase in steady state regression rate with the usage of blanket-mesh-coil system. Figure 77 shows the regression rate in mm/min with the prototype blanket burner. The regression rate reached an optimum value of 17 mm/min at 48 coils (SH) placed on circumference. This is ~ 480% increase over the baseline case (3 mm/min). The enhanced value is more than 3 times of the burning rate of high volatile gasoline pool fires (1 m diameter gasoline pool fire have a steady state regression rate of ~ 5 mm/min). [3, 4]

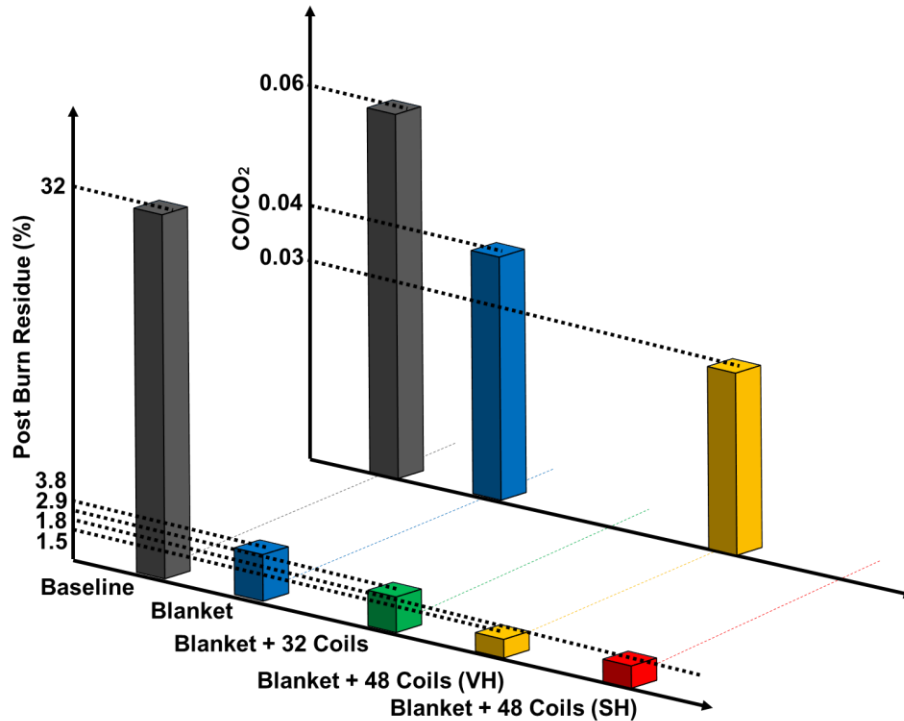


Figure 77: Post burn residue and carbon monoxide per carbon dioxide production ratio, SH: Same height, VH: Various heights

The second outcome, the reduction of post burn residue due to blanket burner is shown in Fig. 77. Evaluation of the amount of post burn residue left on the water is important because it shows how efficiently the blanket burns the tar (heavy components of oil collected in the blanket) and reduces the post burn cleaning efforts/cost. In the baseline case, heat loss to the water sublayer resulted with a low burning efficiency. Figure 77 shows that only 68 percent (63 kg fresh oil pumped, 20 kg residue collected) of the oil pumped into the burner ring was burned. The enhanced heat transfer and nucleate boiling occurring on the blanket promoted efficient burning of the oil residue. As an example, only 1.8% of the oil pumped into the system was left on water when blanket+48 coils (SH) was used.

Figure 77 also shows the CO/CO₂ ratio in the steady state burning regime for the three cases. When the blanket with 48 coils was placed inside the pool, the ratio of carbon monoxide produced per carbon dioxide, was nearly half that of the baseline case (Fig. 77.) Enhanced burning rate promoted in complete combustion of the fuel and reducing quantity of unburned products of combustion.

5.5 Scale-up of Phase II and III test results to ISB applications

This section presents a discussion of Phase II to Phase III scale-up findings, as well as expected thermal performance of Flame Refluxers in actual ISB applications.

5.5.1 Baseline regression rates

Different test venues and fuels were used in Phase II (indoors, ANS) and Phase III (outdoors, HOOPS). “HOOPS” is a pipeline crude blend with a slightly lower density and a higher concentration of low-boiling point components than ANS crude. However, both are considered medium crudes and the differences in composition are not very significant for field test purposes. Table 10 (Row 7) shows that the baseline pool fire regression rate (R value) at steady state was 3 mm/min in Phase III, compared to 1.1 mm/min in Phase II.

Table 10. Comparison of Phase II and III Baseline fires

		Phase II	Phase III
1	Test venue	Indoors	Outdoors
2	Fuel Type ¹	ANS	HOOPS
3	FR Material	Copper	Copper
4	Pool Diameter, m	0.7	1.4
5	Pool area, m ²	0.38	1.54
6	Mass loss rate, g/s (g/s-m ²)	6.1 (16)	67 (44)
7	Regression rate, mm/min	1.1	3
8	Net heat flux to pool surface, kW/m ²	10	29
9	Heat release rate, MW/m ² -pool area	0.71	1.9

Row 3: ANS = Pipeline crude blend (Alaska North Slope), HOOPS = Pipeline crude blend (Gulf of Mexico)

Row 6: Measured mass loss rate in each test

Rows 7-9: Derived from results in Row 6 – see Appendix I for derivation assumptions

The increased R value in Phase III mainly reflects a well-known behavior pattern in pool fire dynamics: as pool diameters increase from 0.1 m to about 1 m, the flame becomes more turbulent and radiant, resulting in higher temperature differences (“thermal potential”) between the flame and the liquid fuel. As a result, net heat flux (kW/m²) back to the liquid surface increases, causing higher fuel vaporization and increasing R values. With pools greater than 1 m diameter, the transition to a fully turbulent, high-radiance flame is nearly complete and the R values for a given fuel remain essentially constant, even for very large ISB pool fires: the typical average R value for unemulsified crude oil removed in ISB clean-ups larger than 3 m diameter is reported to be 3.5 mm/min [10]. Therefore, the 1.4-meter diameter pool fires tested in the field are dynamically similar to much larger fires, even though they are dimensionally “small scale” in relation to ISB. When Flame Refluxers such as the blanket + coil configuration used in this project are deployed in full scale ISB operations, their thermal performance is expected to be at least commensurate with, but probably better than the very promising results obtained in Phase III, as discussed below.

5.5.2 Blanket performance

Table 11 (Row 6) shows that the increased mass loss rate in Phase III attributed to the blanket was 58 g/s compared to 2.3 g/s for Phase II. After adjustment for pool area, this increase equates to a flame-to-blanket-to-liquid fuel total heat transfer of 6 kW/kg-Cu vs. 0.83 kW/kg-Cu in Phases III and II respectively (Row 8)). This dramatic increase in blanket thermal performance achieved in Phase III is attributed first to a higher plume temperature and therefore higher “thermal potential” (= Average plume temperature minus fuel saturation temperature), due to the above-discussed transition of baseline flame dynamics to a regime of fully developed turbulence and high radiant flux. A second, coupled factor is the higher thermal potential between the blanket and the fuel in Phase III, which also resulted in reduced thermal resistance due to further increased rate of nucleate boiling on the (hotter) surfaces of the blanket filaments.

Table 11. Comparison of Phase II and III Blanket-only test results

		Phase II	Phase III
1	Baseline pool parameters	See Table 10	
2	Blanket mass, kg	1.8	6.5
3	Blanket mass/pool area, kg/m ²	4.7	4.2
4	Total MLR, g/s (g/s-m ²)	8.4 (22)	125 (81)
5	R, mm/min	1.5	5.6
6	ΔMLR, g/s (g/s-m ²)	2.3 (6)	58 (38)
7	BHF, kW/m ²	3.9	25
8	THT per mass Cu, kW/kg-Cu	0.83	6.0

Row 6: ΔMLR = Total MLR – Baseline MLR

Row 7: BHF = Net Blanket heat flux = blanket heat transferred to liquid fuel per m² of pool surface (see Appendix I for derivation assumptions)

Row 8: THT = Total Heat Transfer per mass Cu = Row 7/Row 3

5.5.3 Blanket + Coil performance

The combined results shown in Table 12 further amplify the difference in Flame Refluxer performance between Phase II and III, which occurs for the same reasons as explained for the blanket-only case above. As shown in Row 7, the maximum regression rate increased from 3.1 mm/min in Phase II up to 17 mm/min with 48 coils (SH) + blanket in Phase III. In thermal performance terms, as shown in Row 11, the highest output blanket + coil configuration in Phase III transferred 14 kW per kg of total copper vs only 2.2 kW/kg-Cu in Phase II.

Table 12. Comparison of Phases II and III Blanket+ Coil test results

		Phase II	Phase III
1	Baseline pool parameters	See Table 10	
2	Blanket parameters	See Table 11	
3	Total Coil + blanket mass kg-Cu	5.2	18
4	Total Cu mass/pool area (kg-Cu/m ²)	13.7	11.7
5	# Coils	24	48 (SH)
6	Total MLR, g/s (g/s-m ²)	17.5 (46)	382 (248)
7	R, mm/min	3.1	17
8	ΔMLR, g/s	11.4	315
9	ΔMLR per mass Cu, g/s-kg-Cu	2.2	17.5
10	B+CHF, kW/m ²	30	162
11	B+CTHT per mass Cu, kW/kg-Cu	2.2	14

Row 8: ΔMLR = (Blanket + Coil) MLR – Baseline MLR

Row 10: B+CHV = net (Blanket + Coil) heat flux = heat transferred per m² of pool surface (see Appendix I for derivation assumptions)

Row 11: B+CTHT = Blanket + Coil Total Heat Transfer per mass Cu = Row 10 / Row 4

Table 13 illustrates a strong nonlinearity in FR performance within Phase III as the number of coils was increased from 32 to 48 (SH). Increasing the number of coils from 32 to 48 resulted in an increase in coil output from 5.6 kW to 33 kW per kg of copper in the added coils (Row 9).

Table 13. Comparison of 32-Coil and 48-Coil test results in Phase III

		32 coils	48 coils (SH)
1	Baseline pool parameters	See Table 10	
2	Blanket parameters	See Table 11	
3	Cu mass per coil, kg	0.24	0.24
4	Δ Cu Mass per area, kg-Cu/m ²	5	2.5
5	Total MLR, g/s	190	382
6	R, mm/min	8.4	17
7	ΔMLR, g/s	65	192
8	CHF, kW/m ²	28	82
9	CTHT per mass Cu, kW/kg-Cu	5.6	33

Row 4: Δ Cu Mass Coils = (32 coils x 0.24 kg/Coil)/1.54 m² for 32-coil test and (16 coils x 0.24 kg/Coil)/1.54 m² for 48-coil test

Row 7: ΔMLR = (32-Coil Total MLR – blanket total MLR)/pool area for 32-coil test, and (48-Coil Total MLR – 32-coil Total MLR)/pool area for 48-coil test

Row 8: = Coil heat flux per unit pool area corresponding to Row 7 (see Appendix I for derivation)

Row 9: =Coil Total Heat Transferred per kg of coil copper (Row 8/Row 4)

In other words, the 32-coils weighed approximately the same as the blanket and added approximately the same heat transfer as the Phase III blanket-only (6.0 kW/kg-Cu, see Table 11 Row 8). The additional 16 coils in the 48-coil (SH) test added 33 kW/kg-Cu. Possible explanations are that the additional 16 coils were positioned in an inner ring where plume temperatures may have been higher than on the circumference because of flame tilting by the wind, and/or that the 16 added coils caused the blanket temperature to increase sufficiently to cause a sudden change in the nucleate boiling heat transfer coefficient. These effects cannot be quantified with current knowledge and test data. While the output increase in the 48-coil (VH) test vs 32-coils was not as prominent as the 48-coil (SH) test, a non-linear increase occurred nonetheless (see Fig 67. above).

5.5.4 Blanket + Coil performance

Based on Flamer Refluxer thermal performance successes achieved in the field trials as discussed in the preceding sections, an ISB-scale Flame Refluxer (ISB-FR) is conservatively projected to achieve a six-fold increase in the regression rate compared to current ISB technology, possibly reaching a ten-fold increase through more efficient FR configurations and further favorable scale-up effects. The appropriate size and configuration of an ISB-FR needs to be determined based on deployment considerations, such as slick size, FR robustness, ease of handling, weight, drag and retrieval method following completion of the burn. These aspects are outside the scope of this study.

6. Computational Model

A numerical model is developed to predict the regression rate of the oil slick in the presence of an immersed blanket represented as porous metal wool of known porosity. A schematic representation of the problem studied is shown in Fig. 78 where the geometry is divided into three layers. The upper layer comprises thermally conductive metal wool (porous media) and fuel. The middle layer is composed of fuel alone and the bottom layer is composed of water.

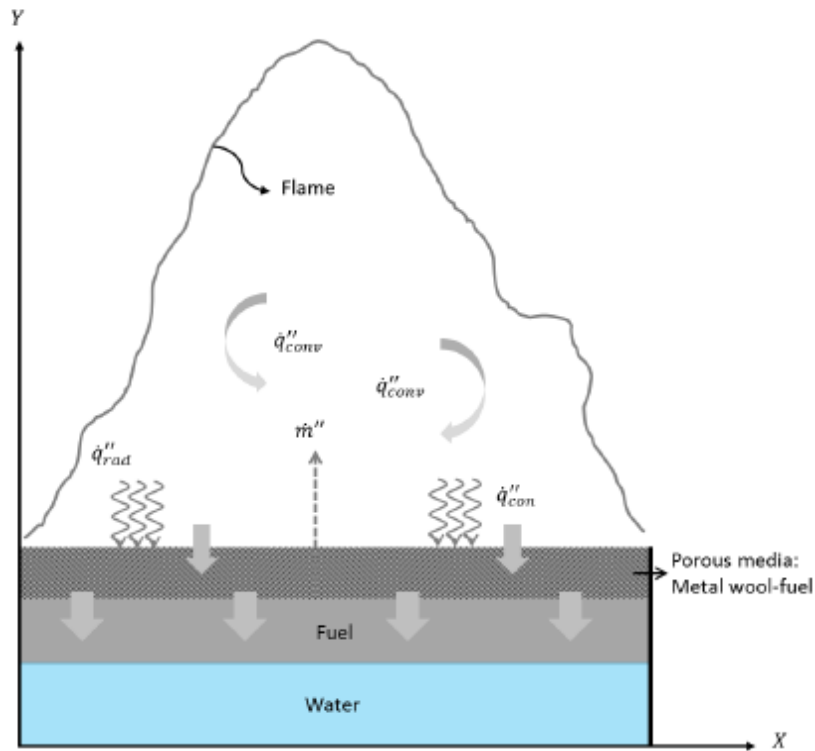


Figure 78: The mass and heat transfer mechanisms for a pool fire with the presence of an immersed metal wool in fuel layer.

Heat is transferred via flame radiation and convection to the blanket. As a first step, the collector coils which provide a conductive path for heat transfer are not modeled (will be modeled in Sec 6.7). As the fuel burns, the metal wool transfers heat horizontally (in the x direction) and vertically (in the y direction) thus enhancing the fuel evaporation rate. Heat is also transferred to the fuel layer below the metal wool and dissipated to the water layer. Heat transfer in porous media is modeled using a two-dimensional conduction heat transfer equation with an effective conductivity. The evaporation rate is coupled with the heat transfer using an energy balance at the fuel surface. The model assumptions are: (1) the metal wool is homogeneous, (2) density, specific heat, and the thermal conductivity of fuel and water are constant, (3) in-depth radiation and the liquid convective motion are neglected.

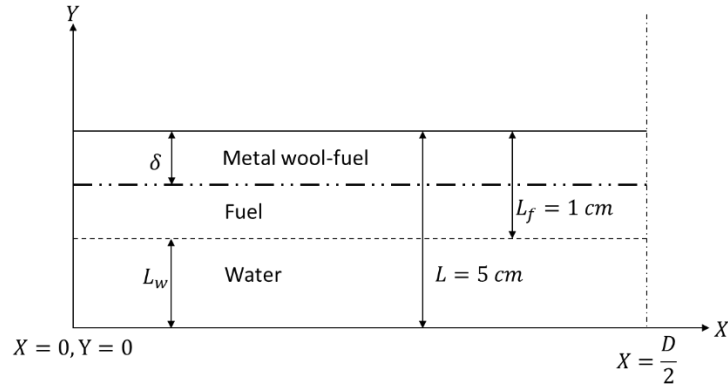


Figure 79: Simplified geometry of the problem

The geometry is subdivided into three parts representing (a) an aluminum metal wool layer fully immersed in fuel (dodecane), (b) fuel only, and (c) a bottom layer of water (Fig. 79). The heat transfer is calculated by a transient two-dimensional model given by Eq. 12.

$$\rho C_p \frac{\partial T}{\partial t} = \frac{\partial}{\partial x} k \frac{\partial T}{\partial x} + \frac{\partial}{\partial y} k \frac{\partial T}{\partial y}, \quad (12)$$

where ρ , C_p , and k are density, specific heat, and thermal conductivity of the representative layer being modeled. In depth radiation transfer and convection are assumed to be negligible. The boundary condition for part (a) include a non-uniform flame heat flux on the surface of the fuel and adiabatic walls from the left and right sides of the geometry. The conductive term is discretized with a central differencing scheme. A fully implicit Euler's method is used for the time integration to ensure a stable numerical solution and the coefficient matrix for the system of linear equations is solved by a sparse direct solver available in MATLAB ®.

The temperature of the porous media (metal wool-fuel) is calculated using an effective thermal conductivity of the porous medium. The details of the porous media model are given in the next section.

6.1 Heat transfer in metal wool - fuel

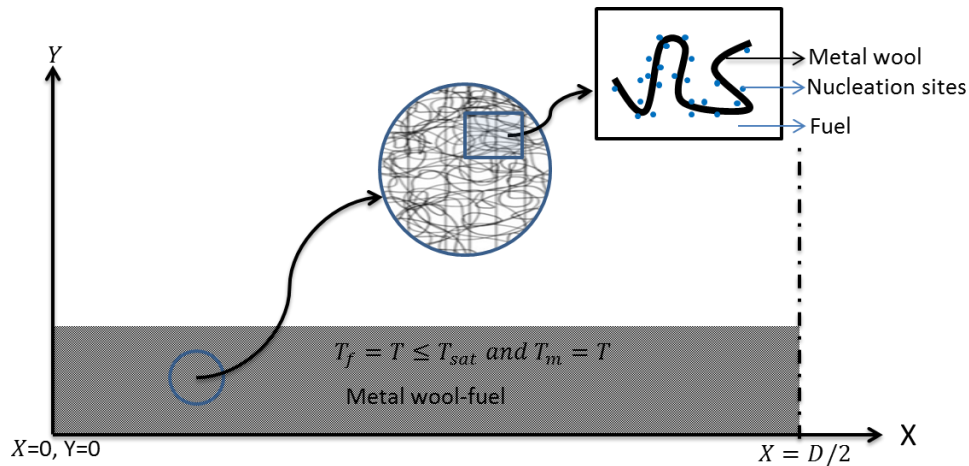


Figure 80: Schematic representation of the saturated porous media

A schematic representation of metal wool-fuel porous media is given in Fig. 80.

The heat transfer in the metal wool – fuel mixture is given by;

$$\rho_{eff} C_{p,eff} \frac{\partial T}{\partial t} = \frac{\partial}{\partial x} k_{eff} \frac{\partial T}{\partial x} + \frac{\partial}{\partial y} k_{eff} \frac{\partial T}{\partial y} + h_{m-f} (T_{sat} - T). \quad (13)$$

It is assumed that the metal-wool fuel medium is isotropic and radiative effects and viscous dissipation are negligible. Also, it is assumed that there is local thermal equilibrium. The effective density ρ_{eff} and heat capacity $C_{p,eff}$ are the weighted arithmetic mean of the densities and heat capacities of the solid and the liquid phase. The fuel and the metal wool temperatures are calculated as:

$$T_{fuel} = T \text{ when } T \leq T_{sat},$$

$$T_{fuel} = T_{sat} \text{ when } T \geq T_{sat}, \quad (14)$$

$$\text{and } T_{metal} = T.$$

The effective thermal conductivity of the metal wool - fuel system is given by [11],

$$k_{eff} = k_f \left\{ 1 - \sqrt{1 - \varphi} + \frac{2\sqrt{1 - \varphi}}{1 - \zeta} \left[\frac{(1 - \zeta)B}{(1 - \zeta B)^2} \ln \left(\frac{1}{\zeta B} \right) - \frac{B - 1}{1 - \zeta B} - \frac{B + 1}{2} \right] \right\}, \quad (15-a)$$

$$\text{where, } B = C \left(\frac{1-\varphi}{\varphi} \right)^\gamma \quad (15-b)$$

$$\text{and } \zeta = \frac{k_{metal}}{k_{fuel}} \quad (15-c)$$

With $\gamma = 10/9$. φ is the porosity of the blanket. The constant C is the shape factor and equals 1.25, 1.4 and 2.5 for spheres, irregular particles and cylinders respectively. The effective thermal conductivity of the metal wool-fuel system for $\varphi = 0.9$ is $0.23 \text{ W m}^{-1}\text{K}^{-1}$ and when the porosity, $\varphi = 0.8$, the effective thermal conductivity of the metal wool-fuel system is $0.41 \text{ W m}^{-1}\text{K}^{-1}$. This simple calculation indicates that, the effective thermal conductivity is very sensitive to the porosity. The current study uses porosity $\varphi = 0.9$ which is calculated experimentally. The current study assumes $C = 1.4$. The model equations 15a – c proposed by Zehner and Schlunder [12] have been validated by Kandula [11] for a wide range of solid-to-fluid thermal conductivity up to 2000 for a range of solid fractions of 0 % - 100%. In the present study, the solid-to-fluid thermal conductivity ratio, $\frac{k_m}{k_f} \cong 1700$ and the solid fraction $(1 - \varphi)$ is 10 %.

6.2 The convective heat transfer coefficient

The surface convective heat transfer coefficient h_s is calculated using Nusselt number correlations for variable ambient temperature [13]. The variable Nusselt number for flat plate approximation can be given as;

$$Nu_{y-Fp} = (Gr_y)^{0.25} \frac{0.75Pr^{1/2}}{(4(0.61 + 1.22Pr^{0.5} + 1.24Pr))^{0.25}}, \quad (16)$$

where, Gr_y is the Grashof number,

$$\left(Gr_y = \frac{g\beta(T_s - T_\infty)\Delta y}{\nu^2} \right). \quad (17)$$

T_s and T_∞ are the surface and ambient temperature respectively. And g, β, ν are gravity constant, volumetric expansion coefficient, and kinematic viscosity respectively.

Once the number correlations are calculated; the convective heat transfer coefficient is given by:

$$\text{Flame-fuel} \quad h_s = \frac{Nu_{y-fp} k_g}{\Delta y} \quad (18)$$

$$\text{Metal-wool-fuel} \quad h_{m-f} = \begin{cases} \frac{Nu_{y-fp} k_g}{\Delta y}, & (T - T_{sat}) < 0, \\ \frac{\dot{q}_s''}{T_{metal} - T_{sat}}, & (T - T_{sat}) \geq 0. \end{cases} \quad (19)$$

The second term in the convective heat transfer coefficient arises because of boiling heat transfer as shown in Fig. 80.

6.3 Initial and boundary conditions

Figure 81 shows the flame $T_{fl}(x)$ and gas phase $T_g(x)$ temperature profiles. The experimental observations show that the temperature profile in gas phase at the surface of the fuel reaches its highest values between the center of the pool and the edges. The temperature values at the edge of the pool are slightly higher than that of the center. Therefore, the temperature profile shape presented in Fig. 81 can be obtained for the gas phase temperature based on the experimental measurements. The gas phase temperature at the center of the pool is taken as 550 K and the maximum gas phase temperature is taken as 590 K.

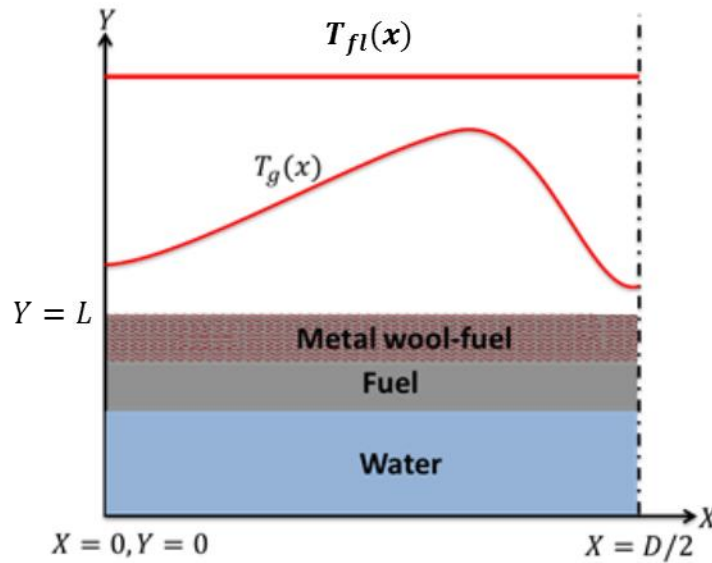


Figure 81: Assumed flame and gas phase temperature profile.

Boundary and initial conditions for the computational domain are given as;

$$(t, x = 0, y), \frac{\partial T}{\partial x} = 0,$$

$$(t, x, y = 0), \frac{\partial T}{\partial y} = 0,$$

$$\left(t, x = \frac{D}{2}, y\right), \frac{\partial T}{\partial x} = 0, \quad (20)$$

$$(t, x, y = L), k_{eff} \frac{\partial T}{\partial x} = \dot{q}_s'',$$

$$(t, x, y = L - \delta), T = \min(T_{sat}, T),$$

$$T(t = 0, x, y) = 298K.$$

$\frac{D}{2}$ and L are the geometric dimensions of the pool fire, shown in Fig. 79, in x and y directions respectively. The thermal properties, k_{eff} and \dot{q}_s'' are the porous region thermal conductivity and the total heat flux rate comprising of radiative, conductive and convective heat transfer on the pool surface. Total heat flux rate, \dot{q}_s'' is described in detail in subsequent sections. T_{sat} , is defined as the liquid fuel saturation temperature.

6.4 Mass loss rate (burning rate)

The heat required to vaporize unit mass of the liquid at any temperature below the saturation point is given by [14];

$$\Delta H_{vap} = L_v + c_{p,f}(T_{sat} - T), \quad (21)$$

where ΔH_{vap} , L_v , $c_{p,f}$ and T_{sat} are the heat for vaporization, the latent heat of vaporization, liquid fuel specific heat and the liquid fuel saturation temperature.

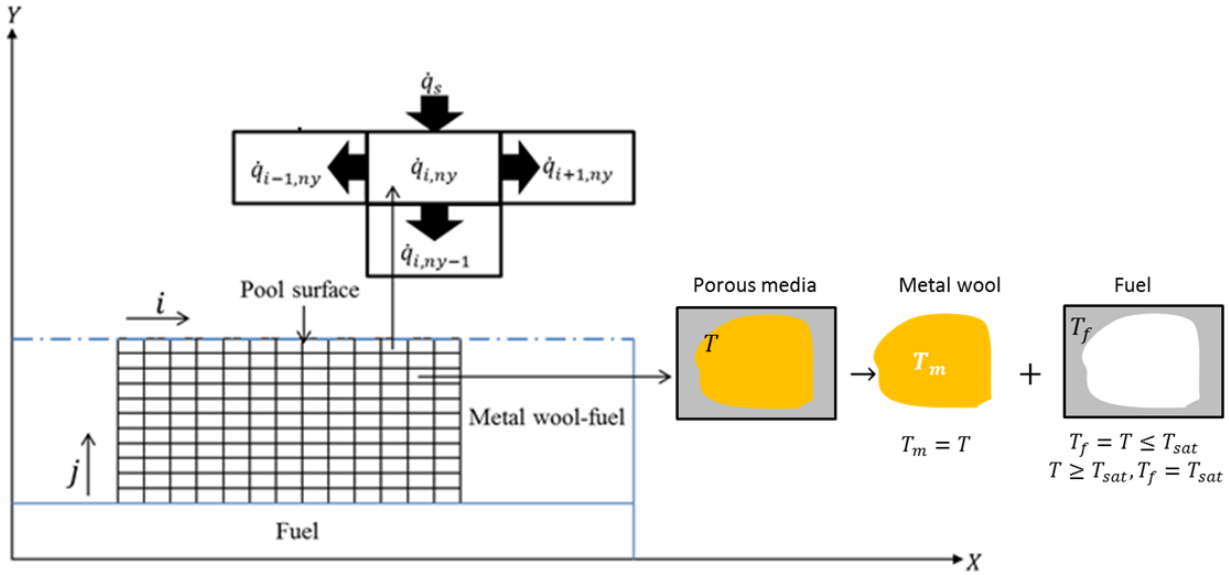


Figure 82: Mass loss rate mechanisms for the liquid pool fire with the immersed thermally conductive metal wool

As shown in Fig. 82, evaporation occurs both from the fuel surface as well as on the metal-wool because of the boiling regimes (nucleate and transition). The evaporation rate in a computational cell located on the surface is calculated using an energy balance given by

$$\dot{q}_{i,ny} = \dot{q}_s - \dot{q}_{i-1,ny} - \dot{q}_{i+1,ny} - \dot{q}_{i,ny-1}, \quad (22)$$

where \dot{q}_s is the total heat flux from the flame into the (i, ny) cell as shown in Fig. 82 given by,

$$\dot{q}_s = \dot{q}_{s,c} + \dot{q}_{s,conv} + \dot{q}_{s,R}. \quad (23)$$

$\dot{q}_{s,c}$, $\dot{q}_{s,conv}$ and $\dot{q}_{s,R}$ are the conductive, convective, and radiative heat fluxes respectively and calculated as:

$$\dot{q}_{s,c} = Ak \frac{\partial T}{\partial y}, \quad (24)$$

$$\dot{q}_{s,conv} = Ah(T_g - T), \quad (25)$$

$$\dot{q}_{s,R} = A\sigma\epsilon(T_{fl}^4 - T^4). \quad (26)$$

k , h , and A are the thermal conductivity, convective heat transfer coefficient, and the surface area of the (i, ny) cell adjacent to the fuel surface respectively. The radiative heat flux constants, σ and ϵ are the Stefan-Boltzmann constant and the surface emissivity respectively. By using Eqs 18-21, the mass evaporation rate from the (i, ny) cell adjacent to the fuel surface can be calculated as:

$$\dot{m}_{s,(i,ny)} = \frac{\dot{q}_{i,ny}}{\Delta H_{vap}}, \quad (27)$$

and the total mass loss rate from the fuel surface, \dot{m}_s is the summation of the mass evaporation rate of each (i, ny) cell adjacent to the fuel surface,

$$\dot{m}_s = \sum_{i=1}^{nx} \dot{m}_{s,(i,ny)}. \quad (28)$$

Fuel evaporation occurs inside the porous media when $T_m \geq T_{sat}$, and the evaporation rate from an (i, j) cell inside the metal wool is calculated as:

$$\dot{m}_{p,(i,j)} = \frac{h_{m-fuel} A_b (T_m - T_{sat})}{\Delta H_{vap}}, \quad (29)$$

Where h_{m-fuel} is the convective heat transfer coefficient from metal wool to liquid fuel. T_m and T_{sat} represent the metal wool temperature and the saturation temperature of the liquid fuel respectively. A_b is the blanket surface area and is calculated as follows;

$$A_b = A_{dens} Cellv, \quad (30)$$

where $Cellv$ is the volume of the computational cell and A_{dens} is the area density. In porous blankets containing a wool, it is hard to obtain precise surface area of the solid fluid interface, as both solid-solid contact and solid-fluid contact are present. In this context, the area density, A_{dens} , is obtained through calibration with the baseline experiment. An area density of $2.5 \text{ m}^2/\text{m}^3$ is used for the porous blanket.

The total mass loss rate is then obtained from Eq. 28 and 29 as:

$$\dot{m}_p = \sum_{j=ny-nymo}^{ny} \sum_{i=1}^{nx} \dot{m}_{p,(i,j)}. \quad (31)$$

The aggregate mass loss rate of the pool fire is then ascertained by the summation of the MLR of porous media (due to nucleate boiling) and pool surface (evaporation).

6.5 Application to Phase I

The physical properties of the fuel and the metal wool used in the simulations are given in Table 14. These physical parameters are taken at a temperature of 298 K and a pressure of 1 atm. The thermo-physical properties of dodecane and air are kept constant during the simulations. However, the properties of the metal (aluminum for Phase 1 and Copper for Phase 2 and 3) are allowed to vary with temperatures shown in Table 15. The geometric details of the test cases selected for the simulations are given in Table 16. The heat transfer from the flame to the fuel surface occurs via radiation, convection, and conduction. The heat transfer in porous media is calculated by estimating the effective thermal conductivity coefficient in the porous structure. Further, the heat transfer from metal wool to the liquid fuel above the liquid saturation temperature is assumed to occur by convection only. The convective heat transfer coefficient is calculated from a log normal distribution of the experimental data for light hydrocarbon fuels [15] and water boiling curves. Fig. 83 shows the estimated boiling curve for dodecane. The critical heat flux or the heat flux beyond which nucleate boiling transitions to film boiling leading to a drop in the convective heat transfer coefficient occurs at an excess temperature of 42.6 K.

Table 14: Thermo-physical properties [16]

Properties	Units	Dodecane	Copper	Aluminum	Air
Density	Kg m ⁻³	749.5	8960	2702	1.1839
Specific heat	J Kg ⁻¹ K ⁻¹	2211.8	385	903	-
Saturation temperature	K	491	-		-
Thermal conductivity	W m ⁻¹ K ⁻¹	0.14	386	237	0.271
Emissivity	-	0.2	0.07		-
Stefan-Boltzmann constant	W m ⁻² K ⁻⁴	5.67E-08	-		-
Heat of vaporization	kJ kg ⁻¹	256	-		-
Vapor thermal conductivity	W m ⁻¹ K ⁻¹	0.0234	-		-

Table 15: Temperature dependent specific heat and thermal conductivity of copper [17].

T(K)	293	300	350	373	400	450	473	500	550	573	600	650
C_p (J Kg ⁻¹ K ⁻¹)	400.7	401	396.8	395.2	393	389.9	388.4	386.5	383.1	381.5	379	376
k (W m ⁻¹ K ⁻¹)	383.5	385	392	394.7	398.4	403	405.9	408	412	414.8	417	421

Table 16: Geometry of the test cases used in simulations.

Pool diameter, $D = 140$ cm; fuel layer thickness, $L_f = 1$ cm; water layer thickness $L_w = 4$ cm					
Porous media thickness	Number of grids in x direction	Number of grids in porous media: y direction	Number of grids in oil: y direction	Number of grids in water: y direction	Number of grids in y direction
δ	nx	$nymo$	nyo	nyw	ny
0.15 cm	31	7	9	39	55
0.25 cm	31	11	9	39	59
0.5 cm	31	21	9	39	69
0.75 cm	31	31	9	39	79

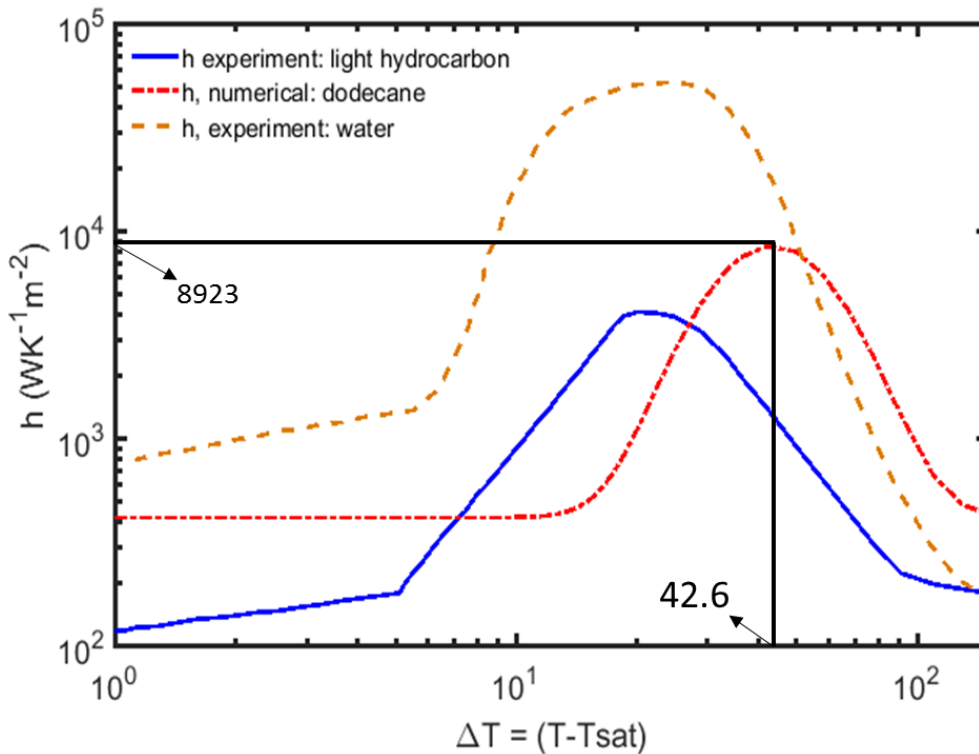


Figure 83: Convective heat transfer coefficient for dodecane. Boiling curves of water and light hydrocarbons [15] is also shown for comparison.

The model is validated using an experimental set up comprising a 10 cm diameter and 5 cm deep stainless steel vessel filled with water to a depth of 4 cm and fuel (dodecane) 1 cm thickness.

Aluminum metal wool with thicknesses of 0.25 and 0.5 cm is then placed in the fuel layer to form a three-layered geometry as shown in Fig. 78 and 79. Experimentally measured mass burning rates and in-depth temperature distributions from the experiments are used to validate the model. Additional details are provided in Sezer et al. [18].

6.5.1 Model Validation

The mass loss rate of the fuel is shown in Fig. 84. The convective heat transfer coefficient (h_{m-fuel}) for dodecane is calibrated with the of 0.5 cm metal-wool layer test results and the calibrated h_{m-fuel} values have been used for the second experimental trial (0.25 cm metal wool). This causes a slight under prediction of the experimental results for the 0.25 cm metal wool experimental trial. However, as shown in Fig. 84 the model predicts experimental trends reasonably well. Figure 85 shows the comparison between experimental and predicted temperature at a monitor point located 0.5 cm below the fuel surface. The simulations are in good agreement with the experimental measurements during the first 400s. However, beyond this value, it is observed that the model over predicts the temperature. The 0.25 cm metal wool case reaches steady state earlier. This observation is consistent with the experimental results as well.

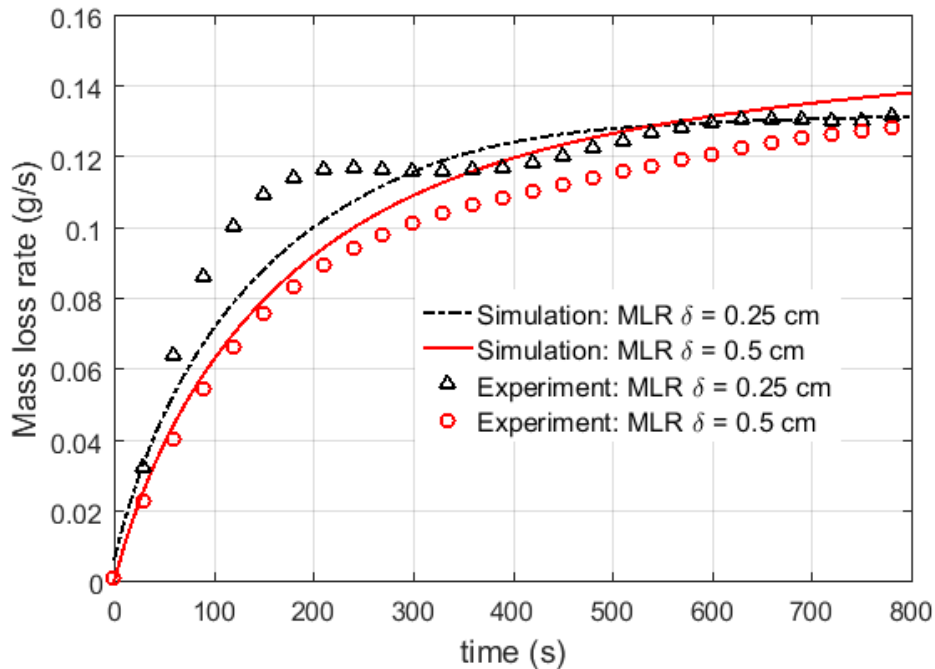


Figure 84. Experimental and predicted MLR during burning of the dodecane pool fire for metal wool thickness of 0.5 and 0.25.

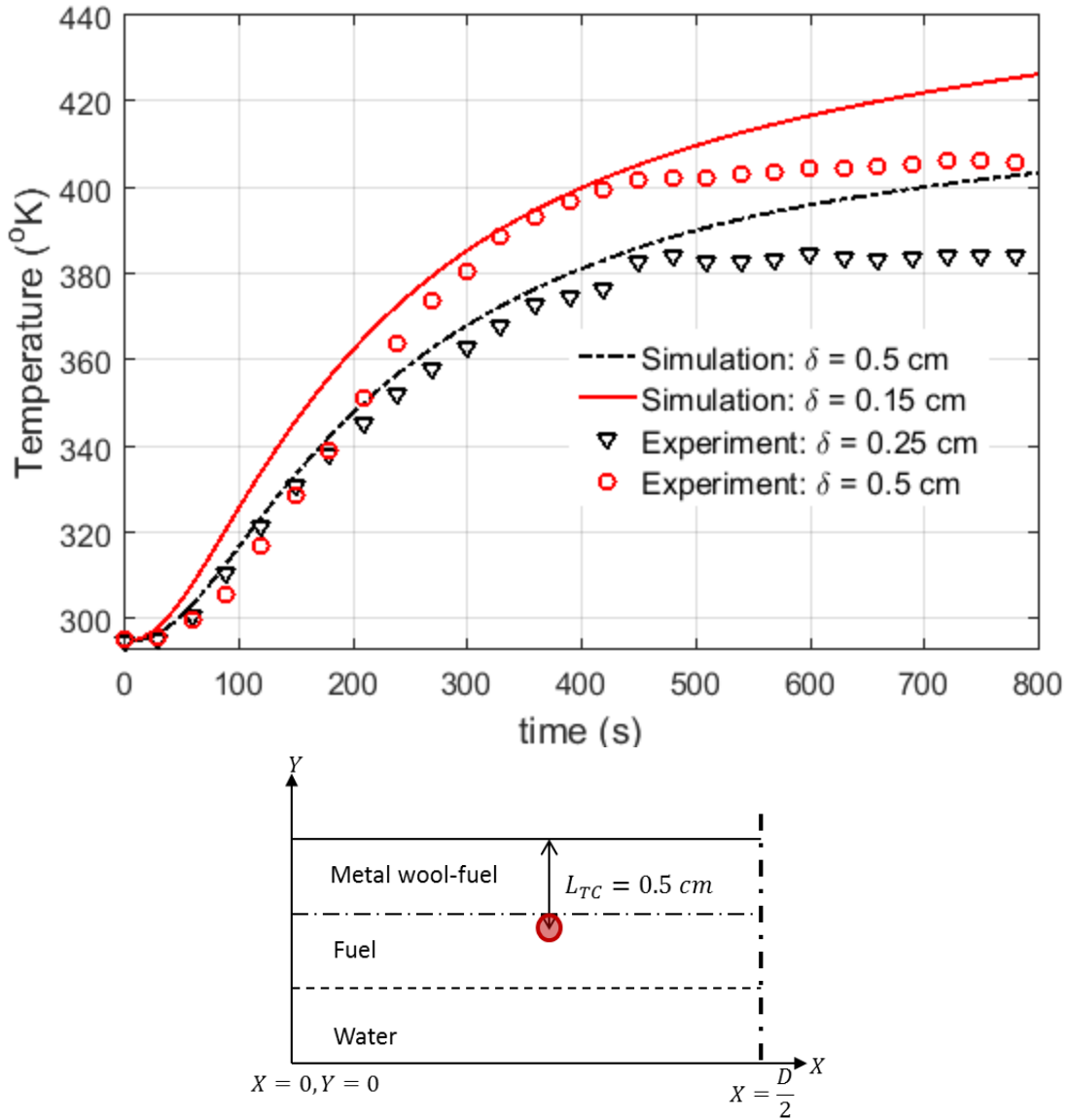


Figure 85. The temperature variation of a monitor point at 0.5 cm beneath the fuel surface during gradual burning of the fuel, and corresponding experimental results.

6.5.2 Influence of metal wool thickness

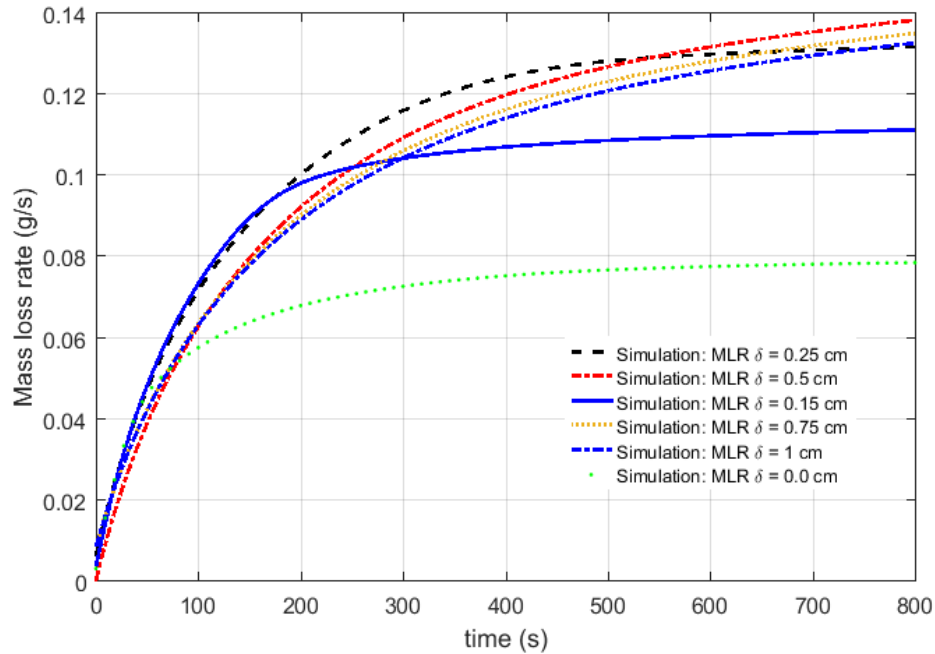


Figure 86: Influence of thickness of metal wool on the burning rate.

Figure 86 shows model predictions of mass loss rate of the pool fire with an immersed metal wool layer with varying thickness (δ) of 0.15 to 0.75 cm. The baseline mass loss rate (with no blanket) is around 0.08g/s. With the addition of a blanket with thickness, $\delta = 0.15$ cm, the burning rate increases very quickly to the peak value of 0.115g/s. As the thickness increases, the peak burning rate value increases with the maximum occurring at $\delta = 0.5$ cm and decreasing thereafter. The highest mass loss rate in the shortest time duration is obtained when $\delta = 0.25$ cm at ~ 550 s as shown in Fig. 86. As the blanket thickness increases further, $\delta = 0.75$ cm the burning rate decreases and when $\delta = 1$ cm, the burning rate is around 0.105 g/s. At $\delta = 1$ cm, the blanket surface touches the water at the bottom. It is interesting to note that burning rate is still higher than the baseline value. This is because of the high porosity of the metal wool ($\varphi = 0.9$) causing the effective thermal conductivity of the blanket to be low ($0.23 \text{ W m}^{-1}\text{K}^{-1}$) and comparable to that of the fuel layer ($0.14 \text{ W m}^{-1}\text{K}^{-1}$). The lateral transfer of heat is enhanced mainly by convection in this case. The metal wool is able to retain significant heat because of an increase in volumetric heat capacity. This is explained further in Section 6.8.

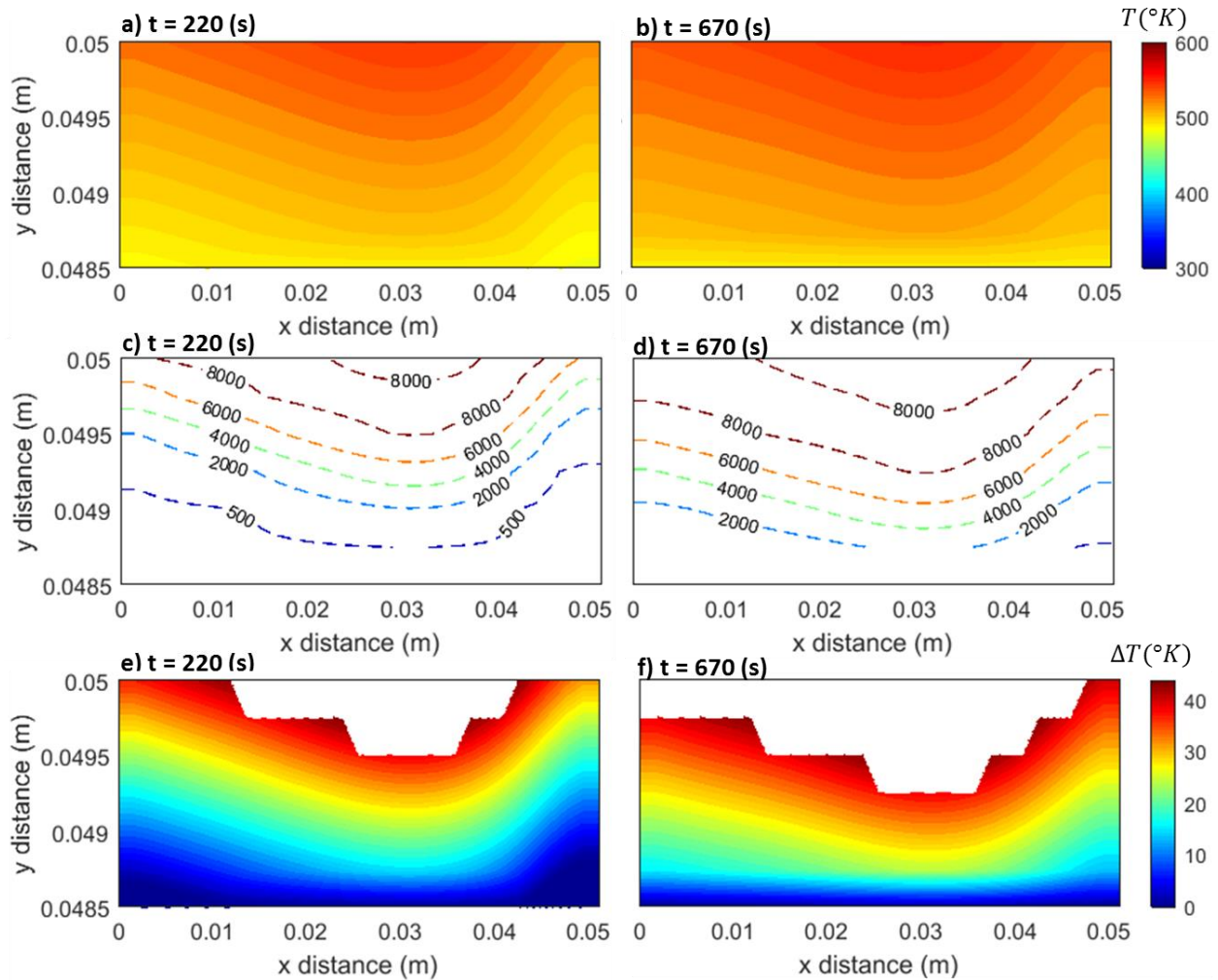


Figure 87: Contours of the temperature colored by the temperature magnitude at different time of a) 220 s, b) 670 s Contour line of the convection heat transfer coefficient inside the blanket at different time of c) 220 s, d) 670 s. Contour line of temperature difference (< excess temperature of critical heat flux, i.e. nucleate boiling regions) e) 220 s, f) 670 s for aluminum wool thickness of 0.15 cm.

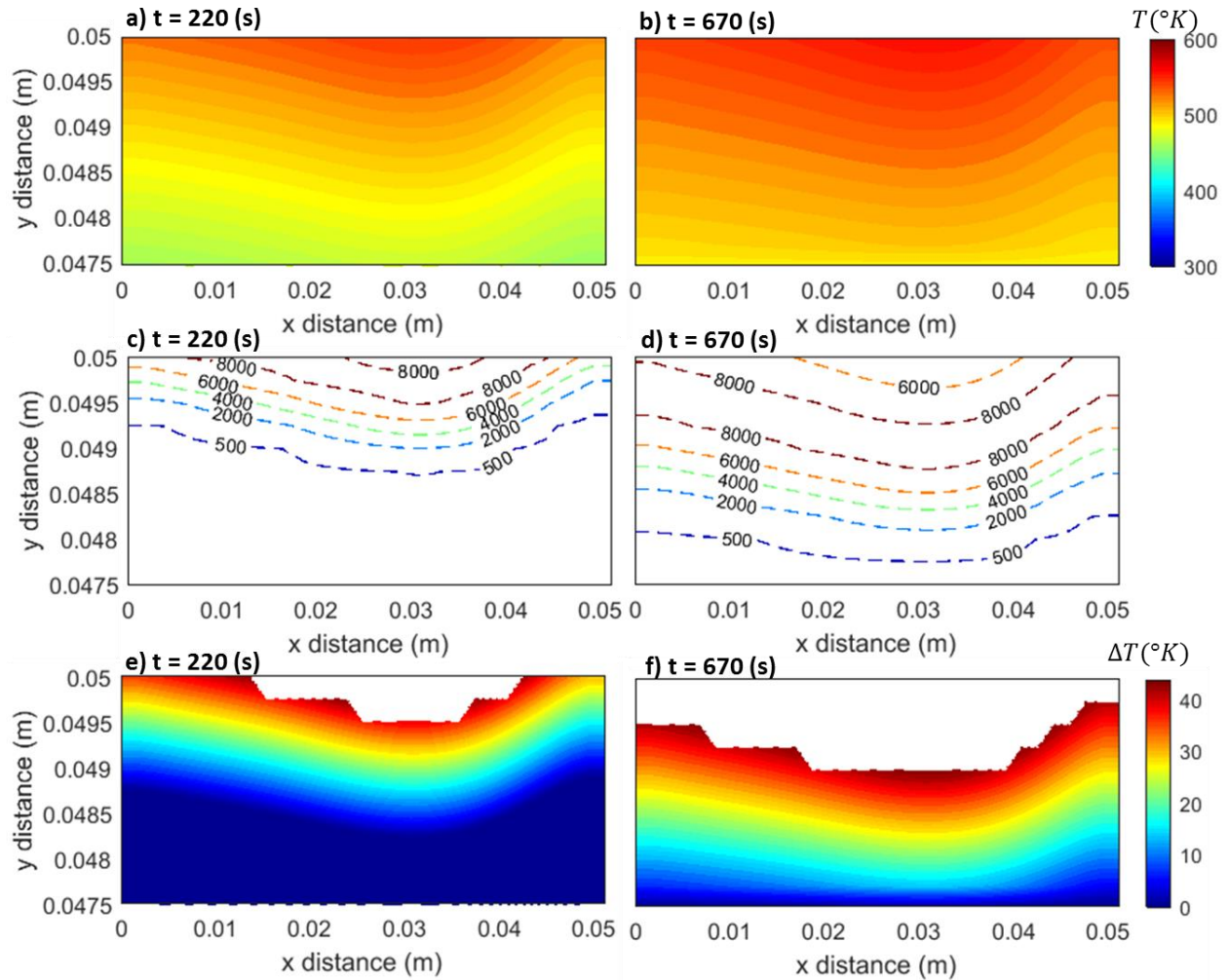


Figure 88: Contours of the temperature colored by the temperature magnitude at different time of a) 220 s, b) 670 s for aluminum blanket thickness of 0.25 cm. Contour line of the convection heat transfer coefficient inside the blanket at different time of c) 220 s, d) 670 s for aluminum blanket thickness of 0.25 cm. Contour line of temperature difference ($<$ excess temperature of critical heat flux, i.e. nucleate boiling regions) e) 220 s, f) 670 s for aluminum blanket thickness of 0.25 cm.

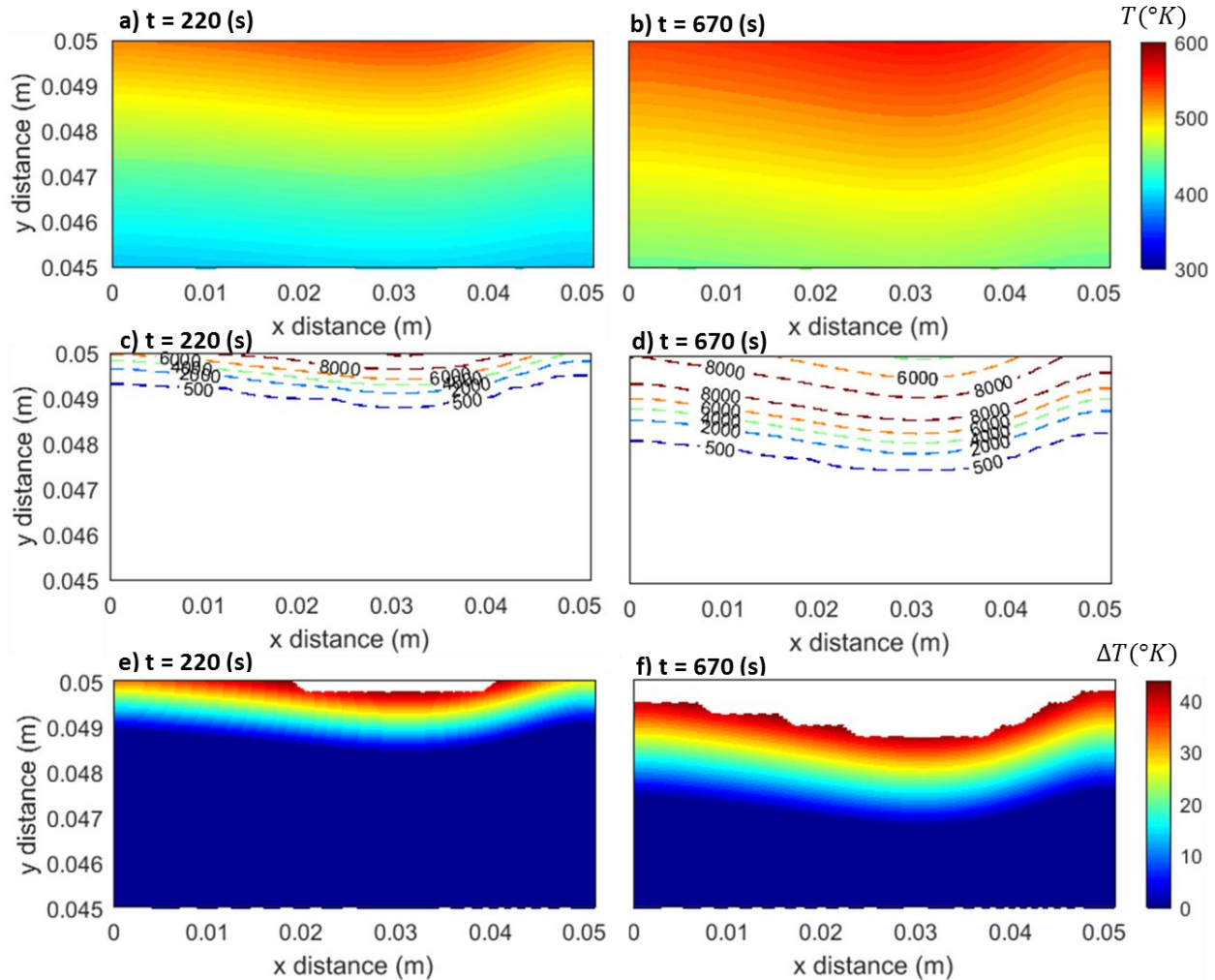


Figure 89: Contours of the temperature colored by the temperature magnitude at different time of a) 220 s, b) 670 s for aluminum blanket thickness of 0.5 cm. Contour line of the convection heat transfer coefficient inside the blanket at different time of c) 220 s, d) 670 s for aluminum blanket thickness of 0.5 cm. Contour line of temperature difference ($<$ excess temperature of critical heat flux, i.e. nucleate boiling regions) e) 220 s, f) 670 s for aluminum blanket thickness of 0.5 cm.

Figure 87-89 a and b show the temperature distribution inside the metal wool for $\delta = 0.15$ cm, 0.25 cm and 0.5 cm respectively at $t = 220$ s and $t = 670$ s. The contours values are presented at 220 and 670 seconds because of the mass loss rate and temperature trends shown Fig. 84 & 85. At 220 second, the mass loss rate increases rapidly and then it reaches steady state value later at 670 seconds. Similarly, the temperature increases rapidly around 220 seconds and then it reaches circa steady state later at 670 seconds.

The convective heat transfer coefficient is calculated from the boiling curve and plotted in Fig. 87-89 c and d. Finally, Fig 87-89 e and f show the contour lines of excess temperature with the region with $\Delta T > 42.6K$ represented in white. Because of the nature of the boiling regimes of the fuel, the convective heat transfer coefficient decreases beyond a certain temperature difference.

Therefore, the effective area in which the transition boiling occurs is larger in the case of $\delta = 0.15$ and 0.25 cm compared to $\delta = 0.5$ cm as shown in Fig. 87-89. On the other hand, the effective area in which the nucleate boiling is present increases from $\delta = 0.15$ cm to $\delta = 0.5$ cm. This is also the reason for the highest mass transfer in the case of $\delta = 0.5$ cm, because of an increase in nucleate boiling.

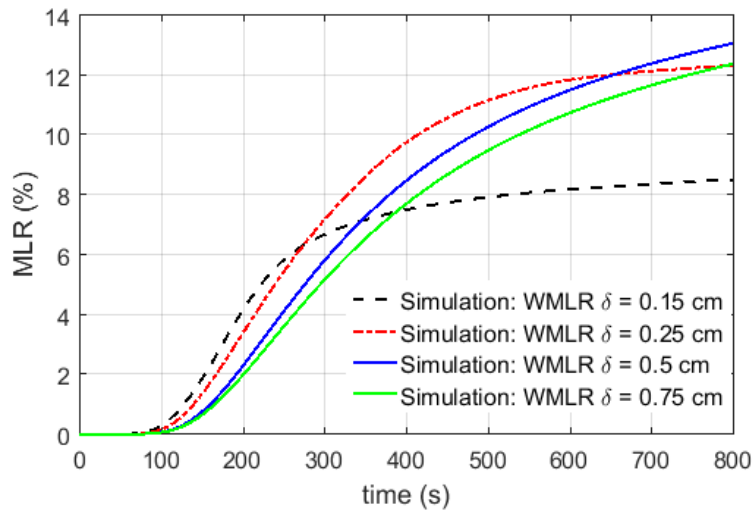


Figure 90: The ratio of nucleation induced MLR to total MLR for different thickness of metal wool.

Figure 90 shows model predictions of nucleation induced mass loss rate with varying thickness (δ) of 0.15 to 0.75 cm. For $\delta = 0.15$ cm, the burning rate due to the nucleation increases very quickly to the steady state trend because of the rapid heating of metal wool as shown in Fig. 87 a and b. As the thickness increases, the steady state value increases with the maximum occurring at $\delta = 0.5$ cm and decreasing thereafter because of the heat transfer to the water sub layer.

6.6 Application to Phase II

The mathematical model validated in Phase I is used to determine the Phase II blanket thickness. Figure 91 shows the regression rate of the fuel in a 70 cm diameter burner for different Cu blanket thicknesses. Dodecane was used in the mathematical model because it is a single component medium flash point hydrocarbon that represents the median volatile-fraction of a typical crude oil.

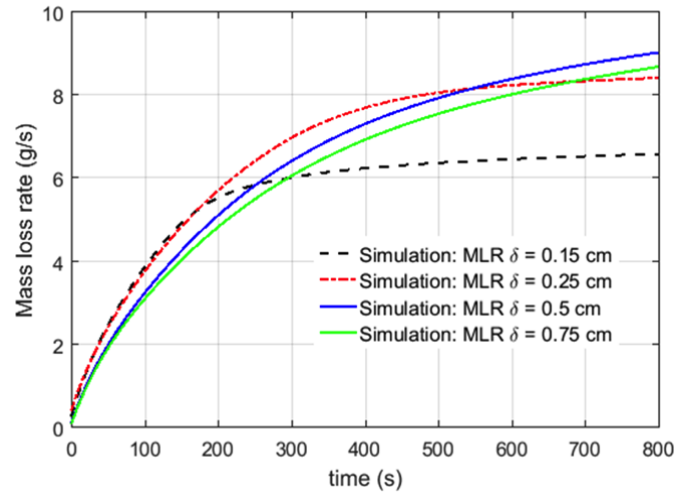


Figure 91: The time trace of the regression rate during the burning of the 0.7 m diameter dodecane pool fire for blanket thicknesses of 0.15-0.75 cm

The results demonstrated that the maximum regression rate can be obtained when the blanket thickness, δ , is between 0.25 cm and 0.5 cm. Based on the results, 0.35 cm thick blanket was used in Phase II experiments.

6.7 Application to Phase III

In Phase III application, the effect of coils on the heat penetration inside the pool is investigated. The only difference between the computational model implemented in phase I and phase III is the heat flux from the top boundary of the computational domain.

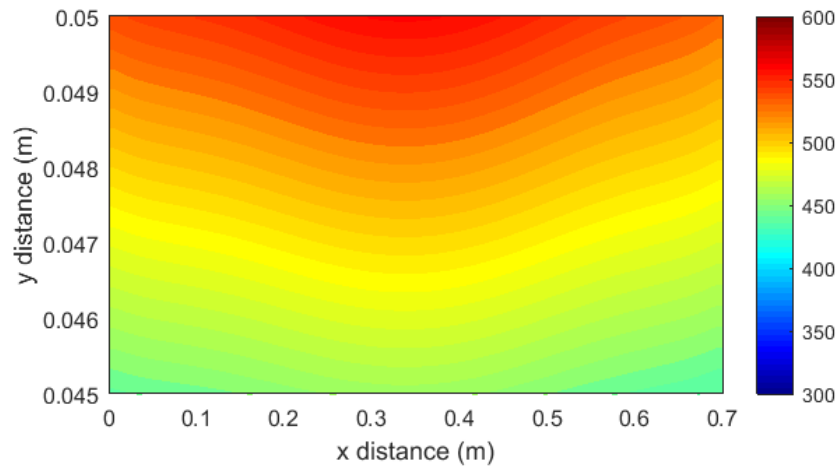


Figure 92: The temperature contours inside the blanket region at steady state for blanket case

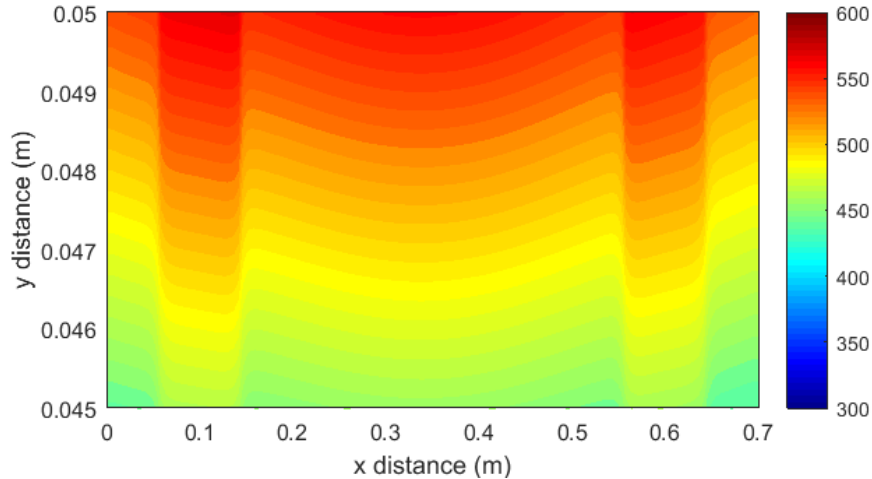


Figure 93: The temperature contours inside the blanket region at steady state for blanket + coils.

Higher heat flux values are used on the top surface where the coil touches the blanket surface because of the high heat conduction through coils. Figure 92 and 93 show the temperature contours inside the porous region for the blanket case and blanket + coils case respectively. The in-depth heat transfer increases with the coils causing experimentally measured mass loss rate in the case of coils to be higher than that of the only blanket case.

6.8 Extinction for the blanket and the coil system

Experimental results indicate that, the extinction time for the embedded objects tests (i.e. coils and blanket) was much larger than that of baseline. Because of the increased extinction time, more oil was burned during these tests. A simple analysis that calculates the energy stored in the blanket at steady state condition was performed to explore the effect of the embedded object on the extinction process. Figure 94 shows the schematic representation of the stored energy calculation process. The thermocouple locations in the experiment are mapped into a finer grid to obtain higher accuracy as shown in Fig. 94.

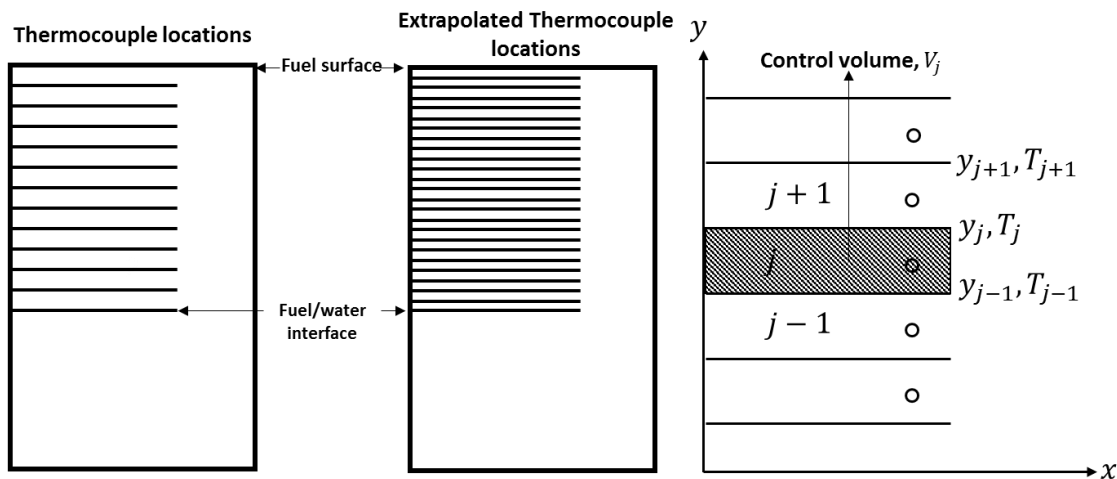


Figure 94: Schematic representation of the energy storage calculation process. Thermocouple locations are mapped into a finer grid to obtain a better accuracy for the energy storage calculation.

The energy stored in a control volume and the total energy stored in the pool layers shown in Fig. 94 are calculated as:

$$\begin{aligned} V_j &= (y_j - y_{j-1})\pi r^2, \\ E_j &= \rho_\alpha C_{p,\alpha} V_j \frac{T_j + T_{j-1}}{2}, \\ E_T &= \sum_{j=1}^{100} E_j. \end{aligned} \tag{32}$$

ρ and C_p are density and specific heat calculated by weighted averaging. r is the radius of the pool (0.7 m for the field trials in Mobile, AL). Subscript α represents the phases inside the pool (fuel, fuel-wool, and water). V_j is the volume shown in Fig. 94. T is the temperature at the face of the control volume.

Figure 95 shows the average temperature profile for the blanket case. Temperature values were averaged between 500 and 800 seconds of the burning process. This time interval was representation of a steady state condition of the burning process. The blanket region was identified by a temperature of 250 °C which is the average boiling point of the crude oil used in the experiments. The energy stored is calculated as,

$$E = \rho C_p V T \tag{32}$$

Where, ρ and C_p are density and specific heat calculated by weighted averaging. V is the volume of the layer. T is the temperature obtained by the experimental measurement.

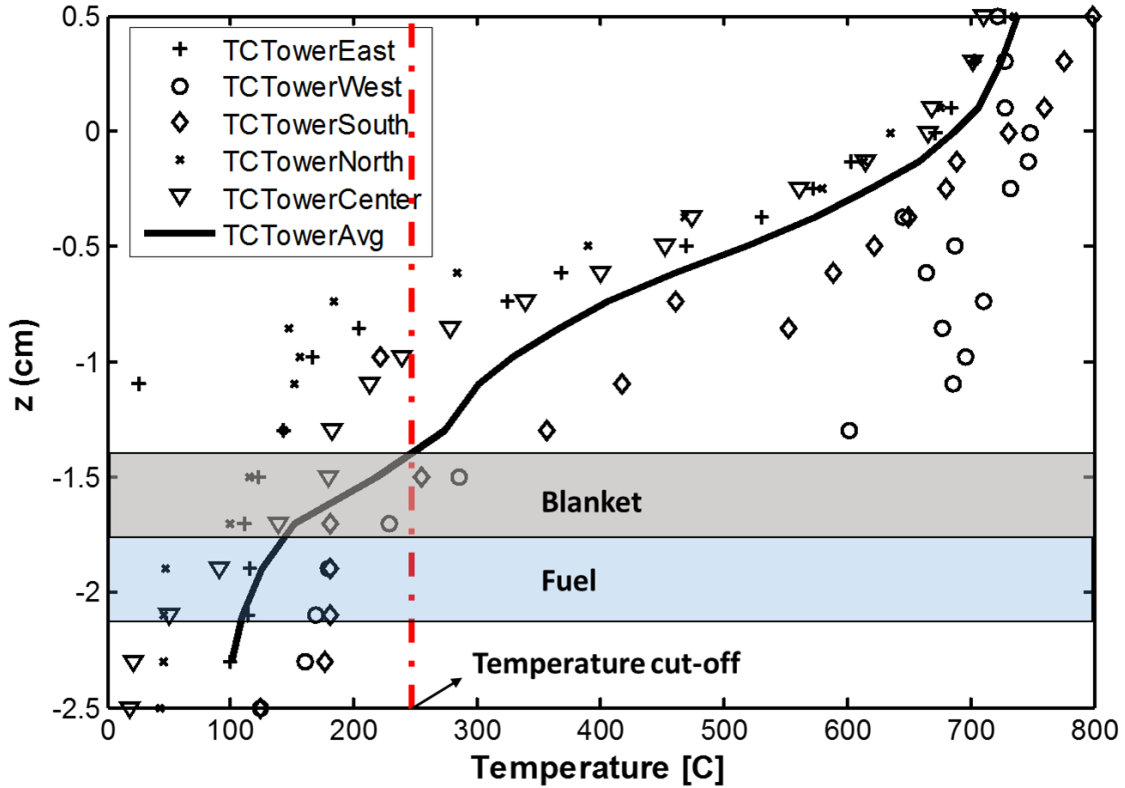


Figure 95: In-depth temperature profile at steady state during the field trial (blanket only case)

Table 17: Energy stored in the blanket and fuel layer

	baseline	Blanket	Blanket + 48 coils
Blanket region	280 MJ	490 MJ	449 MJ
Fuel region	203 MJ	150 MJ	162 MJ
Blanket + Fuel	481 MJ	640 MJ	611 MJ

Table 17 shows the energy stored for blanket and fuel layers for baseline, blanket and blanket + 48 coils. Energy stored in the blanket case is much higher than that of baseline case. In the case of blanket and 48 coils case, the energy stored in the blanket region is similar to that of blanket case. However, it should be noted that, in the coil case, additional energy is stored in the coils that are located in the gas phase.

Table 18: Energy stored during initial stages of the burning

	Baseline (30-70 s)	Blanket (10-40 s)	Blanket + 48 coils (10-40 s)
Blanket region	180 MJ	244 MJ	330 MJ
Fuel region	75 MJ	78 MJ	72 MJ
Blanket + Fuel	255 MJ	322 MJ	422 MJ

Table 19: Energy stored during extinction stage of the burning

	Baseline (940-960 s)	Blanket (1740-1760)	Blanket + 48 coils (1700-1720)
Blanket region	364 MJ	632 MJ	540 MJ
Fuel region	277 MJ	209 MJ	174 MJ
Blanket + Fuel	641 MJ	841 MJ	714 MJ

Similar analyses were performed at the initial and extinction stages of the burning. The results are tabulated in Table 18 for the initial stage and in Table 19 for the extinction stage. It is clear that the blanket is able to retain heat because of an increase in its volumetric heat capacity. This heat retention is most useful during the extinction stage where ~120MJ of additional heat stored in the blanket causes the heavier tar components to also burn off. This significantly improves the efficiency by reducing the post burn residue.

6.9 Conclusions of computational model

A physics based numerical model has been developed to predict the mass loss rate of pool fires with thermally conductive metal wool immersed in the oil layer. The present computation uses a two-dimensional transient conductive heat transfer model for the porous media with temperature dependent thermo-physical properties, and a two-dimensional transient conduction heat transfer model for liquid fuel and water layers. The complex physics of the heat and mass transfer mechanisms is represented using a simplified model. The gas phase temperature and the flame temperature above the fuel are assumed to be constant during the burning process for simplicity. The model with the porous media is implemented for small scale pool fires of 10 cm in diameter as well as large scale pool fires of 140 cm in diameter.

The convective heat transfer coefficient during fuel boiling has been calibrated against the experimental results. The predicted boiling curve for dodecane is found to be between the boiling curves for water and light hydrocarbons. The convective heat transfer coefficient for the crude oil experiments is calibrated against the crude oil tests. However, the calibration of the boiling curve for a multi-component liquid such as crude oil is very difficult. Therefore, it is vital to obtain the boiling curve of the multi-component hydrocarbon oils to further investigate the Flame Refluxer technology.

The numerical results are in good agreement with the experimental observations for different metal wool thickness. The optimum blanket thickness is found to be in the range of 0.25 – 0.5 cm, however the optimum blanket thickness depends on the thermo-physical properties of the materials involved in the burning process and the porosity. During initial burning stages, the blanket acts like a heat sink until it achieves a sufficient temperature to provide heat for the oil layer. The current model can be used to optimize the thickness and material selection of the embedded blanket and to maximize the burning efficiency.

To further enhance heat feedback from the pool fire, additional heat collectors (coils) are integrated with the blanket system during the experimental tests. The additional heat from the collectors is adopted into the model as additional heat flux at the gas-fuel interface. The coupling between the coils and blanket is a complex problem and was beyond the scope of the current work. However, the simple addition of heat was shown to increase the thermal penetration, thereby increasing burning rate. The collectors also cause a reduction in black carbon soot emissions.

7. Conclusion and Future Study

The two-year study applied the Flame Refluxer concept towards burning oil slicks (0.01m thick) with high efficiency and reduced emissions. The *Flame Refluxer™* collects radiative and convective heat generated by a fire via helical copper coils and transfers it back to the fuel to create a feedback loop that sustains a significantly increased burning rate. With thin oil slicks on water, it was shown that “collection” is best achieved at the periphery or rim of the pool fire where flames anchor. A porous metal wool made of copper (blanket) spread across the fuel surface forms the “heater” component of the Flame Refluxer. For ANS and HOOPS crude oil, 1 cm thick, an optimum blanket thickness was found to be $\sim 1/2$ the thickness of the oil slick. The blanket enables lateral heat transfer, increases volumetric heat capacity and increases mass transfer by wicking and nucleate boiling.

Field-tests performed in the outdoor Joint Maritime Test facility in Little Sand Island (LSI) in Mobile Bay, Alabama, showed that the developed blanket-coil prototype was able to burn thin oil slicks (~ 1 cm) achieving an efficiency of 480% above baseline. Further, the high thermal capacity of the blanket sustained combustion even in very thin oil slicks (~ 1 mm). The extended burning time and oil wicking resulted in 1.8% post burn residue (baseline test comprising of no blanket had a post burn residue of 32%). Complete combustion of the fuel caused a reduction in the black smoke as evidenced by the CO/CO₂ ratio reduction by half compared to the baseline.

Field test results indicate that an ISB Flame Refluxer (ISB-FR) is capable of much cleaner combustion and may achieve a six to tenfold enhancement of burning rates as compared to current ISB technology. Field tests also validated the earlier supposition (refer E14PC00043) that Flame Refluxer thermal performance would improve markedly with increasing pool fire sizes. The appropriate size and configuration of an ISB-FR needs to be determined based on deployment considerations, such as slick size, FR robustness, ease of handling, weight, drag and retrieval method following completion of the burn. These aspects were outside the scope of this study and would be a good future direction. Future work should include the actual mechanical design of a sea-worthy, full-scale prototype that can be deployed and tested with boats.

References

1. A. Agueda, E. Pastor, Y. Perez and E. Planas, "Experimental study of the emissivity of flames resulting from the combustion of forest fuels", *International Journal of Thermal Sciences*, vol. 49, p. 543–554, 2010.
 2. P. D. Panetta and S. Potter, "TRL Definitions for Oil Spill Response Technologies and Equipment", Report, BSEE Contract Number E14PC00020, Bureau of Safety and Environmental Enforcement (BSEE), U.S. Department of the Interior, Washington, D.C, 2016.
 3. Worcester Polytechnic Institute, "Burning Behavior of Oil in Ice Cavities", Bureau of Safety and Environmental Enforcement, Project #1007, 2013.
 4. Worcester Polytechnic Institute, "Burning Behavior of Oil in Ice Cavities-II", Bureau of Safety and Environmental Enforcement, Project #1007, 2016.
 5. L.A. Gritzo, V.F. Nicolette. Coupling of large fire phenomenon with object geometry and object thermal response. *Journal of Fire Sciences*, vol. 15, no. 6, pp. 427-442, 1997.
 6. G.D. Wang, H.Y. Wang, J.M. Most. Mathematical modelling of the interaction between wind and aviation-fuel fire engulfing a fuselage-sized cylinder. *Journal of Fire Sciences*, p. 0734904112468579, 2013.
 7. A Worcester Polytechnic Institute, "A Novel Experimental Approach to Enhance Burning Of Oil-Water Emulsions by Immersed Objects" Report No: 1049, Bureau of Environmental and Safety Enforcement, Department of Interior, Washington, DC, 2015.
 8. H. Sezer, K.S. Arsava, S.P. Kozhumal, A.S. Rangwala, "The effect of embedded objects on pool fire burning behavior", *International Journal of Heat and Mass Transfer*, Vol. 108, Part A, 537-548, 2017.
 9. I. Buist, J. McCourt, S. Potter, S. Ross, and K. Trudel, "In situ burning", *Pure Appl. Chem.*, Vol. 71, No. 1, 43–65, 1999.
 10. I. Buist, J. McCourt, S. Potter, S. Ross and K. Trudel, In situ burning, *Pure Appl. Chem.*, Vol. 71, No. 1, pp. 43–65, 1999.
 11. Kandula, M., "On the effective thermal conductivity of porous packed beds with uniform spherical particles," *Journal of Porous Media*, vol. 14, no. 10, 2011.
 12. P. Zehner, and E.U. Schlunder, "Thermal conductivity of granular materials at moderate temperature (in German)," *Chemie Ingr. Tech*, vol. 42, pp. 933-941, 1970.
 13. C.O. Popiel, "Free convection heat transfer from vertical slender cylinders: a review," *Heat Transfer Engineering*, vol. 29, no. 6, pp. 521-536, 2008.
 14. Kanury, A. Murty, Introduction to combustion phenomena, Notre Dame: Gordon and Breach, Science Publishers, Inc, 1982.
 15. L. Albright, (Ed.), Albright's chemical engineering handbook, CRC Press, 2008.
 16. "The Engineering ToolBox," [Online]. Available: http://www.engineeringtoolbox.com/air-properties-d_156.html. [Accessed 31 August 2017].
 17. "Pure copper," [Online]. Available: <http://www-ferp.ucsd.edu/LIB/PROPS/PANOS/cu.html>. [Accessed 31 August 2017].
 18. H. Sezer, K.S. Arsava, and A.S. Rangwala, "Oil spill clean-up using immersed metal wool", *Journal of Environmental Chemical Engineering*, In Press.
- C1. S. B. Pope, Turbulent Flows, Cambridge University Press, 2000.
- C2. J. Deardorff, "Stratocumulus-capped mixed layers derived from a three-dimensional model," *Boundary-Layer Meteorol*, vol. 18, pp. 495-527, 1980.

- C3. NIST Special Publication 1018-1, "Fire Dynamics Simulator- Technical Reference Guide," National Institute of Standards and Technology, 2016.
- C4. T. Poinso and D. Veynante, Theoretical and Numerical Combustion, Philadelphia: R.T. Edwards, Inc., 2005.
- C5. R. O. Fox, Computational Models for Turbulent Reacting Flows, Cambridge Univ Press, 2003.

- E1. Tukaew (Oat) Panyawat. "Outdoor Gas Emission Sampling System: A Novel Method for Quantification of Fires in Outdoor Conditions", MS Thesis, Worcester Polytechnic Institute, etd-050217-121733

Appendix A – TC measurement correction

The plume temperature measured by the thermocouple was not the same as the actual temperature because of the heat transfer occurs between the thermocouple and the surroundings. The conduction losses, can be omitted if the length of the thermocouple wire is more than 160 times its diameter (Martins et al. 2005). In experiments, the length of the thermocouple wire is nearly 1500 mm and the wire diameter is 0.25 mm, the ratio between the length and the diameter is nearly 6000. Therefore, the conduction losses has been omitted. The corrections needed to obtain the actual temperature are due to convection and radiation losses. Bradley and Mathews (1968) suggested that the losses due to radiation from the thermocouple can be corrected by using the following relation between the actual and the measured temperature,

$$T_g = T_t + \frac{\varepsilon_t \sigma T_t^4}{h_t} \quad (\text{A-1})$$

In Eq. (A-1), T_g represents the actual gas temperature, T_t is the temperature measured by the thermocouple, ε_t is the emissivity of the thermocouple (0.22), σ is the Stefan-Boltzmann constant ($5.67 \times 10^{-8} \text{ W / m}^2 \text{ K}^4$), and h_t is the heat transfer coefficient at the wire surface.

The convective heat transfer coefficient for the thermocouple wire surface was calculated by inverting the Nusselt number;

$$Nu = \frac{h_t D_t}{\lambda_g} = 0.42 \text{ Pr}^{0.2} + 0.57 \text{ Pr}^{0.33} \text{ Re}^{0.5} \quad (\text{A-2})$$

where, D_t , Re and Pr are the diameter of the thermocouple wire, Reynolds and Prandtl numbers, respectively. D_t is 0.025 cm (0.01"), while Pr and Re are taken as 0.72 (for air at 1000 K) and 0.0137 (Bradley and Mathews, 1968), respectively.

The parameter λ_g is the thermal conductivity Coefficient and it is estimated as,

$$\lambda_g = 3.75 * 10^{-5} T_t + 0.04 \quad (\text{A-3})$$

Appendix B – Phase II – Fuel level control system

This section provides a brief overview of the different attempts to achieve a final working system was achieved. The first iteration of the fuel level control system involved the use of an off-the-shelf float switch (Fig. B-1a) This switch was designed to work within harsh environments, and was intended to be located within the burner itself. This concept failed due to the insensitivity of the switch. The range of motion to change from open to close was greater than the allowable 1cm level.

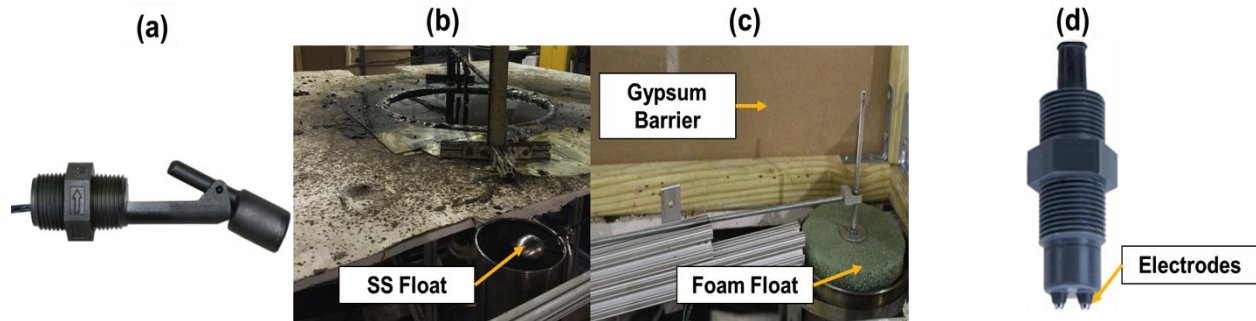


Figure B-1: (a) Float switch (b) Stainless steel float (c) Medium-density foam float (d) Conductive switch

The second iteration of fuel control involved a micro switch and a stainless steel float, which would be suitable for use in a thermally active and saltwater environment (Fig. B-1b). The switch worked well in operating the solenoid valves, but the stainless steel float was inconsistent in its float point, being prone to “bob” with the smallest of impulses. Simply bumping into the test pool would be enough to cycle the switches, which would cause inconsistent functioning. It was determined that direct monitoring of the fuel level was not feasible for this stage of testing.

A fluid level monitor was installed to mirror the fluid levels within the test area. This served to isolate the switching system from vibrations and current action within the testing area, while maintaining an identical fluid level. The stainless steel float continued to be subject to minor influences, giving signals to the solenoid valves at inconsistent fluid levels. A re-configuration solved this, utilizing a longer lever arm, closer to a level orientation, and using a medium-density foam as a float (Fig. B-1c). Utilizing threaded rods at all points within the armature accommodated a great deal of fine tuning. Set points for opening and closing were set within the tolerances of the micro switch itself (2.1mm). Although the design provided a 2.1 mm path of travel between open and closed, it was not sensitive enough for accurate testing. The main objective was to keep the fuel level fluctuation in the range of 1 mm.

In order to increase the sensitivity of the fuel level control system, float mechanism was replaced by a conductive switch (Fig. B-1d) which is actuated when the electrodes are covered by salt water. This system was adopted because it provides 1 mm sensitivity, while sending signals to the solenoid valves at exceptionally consistent fluid levels.

Appendix C – Details of Fire dynamics simulator (FDS)

Numerical simulations have been carried out to predict the plume trajectory and flame height of a pool fire in the presence of unidirectional wind. Three-dimensional, turbulent, unsteady, incompressible, reacting flow calculations have been carried out using the Fire dynamics simulator (FDS) developed by the National Institute of Standards and Technology (NIST). The turbulent flow is modelled using Large Eddy Simulation (LES) with a time marching scheme for the momentum transport. The effect of combustion and radiation are accounted for using source terms in the energy transport equation. The species transport equations are solved using a predictor-corrector scheme. The energy conservation equation is not solved explicitly, but is defined implicitly via the divergence of the flow field, which contains the combustion and radiation source terms.

Solving the entire Navier-Stokes equations are computationally demanding. As pool fires typically involve low speed flows driven by the buoyant forces created by the temperature gradient, the governing equations are simplified to form a velocity divergence equation. An explicit predictor-corrector scheme, which is second order accurate in space and time, is used. The turbulent viscosity is modeled using the Deardorff [C1, C2] turbulent viscosity, $(\mu_{LES}/\rho) = C_v \Delta \sqrt{k_{sgs}}$. Here $C_v = 0.1$ and the subgrid scale (sgs) kinetic energy is taken from an algebraic relationship based on scale similarity [C3]. The geometric mean of the local mesh spacing is used as the LES filter width in each direction. Constant turbulent Schmidt and Prandtl numbers are used.

The fuel evaporation rate during the burning is calculated using Clausius-Clapeyron relation based on the liquid temperature, its boiling temperature, and the mass fraction of fuel vapor above the pool surface. Mixing controlled combustion with infinite rate chemistry is assumed. Eddy Dissipation Concept (EDC) [C4, C5] is used to calculate chemical source terms based on the lumped mass fractions of fuel and oxidizer. The volumetric heat release rates are evaluated as products of the rate of production of species and their respective heats of formation. The species transport equations are solved using a predictor-corrector scheme. A single component fuel, n-heptane, is considered for the study. A grid of 2.7648 million cells (320 x 54 x 160) is selected after a grid refinement study. The computational domain is 32 m long, 5.4 m wide and 16 m high. The thermal radiation is accounted for assuming a non-scattering gray gas with an absorption coefficient of 1000 m^{-1} . The radiation transport equation is solved using a finite volume based approach using 100 discrete angles.

All walls are assumed to be adiabatic where the sum of the net convective and radiative heat flux is zero. No slip condition is imposed on walls. The fluid is allowed to flow into or out of the computational domain through open boundaries depending on the local pressure gradient. An upwind boundary condition, where temperature and species mass fractions are assigned their respective exterior values for incoming flows and the values in the adjacent grid cell for outgoing

flows, are used for all open boundaries. A unidirectional wind of 10 Knot (5.14444 m/s) is considered.

The visualization of heat release rate and smoke are shown Fig. C-1. Two instances, showing an early stage of the pool fire (Fig. C-1a) and a stage where the fire is well spread (Fig. C-1b), are shown. The distances are given in feet and time in seconds. Based on this preliminary study, the region of heat release is observed up to 30 ft downstream of the pool. The smoke is seen to spread up to height of 45 ft from the pool. The possibility of fluctuations in the magnitude and direction of wind and their effects on the partial premixing of fuel vapor is not considered in this study. The change in fuel composition during the burning of a multicomponent fuel can also affect the flame trajectory. Hence, the predictions from this model can only be used as a rough estimate of the flame and smoke trajectories.

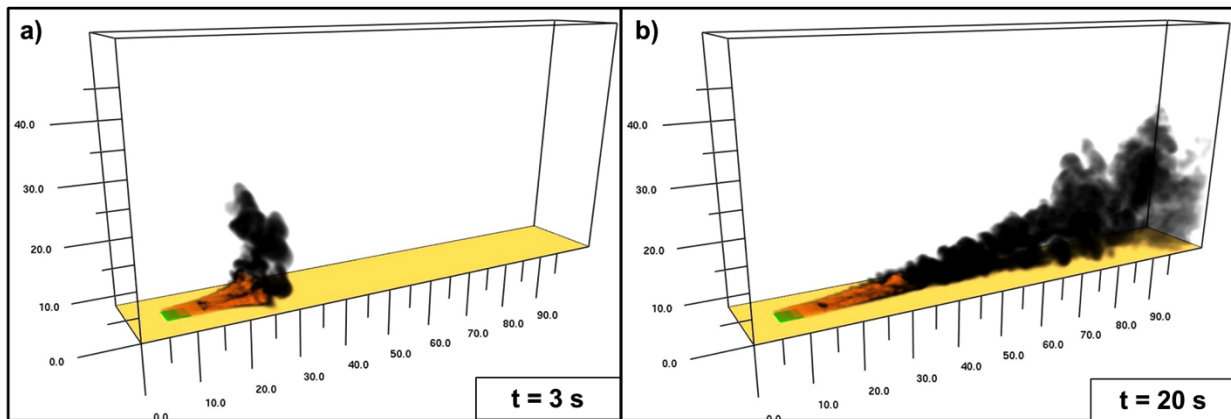
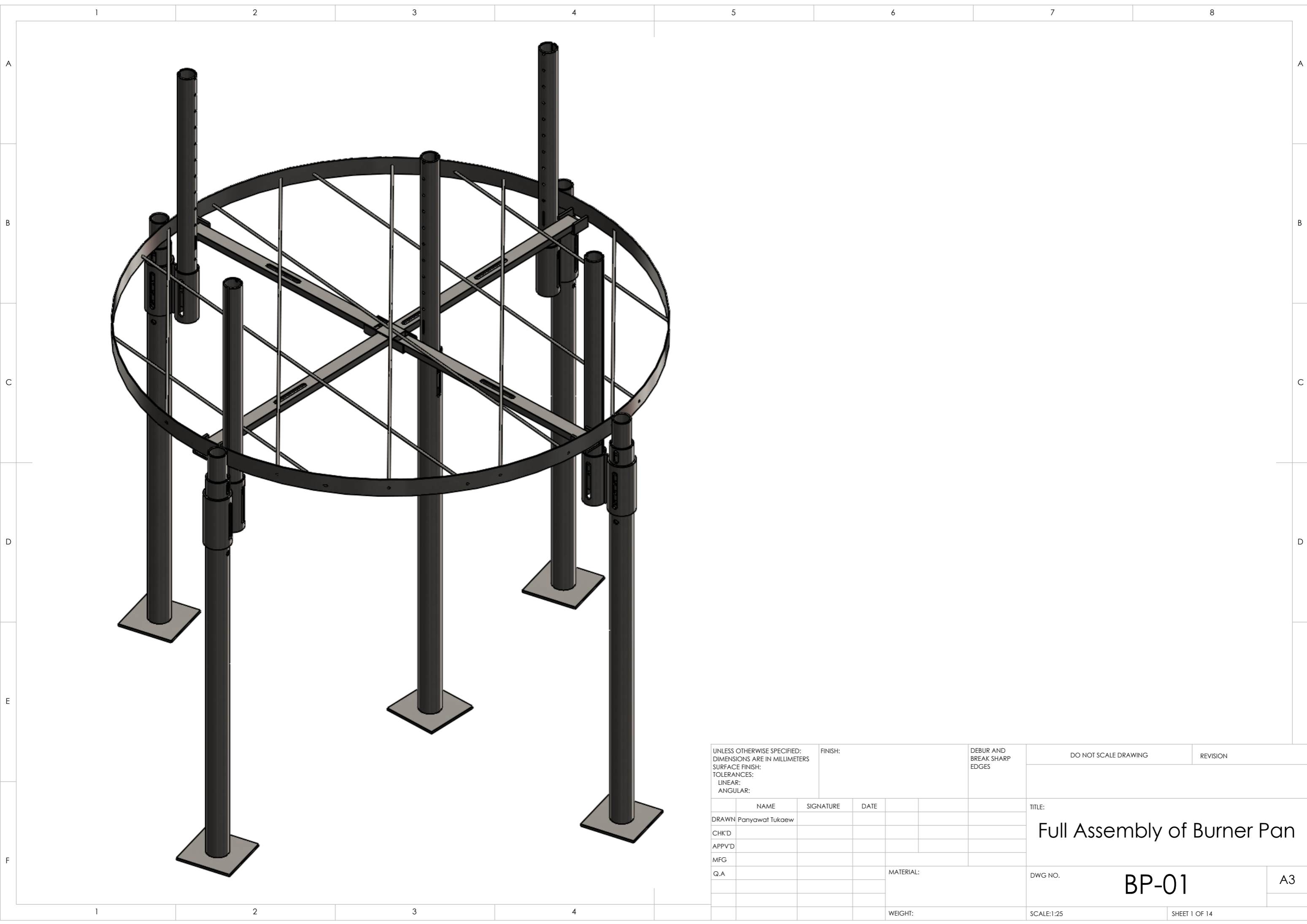
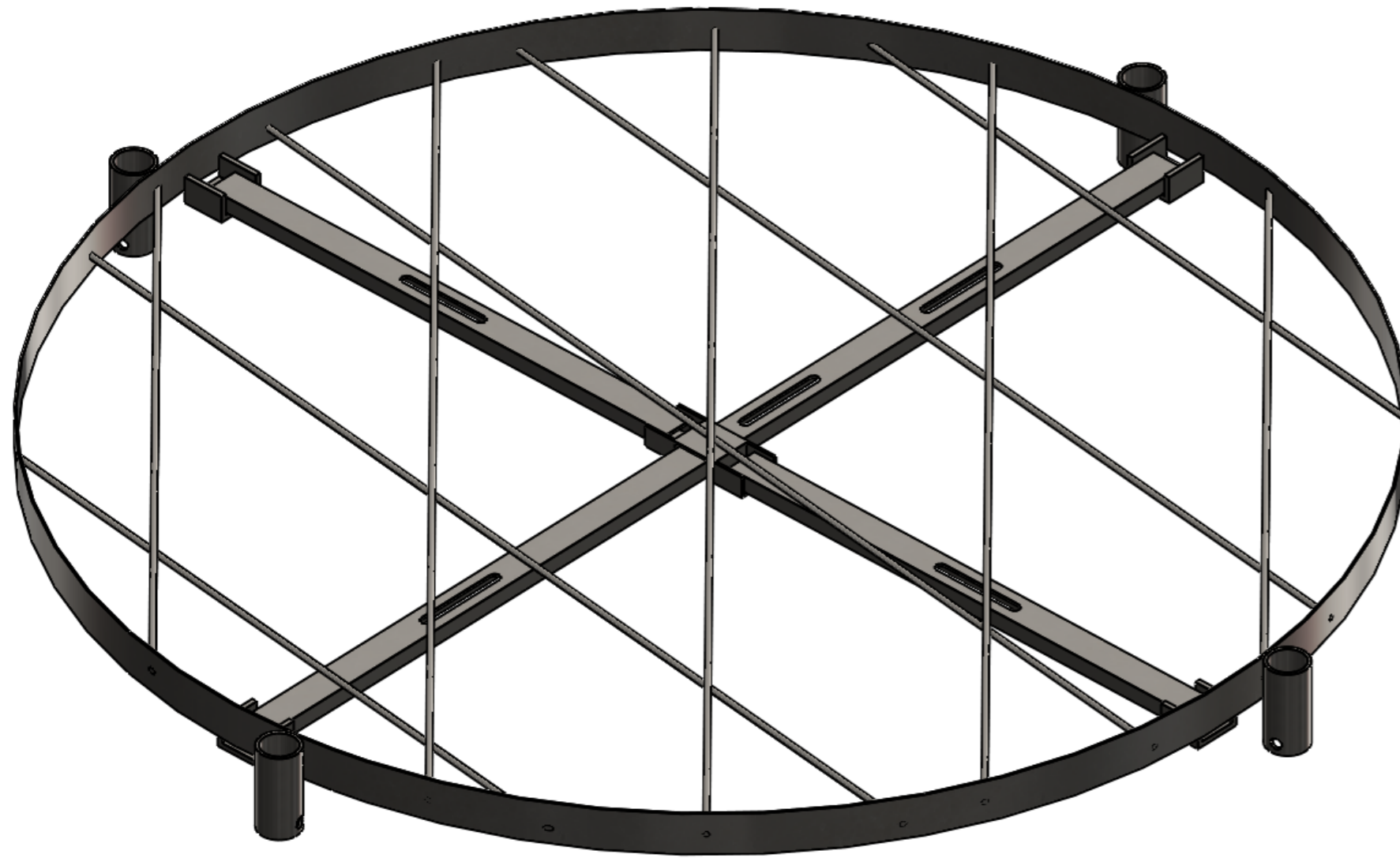


Figure C-1: Visualization of heat release and smoke, a) $t = 3\text{s}$, b) $t = 20\text{s}$.

Appendix D – Details of Phase III burner ring

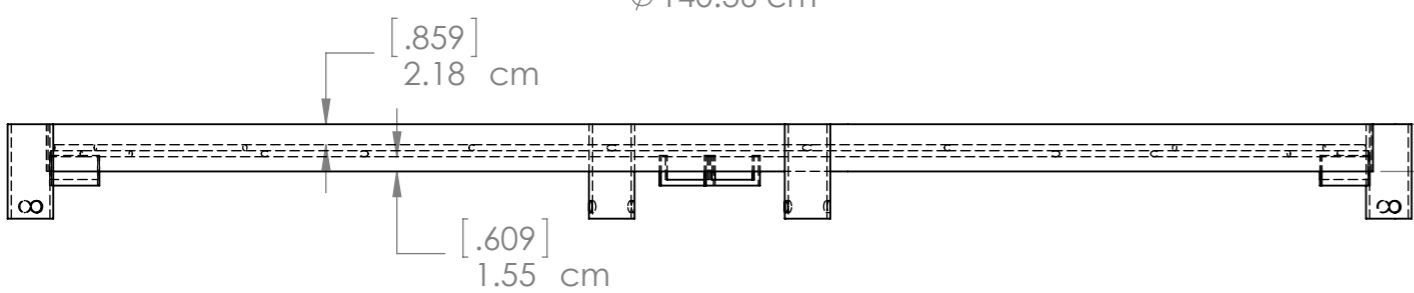
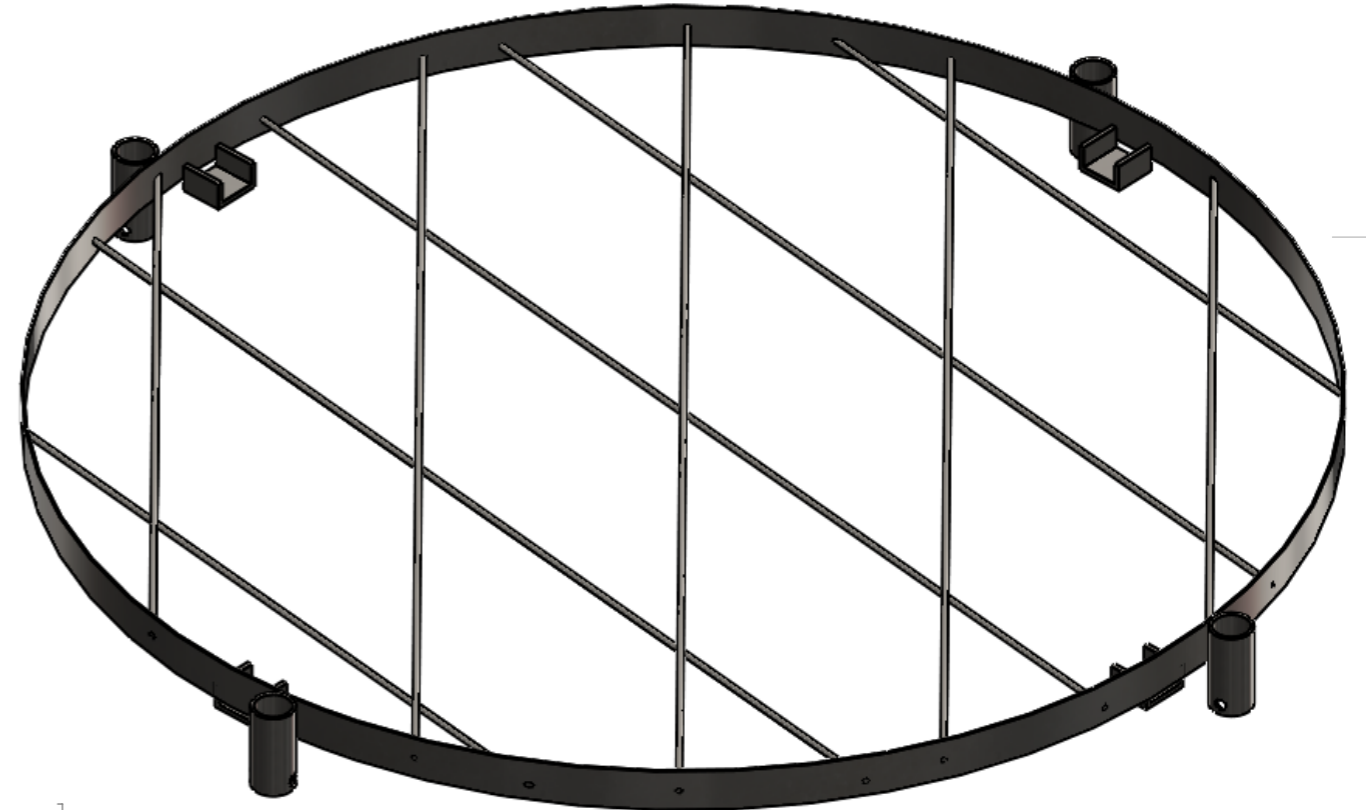
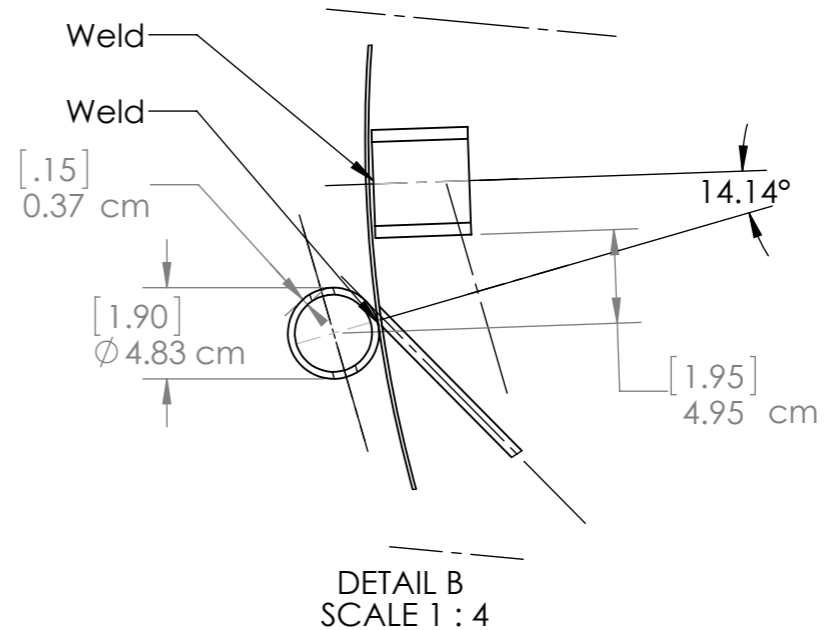
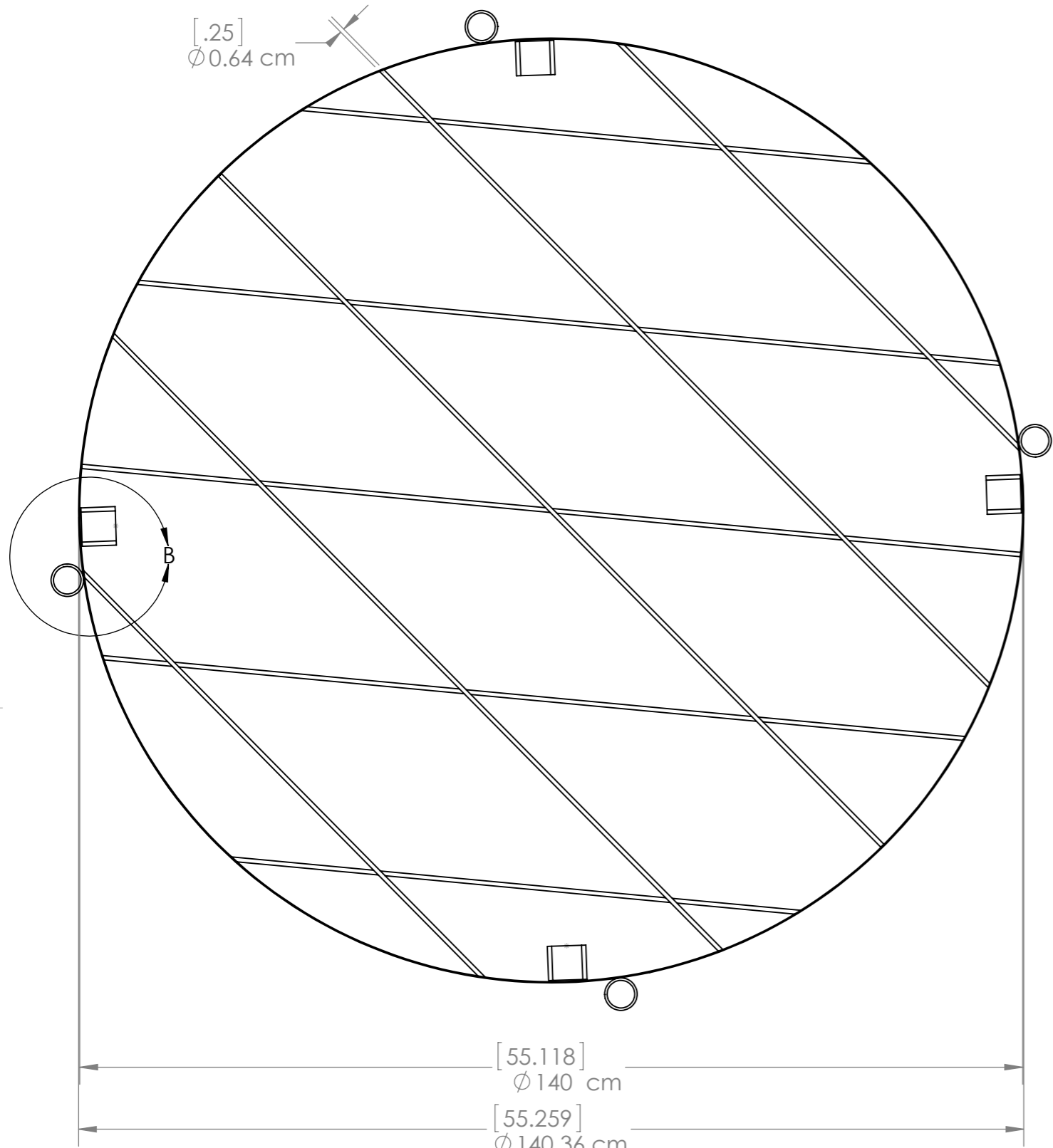


UNLESS OTHERWISE SPECIFIED: DIMENSIONS ARE IN MILLIMETERS SURFACE FINISH: TOLERANCES: LINEAR: ANGULAR:			FINISH:		DEBUR AND BREAK SHARP EDGES		DO NOT SCALE DRAWING		REVISION		
DRAWN Panyawat Tukaew			SIGNATURE		DATE		TITLE:		Full Assembly of Burner Pan		
CHK'D											
APPV'D											
MFG											
Q.A							MATERIAL:		DWG NO.		BP-01
							WEIGHT:		SCALE:1:25		SHEET 1 OF 14
											A3



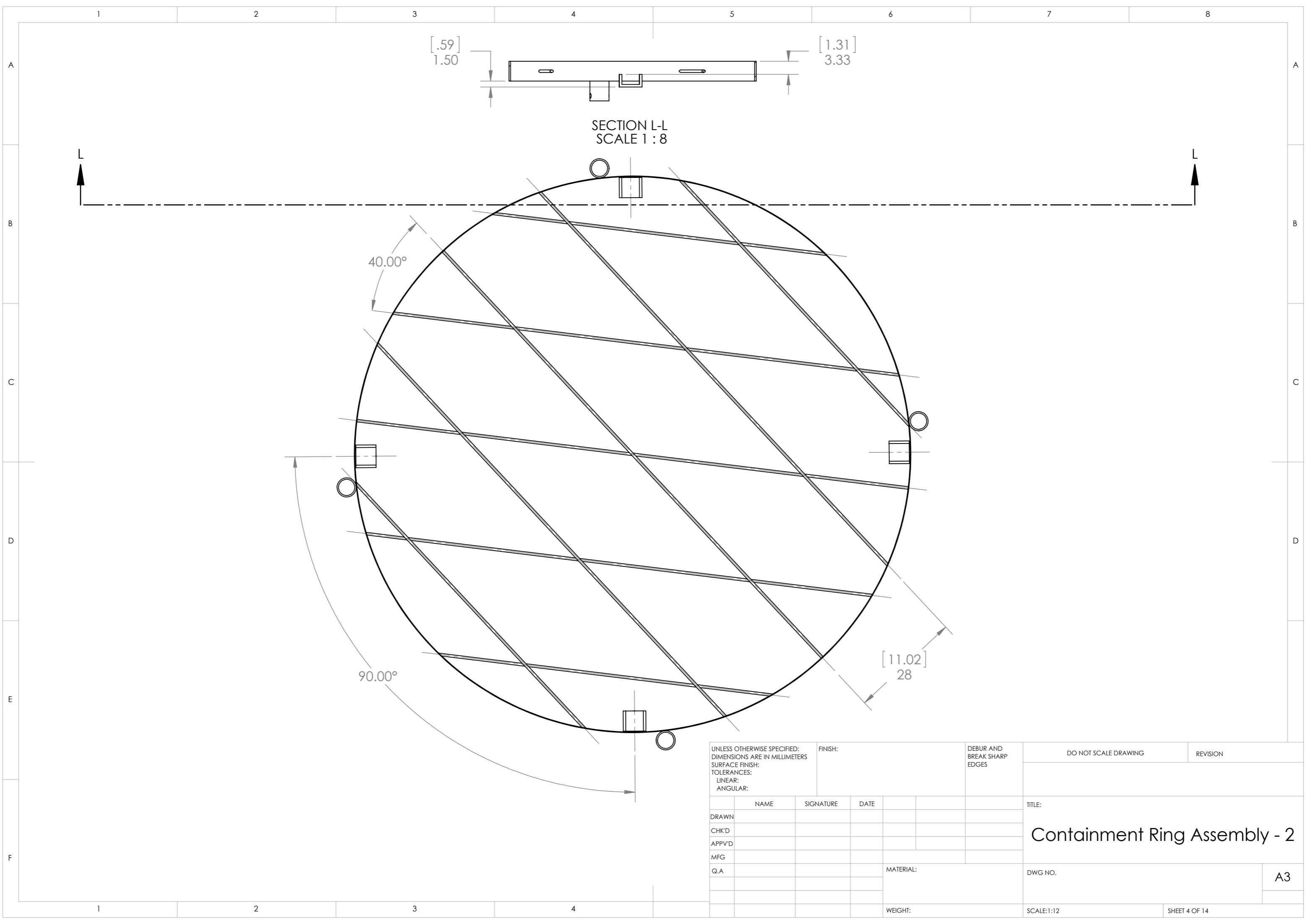
Item No.	Name/Description	Quantity	Material
1	Containment Ring	1	306 Stainless Steel
2	Containment Ring Support	4	306 Stainless Steel
3	Crossbars	10	306 Stainless Steel
4	U-Channel Support	4	306 Stainless Steel
5	U-Channel (Long)	1	306 Stainless Steel
6	U-Channel Saddle Support	1	306 Stainless Steel
7	U-Channel (Short)	2	306 Stainless Steel

UNLESS OTHERWISE SPECIFIED: DIMENSIONS ARE IN MILLIMETERS SURFACE FINISH: TOLERANCES: LINEAR: ANGULAR:			FINISH:		DEBUR AND BREAK SHARP EDGES		DO NOT SCALE DRAWING		REVISION		
DRAWN			NAME		SIGNATURE		DATE		TITLE:		
CHK'D											
APPV'D											
MFG											
Q.A									MATERIAL:		DWG NO.
									WEIGHT:		SCALE:1:12
									SHEET 2 OF 14		A3



[1.97]
5 cm

UNLESS OTHERWISE SPECIFIED: DIMENSIONS ARE IN MILLIMETERS SURFACE FINISH: TOLERANCES: LINEAR: ANGULAR:				FINISH:	DEBUR AND BREAK SHARP EDGES	DO NOT SCALE DRAWING	REVISION
DRAWN	NAME	SIGNATURE	DATE			TITLE: Containment Ring Assembly-1	
CHK'D						DWG NO.	A3
APPV'D						SCALE:	SHEET 3 OF 14
MFG							
Q.A					MATERIAL:		
					WEIGHT:		

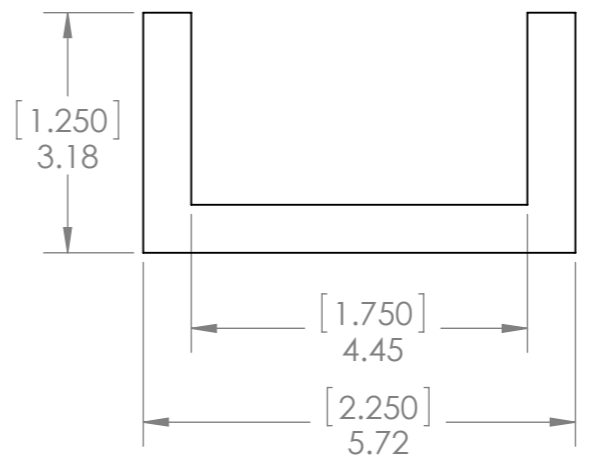
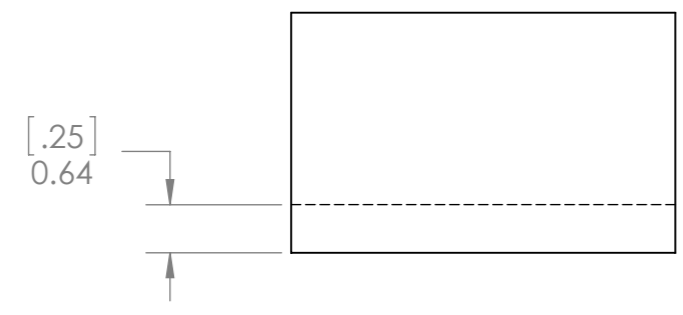
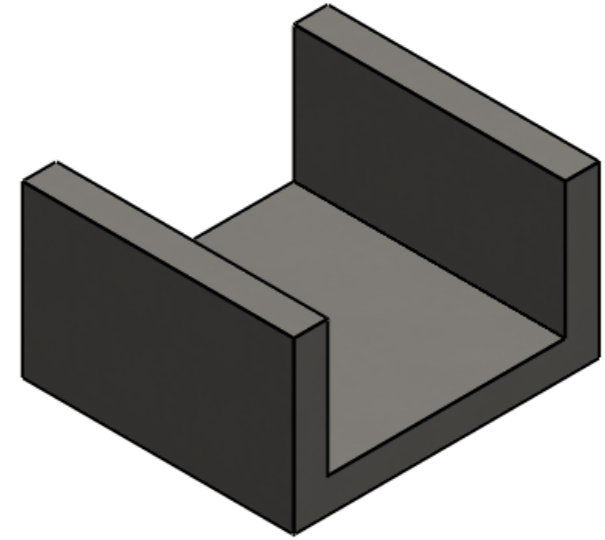
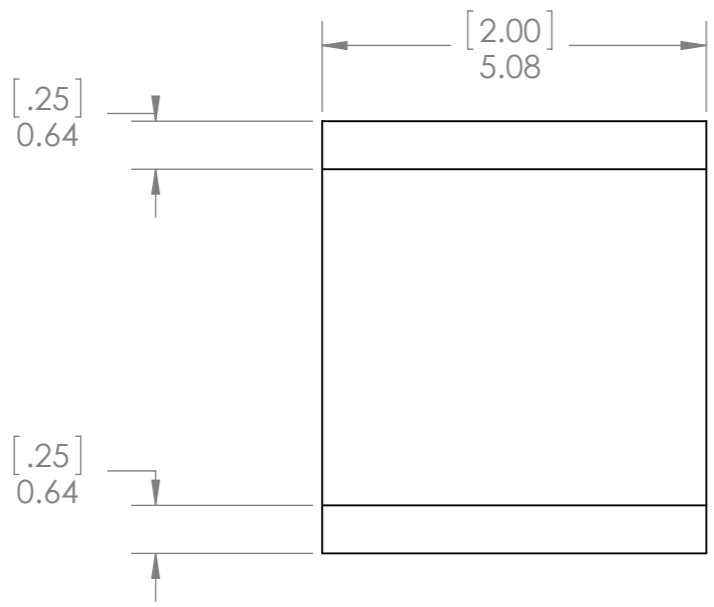


SECTION L-L
SCALE 1 : 8

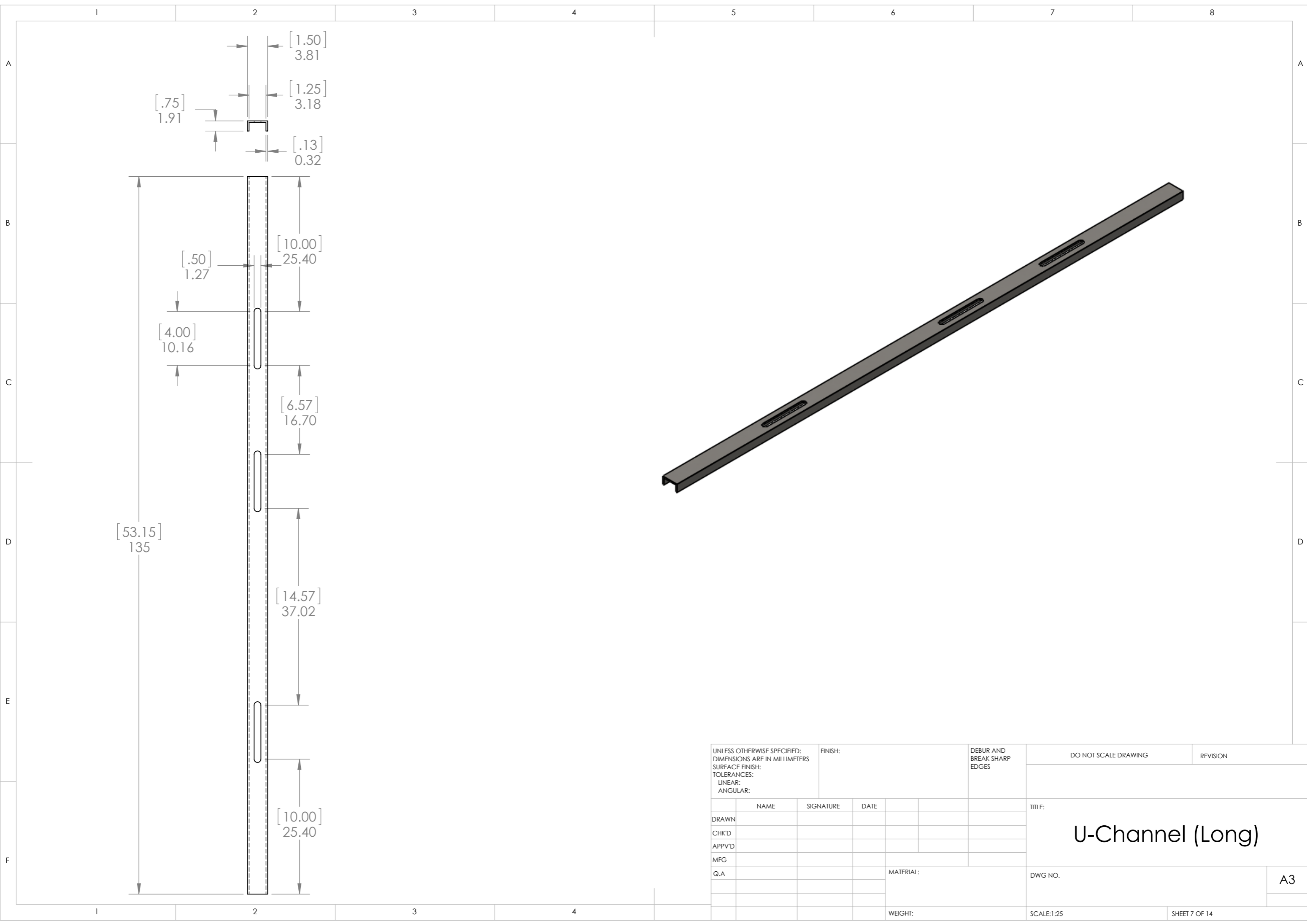
UNLESS OTHERWISE SPECIFIED: DIMENSIONS ARE IN MILLIMETERS				FINISH:		DEBUR AND BREAK SHARP EDGES		DO NOT SCALE DRAWING		REVISION			
SURFACE FINISH:													
TOLERANCES:													
LINEAR:													
ANGULAR:													
DRAWN		NAME		SIGNATURE		DATE		TITLE:		A3			
CHK'D								Containment Ring Assembly - 2					
APPV'D										DWG NO.			
MFG										SCALE:1:12		SHEET 4 OF 14	
Q.A								MATERIAL:					
								WEIGHT:					

1 2 3 4 5 6 7 8

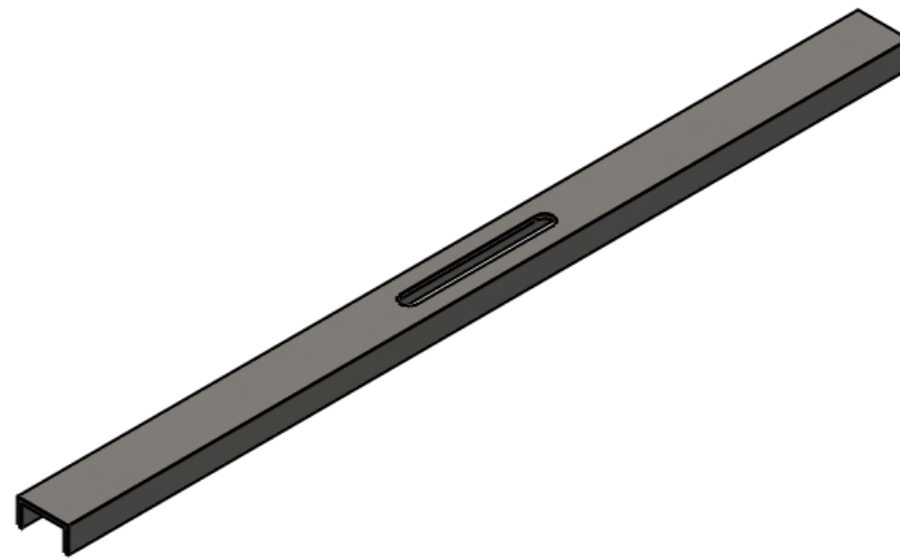
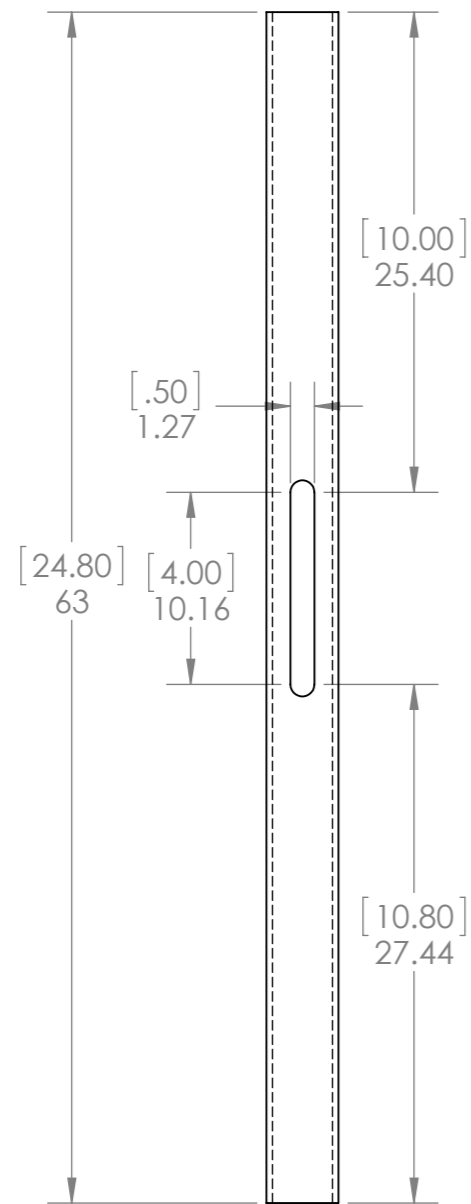
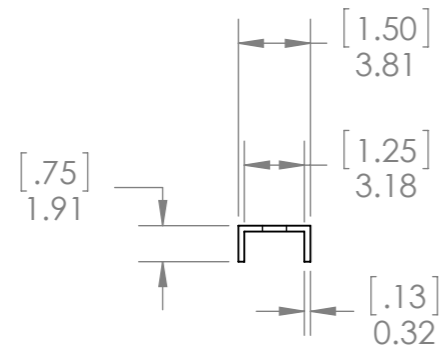
A B C D E F



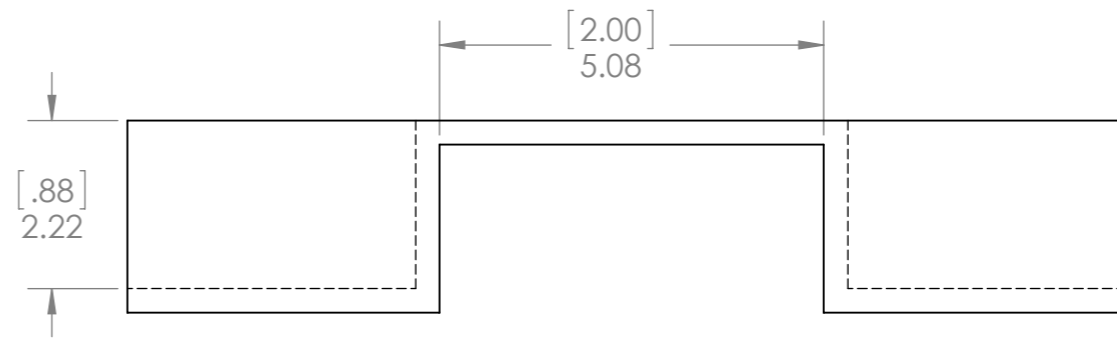
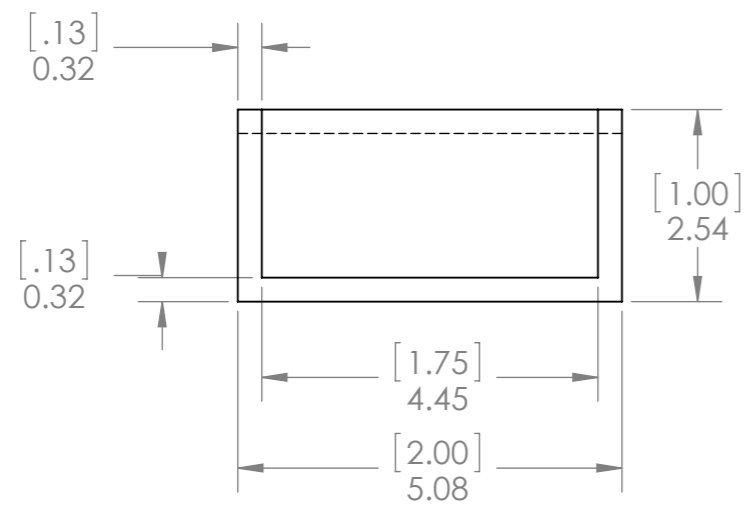
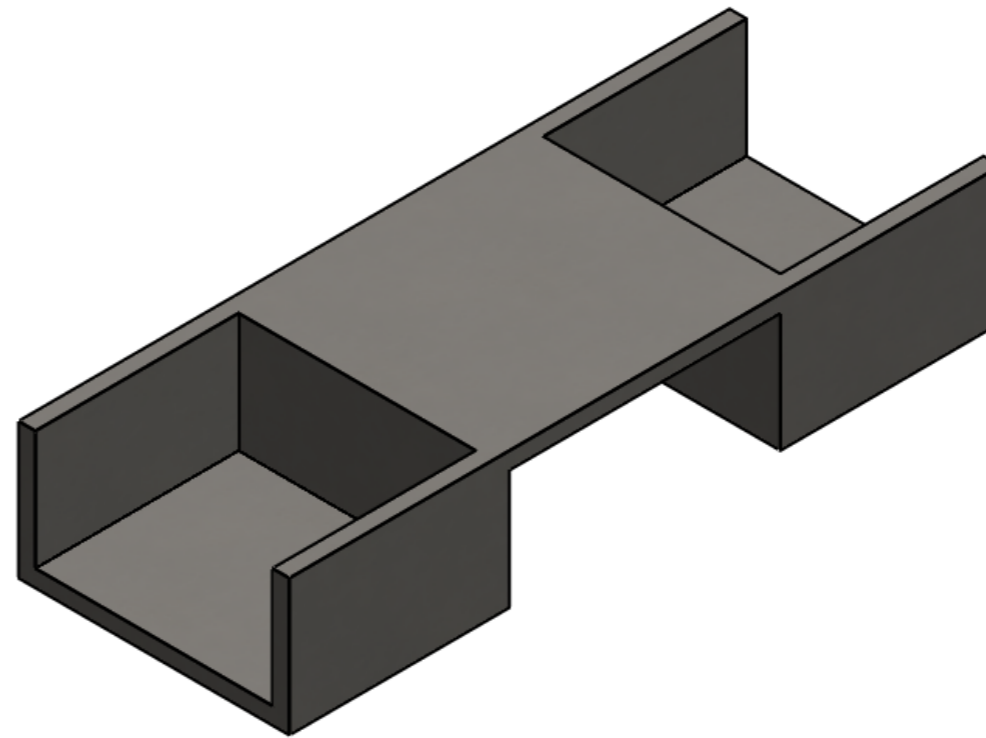
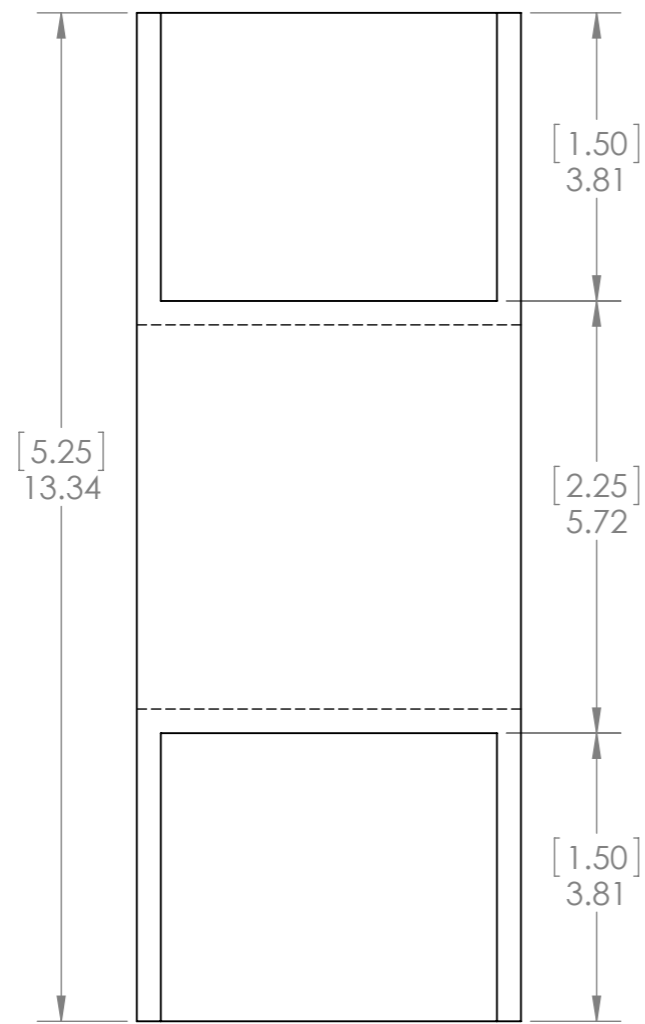
UNLESS OTHERWISE SPECIFIED: DIMENSIONS ARE IN MILLIMETERS SURFACE FINISH: TOLERANCES: LINEAR: ANGULAR:				FINISH:		DEBUR AND BREAK SHARP EDGES		DO NOT SCALE DRAWING		REVISION	
DRAWN				NAME		SIGNATURE		DATE		TITLE:	
CHK'D										U-Channel Support	
APPV'D											
MFG											
Q.A											
						MATERIAL:		DWG NO.		A3	
						WEIGHT:		SCALE:1:25		SHEET 6 OF 14	



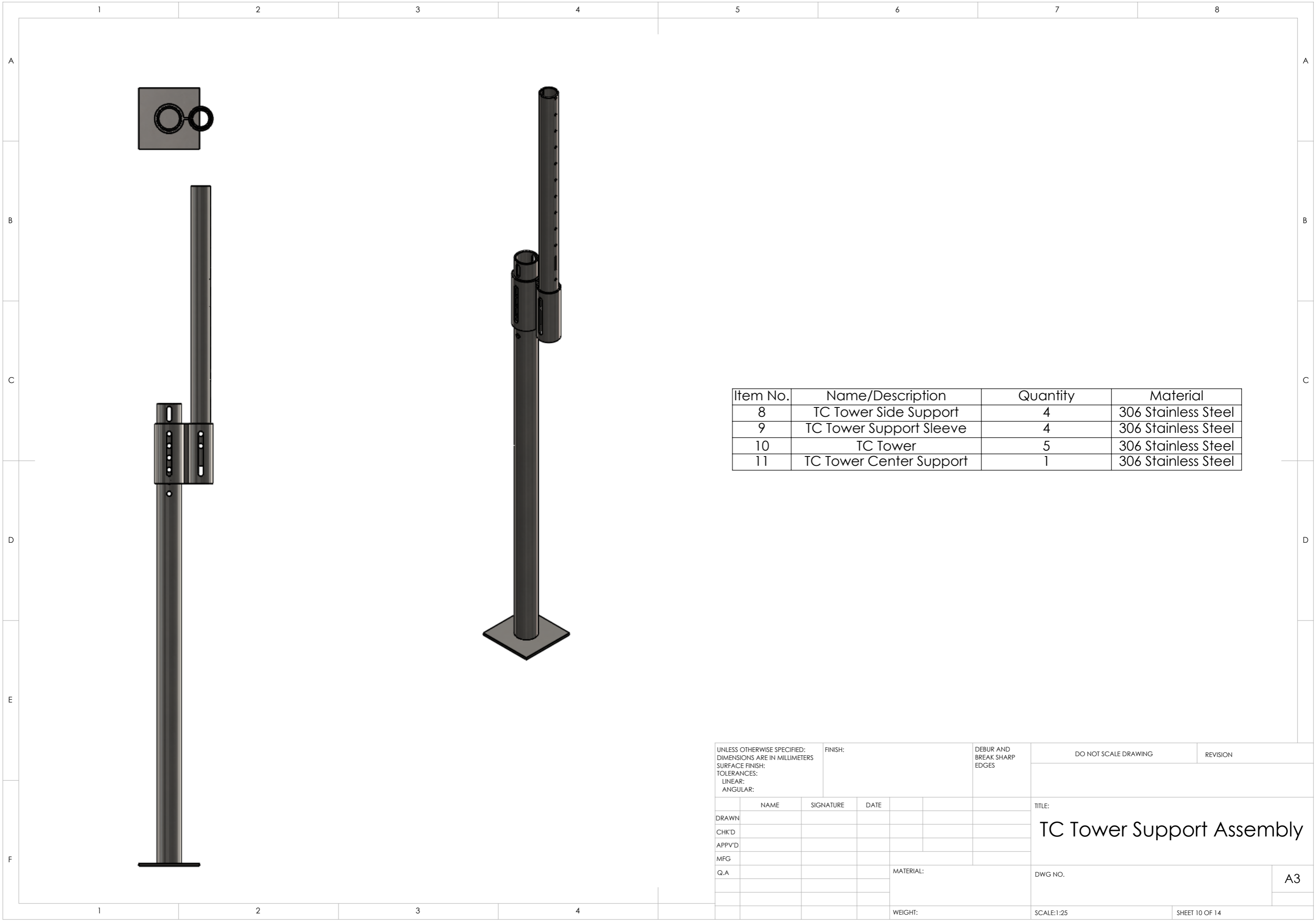
UNLESS OTHERWISE SPECIFIED: DIMENSIONS ARE IN MILLIMETERS				FINISH:		DEBUR AND BREAK SHARP EDGES		DO NOT SCALE DRAWING		REVISION	
SURFACE FINISH:											
TOLERANCES:											
LINEAR:											
ANGULAR:											
DRAWN		NAME		SIGNATURE		DATE		TITLE:		U-Channel (Long)	
CHK'D											
APPV'D											
MFG											
Q.A											
				MATERIAL:				DWG NO.		A3	
				WEIGHT:				SCALE:1:25		SHEET 7 OF 14	



UNLESS OTHERWISE SPECIFIED: DIMENSIONS ARE IN MILLIMETERS				FINISH:		DEBUR AND BREAK SHARP EDGES		DO NOT SCALE DRAWING		REVISION	
SURFACE FINISH:								<p style="text-align: center; font-size: 24px; margin: 0;">U-Channel (Short)</p>			
TOLERANCES:											
LINEAR:											
ANGULAR:											
DRAWN		NAME		SIGNATURE		DATE		TITLE:			
CHK'D											
APPV'D											
MFG											
Q.A						MATERIAL:		DWG NO.			
								A3			
						WEIGHT:		SCALE:1:25			
								SHEET 8 OF 14			

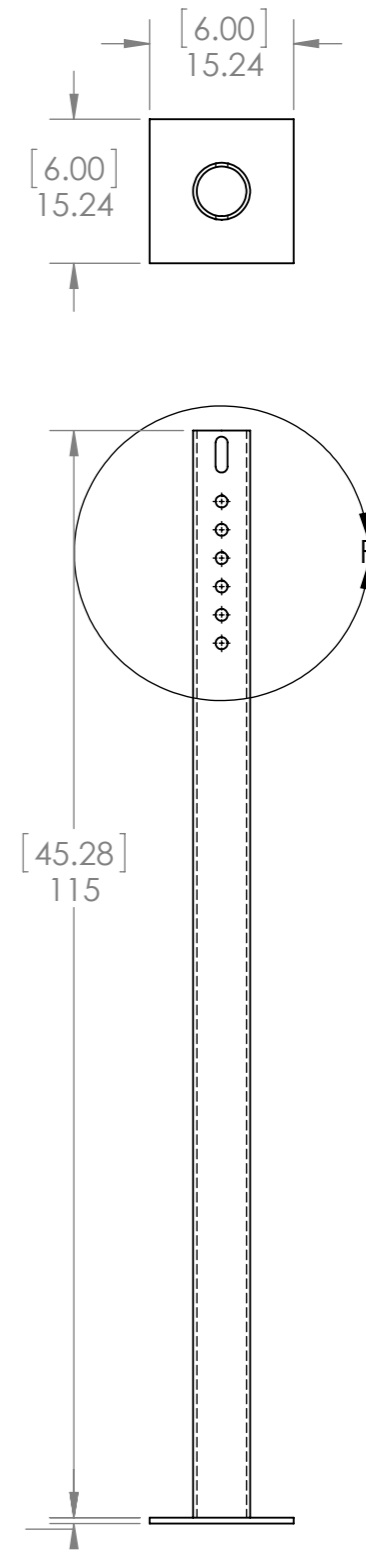
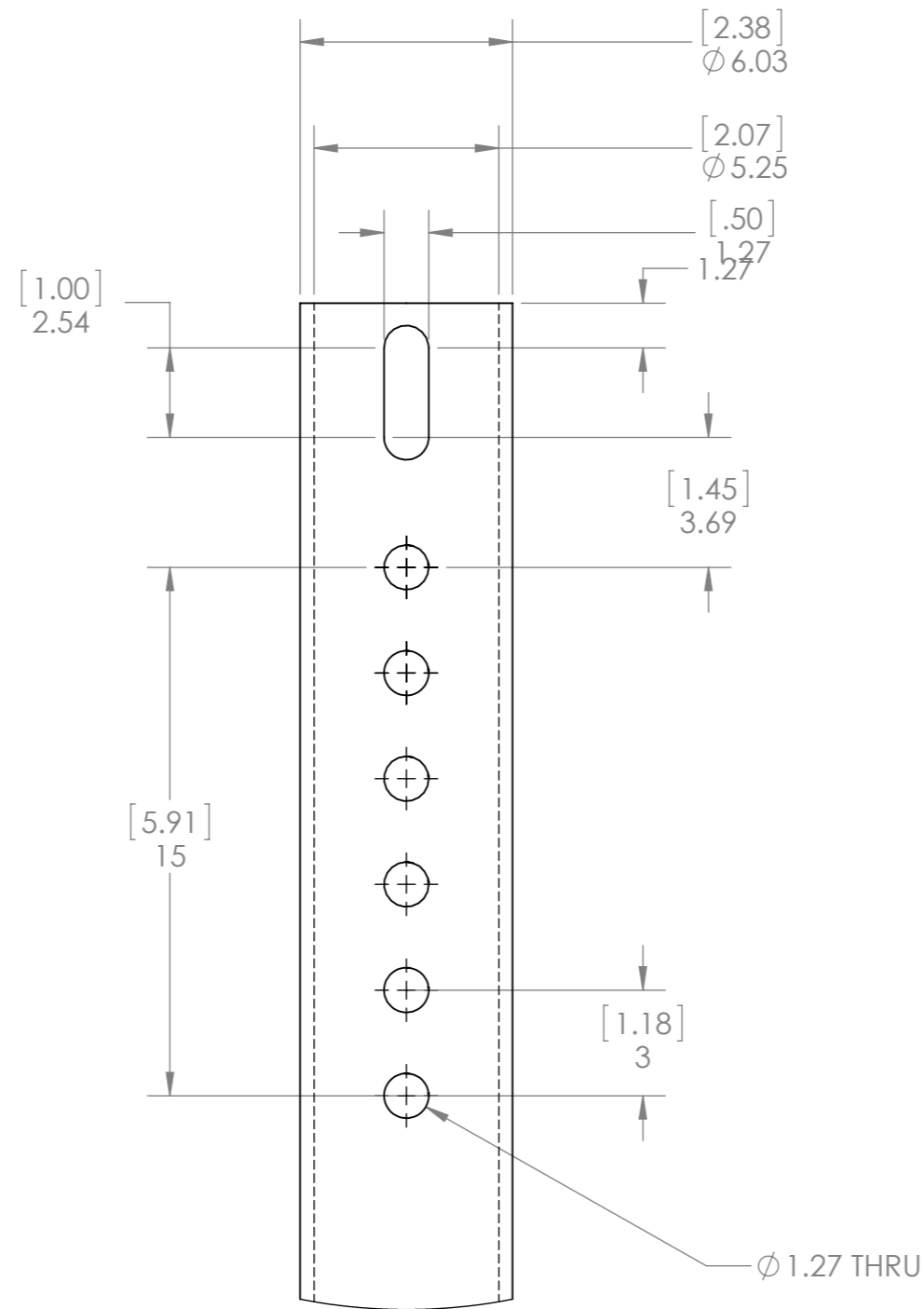
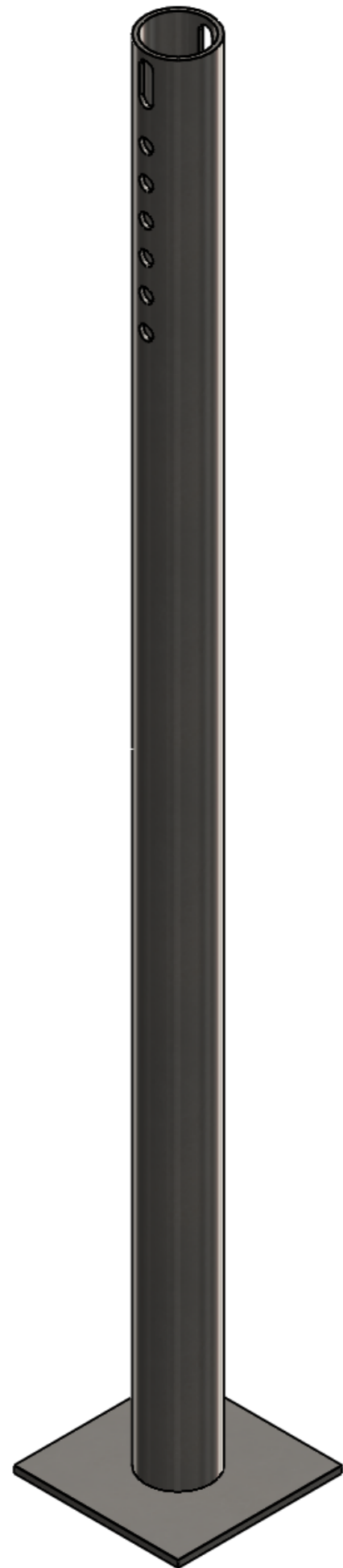


UNLESS OTHERWISE SPECIFIED: DIMENSIONS ARE IN MILLIMETERS		FINISH:		DEBUR AND BREAK SHARP EDGES		DO NOT SCALE DRAWING		REVISION	
SURFACE FINISH:									
TOLERANCES:									
LINEAR:									
ANGULAR:									
DRAWN		NAME	SIGNATURE	DATE			TITLE:		
CHK'D							U-Channel Saddle Support		
APPV'D									
MFG							DWG NO.		A3
Q.A					MATERIAL:				
							SCALE:1:25		SHEET 9 OF 14
					WEIGHT:				

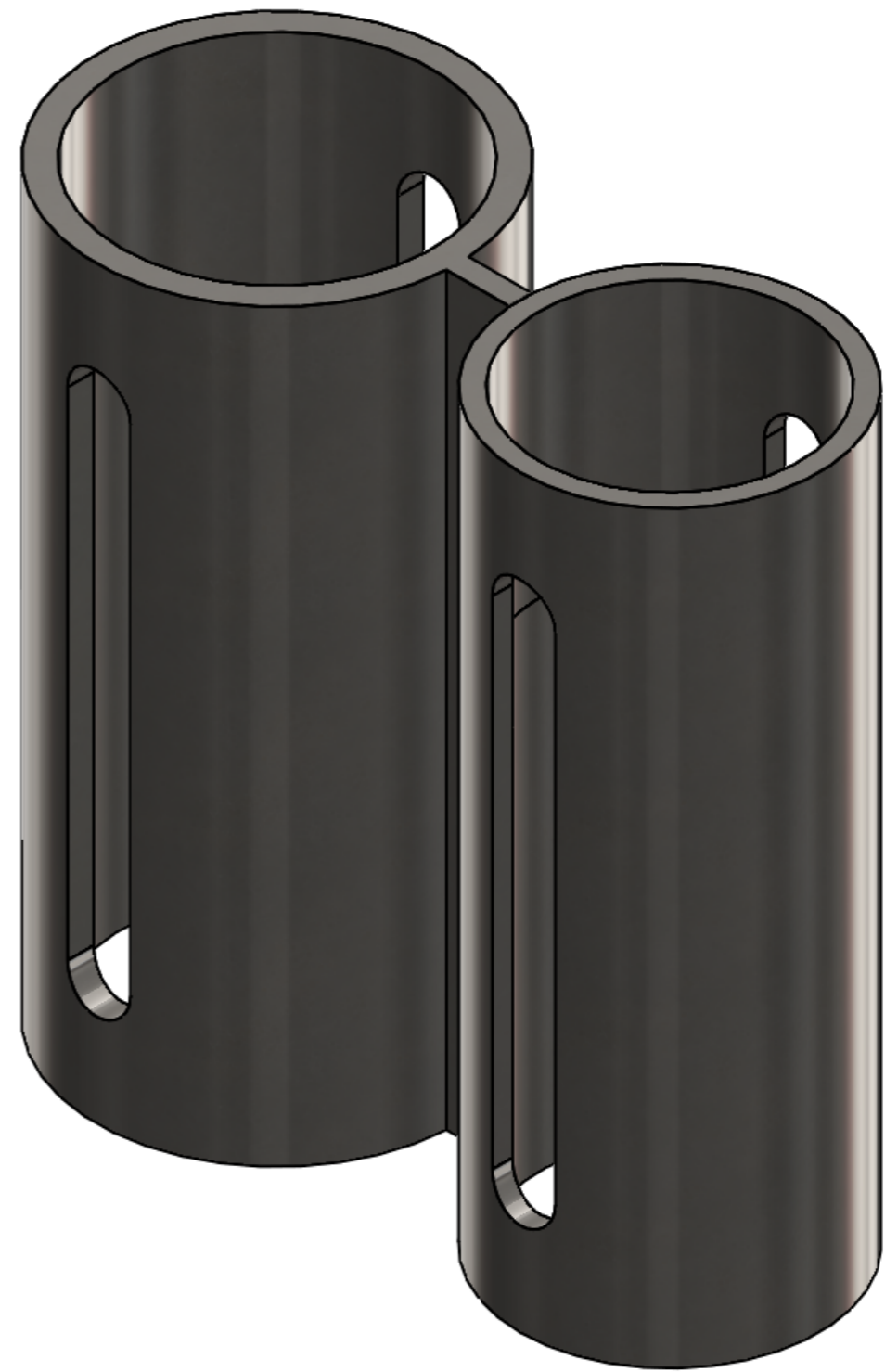
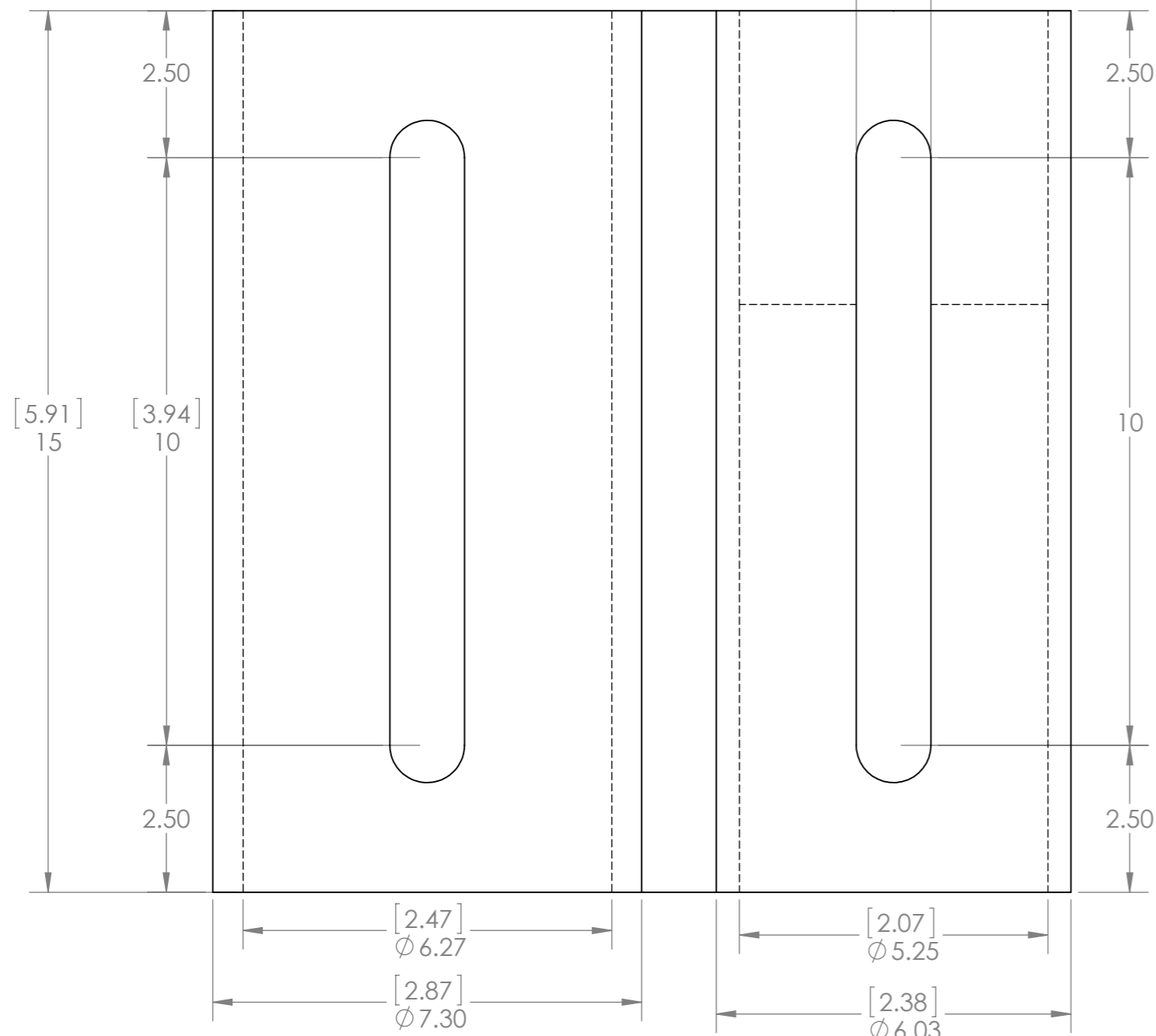
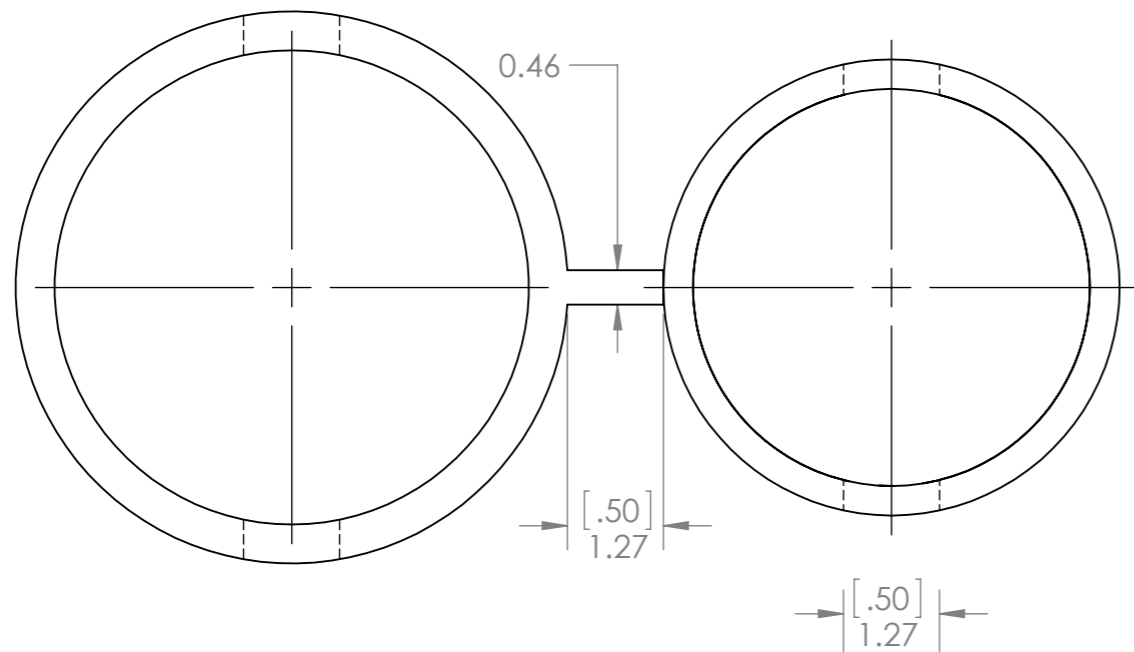


Item No.	Name/Description	Quantity	Material
8	TC Tower Side Support	4	306 Stainless Steel
9	TC Tower Support Sleeve	4	306 Stainless Steel
10	TC Tower	5	306 Stainless Steel
11	TC Tower Center Support	1	306 Stainless Steel

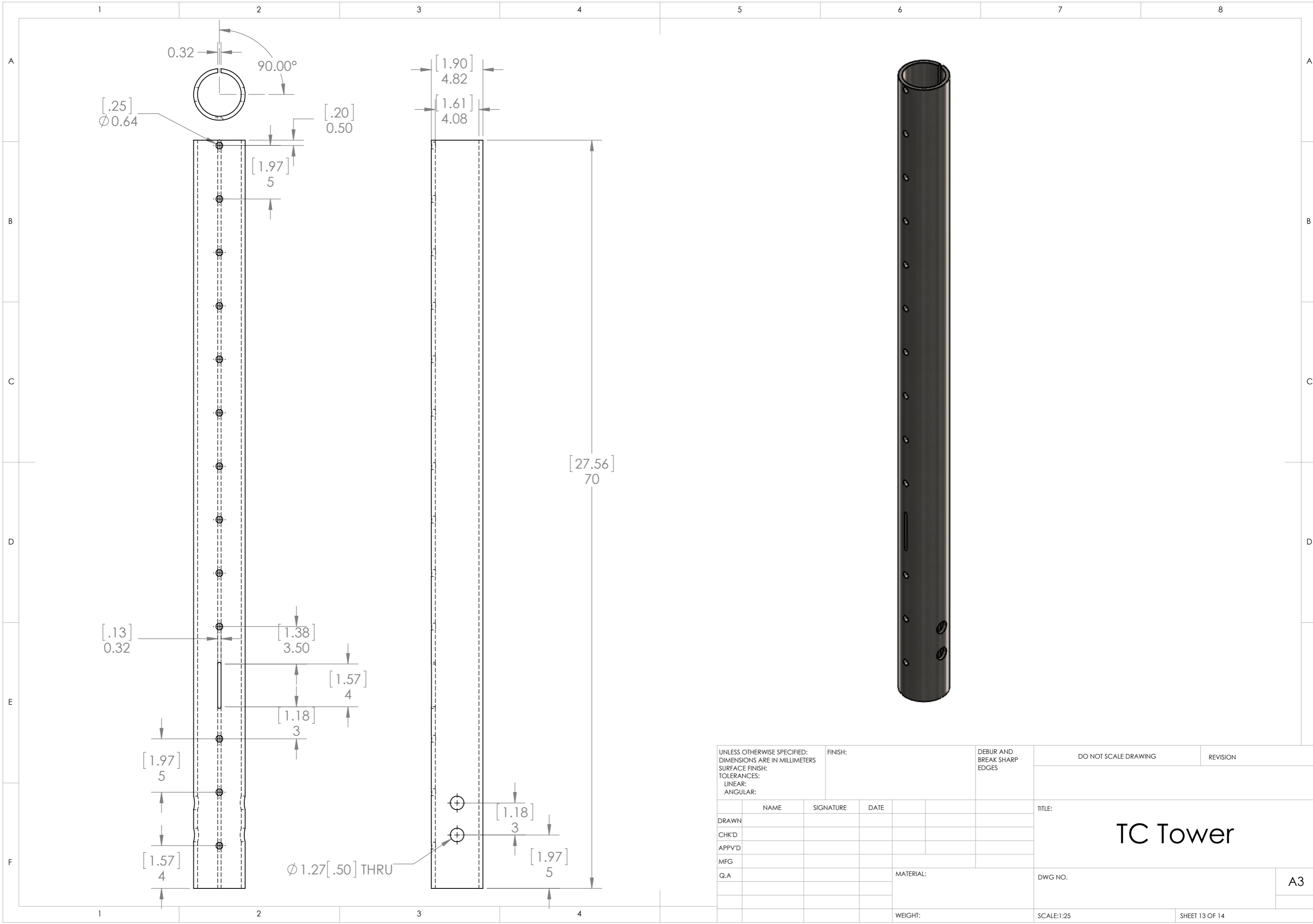
UNLESS OTHERWISE SPECIFIED: DIMENSIONS ARE IN MILLIMETERS		FINISH:		DEBUR AND BREAK SHARP EDGES		DO NOT SCALE DRAWING		REVISION	
SURFACE FINISH:									
TOLERANCES:									
LINEAR:									
ANGULAR:									
DRAWN		NAME	SIGNATURE	DATE	TITLE: TC Tower Support Assembly				
CHK'D									
APPV'D									
MFG									
Q.A					MATERIAL:		DWG NO.		A3
					WEIGHT:		SCALE:1:25		SHEET 10 OF 14



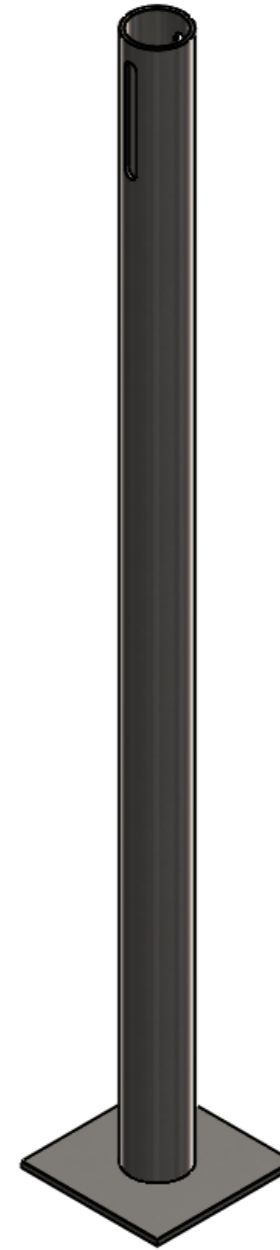
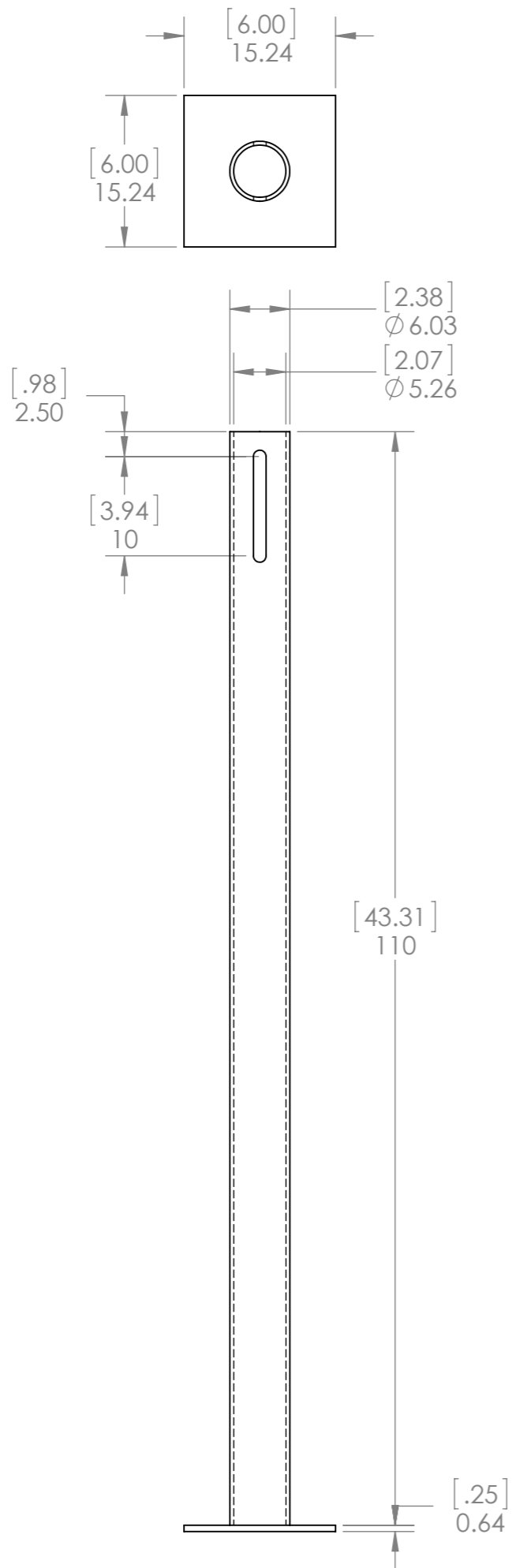
UNLESS OTHERWISE SPECIFIED: DIMENSIONS ARE IN MILLIMETERS SURFACE FINISH: TOLERANCES: LINEAR: ANGULAR:				FINISH:		DEBUR AND BREAK SHARP EDGES		DO NOT SCALE DRAWING		REVISION	
DRAWN				SIGNATURE		DATE		TITLE: TC Tower Side Support			
CHK'D											
APPV'D											
MFG											
Q.A						MATERIAL:		DWG NO.			
								A3			
						WEIGHT:		SCALE:1:25			
								SHEET 11 OF 14			



UNLESS OTHERWISE SPECIFIED: DIMENSIONS ARE IN MILLIMETERS		FINISH:		DEBUR AND BREAK SHARP EDGES		DO NOT SCALE DRAWING		REVISION	
SURFACE FINISH:									
TOLERANCES:									
LINEAR:									
ANGULAR:									
DRAWN		NAME	SIGNATURE	DATE			TITLE:		
CHK'D							TC Tower Support Sleeve		
APPV'D									
MFG									
Q.A					MATERIAL:		DWG NO.		A3
					WEIGHT:		SCALE:1:25		SHEET 12 OF 14



UNLESS OTHERWISE SPECIFIED: DIMENSIONS ARE IN MILLIMETERS SURFACE FINISH: TOLERANCES: LINEAR: ANGULAR:				FINISH:		DEBUR AND BREAK SHARP EDGES		DO NOT SCALE DRAWING		REVISION	
DRAWN				NAME		SIGNATURE		DATE		TITLE:	
CHK'D										TC Tower	
APPV'D											
MFG										DWG NO.	
Q.A								MATERIAL:		A3	
								WEIGHT:		SCALE:1:25	
										SHEET 13 OF 14	



UNLESS OTHERWISE SPECIFIED: DIMENSIONS ARE IN MILLIMETERS				FINISH:		DEBUR AND BREAK SHARP EDGES		DO NOT SCALE DRAWING		REVISION	
SURFACE FINISH:											
TOLERANCES:											
LINEAR:											
ANGULAR:											
DRAWN		NAME		SIGNATURE		DATE		TITLE:		TC Tower Center Support	
CHK'D											
APPV'D											
MFG											
Q.A						MATERIAL:		DWG NO.		A3	
						WEIGHT:		SCALE:1:25		SHEET 14 OF 14	

Appendix E – Outdoor gas emission sampling system (OGES)

The Outdoor Gas Emission Sampling System (OGES) was used to sample and analyze the gas concentrations of O₂, CO₂, and CO (Fig. E-1). The details of the OGES system can be found in Tukaew (Oat) Panywat’s master thesis published in 5/2/17. [E1]

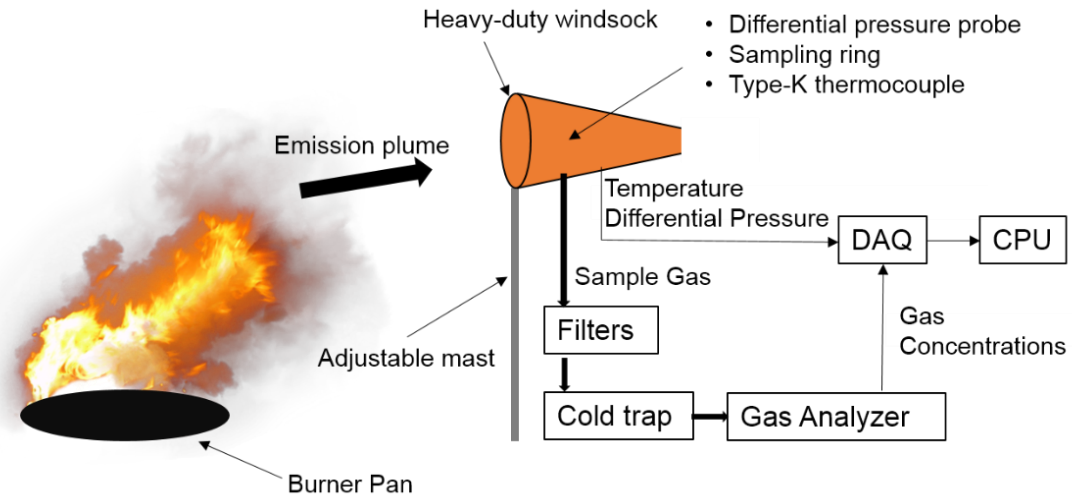


Figure E-1: The Outdoor Gas Emission Sampling System (OGES)

It is anticipated that in conditions where wind is present, the plume will rise upward at an angle in the same direction as the wind. Therefore, a gas emission sampling system placed directly above flame was not be as effective as it would normally be in a laboratory environment. A new solution, shown in Fig. E-1 was designed in order to sample the emission plume when it is traveling in a near-horizontal direction. The solution consists of a heavy-duty windsock mounted on a rigid frame. This allows the emission plume to travel through the windsock and prevent potential build-up inside that could affect the gas sampling data.

A differential pressure probe and a Type-K thermocouple were placed inside the rigid frame and provided data to calculate the mass flow rate through the OGES (Fig. E-2). A stainless steel gas sampling ring was also placed inside of the rigid frame to collect sample gas as it flows through the OGES (Fig. 6b). The sampling ring was connect to a system of filters and thermoelectric cold trap before reaching the Servomex 4200 Industrial Gas Analyzer. (Fig. E-1.) All the instrumentation were connected to the National Instrument PXI System for data acquisition.

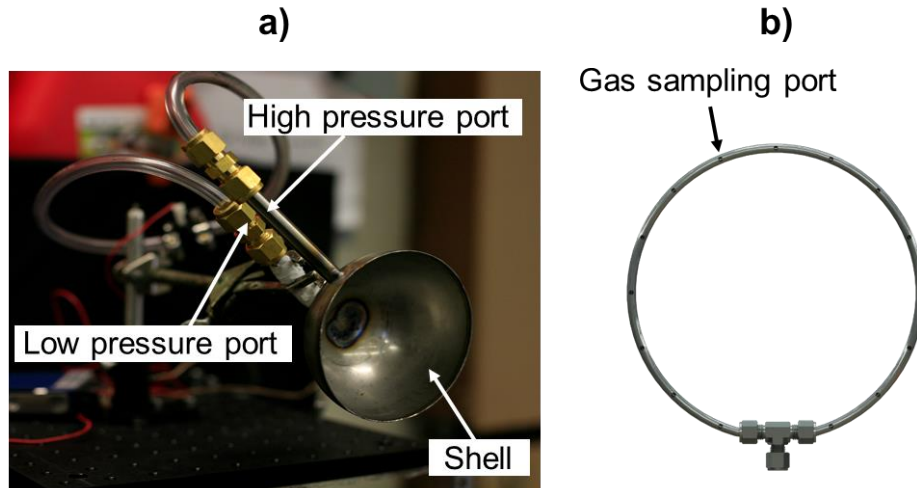


Figure E-2: a) Differential pressure probe b) Gas sampling port

The 7 m tower structure acted as the main support and track for the wheel assembly system. The wheel assembly system, which connected to the rigid frame and adjusted to the appropriate height via a pulley system (Fig. E-3).

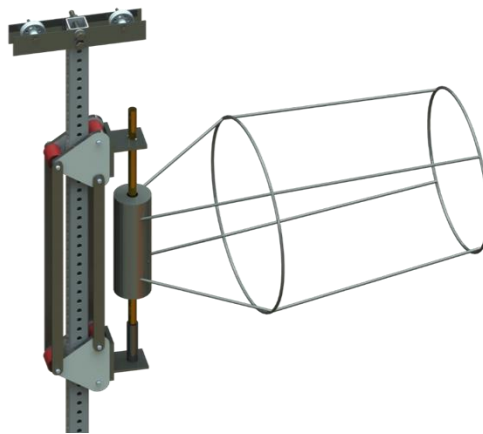


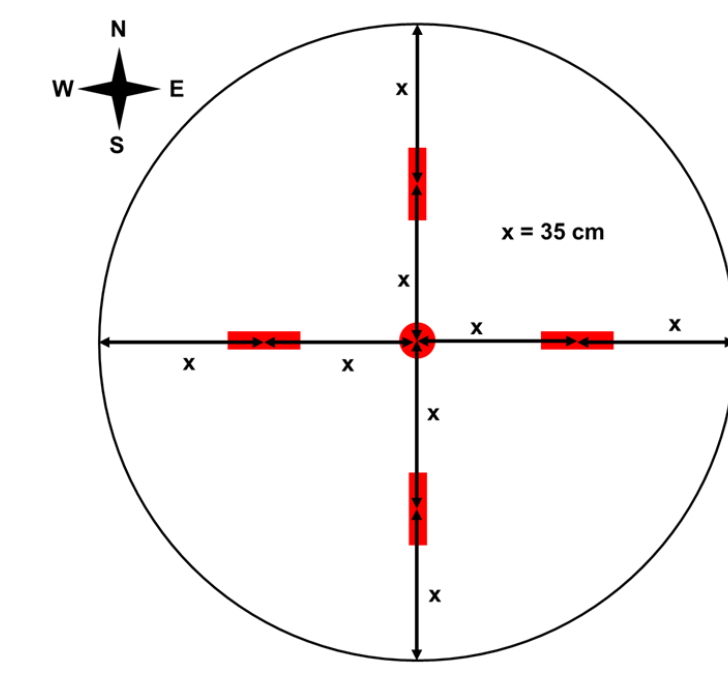
Figure E-3: The pulley system to adjust the height of OGES

Appendix F – Detailed gas-fuel-water temperatures

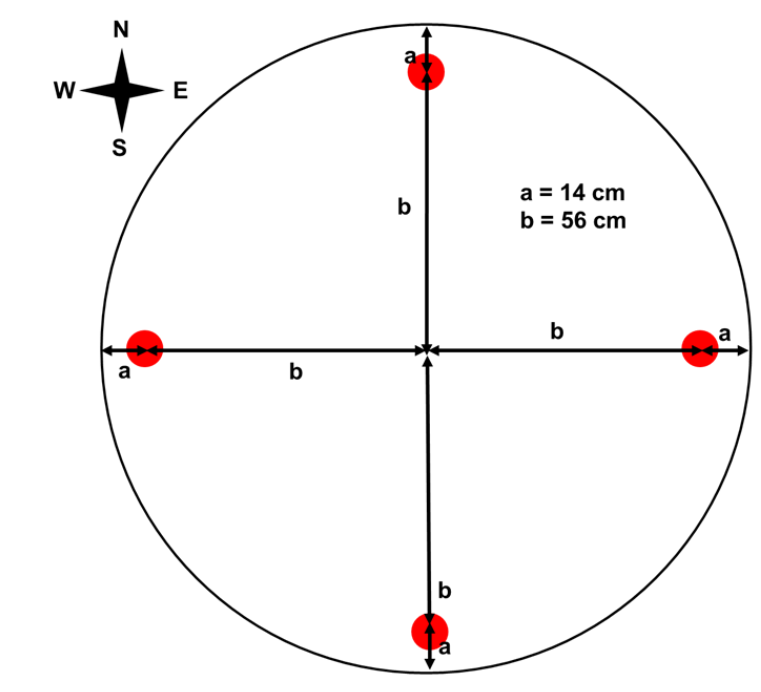
Baseline

Average wind speed : 8.12 mph, W-E direction

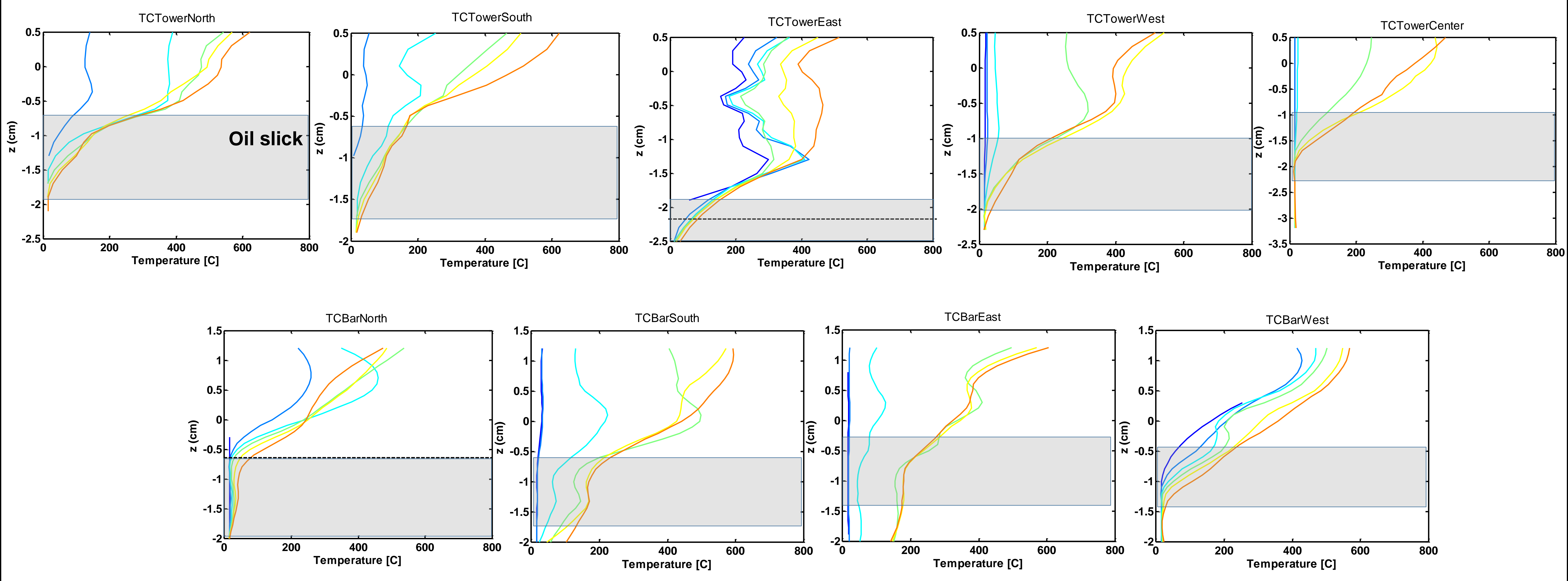
TC BARS



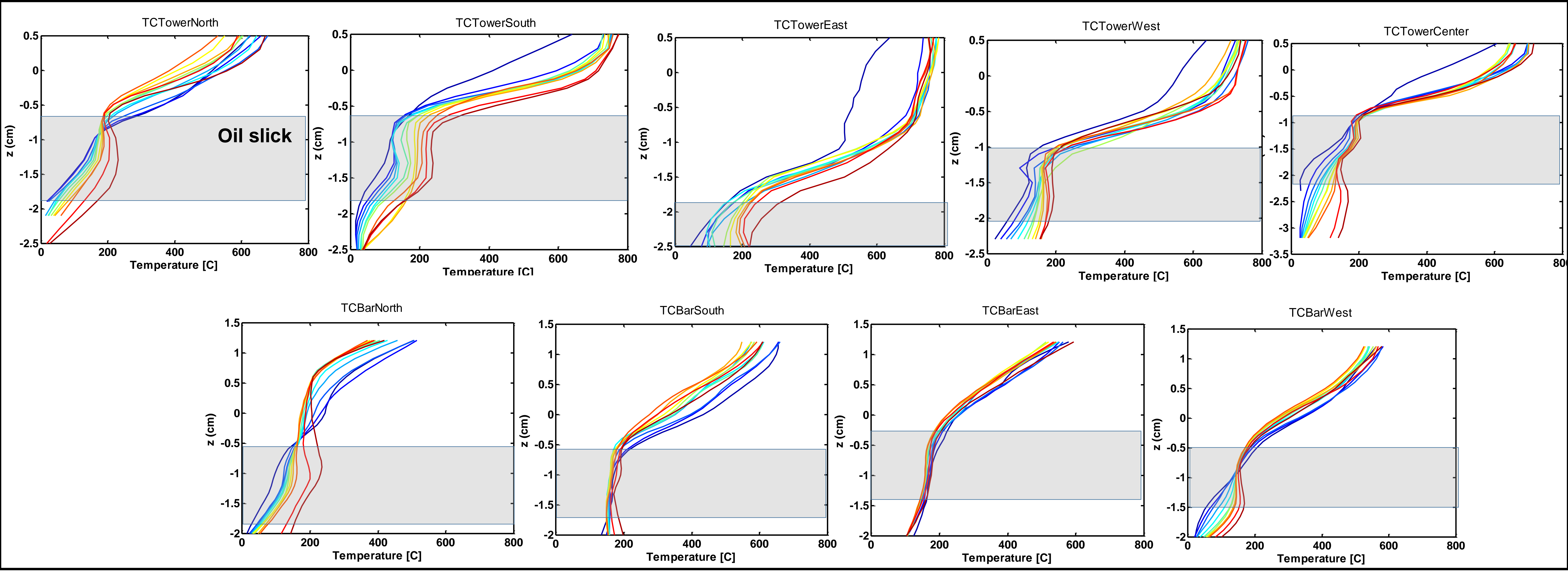
TC TOWERS



Transition
 $t = 10 - 60$ s, $\Delta t = 10$ s



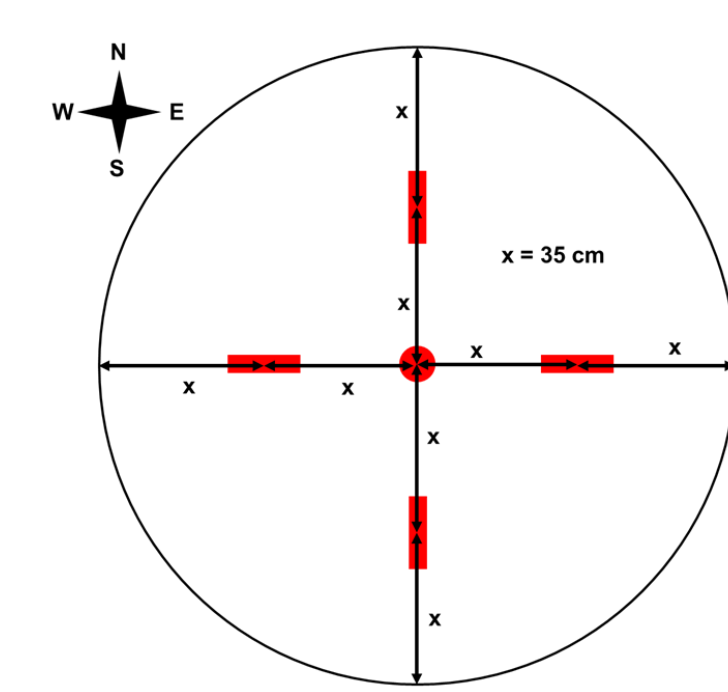
Steady State
 $t = 60 - 800$ s, $\Delta t = 60$ s



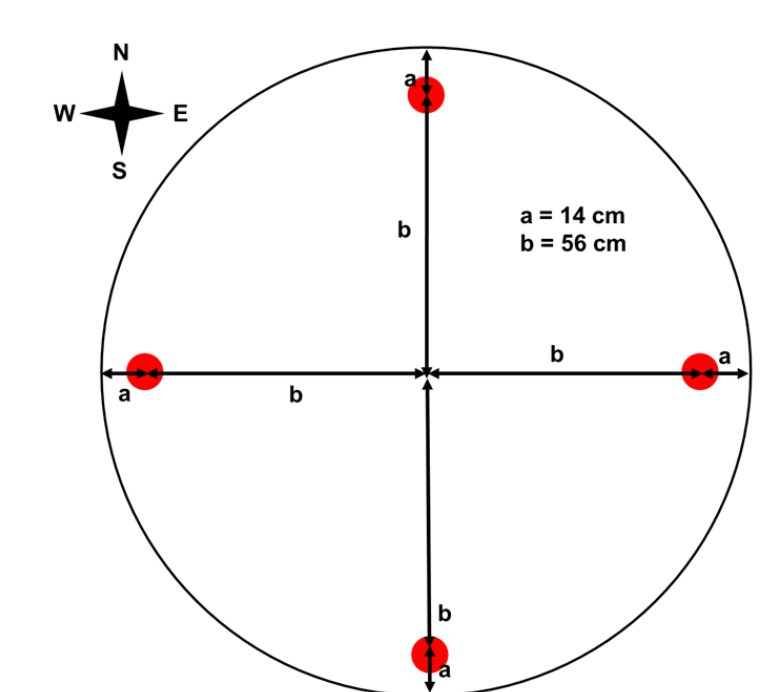
Baseline

Average wind speed : 8.12 mph, W-E direction

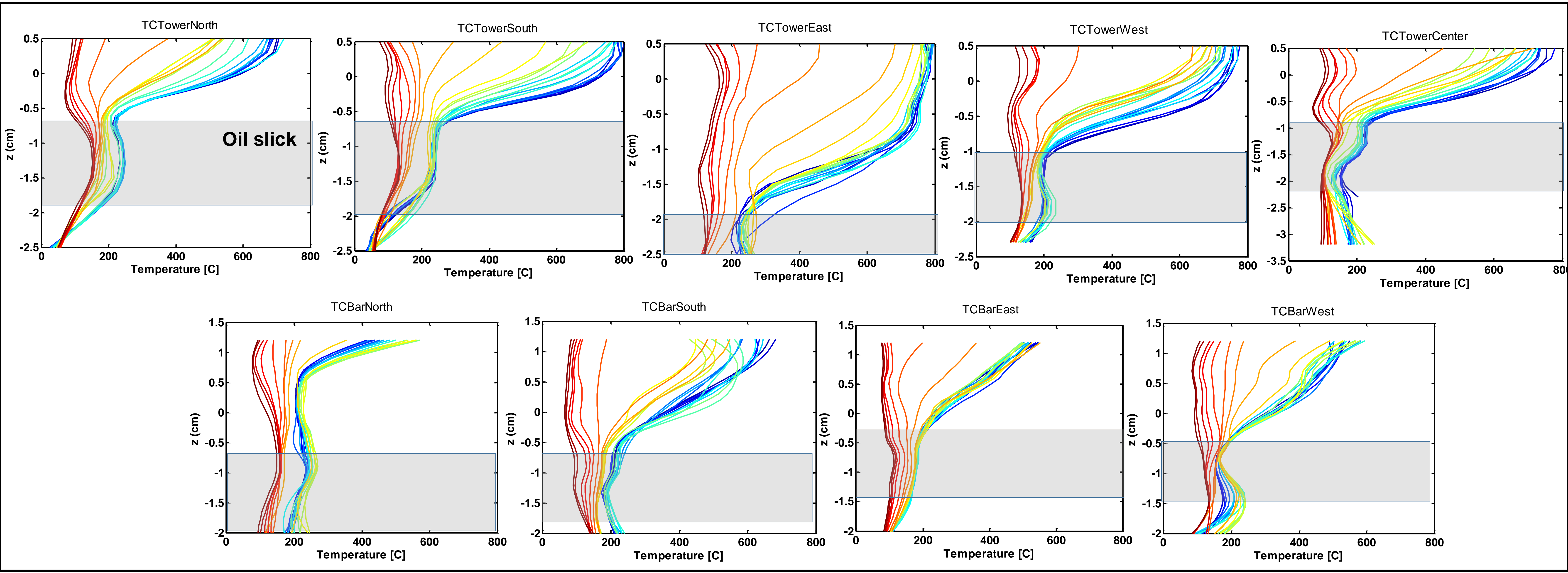
TC BARS



TC TOWERS



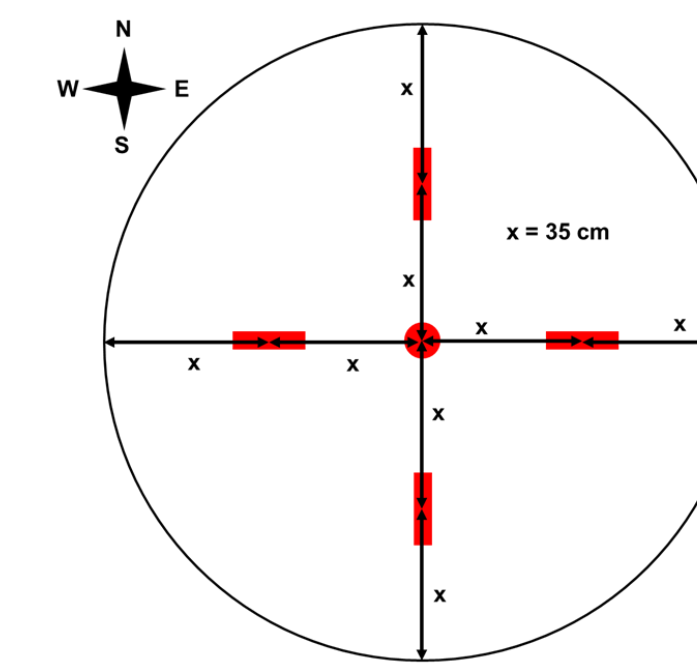
Extinction
 $t = 800 - 1040\text{s}, \Delta t = 60 \text{ s}$



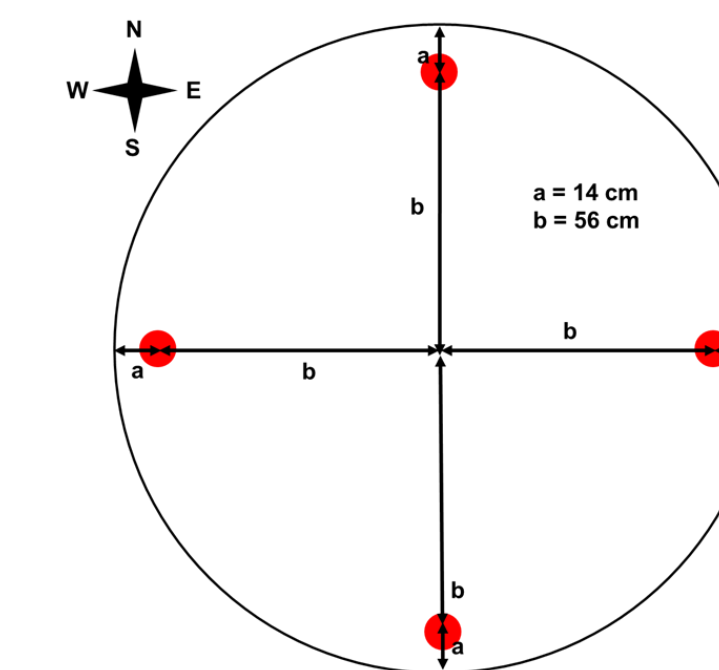
Blanket

Average wind speed : 7.65 mph, N-S direction

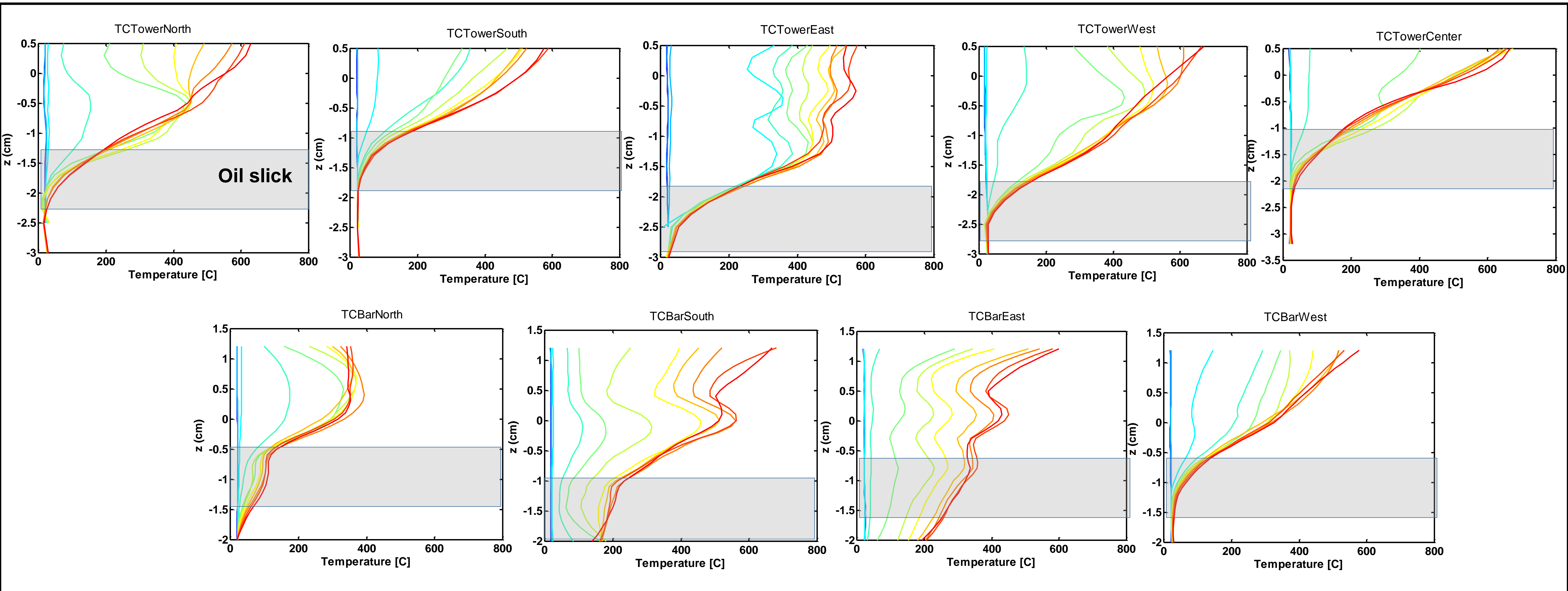
TC BARS



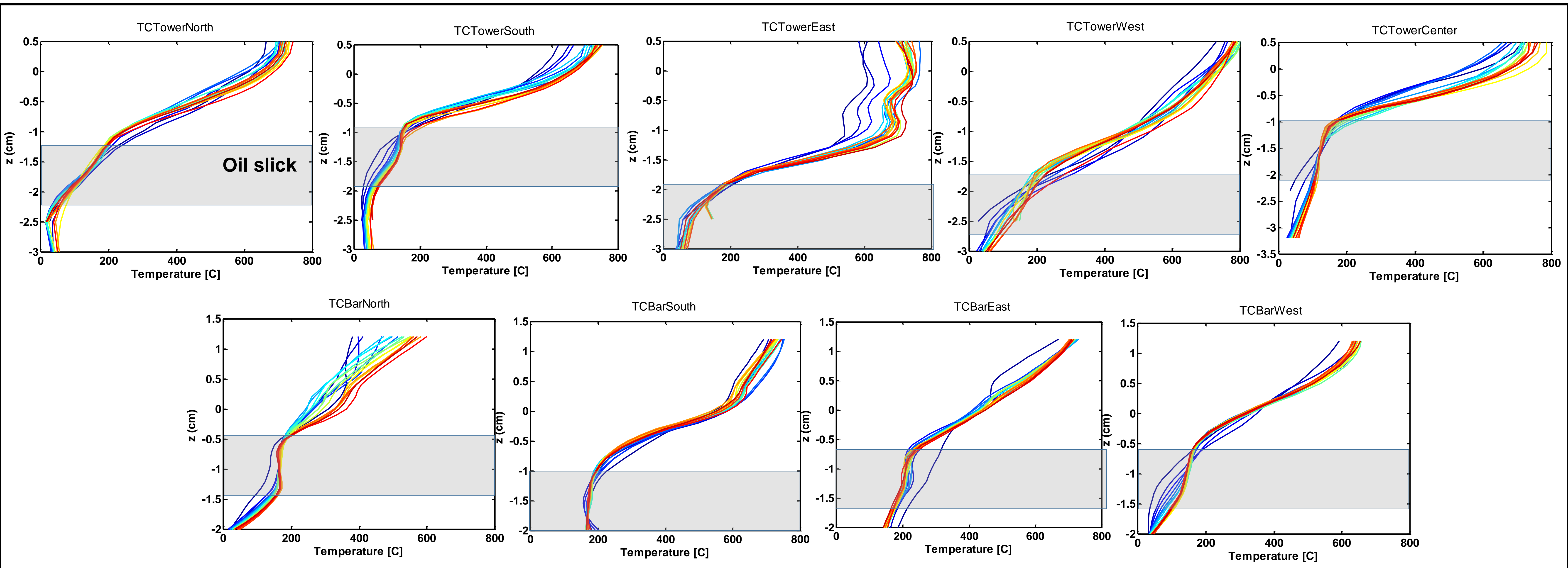
TC TOWERS



Transition
 $t = 10 - 140 \text{ s}, \Delta t = 10 \text{ s}$



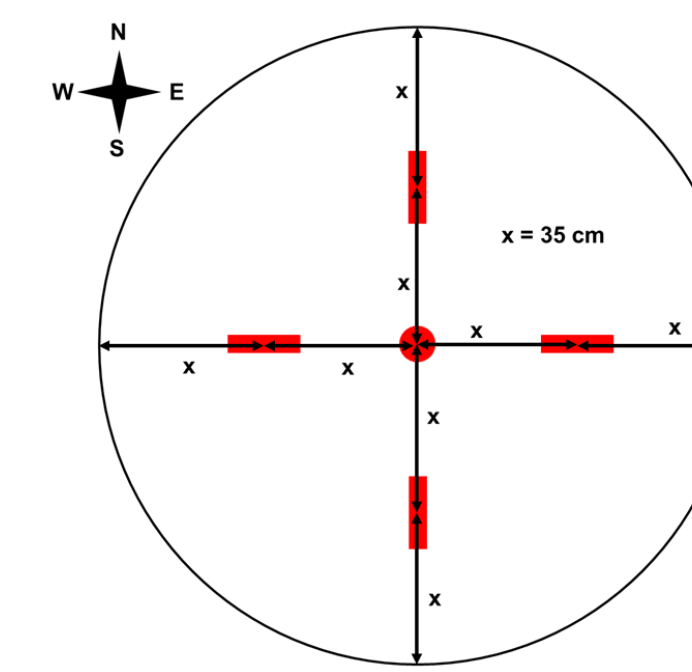
Steady State
 $t = 140 - 1260 \text{ s}, \Delta t = 60 \text{ s}$



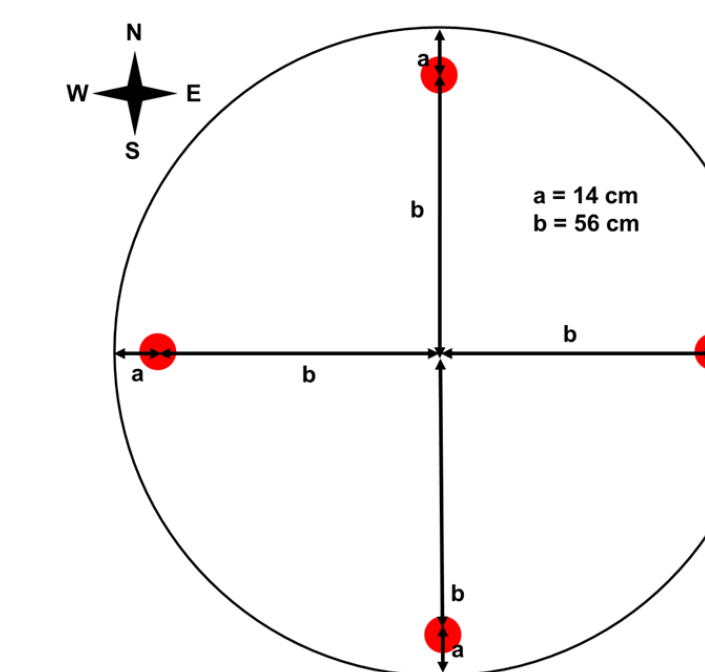
Blanket

Average wind speed : 7.65 mph, N-S direction

TC BARS

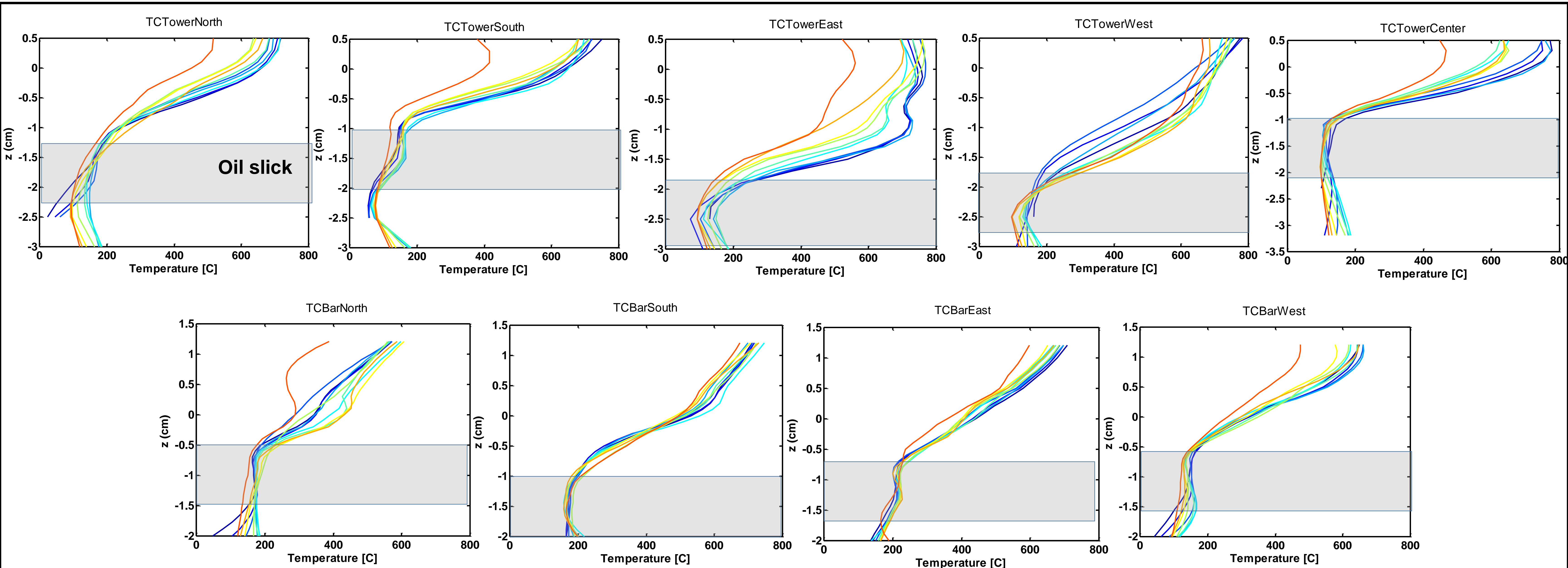


TC TOWERS



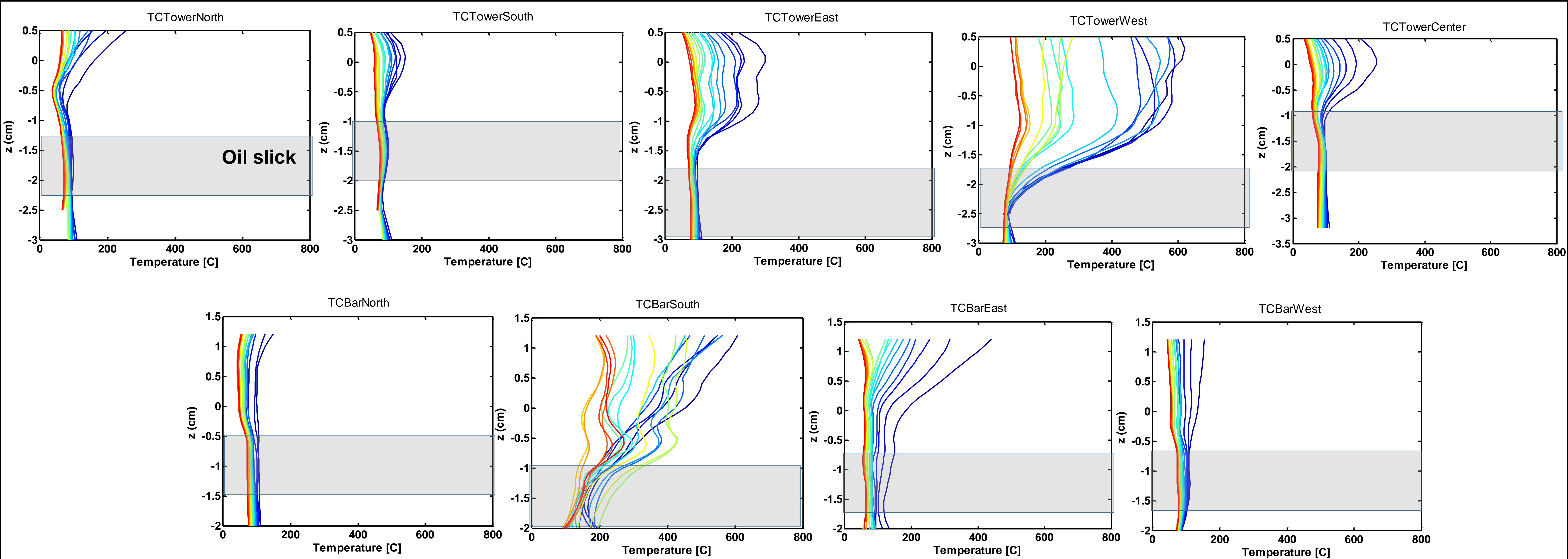
Burning Without Oil Supply

$t = 1260 - 1860 \text{ s}, \Delta t = 60 \text{ s}$



Extinction

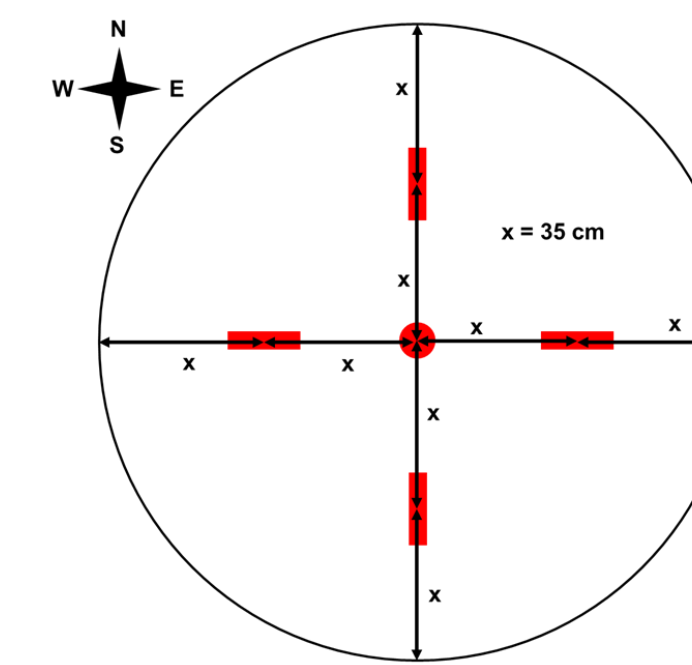
$t = 1860 - 2040 \text{ s}, \Delta t = 10 \text{ s}$



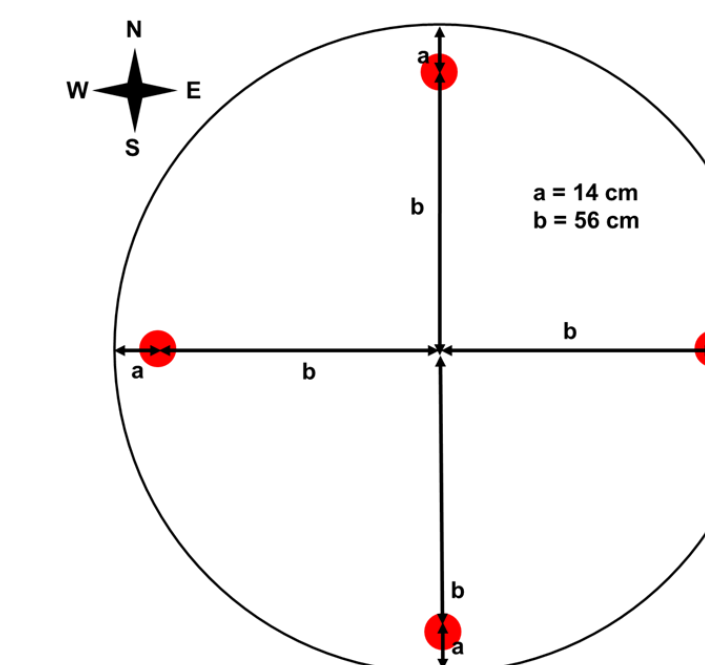
Blanket + 48 Coils

Average wind speed : 9.14 mph, NW-SE direction

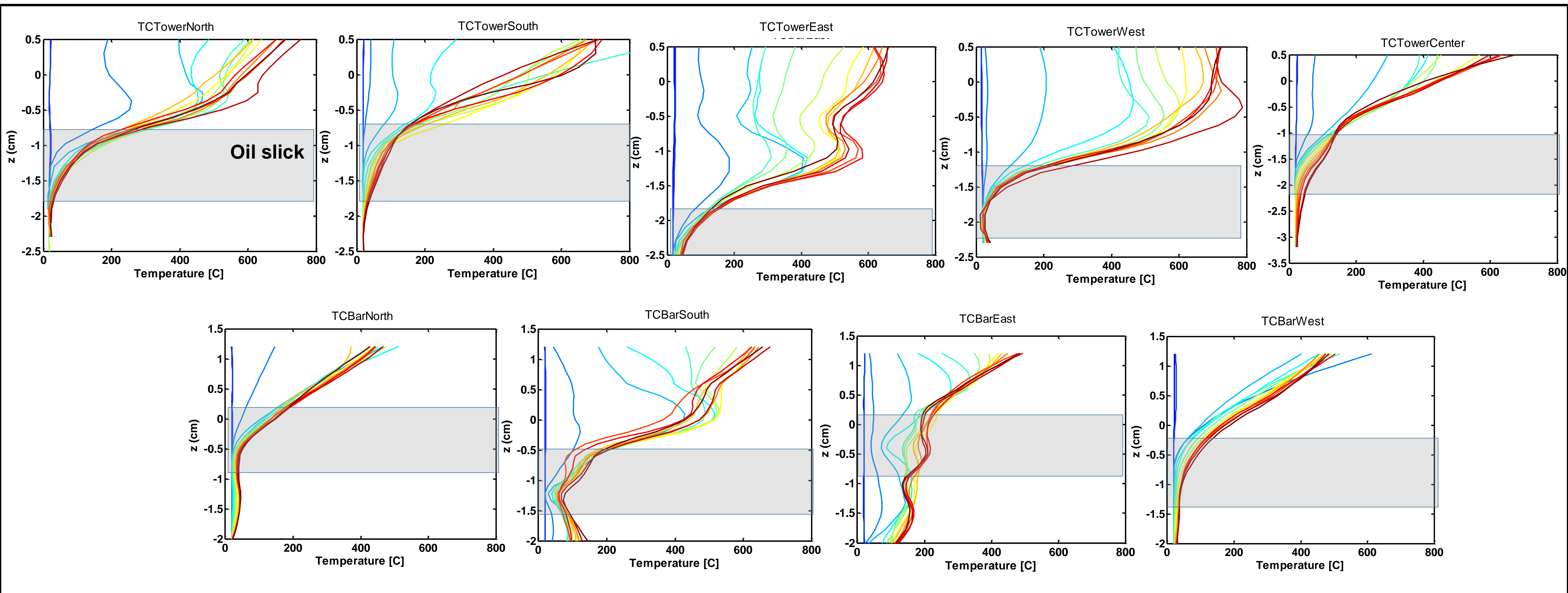
TC BARS



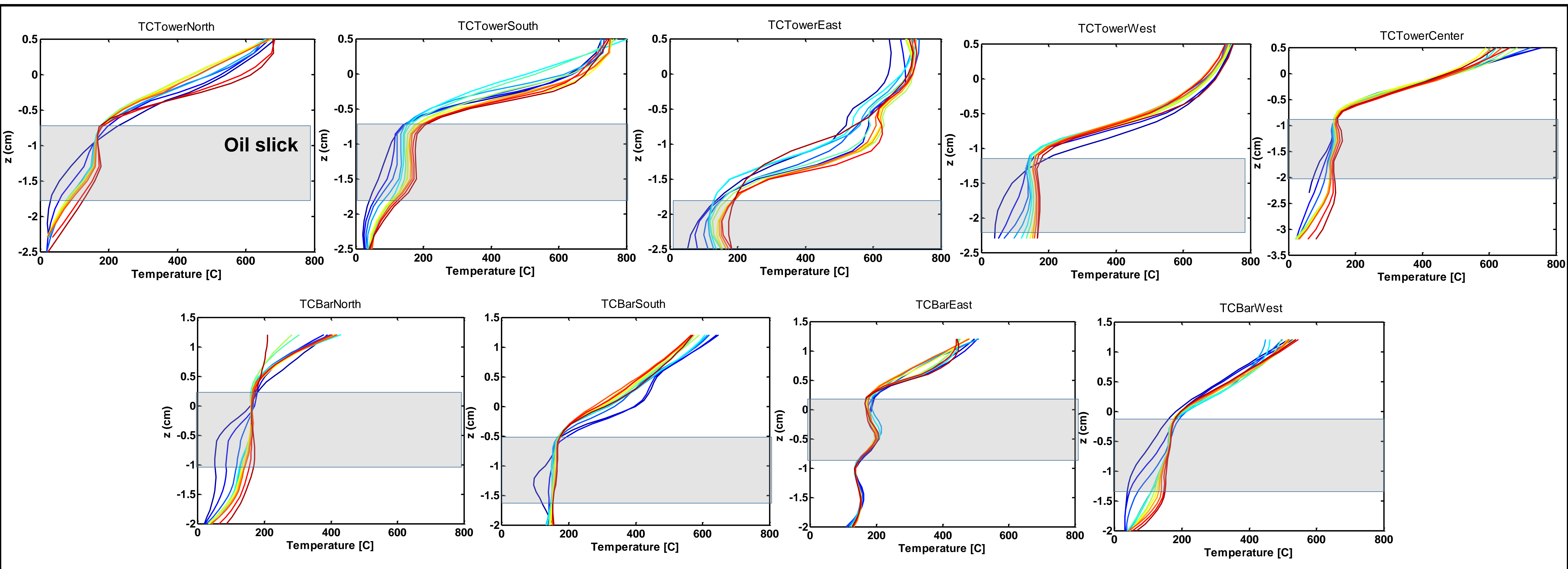
TC TOWERS



Transition
 $t = 10 - 160 \text{ s}, \Delta t = 10 \text{ s}$



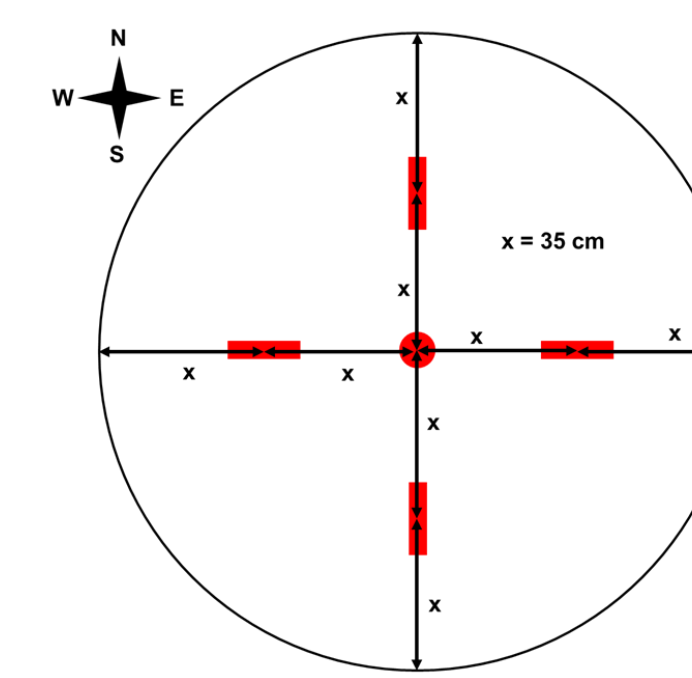
Steady State
 $t = 160 - 840 \text{ s}, \Delta t = 60 \text{ s}$



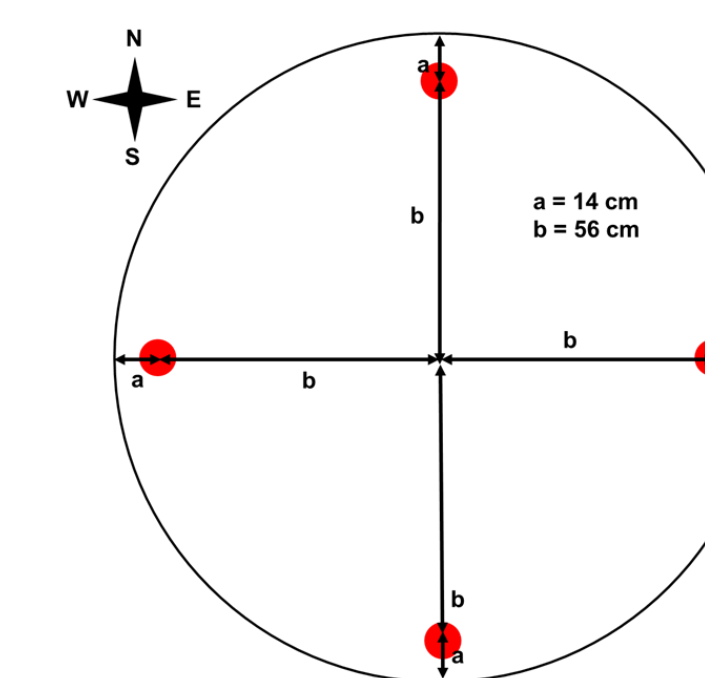
Blanket + 48 Coils

Average wind speed : 9.14 mph, NW-SE direction

TC BARS

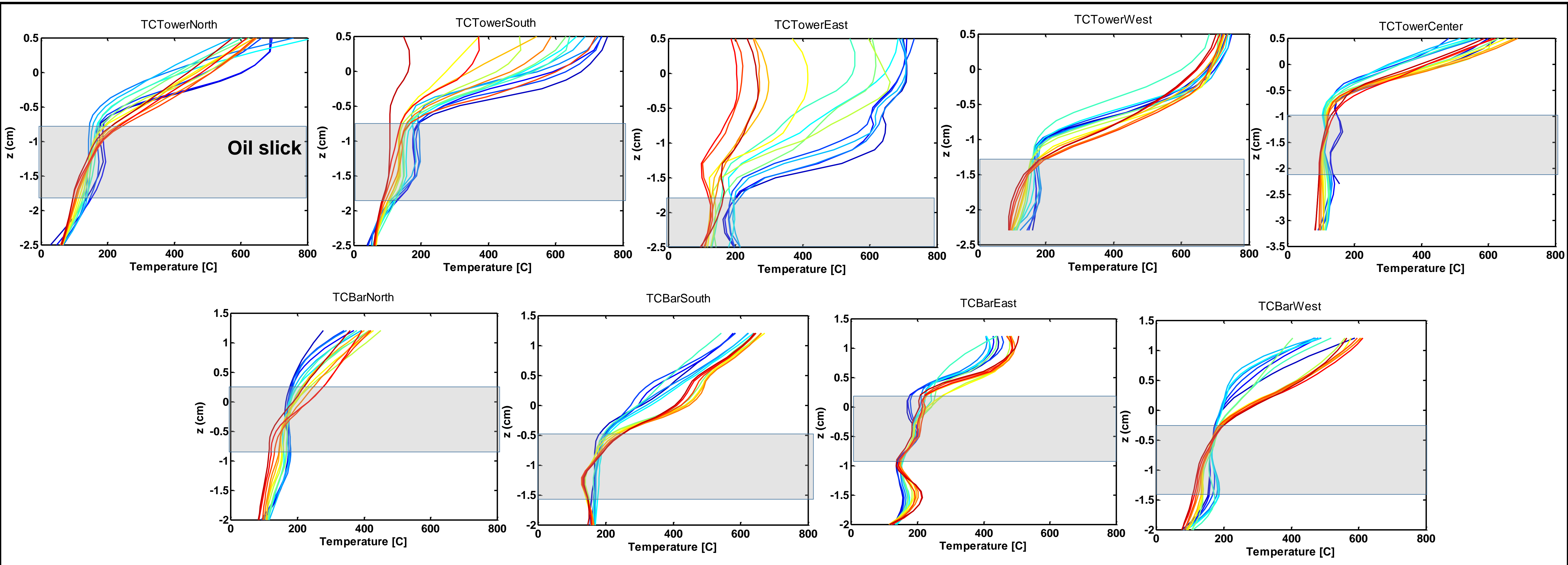


TC TOWERS



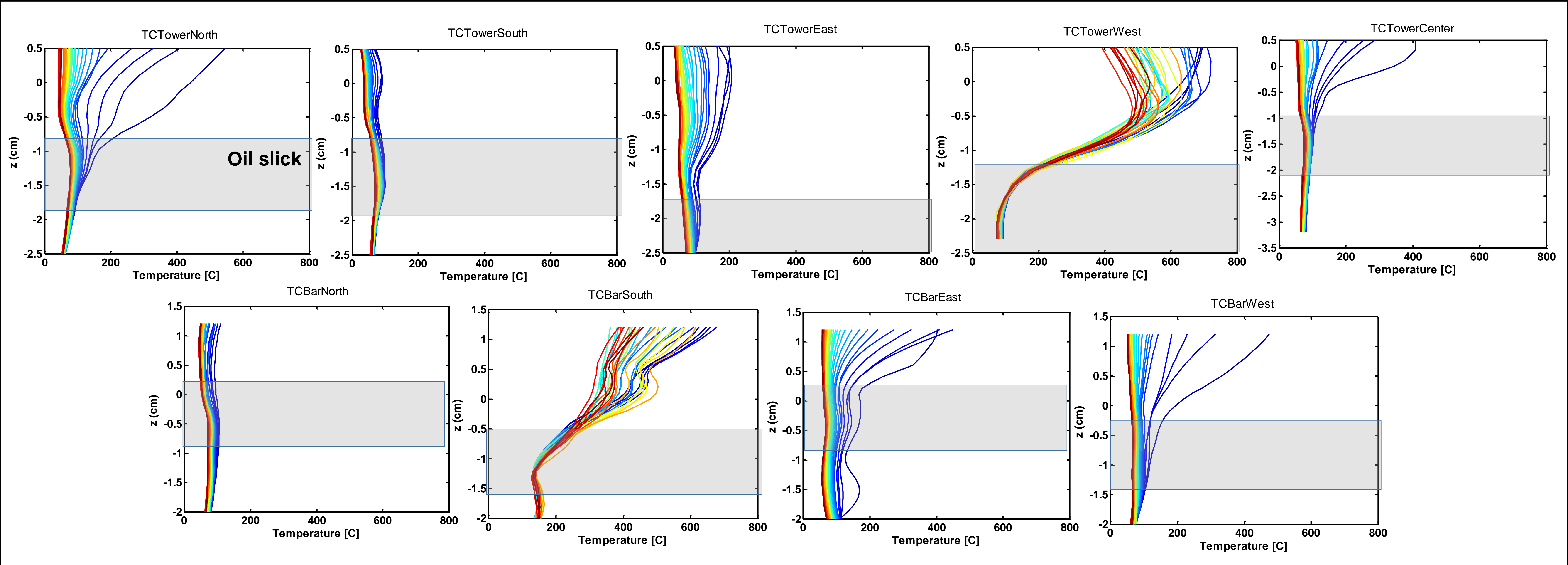
Burning Without Oil Supply

$t = 1240 - 1740 \text{ s}, \Delta t = 60 \text{ s}$



Extinction

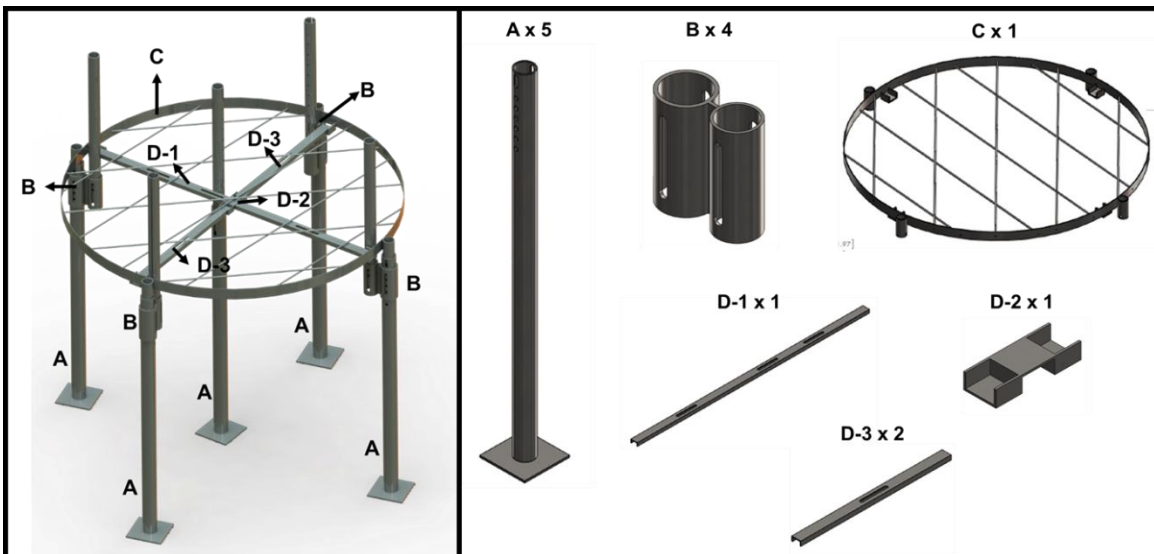
$t = 1740 - 2060 \text{ s}, \Delta t = 10 \text{ s}$



Appendix G – Checklist of Phase III assembly and instrumentation

1- Burner assembly procedure:

- 1) Place five legs. (A) - 3/6
- 2) Insert the TC support sleeves. (B) - 3/6
- 3) Place the oil contamination ring. (C) - 3/6
- 4) Place TC holding bars. - 3/6
 - a. 140 cm long bar (D-1)
 - b. Place connection at center (D-2)
 - c. Place two 70 cm long bars (D-3)

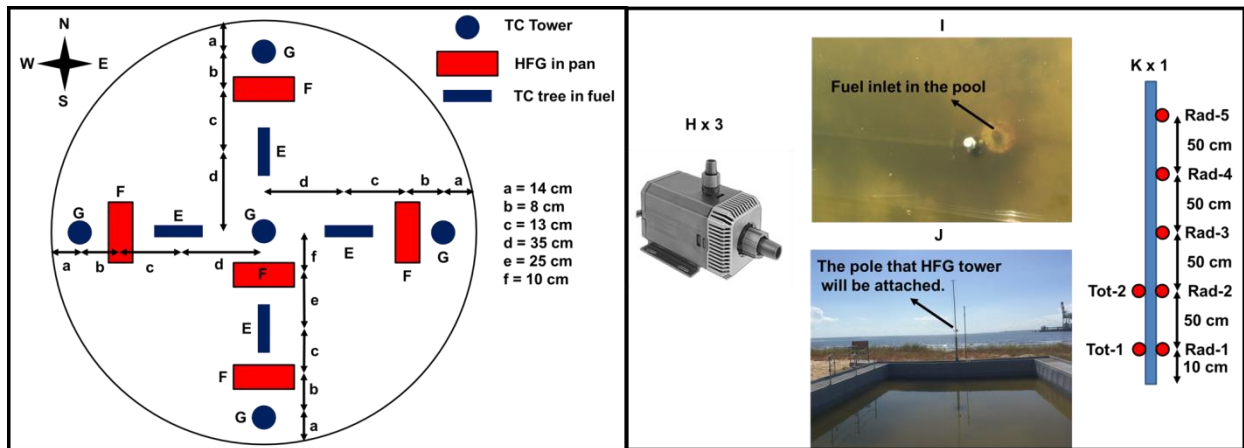


- 5) Connect fuel distribution pipes to the main pipe system in the pool. (I) - 3/6

2- Instrumentation (TC and HFGs):

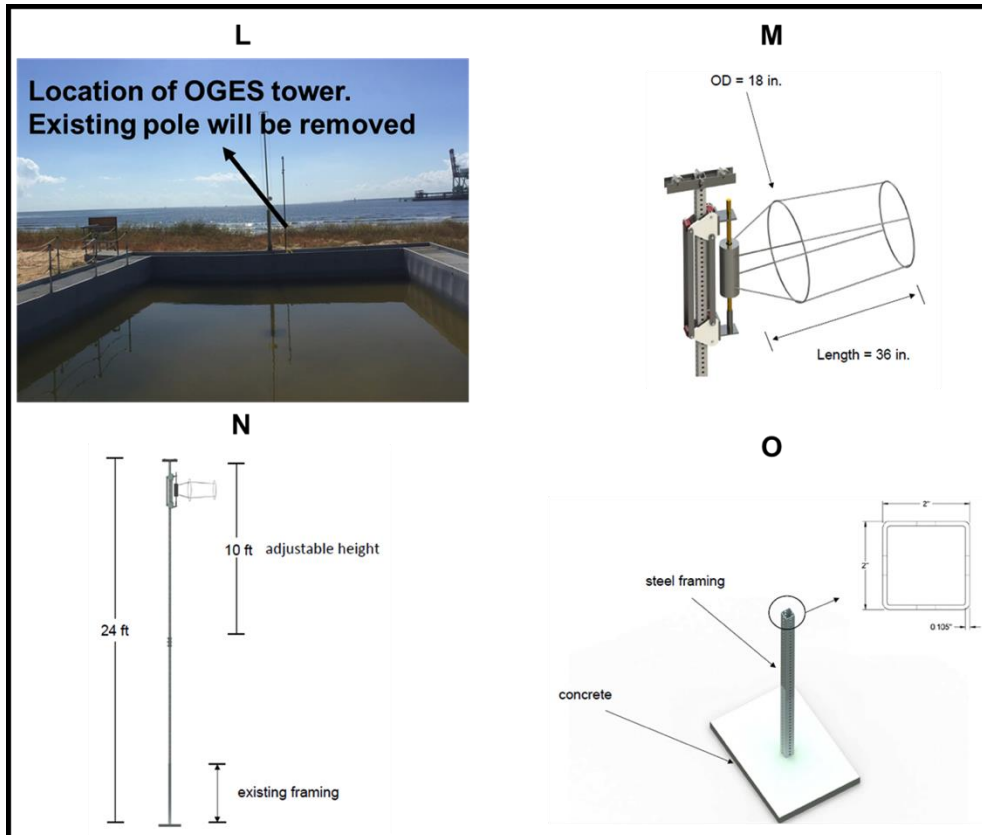
- 6) Assemble the computer in control shed. - 3/6
- 7) Assemble and install PXI housing/shelter - 3/6
- 8) Place HFG into the pan. 5 total, 5 radiative. (F) - 3/7
- 9) Connect cooling lines to HFGs. - 3/7
- 10) Wire and shrink-wrap HFG connections. - 3/7
- 11) Connect HFGs to pump. 2 pumps for 10 HFGs. (H) - 3/7
- 12) Place TC trees into the pan and adjust the level. The mark on the TC tree needs to be 119 cm above the ground. (E) - 3/7

- 13) Place TC towers. The mark on the TC tree needs to be 119 cm above the ground. (G) - 3/7
- 14) Mark the water level on the pan (119 cm above the ground). - 3/7
- 15) Place cameras on the North and South legs of the burner. - 3/7
- 16) Place HFG tower to the south end of the pool and attach to the pole with zip ties. (J) - 3/7
- 17) Place HFG's to the tower. 2 total, 5 radiative. (K) - 3/7
- 18) Connect HFG to pump. 1 pump for 7 HFGs. (H) - 3/7
- 19) Run wires to DAQ. - 3/7
- 20) Run the fiber optic cable from DAQ to the control shed through the trench. - 3/7
- 21) Connect fiber optic cable to the computer. - 3/7



3- Instrumentation (OGES):

- 22) OGES will be placed on the South end of the pool. (L) - 3/8
- 23) Attach the tubing, TC and windsock to the windsock frame. (M) - 3/8
- 24) Attach the windsock frame, wheels, wire and pulleys to 12 ft tower. (M) - 3/8
- 25) Connect two towers and insert into the existing frame. (N, O) - 3/8
- 26) Connect guiding wire to the pulley on the ground. - 3/8
- 27) Connect tubing to the gas analyzer. Gas analyzer will be placed close to the OGES tower. - 3/8
- 28) Run the wiring to the DAQ. - 3/8



4- Oil feeding system - Outside:

- 29) Connect recirculation system to the pump. - 3/8
- 30) Place the throttle valve. - 3/8
- 31) Place flow meter and connect to the main tubing. - 3/8
- 32) Connect to DAQ module and system check the Toughbook. - 3/8
- 33) FULL SYSTEM CHECK- 3/8
 - a. Tower TCs
 - b. Fuel TCs
 - c. Fuel HFGs
 - d. Tower HFGS
 - e. OGES
 - f. Blower
 - g. Cameras
 - i. Underwater
 - ii. Go-pros
 - iii. Video cameras
 - iv. Hand cameras

Appendix H – Checklist of Phase III experiments Baseline (Tuesday - 3/14)

1) Pre-test

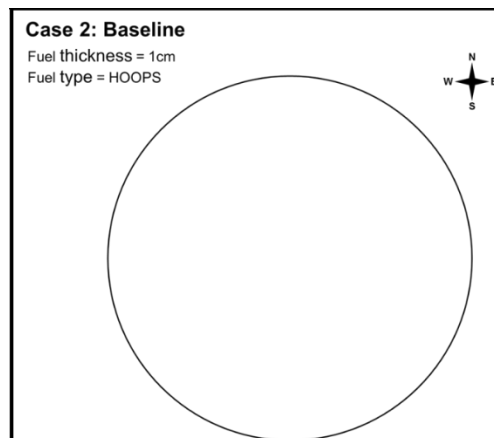
- a) Weigh clean air filters - Oat
- b) Collect samples from water (2 bottles) - Dave
- c) Start HFG pumps – Dave
- d) Start computer and main DAQ system (TC/HFG/OGES) – Oat
- e) Start Toughbook and underwater cameras -Trevor
- f) Start pumping oil until it reaches 1 cm thick. (15.4 lt ~ 4.1 gal ~ 13.4 kg) -Trevor
- g) Start the cameras (3 GoPros, 2 video cameras) - Kemal
- h) Measure the ambient wind speed by vane anemometer - USCG
- i) Make sure emergency provisions are in place. - USCG

2) Ignition

- j) Ignite oil by the torch with extended arm – USCG
- k) Control the fuel level and record the mass pumped – Trevor
- l) Control DAQ - Oat
- m) Take pictures with IR – Dave
- n) Take pictures with hand camera – Kemal
- o) Collect wind data - USCG

3) Post-burn

- p) Save the DAQ data – Oat and Trevor
- q) Collect the data from cameras – Kemal and Oat
- r) Stop HFG pumps - Dave
- s) Collect and weigh the dirty air filters – Oat
- t) Collect the oil residue by absorbent pads – Trevor, Kemal and Dave
- u) Weigh the oil residue – Trevor, Dave and Kemal
- v) Collect water samples (2 bottles) – Dave



Blanket (Thursday - 3/16)

1) Pre-test

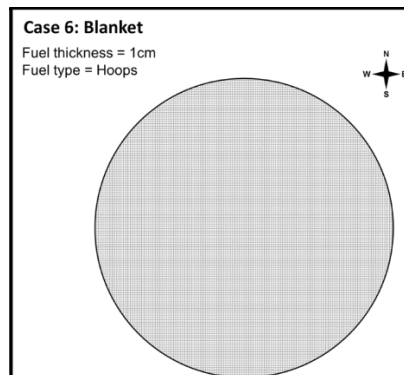
- a) Weigh clean air filters - Oat
- b) Collect samples from water (2 bottles) - Dave
- c) Start HFG pumps – Dave
- d) Start computer and main DAQ system (TC/HFG/OGES) – Oat
- e) Place the blanket into the pan – Dave and Kemal
- f) Start Toughbook and underwater cameras -Trevor
- g) Start pumping oil until it reaches 1 cm thick. (15.4 lt ~ 4.1 gal ~ 13.4 kg) -Trevor
- h) Start the cameras (3 GoPros, 2 video cameras) - Kemal
- i) Measure the ambient wind speed by vane anemometer - USCG
- j) Make sure emergency provisions are in place. - USCG

2) Ignition

- k) Ignite oil by the torch with extended arm – USCG
- l) Control the fuel level and record the mass pumped – Trevor
- m) Control DAQ - Oat
- n) Take pictures with IR – Dave
- o) Take pictures with hand camera – Kemal
- p) Collect wind data - USCG

3) Post-burn

- q) Save the DAQ data – Oat and Trevor
- r) Collect the data from cameras – Kemal and Oat
- s) Stop HFG pumps - Dave
- t) Collect and weigh the dirty air filters – Oat
- u) Remove the blanket – Trevor, Kemal and Dave
- v) Weigh the soaked blanket – Trevor, Kemal and Dave
- w) Collect the oil residue by absorbent pads – Trevor, Kemal and Dave
- x) Weigh the oil residue – Trevor, Dave and Kemal
- y) Collect water samples (2 bottles) – Dave
- z) Collect sample from the blanket
- aa) Remove all the instrumentation and prepare them for shipping. – Trevor, Oat, Kemal and Dave



Appendix I –Derivation of Heat Flux Values in Sec 5.5.

		Rod Burner		Blanket	
		Phase II	Phase III	Phase II	Phase III
1	Test Location	Indoors	Indoors	Indoors	Outdoors
2	Fuel Type	ANS	40% Water – 60% ANS	ANS	HOOPS
3	FR Material	Stainless Steel	Copper	Copper	Copper
4	Pool Diameter, m	0.5	1	0.7	1.4
5	Pool area, m ²	0.2	0.79	0.38	1.54
6	Baseline MLR, g/s (mm/min)	2.5 (0.87)	6.67 (0.6)	6.1 (1.1)	67 (3)
	Blanket MLR, g/s (mm/min)	-	-	8.4 (1.5)	125 (5.6)
	Max MLR with FRs, g/s (mm/min)	6.41 (2.25)	51.7 (4.3)	17.5 (3.1)	382 (17)
7	Baseline HRR , MW	0.11	0.18	0.27	3
	Max HRR with FRs, MW	0.28	1.39	0.79	17.2
8	ER (MW/MW) (mm/min)	2.6	7.75	2.9	5.7
9	Baseline \dot{Q}_{VAP} , KW (KW/m ²)	1.55 (8.1)	8.97 (11.35)	3.84 (10)	42.3 (29)
	Blanket \dot{Q}_{VAP} , KW (KW/m ²)	-	-	1.44 (3.9)	36.53 (25)
	Max \dot{Q}_{VAP} with FRs, KW (KW/m ²)	4 (21)	69.58 (88.07)	10.96 (30)	240.38 (162)
10	Total FR Mass (kg)	8.45	19.01	5.2	18
11	# Collectors	30	59	24	48
12	Mass of collector (kg)	5.88	13.22	3.4	11.5
13	Effective collector \dot{Q}_{VAP_EC} , KW	2.45	60.61	5.68	161.55
14	Effective FR \dot{Q}_{VAP_EFR} , KW	2.45	60.61	7.12	198.1
15	Collector flux (KW/cm ²)	0.10	1.29	1.15	16.8
16	$dT/dx_{x=0}$ (°C/cm ²)	625	322	820	6675
17	Thermal Output, \dot{Q}_{VAP_EC} / Collector mass, KW/kg	0.42	4.58	1.67	14.04
18	Thermal Output, \dot{Q}_{VAP_EFR} / Total mass, KW/kg	0.29	3.18	1.36	11

Table Notes:

$$5. A = \pi D^2 / 4$$

6. MLR = Mass Loss Rate (as measured in tests)

7. HRR = “Heat Release Rate” = MLR × Heat of combustion (45 MJ/kg for pure crude oil and 27 MJ/kg for the 40% water/ANS emulsion).

8. ER = Enhancement ratio = Maximum case with FRs/Baseline

9. Baseline \dot{Q}_{VAP} = Baseline MLR × ΔH_{VAP}

$$\text{Blanket } \dot{Q}_{VAP} = (\text{Blanket MLR} - \text{Baseline MLR}) \times \Delta H_{VAP}$$

$$\text{Max } \dot{Q}_{VAP} = \text{Max MLR} \times \Delta H_{VAP}$$

ΔH_{VAP} = Heat of vaporization, ΔH_{VAP} of crude oil = 627 KJ/kg

ΔH_{VAP} of Water = 2257 KJ/kg

$$\Delta H_{VAP} \text{ of Emulsion} = \frac{(12 \text{ kg of water} \times 2257 \frac{\text{kJ}}{\text{kg}}) + (15.21 \text{ kg of ANS} \times 627 \text{ kJ/kg})}{(12 + 15.21 \text{ kg})} = 1345.85 \text{ kJ/kg}$$

It is noted that the calculated values for ΔH_{VAP} of crude oil and the 40% emulsion are a rough approximation assuming crude oil has the heat capacity similar to a long chain alkane molecule such as nonadecane (19 carbon atoms) and has a boiling point of ~250 °C. Crude oil does not “boil off” in a pool fire. Light fractions may boil off but the more predominant heavy components break down into lighter molecules and vaporize at temperatures in the range of 250 – 350 °C. This breakdown is endothermic and is assumed equivalent to a latent heat of vaporization of ~ 200 KJ/kg.

10.

		FR height (cm)	Diameter (cm)	Volume (cm ³)	Density (kg/cm ³)	# of FRs	Total Mass (kg)
Rod Burner	Phase II	46	1	36.13	7.8	30	8.45
	Phase III				8.92	59	19.01
Blanket	Phase II	Load cell measurements					5.2
	Phase III						18

11, 12.

		Collector height (cm)	Diameter (cm)	Volume (cm ³)	Density (kg/cm ³)	# of FRs	Total Mass (kg)
Rod Burner	Phase II	32	1	25.13	7.8	30	5.88
	Phase III				8.92	59	13.22
Blanket	Phase II	Load cell measurements					3.4
	Phase III						11.5

13. Effective collector $\dot{Q}_{VAP_EC} = [\text{Max } \dot{Q}_{VAP}] - [\text{Baseline } \dot{Q}_{VAP} + \text{Blanket } \dot{Q}_{VAP}]$

14. Effective FR $\dot{Q}_{VAP_EFR} = [\text{Max } \dot{Q}_{VAP}] - [\text{Baseline } \dot{Q}_{VAP}]$

15. Collector flux = [KW per collector] / [cross section area] = $\dot{q}''_{COND, x=0}$ = the conductive heat flux corresponding to the collector output at the fuel interface.

		Number of FRs	Diameter (cm)	Cross sectional Area (cm ²)	\dot{Q}_{VAP_EC} [13]	KW/Collector	KW/Collector/ Cross sectional Area
Rod Burner	Phase II	30	1	0.79	2.45	0.08	0.10
	Phase III	59	1	0.79	60.61	1.02	1.29
Blanket	Phase II	24	0.3	0.07	5.68	0.23	3.28
	Phase III	48	0.4	0.126	161.55	3.36	26.7

16. $dT/dx_{x=0} = \dot{q}''_{COND, x=0} / k$ = temperature gradient corresponding to the collector heat flux [note 15] at the interface of the collector with the heater (also at the liquid surface).

		Collector flux (KW/cm ²)	Thermal Conductivity (W/m-K)	$dT/dx_{x=0}$
Rod Burner	Phase II	0.10	16	625
	Phase III	1.29	400	322
Blanket	Phase II	3.28	400	820
	Phase III	26.7	400	6675

17. Thermal output per collector mass = $\dot{Q}_{VAP_EC} / \text{Collector mass}$

18. Thermal Output per total mass, $\dot{Q}_{VAP_EFR} / \text{Total mass}$

Assumption is made that Blanket and Direct Flame (= "baseline") heat reflux are constant for all tests in each Phase. There may be significant coupling (synergy) effects, especially in Phase III. But the individual contributions (blanket vs flame vs coils) to combined reflux (= Total \dot{Q}_{VAP}) cannot be determined from the test data.